



Influence of multiphysics couplings across scales: from digital rock physics to induced fault reactivation

Author:

Lesueur, Martin

Publication Date:

2020

DOI:

<https://doi.org/10.26190/unsworks/21844>

License:

<https://creativecommons.org/licenses/by-nc-nd/3.0/au/>

Link to license to see what you are allowed to do with this resource.

Downloaded from <http://hdl.handle.net/1959.4/66874> in <https://unsworks.unsw.edu.au> on 2024-04-29



UNSW

THE UNIVERSITY OF NEW SOUTH WALES

Influence of multiphysics couplings across scales: from digital rock physics to induced fault reactivation

Martin Lesueur

School of Minerals and Energy Resources Engineering
Faculty of Engineering
University of New South Wales

A dissertation submitted in partial fulfilment
of the requirements for the degree of
Doctor of Philosophy

Supervisors: Thomas Poulet (CSIRO)
Manolis Veveakis (Duke University)
Klaus Regenauer-Lieb (UNSW)

Reviewers: Yves-Marie Leroy (TOTAL)
Anonymous reviewer

March 2020

Abstract

This work addresses the problem of pressure equilibration across a seemingly sealing fault, which has been observed during reservoir production. Considering the detrimental industrial consequences of seal failure, predictive occurrence of such events, pointing to a temporarily drastic increase of the fault's permeability, becomes necessary for safe subsurface operations. Yet, there is currently no consensus concerning the explanation of this complex phenomenon. The dissertation focuses on carbonate reservoirs under relatively high P,T conditions, whereby suggesting that permeability increase stems from chemical dissolution during the fault reactivation. The production-enhanced shear-heating of the creeping fault leads to thermal runaway, subsequently activating the chemical reaction. This contribution presents a three-scale numerical framework using the REDBACK simulator to account for multiphysics couplings in faults during fluid production. This approach links the reservoir (km) scale - implementing poromechanics both for the fault interface and its surrounding reservoir - with the fault at the meso-scale (m) - implementing a THMC reactivation model - and the micro-scale (μm) - implementing a hydro-chemical model on meshed μCT -scan images. This model can explain the permeability increase during fault reactivation and successfully replicate fault activation, evolution and deactivation features, predicted by common fault reactivation models, yet with continuous transitions between phases. The influence of the rock microstructure on fault and reservoir behaviour is quantified in a simulation where a hydraulically imperceptible difference in the microstructure's geometry results in a different duration of the reactivation event at the macro-scale. We demonstrate the advantage of dynamically upscaled laws compared to empirical laws as we capture permeability hysteresis during dissolution/precipitation of the fault. The alteration of the microstructure also influences mechanical properties and its weakening effect on the homogenised yield stress of 3D printed microstructure samples is accurately predicted by our numerical model. Ultimately, this thesis identifies the potential hazard of fluid production next to a sealing fault under high P,T conditions, which is of great significance as operations are taking place at ever increasing depths. In this regard, we suggest the first model to predict the occurrence and consequences of chemical fault reactivations.



Thesis/Dissertation Sheet

Surname/Family Name	: Lesueur
Given Name/s	: Martin
Abbreviation for degree as give in the University calendar	: PhD
Faculty	: Faculty of Engineering
School	: School of Minerals and Energy Resources Engineering
Thesis Title	: Influence of multiphysics couplings across scales: from digital rock physics to induced fault reactivation

Abstract 350 words maximum: (PLEASE TYPE)

This work addresses the problem of pressure equilibration across a seemingly sealing fault, which has been observed during reservoir production. Considering the detrimental industrial consequences of seal failure, predictive occurrence of such events, pointing to a temporarily drastic increase of the fault's permeability, becomes necessary for safe subsurface operations. Yet, there is currently no consensus concerning the explanation of this complex phenomenon. The dissertation focuses on carbonate reservoirs under relatively high P,T conditions, whereby suggesting that permeability increase stems from chemical dissolution during the fault reactivation. The production-enhanced shear-heating of the creeping fault leads to thermal runaway, subsequently activating the chemical reaction. This contribution presents a three-scale numerical framework using the REDBACK simulator to account for multiphysics couplings in faults during fluid production. This approach links the reservoir (km) scale - implementing poromechanics both for the fault interface and its surrounding reservoir - with the fault at the meso-scale (m) - implementing a THMC reactivation model - and the micro-scale (μm) - implementing a hydro-chemical model on meshed μCT -scan images. This model can explain the permeability increase during fault reactivation and successfully replicate fault activation, evolution and deactivation features, predicted by common fault reactivation models, yet with continuous transitions between phases. The influence of the rock microstructure on fault and reservoir behaviour is quantified in a simulation where a hydraulically imperceptible difference in the microstructure's geometry results in a different duration of the reactivation event at the macro-scale. We demonstrate the advantage of dynamically upscaled laws compared to empirical laws as we capture permeability hysteresis during dissolution/precipitation of the fault. The alteration of the microstructure also influences mechanical properties and its weakening effect on the homogenised yield stress of 3D printed microstructure samples is accurately predicted by our numerical model. Ultimately, this thesis identifies the potential hazard of fluid production next to a sealing fault under high P,T conditions, which is of great significance as operations are taking place at ever increasing depths. In this regard, we suggest the first model to predict the occurrence and consequences of chemical fault reactivations.

Declaration relating to disposition of project thesis/dissertation

I hereby grant to the University of New South Wales or its agents the right to archive and to make available my thesis or dissertation in whole or in part in the University libraries in all forms of media, now or here after known, subject to the provisions of the Copyright Act 1968. I retain all property rights, such as patent rights. I also retain the right to use in future works (such as articles or books) all or part of this thesis or dissertation.

I also authorise University Microfilms to use the 350 word abstract of my thesis in Dissertation Abstracts International (this is applicable to doctoral theses only).

Signature

Witness Signature

.....14/09/2019.....
Date

The University recognises that there may be exceptional circumstances requiring restrictions on copying or conditions on use. Requests for restriction for a period of up to 2 years must be made in writing. Requests for a longer period of restriction may be considered in exceptional circumstances and require the approval of the Dean of Graduate Research.

FOR OFFICE USE ONLY Date of completion of requirements for Award:

ORIGINALITY STATEMENT

'I hereby declare that this submission is my own work and to the best of my knowledge it contains no materials previously published or written by another person, or substantial proportions of material which have been accepted for the award of any other degree or diploma at UNSW or any other educational institution, except where due acknowledgement is made in the thesis. Any contribution made to the research by others, with whom I have worked at UNSW or elsewhere, is explicitly acknowledged in the thesis. I also declare that the intellectual content of this thesis is the product of my own work, except to the extent that assistance from others in the project's design and conception or in style, presentation and linguistic expression is acknowledged.'

Signed

Date 30/08/19

COPYRIGHT STATEMENT

'I hereby grant the University of New South Wales or its agents a non-exclusive licence to archive and to make available (including to members of the public) my thesis or dissertation in whole or part in the University libraries in all forms of media, now or here after known. I acknowledge that I retain all intellectual property rights which subsist in my thesis or dissertation, such as copyright and patent rights, subject to applicable law. I also retain the right to use all or part of my thesis or dissertation in future works (such as articles or books).'

'For any substantial portions of copyright material used in this thesis, written permission for use has been obtained, or the copyright material is removed from the final public version of the thesis.'

Signed

Date

AUTHENTICITY STATEMENT

'I certify that the Library deposit digital copy is a direct equivalent of the final officially approved version of my thesis.'

Signed

Date

INCLUSION OF PUBLICATIONS STATEMENT

UNSW is supportive of candidates publishing their research results during their candidature as detailed in the UNSW Thesis Examination Procedure.

Publications can be used in their thesis in lieu of a Chapter if:

- The student contributed greater than 50% of the content in the publication and is the “primary author”, ie. the student was responsible primarily for the planning, execution and preparation of the work for publication
- The student has approval to include the publication in their thesis in lieu of a Chapter from their supervisor and Postgraduate Coordinator.
- The publication is not subject to any obligations or contractual agreements with a third party that would constrain its inclusion in the thesis

Please indicate whether this thesis contains published material or not.

This thesis contains no publications, either published or submitted for publication

Some of the work described in this thesis has been published and it has been documented in the relevant Chapters with acknowledgement

This thesis has publications (either published or submitted for publication) incorporated into it in lieu of a chapter and the details are presented below

CANDIDATE'S DECLARATION

I declare that:

- I have complied with the Thesis Examination Procedure
- where I have used a publication in lieu of a Chapter, the listed publication(s) below meet(s) the requirements to be included in the thesis.

Name	Signature	Date (dd/mm/yy)
MARTIN LESUEUR		30/08/19

Acknowledgements

I would like to express my utmost gratitude to my two supervisors Dr. Poulet and Dr. Veveakis for taking me on board on this wonderful journey and for their guidance throughout the whole duration of this PhD. I am so fortunate to have been granted the freedom to satisfy my scientific curiosity while being kept on track to produce this meaningful dissertation. Dr. Poulet's sharp sense of logic and extreme care to detail helped me question my own research to be able to really understand it. I am particularly grateful for his time invested during the writing phase of the dissertation and the moral support he provided. I owe Dr. Veveakis my newfound interest in geomechanics, reinforced by his teachings of the discipline. I must also thank him for making me realise the value of my work.

I thank Dr. Leroy for the time and effort he put in reviewing my Thesis and I am grateful for his positive and encouraging comments.

This research was financially supported by UNSW, through my supervisor Prof. Regenauer-Lieb ; CSIRO, through Jens Klump ; and Duke University, through Dr. Veveakis who hosted me for a research exchange in the Multiphysics Geomechanics laboratory to produce the experimental results present in this dissertation.

I acknowledge the technical help provided by the MOOSE mailing list, with specific mentions to John W. Peterson, Fande Kong, Wen Jiang and Andrea Rovinelli.

I thank Dr. Alevizos for his passionate and clear teachings on the theory of multiphysics and multiscale geomechanics and Dr. Rattetz for his thought-provoking conversations and acknowledge his help on developing interfaces law and designing experiments on 3D printed microstructures.

This work has benefited from the contribution of both María Camila Casadiego, for running flow simulations on CT-scans and Timothée Klaeylé, for running mechanical compressions on 3D printed materials.

This research was undertaken with the assistance of resources from the National Computational Infrastructure (NCI Australia), an NCRIS enabled capability supported by the Australian Government and from the Pawsey Supercomputing Centre with funding from the Australian Government and the Government of Western Australia.

I personally thank my dad, Jean-Louis Lesueur, for his industrial feedback.

Last but not the least, I would like to thank my family, my partner, my cat, my colleagues of the Unconventional Geomechanics Group and the ultimate frisbee clubs of UNSW, Duke and Disc Graceful, who all provided me the happiness necessary to pull through this PhD.

Table of contents

List of figures	x
List of tables	xiv
List of symbols	xv
1 Introduction	1
I Three-scale multiphysics framework to model fault reactivation	7
2 Modelling the fault at the physical scale (meso)	8
2.1 Physical formulation	8
2.2 Steady-state behaviour of the system	10
2.3 Rate dependency of the system	12
3 Accounting for the reservoir scale (macro)	15
3.1 Macro-scale model	15
3.1.1 Macro-scale environment	15
3.1.2 Interface laws for the fault	17
3.2 Macro/meso-scale couplings	20
3.2.1 Transfer of boundary conditions	21
3.2.2 Feedbacks to the interface law	21
4 Enriching the meso-scale model from a lower scale (micro)	23
4.1 Micro-scale model	24
4.1.1 Modelling the evolution of the microstructure	24
4.1.2 Representative Elementary Volume (REV)	24
4.1.3 Creating digital rock samples from CT-scan images	25
4.2 Meso/micro-scale couplings	26
4.2.1 Downscaling information from the physical scale	27
4.2.2 Upscaling properties	29

II	Examples of properties homogenised from the micro-scale	32
5	Upscaling of mechanical properties: yield stress	33
5.1	Upper yield: Benchmark of Gurson's criterion	34
5.1.1	Geometry and material considered	35
5.1.2	Homogenisation: Hill-Mandel condition	35
5.1.3	Numerical simulation	37
5.2	Lower yield	40
5.3	Experimental yield	41
5.4	Energetic yield	42
5.5	Summary of the different yield surfaces derived	44
5.6	Validation on 3D printed material	46
5.6.1	3D printing and mechanical testing procedure	47
5.6.2	Proposed experimental protocol to measure the macroscopic yield . . .	51
5.6.3	Mechanical model for 3D printed PLA	54
5.6.4	Forward prediction of the microstructure influence on PLA yields . . .	56
5.7	Application to real microstructure geometry	60
5.7.1	Experimental approach	60
5.7.2	Numerical approach	62
5.7.3	Comparison of the two approaches	64
5.7.4	Extension of the numerical model to viscoplasticity	65
6	Permeability homogenisation of deforming microstructure	68
6.1	Flow simulator (Eulerian)	68
6.1.1	Flow equations at the micro-scale	68
6.1.2	Numerical Implementation	70
6.1.3	Preconditioner	72
6.1.4	Verification of flow simulator	72
6.1.5	Validation of permeability computation	74
6.1.6	Flow on μ CT-scans	78
6.2	Fluid-microstructure coupling scheme (Eulerian-Lagrangian)	79
6.2.1	Mathematical framework	81
6.2.2	Tight vs. sequential coupling	84
6.2.3	Fluid-microstructure interaction under oedometric compression	86
6.3	Influence of chemical dissolution on permeability	88
6.3.1	Erosion/dilation algorithm	90
6.3.2	Deviation of Kozeny-Carman equation due to precipitation	94

III	Influence of multiphysics couplings across scales	97
7	Application to induced fault reactivation	98
7.1	Simulation using the macro/meso-scale model	98
7.1.1	Geological setup	98
7.1.2	Production-induced fault reactivation	101
7.1.3	Slip propagation and synchronisation along the fault	103
7.1.4	Fault deactivation and healing	105
7.1.5	Sensitivity analysis on upscaling points sampling	105
7.2	Comparison with the rate and state law	109
7.3	Influence of the microstructure on the system	112
7.3.1	Permeability hysteresis	112
7.3.2	Influence at the macro-scale	115
8	Summary and conclusions	120
	References	124
	Appendix A Bezier interpolation algorithm	135

List of figures

2.1	Geometry and stress boundary conditions of the fault at the meso-scale, with constant pore pressure and temperature at both extremities.	9
2.2	Stability curves of the system using shear stress as the continuation parameter.	11
2.3	Transient behaviour of the system for an arbitrary loading and unloading.	13
2.4	Transient behaviour of the system for an arbitrary loading and unloading.	14
3.1	Schematic of macro-scale model showing geometry and boundary conditions.	16
3.2	Model used to benchmark the flow interface.	18
3.3	Two-way couplings for the macro/meso-scale model.	20
4.1	Example of meshing workflow on a 2D subsample of the LV60A sand pack (Imperial College Consortium On Pore-Scale Modelling, 2014c).	26
4.2	Meso/micro-scale model: length scales and couplings.	27
4.3	Evolution of the downscaled porosity over time during a fault reactivation for different resolutions $n \times n$ of the micro-scale mesh.	28
4.4	Profiles of porosity across the fault core and damage zone at different time during reactivation (left) and deactivation (right).	29
4.5	Profiles of permeability across of the fault for increasing sampling.	30
5.1	Mesh of the hollow sphere with a porosity of 30%, showing only half for visualisation purposes.	36
5.2	Comparison during a prescribed loading of the hollow-sphere of the two energies defined in Eq. 5.1.	39
5.3	Mesh convergence of respectively the mean (left) and Von Mises (right) stress for the hollow sphere under the loading conditions of Eq. 5.4 with $\alpha = 0.5$ and $\beta = 1$	39
5.4	Mean (left) and Von Mises (right) Stress vs loading time for the hollow sphere of Fig. 5.1, following the loading paths obtained for all couples (α, β) in Table. 5.1.	40
5.5	Yield surface of the hollow sphere in the $p - q$ space for two different porosities $\phi=30\%$ and 12.5%	41
5.6	Lower yield surface for the hollow sphere of porosity $\phi=30\%$ obtained under the loading boundary conditions of Eq. 5.4 for various triaxial ratios.	42

5.7	Figure showcasing the offset method to determine the $X\%$ proof stress. Modified from Ross (1999).	43
5.8	Experimental yield surface for the hollow sphere of porosity $\phi=30\%$ obtained under the loading boundary conditions of Eq. 5.4 for various triaxial ratios.	43
5.9	Derivative of the energy with the loading time vs loading time for various loading paths.	44
5.10	Energetic yield surface for the hollow sphere of porosity $\phi=30\%$ obtained under the loading boundary conditions of Eq. 5.4 for various triaxial ratios.	45
5.11	Different yield surfaces considered in this contribution plotted in the $p - q$ space for the hollow sphere of porosity $\phi=30\%$	45
5.12	Ultimaker 3 at the Innovation co-Lab of Duke University.	47
5.13	Load frame and load cell used for the uniaxial compression testing in this contribution.	49
5.14	Possible deformation modes in compression, figure modified from Kuhn and Medlin (2000).	49
5.15	Displacement fields for deformed sample of different size ratios.	50
5.16	Visualisation of the shear band of the 1.5:1 size ratio sample of Fig. 5.15b at 20% strain under red light.	51
5.17	Stress strain curves of non-porous cylindrical samples of 3D printed PLA for different relaxation times.	52
5.18	Mechanical power dissipated during with loading time.	53
5.19	Stress strain curves of uniaxial compression of 3D printed full cylinders of PLA.	54
5.20	Stress strain curves of uniaxial compression of 3D printed PLA cylinders under different loading rates.	55
5.21	Top view of cylinder compressed at large strains.	56
5.22	Forward prediction of elasticity and characteristic plastic points of 3D printed PLA cylindrical samples with spherical void of varying normalised diameter: 0.6 in red and 0.7 in blue.	57
5.23	Visualisation of the printing quality of the top of the spherical void of the hollow cylinder.	58
5.24	Stress strain curves of uniaxial compression of 3D printed cylinders of PLA containing a spherical void of different normalised diameter: 0.6 in red and 0.7 in blue.	59
5.25	Photos of a hollow cylinder, printed with semi-transparent PLA, in front of red light at two different stages of an uniaxial compression.	59
5.26	Side face of the printed microstructure (a) compared to the digital rock (b).	61
5.27	Top face of the printed microstructure (a) compared to the digital rock (b).	61
5.28	Stress-strain curves of the uniaxial compression of 3D printed samples of digital rock.	62

5.29	Determination of the energetic and experimental yield of the 3D printed samples of digital rock.	63
5.30	Numerical uniaxial compression of a 0.5mm ³ subsample of the Berea sandstone from the Imperial College Consortium On Pore-Scale Modelling (2014a)	64
5.31	Stress-strain curves of the uniaxial compression of 3D printed samples of digital rock.	66
5.32	Simulation results of uniaxial test on a subsample of the LV60A sandpack from Imperial College Consortium On Pore-Scale Modelling (2014c) of size 0.6 mm, meshed with 138,070 elements.	67
6.1	Dimensionless velocity profile on the outlet for Poiseuille flow.	73
6.2	Mesh convergence of the horizontal velocity in the middle of a Poiseuille flow channel, simulated with the Darcy-Brinkman formulation.	74
6.3	Comparison of permeability vs porosity evolution against Kozeny-Carman and results from Larson and Higdon (1989) for a Simple Cubic Packing.	77
6.4	Simulation results on RCP with 942 spheres, showing the flow intensity, streamlines, and mesh elements in parts of the model.	77
6.5	Permeability evolution as a function of the number of spheres for RCP.	78
6.6	Visualisation of pore space and flow intensity and streamlines on a 1.5 mm ³ subsample of LV60A meshed with 1,237,177 elements.	80
6.7	Evolution of permeability with increasing subsample size.	80
6.8	Illustration of the FSI scheme presented in detail in Sec. 6.2.	81
6.9	Benchmark of Eulerian-Lagrangian scheme and selection of numerical value for relaxation parameter ϑ	83
6.10	Validation of Terzaghi's effective stress principle.	84
6.11	Step by step evolution of sequentially coupled hydro-mechanics.	86
6.12	Comparison of convergence between the loose and tight coupling schemes . . .	87
6.13	Oedometric compression for a dry (left) and a saturated (right) digitised rock sample at the peak stress of Fig. 6.14a.	88
6.14	Comparison between purely mechanical and hydro-mechanical simulations. . .	89
6.15	Visualisation of the three types of neighbourhoods.	91
6.16	Erosion of a cube by considering three different types of neighbourhood.	92
6.17	Erosion of a sphere by considering three different types of neighbourhood. . . .	92
6.18	Comparison of the three types of element neighbourhood during the precipitation of a 1.2 mm ³ size sample of the LV60A sand pack from its initial porosity of 37% to a target value of 27%.	93
6.19	Study on the error made on $\Delta\phi$ using the erosion algorithm at different resolutions on a 0.2 mm ³ subsample of the carbonate rock C1 from Imperial College Consortium On Pore-Scale Modelling (2014b)	93

6.20	Permeability evolution (solid line with squares) during the precipitation of a 1.2 mm ³ subsample of the LV60A sand pack from an initial 37.6% porosity down to 5%.	95
6.21	Assessment of the REV non-convergence of the LV60A sample of Fig. 6.20, precipitated to 8% of porosity.	96
7.1	Schematic of boundary conditions.	100
7.2	Outputs of an event of chemical fault reactivation induced by reservoir production, following the setup of Sec. 7.1.1.	102
7.3	Profile of pore pressure along the fault reaching a steady shape during early production.	104
7.4	Profile of permeability along the fault before the first slip event until the full synchronisation of the fault.	104
7.5	Fault reactivation occurrence and duration depending on number of sampling points considered.	106
7.6	Monitoring of the middle of the fault during a chemical fault reactivation induced by reservoir production.	107
7.7	Schematic interpretation of numerical results showing the pressure distribution in the reservoir and fluid velocity in the right-hand-side compartment at different times during the reactivation event.	108
7.8	Velocity vs shear stress of the fault.	111
7.9	Outputs of an event of chemical fault reactivation, following the setup of Sec. 7.1.1, obtained with our multiscale model and with a model implementing a rate and state law for the fault and an empirical permeability evolution.	113
7.10	Visualisation of fluid velocity magnitude at the initial state, peak dissolution and final reprecipitation (left to right respectively) of two different microstructures (α on top and β at the bottom) for the case study of Sec. 7.1.1.	115
7.11	Evolution of permeability of the two different microstructures with respect to porosity.	116
7.12	Outputs during a reservoir production following the setup of Sec. 7.1.1.	118
7.13	Diagram showing a simplified loop of coupled scales and physics allowing for fault reactivation and healing.	119
A.1	Comparison of different weights used to calculate the distance of the control points to the anchor point in the Bezier interpolation of the permeability profile.	136
A.2	Problem (left) and solution (right) with the tangents used for the Bezier interpolation of the permeability profile.	137
A.3	Comparison of the profile of permeability across of the fault at different times for a fault reactivation simulation interpolated linearly or with Bezier between the same five sampling points.	137

List of tables

1	Table of symbols	xv
5.1	Different combinations of α and β values that correspond to loading paths of different triaxiality ratios following Eq. 5.4. The loadings vary from pure shear on the left to isotropic extension on the right.	38
5.2	Mechanical properties measured for the experimental and numerical results of the uniaxial compression of hollow cylinders.	60
7.1	Parameters for the chemical shear zone model (refer to Sec. 2.1) in the geological environment of Sec. 7.1.1.	99

List of symbols

Table 1 Table of symbols

Symbol	Name	Unit of measure
Ar	Arrhenius number	-
K	Kozeny constant	-
Re	Reynolds number	-
α	Thermal conductivity	$kg.m.K^{-1}.s^{-3}$
β	Compressibility	Pa^{-1}
χ	Taylor-Quinney coefficient	-
ε	Solid strain	-
κ	Permeability	m^2
λ	Thermal expansion coefficient	K^{-1}
ω	Molar reaction rates	$mol.m^{-3}.s^{-1}$
μ	Friction	-
μ_f	Fluid viscosity	$Pa.s$
ν	Poisson Ratio	-
ϕ	Porosity	-
ψ	Test function	-
Φ	Trial function	-
ρ	Density	$kg.m^{-3}$
σ	Solid stress tensor	Pa
τ	Shear stress	Pa
ϑ	Relaxation factor	-
A	Pre-exponential factor	s^{-1}
C_p	Specific heat capacity	$m^2.K^{-1}.s^{-2}$
c	Cohesion	Pa
d_s	Grain/sphere diameter	m
D	Thickness	m
E	Young's modulus	Pa
$E_{+,-}$	Activation energy of forward or reverse reaction	$J.mol^{-1}$
g	Standard gravity	$m.s^{-2}$
H_F	Fault thickness	m
h	Height	m
k	Permeability	D
L	Length	m
M	Molar mass	$kg.mol^{-1}$
n	Normal unit vector	-
p_f	Fluid pressure	Pa
p	Mean stress	Pa
q	Von Mises stress	Pa
R	Gas constant	$J.K^{-1}.mol^{-1}$
S	Specific surface area	m^{-1}
s	Solid ratio	-
T	Temperature	$^{\circ}C$
t	Traction	Pa
u	Displacement	m
V	Volume	m^3
v	Velocity	$m.s^{-1}$
w	Tangent unit vector	-
\cdot^*	Normalised variables	-
\cdot^{ref}	Reference values	-
X_m	Mixture average	$(1 - \phi)X_s + \phi X_f$

Chapter 1

Introduction

Faults are characteristic features of a subsurface reservoir because of their pronounced role in its fluid trapping and integrity. Faults can act as fluid conduits or barriers (Faulkner et al., 2010), which makes them critical to reservoir compartmentalisation, an essential aspect for the design of any energy application, from traditional petroleum accumulation and production, to CO₂ storage or geothermal energy. Compartmentalisation occurs when flow is prevented across ‘sealed’ boundaries in the reservoir, usually faults. This common exaggerated description actually refers to formations of very low permeability, at the reservoir boundaries, that reduce cross-flow to infinitesimally slow rates (Jolley et al., 2010), allowing fluids and pressures to equilibrate across a boundary over geological timescales, but acting as seals over production time-scales (Wibberley et al., 2008). As such, during energy operations, direct contact with faults is usually actively avoided throughout the drilling phase. Nonetheless, interferences of wells with a side-seal fault during injection or stimulation phases remain frequent, with the most notable risk being those of induced earthquakes during CO₂ injections (Zoback and Gorelick, 2012) or hydraulic fracturing of unconventional reservoirs (Holland, 2013) for instance.

Fluid injection is not the only cause of fault slippage, however, and fluid production is also known to induce stress changes in the reservoir that can be large enough to reactivate nearby dormant faults (Segall, 1989). Indeed, on top of eye-opening cases like the Lacq field (Segall et al., 1994) and several cases in the North Sea (Zoback and Zinke, 2002) in the 1980s, the detailed database of Wilson et al. (2017) of recorded induced seismicity around the world exposes how frequently these events occur, with currently a growing concern in Oklahoma, for instance, about the multiplication of such events (Keranen et al., 2014).

Interestingly, following the reactivation of a fault, pressure equilibration between the two sides of the fault can sometimes be observed, as mentioned below. A sealing fault then becomes a flow channel, at least temporarily, which can provoke two types of situations depending on the fluid pressure of the rock layer adjacent to the produced reservoir. If its pressure is below the producing pressure, leakage of the reservoir into the adjacent layer will take place. A detailed example of this scenario is studied by Wiprut and Zoback (2000). For the opposite case of overpressure, fluid invasion will happen in the reservoir and this can lead to the problematic early water breakthrough (Correa et al., 2013; Dos Santos and Oliveira, 2014). Both cases

are extremely detrimental and can render a reservoir completely inoperable at engineering time-scales, irrespective of the type of application.

This process of a fault reactivating with simultaneous permeability increase is characteristic of a *fault-valve* behaviour, as described in the seminal work of [Sibson et al. \(1988\)](#). The accumulation of fluids at the fault builds up the stress that eventually forces the fault to reactivate. The fluid is discharged along the fault for a short period of time, usually followed by a self-healing of the fault due to mineral precipitation of those flowing fluids in the fault veins. This phenomenon happens also during the hydrocarbon migration phase when a potential trap is charging in hydrocarbons but the accumulation of fluid reactivates the fault and the hydrocarbons escape along the fault in overlying reservoirs ([Faulkner et al., 2010](#)). The modelling of this complex phenomenon during petroleum production is announced as one of the modern challenges in geomechanics, particularly in Brazil for instance, where "*reactivation must be avoided at any cost*" ([Serra de Souza and Lima Falcão, 2015](#)).

Current state-of-the-art considerations in fault reactivation modelling usually start with a poroelastic model describing the reservoir, in order to first account for the stress changes at the fault due to the pressure depletion induced by the fluid production. In such an approach, the fault is treated as a frictional interface, and reactivation triggering follows the coulomb failure criterion ([Jaeger, 2007](#)), allowing to determine the location and timing of reactivation events. Furthermore, the resulting evolution of the slip rate can be modelled with a rate and state ([Dieterich, 1979](#)) or a linear slip-weakening law ([Andrews, 1976](#)). This purely poromechanical framework has proven capable of matching multiple case studies already (e.g. [Cappa and Rutqvist, 2011](#)), but more physical effects remain to be accounted for, like temperature effects for instance, since thermal pressurisation was shown to be a predominant term in the weakening of some faults ([Rice, 2006](#)). Temperature, however, is rarely modelled during fault reactivation due to the complexity of handling its impact at the various time scales involved for the stress, pore pressure and heat propagations, around the fault and in the reservoir. Accounting for temperature is therefore more complex than directly implementing an empirical interface law and requires multiscale modelling. Following the same concept, the interface law at the reservoir-scale can be enriched by including different information such as the multi-porosity/multi-permeability nature of porous media from the study of [Wang and Sun \(2018\)](#).

Regardless of the degree of realism reached for the mechanical slip, a notable limitation to both the Coulomb Failure Stress and Rate and State approaches is their inability to explain effectively a permeability increase concomitant to the fault's reactivation. In order to couple the reactivation to an increase of permeability, faults are commonly characterised by their aperture, which evolves with the normal and shear strain ([Olsson and Barton, 2001](#)). This theory allows to fit multiple case studies (e.g. [Bandis et al., 1983](#); [Olsson and Barton, 2001](#)), however it suffers from a difficult calibration process and does not provide an explanation for the healing of the fault since the accumulation of shear strain is an irreversible process. In addition, studies have shown that purely mechanical models cannot model orders of magnitude of permeability increase

observed in some case studies (Cleary et al., 2015; Zhang et al., 2016) and Zhang et al. (2016) suggest another physical explanation for the increase of permeability: chemical dissolution.

The aim of this work is to provide the multiscale and multiphysics numerical tools to model specific fault reactivation events linked to permeability evolution, due to fluid-producing chemical reactions. In such cases, hereinafter referred to as chemical fault reactivations, the fault slip can lead to a multiphysics chain of events characterized by an increase of pore pressure and temperature, as well as chemical reactions. This phenomenon was shown to occur naturally at great depths (Poulet et al., 2014b), but can also be expected at lower depths when induced by external events like subsurface operations. Indeed, puzzling cases of permeability evolution caused by fault reactivation events have already been observed at reservoir operating depth, e.g. 3.5 km (Eyre et al., 2019) and less than 1 km (Pizzino et al., 2004; Sulem et al., 2005). We suggest that such events could be symptomatic of chemical fault reactivations, noting in particular the existing microstructural observations of dissolution from laboratory experiments in brittle conditions (Han et al., 2007; Toro et al., 2011). As a final reference, we quote Plane et al. (2017) that notes:

“the capacity of carbonate minerals (calcite and dolomite) to deform by ductile and physico-chemical processes, like dynamic re-crystallization or fluid assisted pressure-solution even at conditions of shallow burial (<3 km)”

With that hypothesis in mind, we focus on cases with specific conditions where a fault of appropriate chemical composition is already close to criticality and we model the resulting production-induced reactivation event. Such fault behaviours are particularly non-intuitive in the context of petroleum engineering, as they occur in a brittle environment, yet they involve ductile processes. Not only could our hypothesis provide a novel understanding for perplexing cases, but the ductile nature of the phenomenon also yields results which are mainly tied to the physics of the processes involved, making the analysis of such scenarios much more tractable than for brittle events, influenced instead by geometrical and material heterogeneities. The occurrence of such fault reactivations could therefore be more predictable than traditional events, which sparks the interest in developing a first theoretical model of the processes at play during this unique phenomenon. Note that the calibration of the model for historical cases is a non-trivial exercise which would require specific data and falls therefore outside the scope of this work.

Chemically active faults are treated as elasto-viscoplastic domains, with mineralogies that are prone to dissolution/precipitation reactions triggered by temperature increase during slip. The reactivation of such chemically active faults can be modelled with the chemical shear zone model of Alevizos et al. (2014), which extends the rate and state law for ductile rocks that are temperature and rate sensitive in a chemical environment. That theory has been successfully applied to explain the stick-slip behaviour of subduction zones (Veveakis et al., 2014), as well as spatial features of exhumed carbonate thrusts (Poulet et al., 2014b), all requiring specific temperature conditions involving depths of several kilometres (Poulet et al., 2014b) for episodic reactivation events to take place. The same model can also lead to one-off events much more easily, in environments with much lower forces involved (Poulet et al., 2014a). Given the fact that

more than 50% of global gas reserves are estimated to be held in carbonate reservoirs (Burchette, 2012), this chemical type of fault reactivation actually represents a major case study that will only become more relevant as reservoir operations are getting increasingly deeper. Considering this type of reactivation, a substantial permeability increase can get generated during fault slip by chemical dissolution, and the healing of the fault after discharge can easily be explained with a precipitation sealing mechanism.

The relationship between chemical dissolution or precipitation and permeability is commonly modelled with an empirical law between porosity and permeability, Kozeny-Carman arguably being the most famous one. While the law provides a satisfactory fit for most cases, its limitations are well-known (Scheidegger, 1974) and particularly for our case study, does not work well using porosity changes stemming from shear deformations (Wong and Li, 2001). The reason is that the porosity scalar only represents one of the possible variables to characterise the microstructure and can therefore not capture all microstructural effects effectively. Arns (2009) focused on deriving more of those characteristic numbers that can be obtained from micro Computed Tomography (μ CT) images. The other possible approach is not to reduce the information contained in the microstructure. Indeed, CT technology has reached a level of maturity such that research based on CT-scan images has moved from pure visualisation to quantified characterisation, opening the door to physical modelling. Access to digital porous rocks at high resolution has enabled the development of computational approaches to complement - with the goal of ultimately replace - more expensive laboratory experiments. Such numerical approaches resolve directly the transport equations in micro-tomographic images (Mostaghimi et al., 2012) and remove the uncertainties introduced by the empirical nature of the scaling factors used to fit the experimental data (Andrä et al., 2013).

Fluid flow at the pore-scale is governed by the Navier-Stokes equations (Batchelor, 2000), which can be challenging to solve efficiently on 3D digital rocks. Pioneering methodologies are based on discretisation of the continuum equations by means of numerical schemes like the finite difference (FDM) (Manwart et al., 2002; Mostaghimi et al., 2012), finite volume (FVM) (Guibert et al., 2015; Petrasch et al., 2008), or finite element (FEM) (Borujeni et al., 2013; Narváez et al., 2013) methods. These methodologies compute permeability by estimating volume-averaged physical properties. Another traditional approach to evaluate pore-scale flow is the Lattice Boltzmann (LBM) method, which is a simplification of the Navier-Stokes problem that considers fluid as fictitious particles instead of solving the continuum conservation equations (Manwart et al., 2002; Narváez et al., 2013). All these methods have been proven capable of computing permeability and other effective properties directly on μ CT images (Andrä et al., 2013), with particular methods being selected depending on the end goal application. Some methodologies have proven more popular than others, including the LBM and FDM/FVM due to their computational efficiency. Such techniques allow the flow computation on 3D meshes with refinements approaching the resolution of the most recent CT-scanners. This numerical efficiency, however, can come at the cost of flexibility and those popular techniques are not necessarily the most adequate to solve extended systems of equations, when other physical processes are

considered. Indeed, in order to quantify the effect of chemical alterations on permeability, the fluid flow needs to be fully resolved on the deformed microstructure, and then homogenised to a permeability value. Since the current focus in pore-scale flow simulations has turned to computation on deforming microstructure, these homogenised laws of permeability are generated from hydro-mechanical or -chemical simulations, using, however, a predefined deformation path. While such homogenised laws can prove useful at a larger scale for relatively homogeneous deformations, they remain valid only for this specific deformation path. They would particularly fail to display any permeability hysteresis, that Teklu et al. (2016) showed experimentally for instance, because the law obtained is completely reversible. Conversely, we suggest using a homogenisation of permeability embedded in a multiscale framework, where the deformation path is dynamically dictated by the meso-scale, so that the law obtained applies literally and can take into account the history of deformations of the medium.

The current investigation presents a fluid flow implementation at the μm -scale using the Multiphysics Object-Oriented Simulation Environment (MOOSE) (Gaston et al., 2009), a FEM platform. As such, this flow simulator can be easily linked to solid mechanics models, in particular the elasto-viscoplastic approach implemented in REDBACK (Rock mEchanics with Dissipative feedBACKs) (Poulet et al., 2017). The flow simulator can deal with complex pore geometries and boundary conditions that allow a rigorous solution of the Navier-Stokes equations (Zabaras and Samanta, 2004). This solution works on unstructured meshes, which are appealing for pore-scale modelling because local refinement allows an accurate description of heterogeneous porous media and avoids the unnecessary computational power of full refinement (Borujeni et al., 2013). The modularity of the FEM libraries facilitates the coupling of this flow module with other physical modules, either in a sequential or tightly coupled manner. In this contribution we present applications using both approaches to highlight their respective potentials.

To account for the role of the outer domain (reservoir) on the stresses acting on the fault, we use a multiscale approach. At the reservoir (km) scale, the reservoir is modelled as a poro-elastic medium and the fault is treated as a frictional interface, with its frictional response calculated at a separate lower-scale simulation. At the fault (m) scale, the fault is allowed many more physical mechanisms, being considered as a thermo-hydro-chemo-elasto-visco-plastic domain. The micro-scale (μm) is added for the refinement of the permeability evolution, implementing a hydro-chemical model on meshed μCT -scan images.

The macro and meso scales are solved with FEM as well, as commonly done for continuum modelling of mechanical problems. The use of a common platform, REDBACK, for this FE^3 framework is enabled by the use of the *multiapp* capability of MOOSE that manages the distribution of embedded applications (called *subapps*) automatically and the transfer functions that can pass information to each *subapp*.

We start by introducing the implementation of this three-scale framework in Part I, with the governing laws at each scale (macro, meso and micro in Chapters 2, 3 and 4 respectively) as well as the coupling schemes between them. Part II presents specifically some important

homogenisation results between the micro- and meso-scales, upscaling in Chapter 5 the rock yield and in Chapter 6 the permeability due to mechanical and chemical deformations. Part III presents the application of the framework of Part I, linking all its elements in Chapter 7, to the upscaling of permeability during a generic geological scenario of induced chemical fault reactivation. Eventually Chapter 8 summarises how all the components were successfully put together and highlights the main findings of this thesis.

We bring to your attention that most of the content of Chapters 2-3-4-8, as well as Sections 6.3, 7.1 and 7.3 were published in (Lesueur et al., 2020). Most of the content of Sections 6.1 and 6.2 was published in (Lesueur et al., 2017).

Part I

Three-scale multiphysics framework to model fault reactivation

Chapter 2

Modelling the fault at the physical scale (meso)

The system of equations controlling the behaviour of the fault at the centimetre to metre scale (Figure 2.1) is derived in detail in (Alevizos et al., 2014) and briefly summarized in this chapter. The reader is referred to (Poulet et al., 2017) for further precision. In essence, the fault initially in a creeping regime, with negligible displacement at engineering time scales, yet produces heat from internal friction which can lead to thermal runaway (Regenauer-Lieb and Yuen, 1998). The sudden increase in temperature from the fault reactivation triggers a calcite decomposition reaction which dramatically increases the permeability of the fault, allowing pressure equilibration across. This evolution can be described through the mass, momentum and energy balance equations with a set of constitutive laws.

2.1 Physical formulation

The calcite decomposition reaction responsible for the permeability increase can effectively be written as $CaCO_{3(s)} \rightleftharpoons CO_{2(f)} + CaO_{(s/f)}$, as supported by the laboratory experiments of Han et al. (2007). We note that the calcium oxide, however, is an unstable product that would in turn react further. As such, we consider that half of it ends up being dissolved through reactions that go beyond the scope of this study, since the exact identification and quantification of such chemical reactions remains an active research topic in geochemistry. Previous studies (Alevizos et al., 2014; Poulet et al., 2014a,b; Veveakis et al., 2014) showed that this assumption allows to capture appropriately the response of the system. The dissolution reaction can be cast in a more generic framework of endothermic chemical dissolutions expressed as $AB_{(solid)} \rightleftharpoons A_{(solid)} + B_{(fluid)}$. This reaction is characterised by its energetics properties (activation energy E , Arrhenius number Ar_c) as well as its kinetics ones (forward and reverse reaction rates and pre-exponential factors A). The advancement of the chemical reaction is described implicitly through its temperature and pressure evolution. Specifically, the forward (subscript +) and reverse (subscript -) reaction

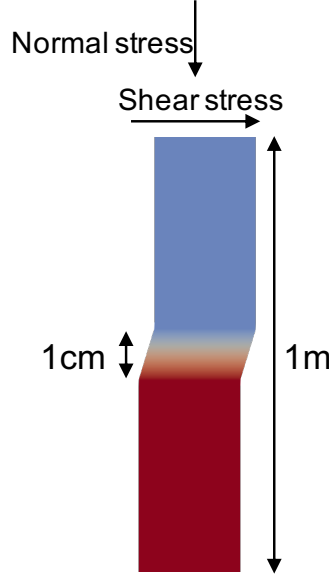


Fig. 2.1 Geometry and stress boundary conditions of the fault at the meso-scale, with constant pore pressure and temperature at both extremities. Fault transverse size is cropped for visualisation purposes.

rates ω_+ and ω_- are defined as

$$\omega_+ = A_+(1-s)(1-\phi) \frac{\rho_{AB}}{M_{AB}} e^{-E_+/RT} \quad (2.1a)$$

$$\omega_- = A_- s(1-\phi) \Delta\phi_{chem} \frac{\rho_A \rho_B}{\rho_{AB}} \frac{M_{AB}}{M_A M_B} e^{-E_-/RT} \quad (2.1b)$$

with all symbols defined in Table 1.

The energy balance equation provides the temperature evolution within the fault

$$(\rho C_p)_m (\partial_t T + v_i^{(m)} \partial_i T) = \nabla(\alpha \nabla T) + \chi \sigma_{ij} \cdot \dot{\epsilon}_{ij}^p - (E_+ - E_-)(\omega_+ - \omega_-) \quad (2.2)$$

with χ the Taylor-Quinney coefficient. $V_i^{(k)}$ represents the velocity for the phase $k \in \{s, f\}$. This equation shows that the temperature of the fault can increase due to mechanical dissipation (shear heating) and is balanced by the diffusion term and the energy sink coming from the endothermic chemical reaction considered.

The mass balance equation for a fully saturated rock modelled as a solid(s)-fluid(f) mixture, using Darcy's law, can be expressed as

$$\beta_m \partial_t p_f - \lambda_m \partial_t T + v_i^\beta \partial_i p_f - v_i^\lambda \partial_i T - \partial_i \left(\frac{k}{\mu_f} (\partial_i p_f - \rho_f g_i) \right) + \partial_i (v_i^{(s)}) = \left(\frac{1}{\rho_f} - \frac{1}{\rho_s} \right) \omega_+ M_B \quad (2.3)$$

with $v_i^\beta = [(1-\phi)\beta_s v_i^{(s)} + \phi\beta_f v_i^{(f)}]$ and $v_i^\lambda = [(1-\phi)\lambda_s v_i^{(s)} + \phi\lambda_f v_i^{(f)}]$. Equation 2.3 uses a simplified Equation of State of the form $\frac{d\rho^{(i)}}{\rho^{(k)}} = \beta^{(k)} dp_f - \lambda^{(k)} dT$, $k \in \{s, f\}$. This mass balance

equation accounts for the Thermo-Hydro-Mechanical-Chemical processes modelled through the compressibility, thermal expansion, volumetric strain and chemical flux between solid and fluid phases. The permeability k is assumed to evolve, following the common Kozeny-Carman law as a function of porosity $\frac{k}{k_0} = \frac{\phi^3 (1-\phi_0)^2}{\phi_0^3 (1-\phi)^2}$. Note that the porosity variable evolves with the volumetric strain.

The mechanical deformation is solved by the momentum balance under quasi-static assumption (Alevizos et al., 2014), leading to the evolution of effective stress σ' as

$$\partial_j \sigma'_{ij} - \partial_i p_f + \rho_m g_i = 0 \quad (2.4)$$

We assume an elasto-visco-plastic model. Isotropic linear elasticity is described by Young modulus and Poisson ratio ; plasticity is modelled with an overstress visco-plastic formulation using a flow law of the type $\dot{\epsilon} = \dot{\epsilon}_0 (\Delta\sigma)^m e^{-Ar_m \frac{T_0}{T}}$, where $\Delta\sigma$ represents the overstress. This model presents a rate-hardening effect and in opposite a temperature softening. We use a J2 yield envelope to respect the fact that the existing fault consists of already pulverised grains and shears without volume change (Rattez et al., 2018). For this reason, we selected $\chi = 1$ to represent the fact the mechanical energy is not consumed through grain size reduction but solely with shear heating.

This multiphysics system of equations highlights the complexity of the various feedback processes involved, which are solved in dimensionless form for the displacement, temperature and pore pressure, using the finite element simulator REDBACK (Poulet et al., 2017). Even though the problem is 1D, the system is solved in 2D plane strain with periodic boundary conditions, in order to access both normal and shearing components of the stress. While we are interested only in the behaviour of the plastic fault core, heat still dissipates further than the fault core in the elastic region. We therefore model a larger cross section, see Fig. 2.1, up to where shear heating gets dissipated and far field boundary conditions of temperature can be applied. Moreover, this distance was shown to be the physical length scale of the shear zone system by Poulet et al. (2017), which makes this scale in a sense the master-scale of the system, also referred to physical scale in this contribution. By capturing the physics at this scale only, Alevizos et al. (2014) have indeed been able to match real case studies of episodic tremors for example.

2.2 Steady-state behaviour of the system

The first step to understand the behaviour of the model is to investigate its stability regimes with respect to some parameters of interest by solving the system of equations in steady-state. The sensitivity analysis is performed using a numerical bifurcation analysis in REDBACK (Tung et al., 2017) based on a pseudo-arclength continuation method from Keller (1977). It can provide a continuous evolution of the mathematical solution of the steady-state system with respect to a given parameter, including unstable solutions. This approach is particularly well adapted to track

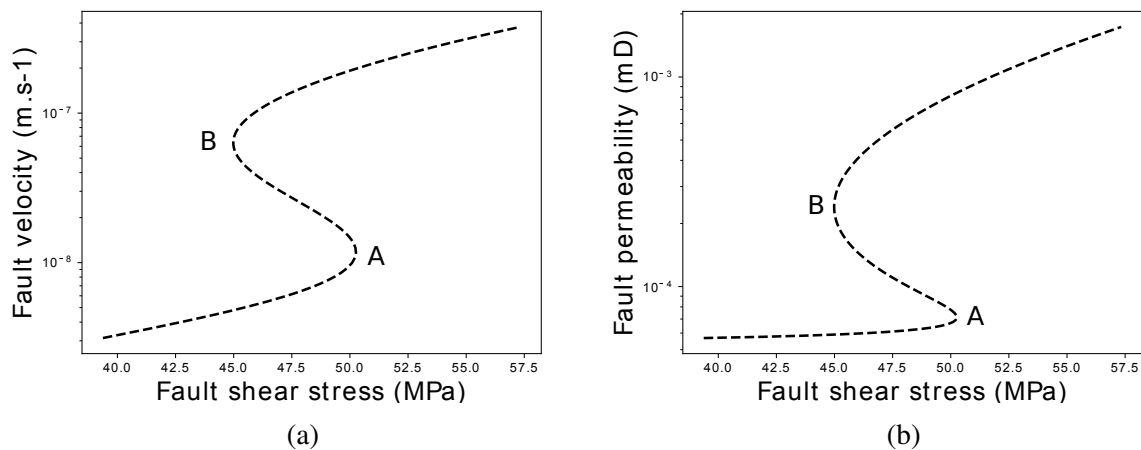


Fig. 2.2 Stability curves of the system using shear stress as the continuation parameter.

the influence of parameters leading to instabilities such as fault reactivation as can be seen in the original study of the chemical shear zone problem (Alevizos et al., 2014). For the problem of fault reactivation described in Section 7.1.1, the critical parameter controlling the fault movement at the meso-scale is the deviatoric stress of the fault i.e. shear stress, which is evolving at the reservoir scale during production. We select therefore the shear stress boundary condition as continuation parameter to study its influence on the fault stability at the meso-scale.

Fig. 2.2a and 2.2b show respectively the evolution of slip rate and permeability of the fault and both illustrate the same behaviour. Both figures display a characteristic "S-curve" response of the system explained in details in Alevizos et al. (2014), with three distinct branches. The main driver of the system is the temperature evolution, governed by the thermo-mechanical coupling between shear heating and thermal weakening of the flow law, quantified by the Arrhenius number Ar_m . The lower branch, displayed in solid line on Fig. 2.2, corresponds to the creeping regime in which the fault is slipping at low velocity (in the order of cm/year) over the whole range of shear stresses. It represents the case where the fault is shearing slowly enough for the corresponding frictional heat produced to be diffused, keeping the system in the slow creep regime. The thermally activated chemical decomposition is therefore proceeding slowly and the permeability of the fault remains nearly constant, at a low value. The second branch forming the S, displayed in dashed line, is the unstable part of the curve (see Alevizos et al., 2014) and represents a separatrix between the stable lower and upper branches for the range of shear stress values (between 45 and 50 MPa approximatively) where three possible solutions exist. The higher branch corresponds to the reactivated fault, creeping at much faster rate and characterised by a much higher permeability as the chemical decomposition is fully active. This branch corresponds to the case where the heat generated exceeds its diffusion rate and triggers the chemical decomposition reaction

Having established the stability regimes of the system, we now run a transient simulation simulating an induced chemical fault reactivation then deactivation, starting at an initial shear stress value of 47.6 MPa corresponding to the geological conditions of a carbonate fault near

criticality at 4km depth, dipping at 60° (scenario from Sec. 7.1). The shear stress is then arbitrarily moved in two successive phases detailed below. Fig. 2.3 superposes the results of this transient simulation on top of the steady-state continuation curve displayed on Fig. 2.2.

During a first phase, the shear stress is increased up to a value of 51.5 MPa to reproduce the scenario of nearby well production. The results show on Fig. 2.3 that the velocity is initially increasing continuously with shear stress from the initial state (marked with a star) to the first turning point of the stability curve (point A1). This increase of slip velocity is augmenting progressively, along with temperature, due to the thermo-mechanical coupling between shear heating and thermal weakening of the flow law, quantified by the Arrhenius number Ar_m . Bratu (1914) showed that this behaviour is unstable, leading to a thermal runaway. Passed a critical value of shear stress, 50 MPa (point A1), the fault then reactivates as the slip velocity jumps by more than two orders of magnitude, reaching the upper branch at point A2. The capping of the thermal runaway is due to the endothermic nature of the chemical reaction (Veveakis et al., 2010), which stops the temperature instability and keeps the fault in a stable, activated state. The fault activation event is marked simultaneously by a corresponding jump in permeability (see Fig. 2.3b) as the temperature activated chemical decomposition is actively producing fluid. Further increase of the shear stress moves the system along the upper branch of the S-curve, keeping the velocity and permeability of the fault to high values and augmenting with shear stress (up to the arbitrary end value of 51.5 Mpa).

During a second phase we simulate a stress drop that the fault would experience after activation due to its resulting increased slippage. The stress is decreased from the end value of the first phase, 51.5 MPa, to an arbitrary end value of 43.6 MPa. During the first phase of this stress decrease, we can see that the fault stays activated, as the corresponding steady-state tracing the segment of the upper branch of Fig. 2.3 between the points A2 and B1. The stress decrease leads indeed to progressive reduction in velocity and permeability through the thermo-mechanical coupling. This process continues until a critical value of stress is reached, 45 MPa, at which point (B1 on Fig. 2.3) the amount of energy input into the system through shear heating fails to balance the energy dissipated through heat diffusion and the endothermic chemical dissolution. The response of the fault is to drop from point B1 to B2, on the stable lower branch characteristic of the creeping regime with a low velocity. This drop is accompanied by a return of the chemical state close to its original equilibrium through the reverse precipitation reaction which brings back the permeability to a low value. Passed this event, any further evolution of the shear stress moves the fault along the lower branch as explained in the previous paragraph.

2.3 Rate dependency of the system

This stability analysis conducted in the previous section is critical as a preliminary step to determine the key parameters of our system. It provides for example the existence and location of the critical points A and B (see Fig. 2.2) as well as the velocity of the fault after activation. It

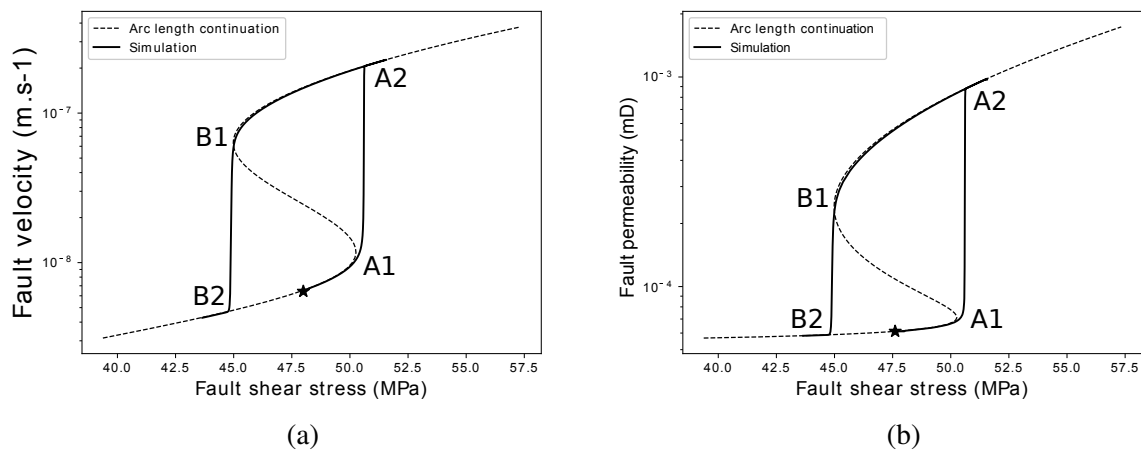


Fig. 2.3 Transient behaviour of the system for an arbitrary loading and unloading. Results are compared with the continuation of Fig. 2.2. The star represents the start of the simulation.

can also determine the permeability of the fault after dissolution when the fault has reactivated which is necessary to characterise the leakage of the reservoir after the loss of fault seal.

This steady-state analysis, however, does not account for the dynamics of the system and it is therefore necessary to solve the transient problem to check whether the short production time, compared to the geological time-scale, affects the general behaviour that can be understood from Fig. 2.2. One could indeed expect some discrepancies due to the transition time required for variables like temperature to switch from one branch to the other. Another interesting aspect to investigate is the rate dependency of the system since the loading rate on the fault depends on the production flow rate applied at the well, which varies during oil and gas operations depending on the production strategy targeted. In this regard, Fig. 2.4 presents two additional transient simulation results based on the same activation/deactivation scenario shown in Fig. 2.3 but with slower and faster loading rates. As expected, the response of the system depends on the flow rate and the three resulting curves of Fig. 2.4 do not superpose, with a difference mostly visible during the unstable path from point B1 to B2 (drop from the higher to the lower branch), and to a lesser extent from point A1 to A2 (jump to from the lower to the higher branch). This difference is easily explained by the fact that the rate dependency is more pronounced during those two transitions, which are quasi-instantaneous. Naturally, a faster loading rate will displace point A2 further along the stress axis and a faster unloading rate will move point B2 to a lower stress value on the lower branch.

It is interesting to note that all results of the transient configurations tested still superpose mostly to the original S-curve. This means that the system remains very close to steady-state when moving along the lower or upper branch and it highlights the critical importance of a steady-state analysis to understand the overall response of a transient scenario. The behaviour of such a chemical fault is mostly driven by the coupled physics of all processes involved and transient phenomena only affect the results at the second order.

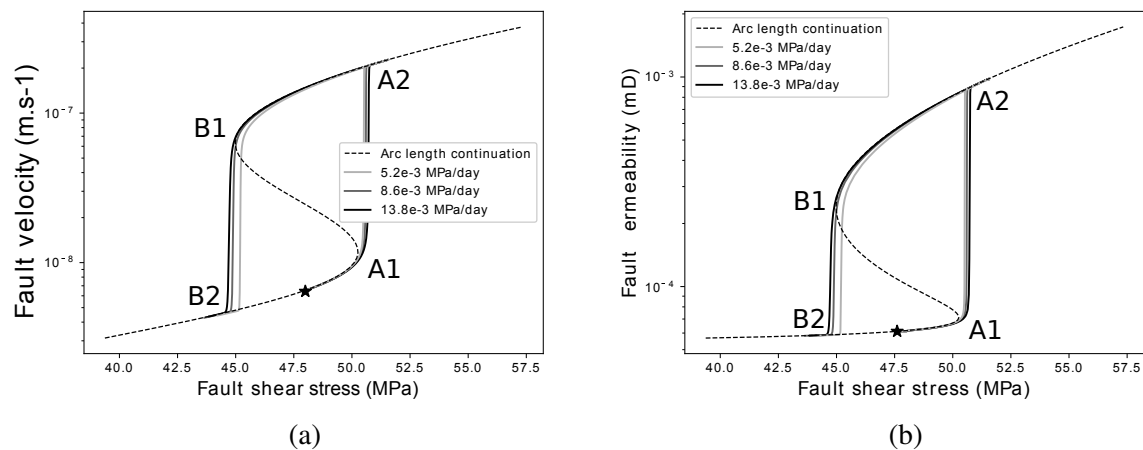


Fig. 2.4 Transient behaviour of the system for an arbitrary loading and unloading. The different curves correspond to different loading/unloading rates and the curves are superposed with the stability analysis of the system. The star represents the start of the simulation.

This section focused on explaining the physical model used for characterising the ductile behaviour of chemically active faults in high P,T environments. The final results obtained in this section show that the transient behaviour of the fault in Fig. 2.3 can be for the most critical parts approximated by the steady state behaviour of Fig. 2.2. Interestingly this figure is directly derived from the combination of the physical mechanisms implemented in Eq. 2.2, 2.3, 2.4. In summary the fault behaviour at such temperatures can be explained predominantly by the physics of the processes involved, contrary to shallower brittle fault where geometry and material heterogeneity control the behaviour of brittle failures. This allows our model to be more predictive towards the detection of fault reactivation and this study showcases the importance of monitoring for example the temperature of deep faults as it is the main tracer of the thermal runaway responsible of the fault activation, discussed in Sec. 2.2.

Chapter 3

Accounting for the reservoir scale (macro)

While the meso-scale model presented in Sec. 2.1 captures accurately the behaviour of a fault during a reactivation event, the evolution of the principal slip zone and fault core cannot be decoupled completely from the larger scale. Far field stresses and fluid pressure perturbations can indeed have major impacts on faults, with studies reporting that injection wells could reactivate faults as distant as 90 km apart with a more accepted average impact distance around 10 km (Peterie et al., 2018). Without neglecting the importance of other scenarios where faults can be reactivated by drilling directly into them, in this contribution we focus on that less intuitive case of distant reactivation.

The steady-state analysis of the fault at the meso-scale (Alevizos et al., 2014) shows that it is possible to observe episodic stick-slip movements under specific circumstances. Such cases, however, are usually restricted to extreme tectonic environments like subduction zones (Veveakis et al., 2014) or megathrusts (Poulet et al., 2014b). For all other cases, the model of Sec. 2.1 leads to constant creep steady-state, whether slow – locked faults at engineering time-scales – or fast. Under those conditions, a fault reactivation can only be triggered by a change in boundary conditions, which can be accounted for by the modelling of the larger scale. This section describes the macro-scale model selected to simulate a fluid pressure perturbation, including its effect on the fault through pore pressure and stress changes (Sec. 3.2.1) as well as the feedbacks of the fault evolution on the larger scale (Sec. 3.2.2).

3.1 Macro-scale model

3.1.1 Macro-scale environment

For the sake of simplicity, we consider a generic 1 km wide model of a fully saturated fluid reservoir, as shown in Fig. 3.1, separated in two distinct compartments by an impermeable dipping fault. Various scenarios could be distinguished based on the possible applications to the fields of nuclear waste storage, carbon capture and storage, groundwater extraction, or oil and gas production, but we keep a non-specific scenario to illustrate the more general approach. A fluid perturbation is induced at a source point, located 50m from the fault, and can affect the

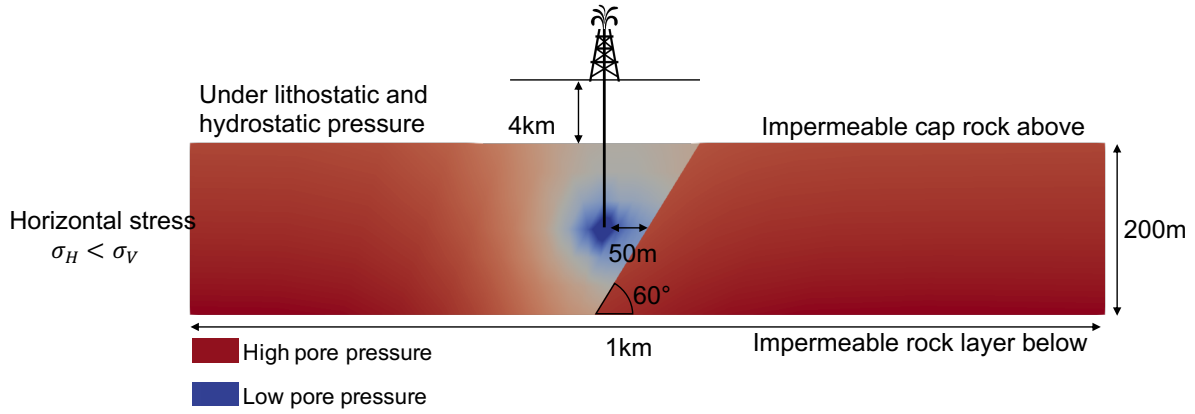


Fig. 3.1 Schematic of macro-scale model showing geometry and boundary conditions.

fault stability through the three physical processes considered: pore fluid pressure, stresses and temperature.

Fluid pressure p and (Cauchy) stress σ_{ij} are linked through the classical poromechanical concept of effective stress (Terzaghi, 1923) $\sigma'_{ij} = \sigma_{ij} - p\delta_{ij}$. A fluid overpressure reaching the fault through diffusion can then classically trigger a fault reactivation through the resulting drop of effective stress (Segall, 1989). This scenario is conveniently illustrated by the Mohr circle, shifted by the pore pressure change and eventually touching a pressure-dependent yield surface.

The existing scale separation between the kilometre-scale reservoir and the fault, with a thickness of the order of metres or less makes the computational costs for resolving such features numerically very high. This results both from the considerable number of fine mesh elements required as well as the associated time-step size reduction to accommodate smaller elements. It is therefore represented by a zero-thickness interface and its behaviour is described using interface laws to link all variables on both sides, as presented in the next section.

The reservoir at the macro-scale is mainly influenced by the fluid's movement and resulting mechanical deformation through the poromechanical couplings. The fluid motion at this scale is largely governed by the permeability and the flow obeys Darcy's law. Note that for the sole purpose of showcasing the framework in this contribution, we focus on the application example of fluid production, see Chapter 7. In addition, the shear heating of the fault has no neighbouring influence at the scale of the reservoir. For these reasons, we consider for the macro-scale model that the temperature in the reservoir remains constant and do not model its evolution. Overall, the large scale model is well characterised by the momentum and mass balance equations, including gravity, written as

$$\partial_j \sigma'_{ij} - \partial_i p + \rho_m g_i = 0, \quad (3.1)$$

$$\partial_i p - \partial_i \left[\frac{k}{\mu_f} (\partial_i p - \rho_f g_i) \right] = 0, \quad (3.2)$$

where ρ_m is the density of the solid-fluid mixture. Even though the fault undergoes some important plastic strain, plasticity usually remains restricted to the principal slip zone and

surrounding fault core. We consider therefore the reservoir to deform elastically even when the fault slips. Without loss of generality, we select an isotropic linear elastic constitutive model characterised by the Young's modulus E and the Poisson ratio ν .

3.1.2 Interface laws for the fault

The negligible thickness of the fault compared to the length scale of the reservoir justifies the choice of modelling the fault as an interface, rather than facing the prohibitive computational costs associated with the discretisation of that feature at the large scale. The fault is then modelled at the meso-scale and considered at steady state at each timestep at the macro-scale, with its impact accounted for at that level through interface laws implemented in REDBACK for the mechanics and fluid flow, allowing us to solve hydro-mechanical simulations with discontinuous fields of pore pressure and displacement.

We take advantage of the support for interfaces in the MOOSE framework, which handles automatically the duplication of nodes at interfaces and allows the handling of discontinuous variables simply through the implementation of the weak form terms needed at the interface.

Hydraulic

The flow behaviour at the fault interface, described by its normal vector $n_i^{(F)}$, is a critical feature for the macro-scale simulation. Faults can indeed form impermeable barriers between reservoir compartments, which have been known to transform temporarily into fluid pathways during fault reactivations, as reported in the cases of [Wiprut and Zoback \(2000\)](#) and [Dos Santos and Oliveira \(2014\)](#). To model this behaviour, the interface is assigned an effective thickness H_F and permeability $k^{(F)}$ so the difference of pore pressure between the two sides of the interface (F), denoted by the exponents (A) and (B), can be computed using Darcy's flow. Assuming fluid incompressibility, the continuity of flux can be written as

$$\frac{k^{(R)}}{\mu_f}(\partial_i p^{(R)} - \rho_f g_i)n_i^{(F)} = \frac{k^{(F)}}{\mu_f}(\partial_i p^{(F)} - \rho_f g_i)n_i^{(F)}, \quad (3.3)$$

where the exponent (F) and (R) refer to the fault (interface) and reservoir respectively. The gradient of pressure across the interface is computed as

$$\partial_i p^{(F)} n_i^{(F)} = \frac{\Delta p}{H_F} = \frac{p^{(A)} - p^{(B)}}{H_F}. \quad (3.4)$$

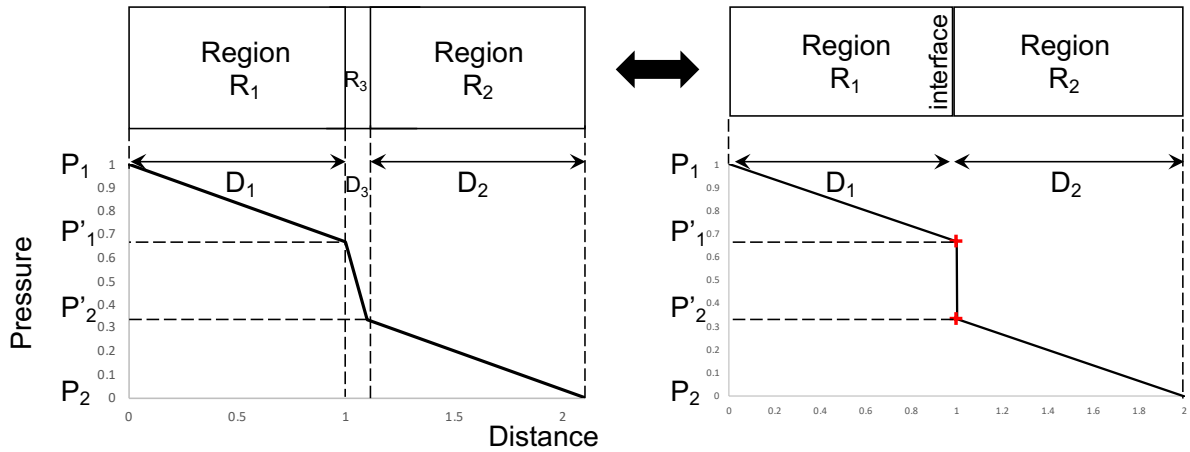


Fig. 3.2 Model used to benchmark the flow interface. The specific case plotted is described by $D_1 = D_2 = 10 \times D_3$; $p_1 = 1$ and $p_2 = 0$; $k_1 = k_2 = 10 \times k_3$. On the left are plotted the result for the system fully resolved and on the right for the reduced system with interface. The system with interface matches with machine precision the results of the full system, highlighted with the red crosses.

Combining 3.4 and 3.3 we end up with an equation for the interface law defined for each pressure variable as:

$$-\frac{k^{(A)}}{\mu_f} p_{,i}^{(A)} n_i^{(F)} + \frac{k^{(F)}}{\mu_f} \frac{p^{(B)} - p^{(A)}}{H_F} + \frac{\rho_f g_i n_i^{(F)}}{\mu_f} (k^{(A)} - k^{(F)}) = 0 \quad (3.5)$$

$$-\frac{k^{(B)}}{\mu_f} p_{,i}^{(B)} n_i^{(F)} + \frac{k^{(F)}}{\mu_f} \frac{p^{(B)} - p^{(A)}}{H_F} + \frac{\rho_f g_i n_i^{(F)}}{\mu_f} (k^{(B)} - k^{(F)}) = 0 \quad (3.6)$$

To verify the implementation of this pore pressure interface, we compare the results against an analytical problem for a simple one-dimensional (1D) case. We consider three regions (R_1 , R_2 , R_3) of various thicknesses (D_1 , D_2 , D_3) and permeability values (k_1 , k_2 , k_3), as shown in Fig. 3.2 and solve for the steady-state of the 1D horizontal flow through. We apply a pressure gradient across these three blocks with constant boundary conditions at each end (p_1 and p_2). The two pressures p'_1 and p'_2 at the interface between the regions 1-3 and 2-3 can be expressed as:

$$p'_2 = \frac{k_1 k_3 D_2 D_3 p_1 + k_2 D_3 (k_1 D_3 + k_3 D_1) p_2}{(k_3 D_2 + k_2 D_3) * (k_1 D_3 + k_3 D_1) - k_3 k_3 D_1 D_2}, \quad (3.7)$$

$$p'_1 = \frac{k_1 D_3 p_1 + k_3 D_1 p'_2}{k_1 D_3 + k_3 D_1}. \quad (3.8)$$

This analytical solution is used to validate the numerical results obtained by solving a similar problem where the middle region is replaced by a flat interface, on Fig. 3.2.

Mechanical

The mechanical behaviour of the fault can also be accounted for at the macro-scale with an interface, to accommodate the displacement generated by a slip event modelled with an arbitrary friction law or in the case of this contribution with the dynamic upscaling of the meso-scale model. Given the negligible thickness of the fault at the large scale, the problem reduces to a sliding block problem and we use the same environment as described above for the flow. We introduce the two displacement fields $u_i^{(A)}$ and $u_i^{(B)}$ on both sides of the fault, marking the discontinuity at the interface.

For a sliding block problem, common interface approaches include frictional laws such as rate-and-state laws. Interestingly, the model presented in Section 2.1 presents a generalisation of the rate-and-state friction law through a physical approach which identifies the role of temperature and pore pressure in the evolution of the effective friction coefficient (Veveakis et al., 2017). This model offers therefore a more general tool in the specific context of chemical shear zones, extending the knowledge from the more empirical approaches. To integrate that model in our multiscale framework we introduce a mechanical interface law which takes for input a displacement jump between each side of the interface and that is compatible with the value of the stresses applied to the fault through the constitutive model assumed.

The displacement jump $\Delta u_i^{(F)}$ follows the equation:

$$u_i^{(A)} - u_i^{(B)} + \Delta u_i^{(F)} = 0 \quad (3.9)$$

It can be noted that the normal displacement discontinuity across the shear zone is negligible since most of the deformations happen in shear and the shear zone itself has a negligible size at the macro-scale. It means that the displacements are discontinuous only tangentially to the fault, with the transversal effects of dilation accounted for at the meso-scale, and it simplifies Eq. 3.9 to

$$u_i^{(A)} - u_i^{(B)} + \Delta u_i^{(F)} w_i^{(F)} = 0 \quad (3.10)$$

with $w_i^{(F)}$ the tangent unit vector of the fault.

In addition to this constraint on the displacement, the mechanical law for the interface needs to respect the stress equilibrium. This condition translates to the continuity of the traction across the interface and this relationship is written as:

$$(\sigma_{ij}^{(A)'} + p^{(A)} \delta_{ij}) n_i^{(F)} = (\sigma_{ij}^{(B)'} + p^{(B)} \delta_{ij}) n_i^{(F)} \quad (3.11)$$

Note that the total stress is continuous despite the fluid pressure discontinuity at the interface (see Sec. 3.1.2), making the effective stress discontinuous as well.

The two conditions (Eq. 3.9 and 3.11) are enforced weakly using a penalty method. Eq. 3.9 is used to define the error $\delta u_i = u_i^{(A)} - u_i^{(B)} - \Delta u_i^{(F)}$, which can be interpreted physically by considering a virtual spring at the interface with a high spring constant α , that we take as the penalty parameter. Following this approach, the traction on each side of the interface is equal

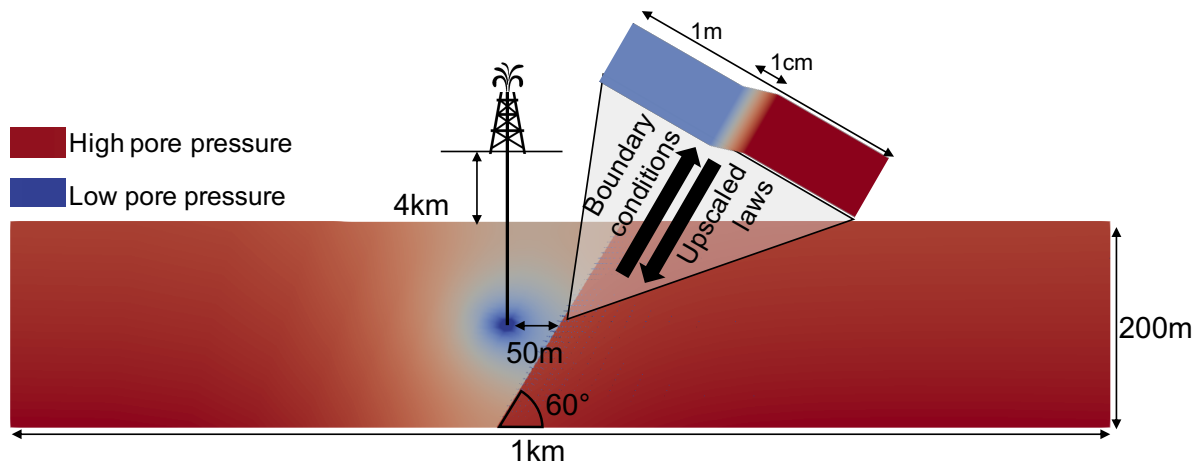


Fig. 3.3 Two-way couplings for the macro/meso-scale model.

to the product of α times the elongation δu_i of the spring, which enforces continuity of the traction across the interface. Numerically, the higher the value of α , the smaller the error δu_i on our displacement discontinuity condition. In this contribution, the value of 10^6 proved to be sufficient.

3.2 Macro/meso-scale couplings

In order to have a model that can study real phenomena of fault reactivation and their consequences, the connection of the macro-scale to the meso-scale is necessary. Indeed, as stated before, the meso-scale cannot simulate a realistic scenario of fault reactivation because the perturbation that cause it happens at a larger scale. On the other hand, the macro-scale model alone is also insufficient: it lacks a physical law for the interface that links the stress experienced by the fault to both the slippage and the evolution of permeability.

These holes can be filled by considering a macro/meso-scale model that couples both the scales. In this multiscale model, the perturbation simulated at the macro-scale is transferred to the interface and applied as a boundary condition for the meso-scale. The meso-scale is now solving for a dynamic boundary value problem that can actually place the fault reactivation in its context. The macro-scale can in turn obtain the missing constitutive law for the interface by upscaling directly the behaviour of the fault from the meso-scale. These couplings are summarised in Fig. 3.3.

In order to have the interface fully characterised, common multiscale models would select directly all the nodes on the interface to perform an upscaling. However, in order to reduce on computational costs, we choose to select only certain points of interest along the interface and interpolate the upscaled properties in between.

3.2.1 Transfer of boundary conditions

The macro scale provides the dynamic boundary conditions for the meso-scale. These boundary conditions are the normal and tangential stress to the fault, the two pore pressures and the temperature that are applied to the fault at the macro-scale.

For simplicity, we consider the fault at the meso-scale in its local referential as seen in Fig. 3.3 (where the fault is horizontal). Since the fault is cutting the reservoir with a dip angle of θ , see Fig. 3.1, the two referential are rotated from one another by θ . It means that we need to transfer from the macro-scale the normal and tangential stress in the local referential of the fault. The formula is derived by decomposing the traction vector at the fault, defined standardly as $t_i = \sigma_{ij}n_j$, into his normal (N) and tangential (T) component in the local referential of the fault.

$$t_i = t_i^{(N)} + t_i^{(T)} = \sigma_{ij}n_j \quad (3.12)$$

$$t_i^{(N)} = (t_j n_j) n_i = ((\sigma_{jk} n_k) n_j) n_i \quad (3.13)$$

$$t_i^{(T)} = t_i - t_i^{(N)} = \sigma_{ij}n_j - ((\sigma_{jk} n_k) n_j) n_i \quad (3.14)$$

As seen in Eq. 3.13-3.14, the formulas make use of the normal vector n_i . Since n_i is computed for each element separately in the finite element simulator. We do not need to assume a linear fault dipping at a given angle θ , the interface can be a curve with a normal vector n_i defined at each discretised segment.

3.2.2 Feedbacks to the interface law

Displacement discontinuity The mechanical interface law takes in input the stress applied to the fault and returns the displacement discontinuity tangential to the fault. Contrary to most interface laws, it does not assume any constitutive law to solve for this discontinuity. Instead it upscales a physical law from the meso-scale.

With the set of boundary conditions provided from the macro-scale, the chemical shear zone model can solve for the displacement across the shear zone. The difference of displacement between each side of the shear zone is the discontinuity of displacement that is transferred to the macro-scale and applied at the interface's corresponding material point using Eq. 3.10.

Permeability evolution The macro-scale needs to capture the evolution of permeability, being solved at the meso-scale, in order to simulate the pressure equilibration that happens after reactivation of the fault. For this reason, the permeability of the fault computed at the meso-scale is transferred and applied on the fault at the macro-scale. The upscaling of this permeability is not straightforward. The reason is that when reactivation occurs, a part of the fault dissolves. The permeability is therefore not homogeneous across the fault at the meso-scale. The homogenisation we want to perform has to respect the condition that the averaged Darcy flow across the fully-saturated fault at the meso-scale is equal to the flow inputted in the interface law of

Sec. 3.1.2. This condition translates to:

$$\frac{k^{(F)}}{\mu_f} \frac{p^{(B)} - p^{(A)}}{H_F} = \frac{1}{H_F} \int_A^B \frac{k^{(M)}}{\mu_f} \partial_i p^{(M)} n_i^{(F)} \quad (3.15)$$

where (M) design the meso-scale values. With Eq. 3.15, we can express the homogenised value of permeability for the fault as:

$$k^{(F)} = \frac{1}{p^{(B)} - p^{(A)}} \int_A^B k^{(M)} \partial_i p^{(M)} n_i^{(F)} \quad (3.16)$$

Chapter 4

Enriching the meso-scale model from a lower scale (micro)

On top of all efforts to homogenise micro-processes at the meso-scale (see Chapter 2), direct modelling of specific phenomena at the micro-scale can add a level of refinement that cannot be accounted for by static homogenisation. In this contribution the lower scale of interest is the one at the micrometre level where the microstructure can be discretised as pore space and solid matrix. At this scale, the complex evolution of the pore microstructure results from the interplay between geometry and the major non-linear feedbacks linking all physical processes involved, mechanical, thermal, hydraulic, chemical. In turn the evolution of this microstructure affects the upper scale in terms of homogenisation of material properties and constitutive relationships. Selecting the list of properties to upscale is a balancing act between accuracy and computational cost. As mentioned in Chapter 2, capturing the essence of a micro-scale process at the meso-scale also presents huge benefits for the stability analysis, which can then quantitatively account for. As such, even though many phenomena are rooted at the micro-scale, only a limited number of critical ones will usually be upscaled numerically for each of the THMC physics.

For the flow, upscaling of permeability has been an active area of research since the discovery of using μ CT-scanning for rocks (see review from [Blunt et al., 2013](#)). The relationship between porosity and permeability for instance, which can even be negatively correlated in some cases (e.g. [Morin, 2006](#)), is inherently dependent on the pore or grain structure. It can't always be represented by empirical laws to use directly at the meso-scale and does require specific modelling at the micro-scale to capture the inherent complexity. The other common upscaling is the mechanical behaviour where discretising the grains using Discrete Element Method allows to upscale directly a constitutive mechanical model at the upper scale ([Nitka et al., 2011](#)) and helps resolve regularisation of the mechanical localisation ([Desrues et al., 2017b](#)). The upscaling of thermal processes is usually not done since the temperature is considered constant at the micro-scale. Regarding the chemistry, the upscaling process is tedious as the micro-scale involves the interplay of numerous chemical reactions.

This contribution covers most processes mentioned above, distributed as follows. Chapter 5 will focus entirely on the upscaling of mechanical properties. The focus will be centred around

the yielding of the material that is particularly important in the context of fault reactivation as it affects directly the onset of the reactivation. Chapter 6 focuses on the upscaling of fluid flow. At the meso-scale the flow is dictated by Darcy's law, which means that it is directly controlled by the permeability selected then as the property to upscale. In the context of a fault reactivation in a reservoir, the permeability is the most important parameter as it affects both the onset of reactivation (Alevizos et al., 2014) and the amount of resulting leakage across the fault. Chapter 5's interest lies specifically on the onset of reactivation and for this reason the influence of the microstructure will be analysed at constant porosity since the change of porosity before the reactivation is negligible. However, Chapter 6 looks at the full evolution of the microstructure because of the permeability influence on the whole behaviour of the fault reactivation. Chapter 6 tackles the main challenge of capturing the permeability evolution with porosity, which has been shown to greatly evolve during the event of reactivation in Chapter 2.

With the objective of simulating the multiphysics problem of induced fault reactivation that involves all three scales in Chapter 7, we select the upscaling of the permeability as the illustrative application for our meso/micro-scale framework, whose description is the purpose of this chapter. We will first cover the necessary aspects of the micro-scale model needed to capture the influence of the microstructure of the pore space. The second section will address the two-way couplings that are used when incorporating the micro-scale in our multiscale framework.

4.1 Micro-scale model

4.1.1 Modelling the evolution of the microstructure

To study the impact of the microstructure on properties like permeability, we need to characterise the evolution of this microstructure, which is influenced by multiple physical processes. Thermal expansion induces the swelling of grains. The competition of the pore pressure and the mechanical stresses can result in either pore collapse or hydraulic fracturing and this hydromechanical feedback will be addressed in Chapter 6. Chemical alterations however, whether dissolution or precipitation, have the most influence in our specific context of chemical fault reactivation. As the predominant driver of the rock microstructure evolution, this process is selected to illustrate the framework in this chapter and will also play a major role in the final three-scale application in Chapter 7. Note that the geometrical modelling of the chemical alterations on the microstructure is detailed in Sec. 6.3.

4.1.2 Representative Elementary Volume (REV)

The homogenisation of a property like permeability requires to be working on a REV of the pore structure for this specific property in order for the homogenisation approach to be valid (Bear, 1972; Hill, 1963). Interestingly, a REV for the geometry of the pore structure itself does not infer that the REV is achieved for the property considered. For example, Mostaghimi et al. (2012) showed for multiple digitised rocks that porosity had a much smaller REV than permeability.

The determination of the REV size for a given microstructure remains a challenging task and for instance even the existence of the REV for heterogeneous rocks like carbonate remains an open question (Mostaghimi et al., 2012). An extra level of complexity gets added when considering chemical alterations. Dissolution and precipitation mechanisms change indeed the geometry of the microstructure dynamically which in turn affects the REV size. For the purpose of showcasing the framework, the difficult question of determining the REV falls outside the scope of this contribution and the REV convergence study is only done when computationally manageable.

4.1.3 Creating digital rock samples from CT-scan images

Simulations at the micro-scale require a 3D mesh capturing the geometry of the pore space and solid matrix. In this section we present the approach for obtaining digital rock samples from μ CT-scan images. As the name implies, the digital rock samples are reconstituted μ CT-scan images in the form of a finite element mesh. Since raw μ CT-scan images display however only a density variation in a continuous grayscale manner, a first pre-processing treatment of the image, called segmentation, is needed in order to differentiate the rock matrix from the pore space. To obtain the final digital rock samples, we have developed a framework (Fig. 4.1) to construct 3D meshes from a stack of already segmented 2D μ CT-scan images in two steps.

Image reader

The first step consists in reading the information from each segmented image (Fig. 4.1a) using the Visualisation ToolKit library (Schroeder and Martin, 2005), where the pore space and grains are represented by black and white pixels respectively, of *intensity* 0 and 1. This pixel data is transformed to domain information on the regular generated mesh (Fig. 4.1b), and the interface between the grains and pore space is automatically tagged. The resolution of the mesh created and the original images are not necessarily linked, even though it is recommended to use the same.

Mesh adaptivity

To optimise the mesh quality while reducing computational costs, a second step can be performed to keep the resolution of the pore-grain interface and coarsen the mesh in the zones far away from this interface. This step is computed by tracking the difference in *intensity* gradient between two neighbouring elements, as this gradient is null between neighbouring voxels of same nature and strictly non-null at the pore-grain interface. The mesh can be coarsened iteratively where the intensity difference is zero (within numerical precision), following a traditional octree method (Meagher, 1982). Note that the MOOSE numerical simulator can handle this type of inconsistent meshes (Gaston et al., 2009). As such, the maximum number of coarsening levels is computed as the exponent of the factor two in the initial pixel number. For example, a mesh of 300 pixels

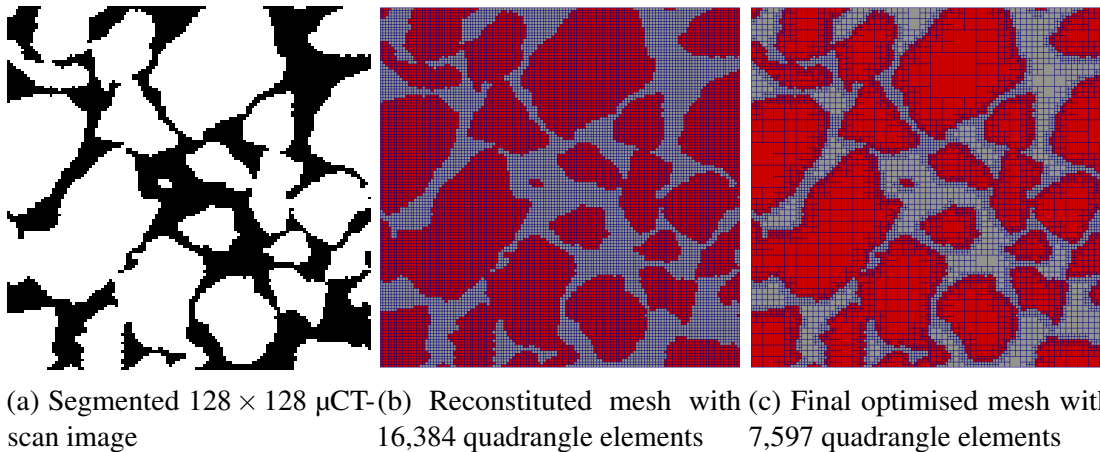


Fig. 4.1 Example of meshing workflow on a 2D subsample of the LV60A sand pack (Imperial College Consortium On Pore-Scale Modelling, 2014c).

in each direction provides a maximum of two levels of refinements since $300 = 75 \times 2^2$. The resolution of the initial mesh is therefore selected in order to maximise the possible coarsening.

In the end we obtain a 3D mesh with optimal refinement from the stack of μ CT-scan images, as shown in Fig. 4.1c.

4.2 Meso/micro-scale couplings

The micro-scale mesh obtained in the previous section can be used to refine the computation of selected material properties for each timestep and on each sampling point of the mesh at the meso-scale. For each chosen point, this is done in sequential steps illustrated in Fig. 4.2. Some meso-scale information is transferred to the micro-scale, where it can be used, most often as boundary conditions, for a separate simulation. The results of that simulation are then upscaled and placed back at the original point of the meso-scale mesh, ready to use for the following timestep.

In our multiscale model, we select the permeability as the property to upscale based on the evolution of the microstructure due to chemical alterations. Chemical reactions at the micro-scale can include many different aspects which remain active fields of research, including fluids mixing, fluid-rock interactions, advection, diffusion, electrochemical migration and all coupled combinations of those processes (see review from Yoon et al. (2015)). A comprehensive micro-scale chemical simulator falls therefore outside the scope of this thesis and we follow instead an illustrative approach by considering a homogenised model of the chemical reaction considered as presented in Chapter 2. For the application to fault reactivation, the advantages of using an analytical computation of chemical porosity evolution at the meso-scale outweigh largely the drawbacks of not simulating the chemical reactions directly at the micro-scale. The benefits are clear in terms of numerical efficiency (speed and convergence) but also for the resulting ability to run stability analyses (Alevizos et al., 2014) to understand and quantify the impact of all material parameters. The change of porosity $\Delta\phi_{chem}$ stemming from chemical dissolution/precipitation is

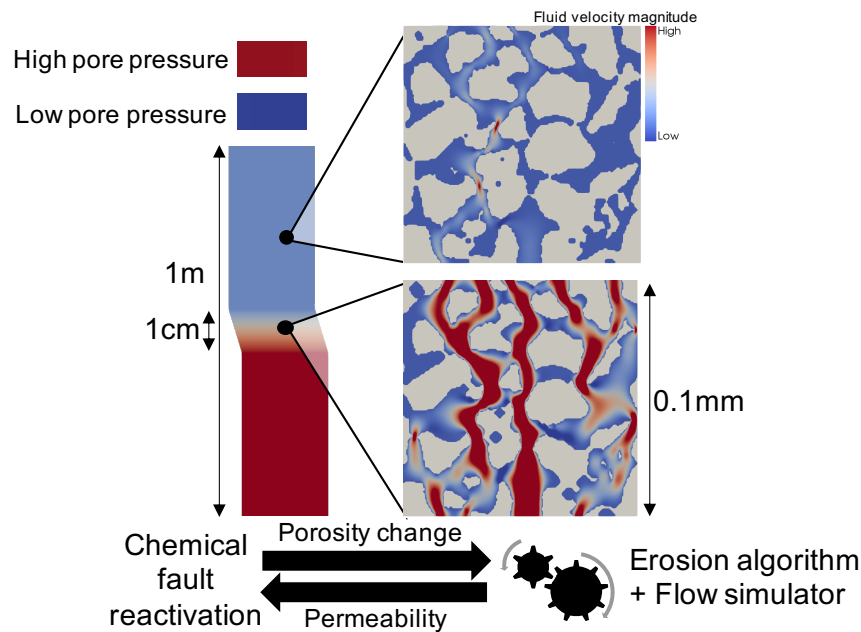


Fig. 4.2 Meso/micro-scale model: length scales and couplings. Note the drastic increase of fluid velocity between a point in the dissolved fault core and one further away from the center.

then computed at the meso-scale and downscaled at the micro-scale through an erosion/dilation algorithm presented in Chapter 6. This allows the permeability to be computed with a flow simulation at that level and upscaled at the meso-scale.

The first section addresses the downscaling of $\Delta\phi_{chem}$ while the second section explains how a smart interpolation is used to upscale the permeability on the whole mesh of the meso-scale with only a few upscaled points of interest.

4.2.1 Downscaling information from the physical scale

In this framework, the information transferred down from the meso-scale is the evolution of porosity due to chemical dissolution/precipitation, $\Delta\phi_{chem}$, which is not passed as a boundary conditions but used directly as a target for the erosion/dilation algorithm to get distributed spatially across the mesh of the microstructure. This erosion algorithm must apply the changes of porosity to the μ CT-scan in the same way the dissolution/precipitation would have been simulated and the detailed explanation of the algorithm and the validity of its assumptions is left for Sec. 6.3.1. Two important aspects, however, are worth mentioning here. Firstly, the erosion algorithm can be qualified of *discrete* in nature. Every element of the mesh is indeed treated in a boolean manner as either grain or pore space, which implies that the distributed porosity cannot be a continuous field. The erosion can then be qualified of discrete in that sense. Secondly, the amount of erosion imposed is applied homogeneously across the whole surface of the pore-grain boundary. Reaching the target $\Delta\phi_{chem}$ is then a matter of eroding or precipitating the appropriate number of layers on that boundary. This discretisation of the erosion affects directly the fitting quality of the porosity evolution in time. Fig. 4.3 compares the evolution of the (continuous)

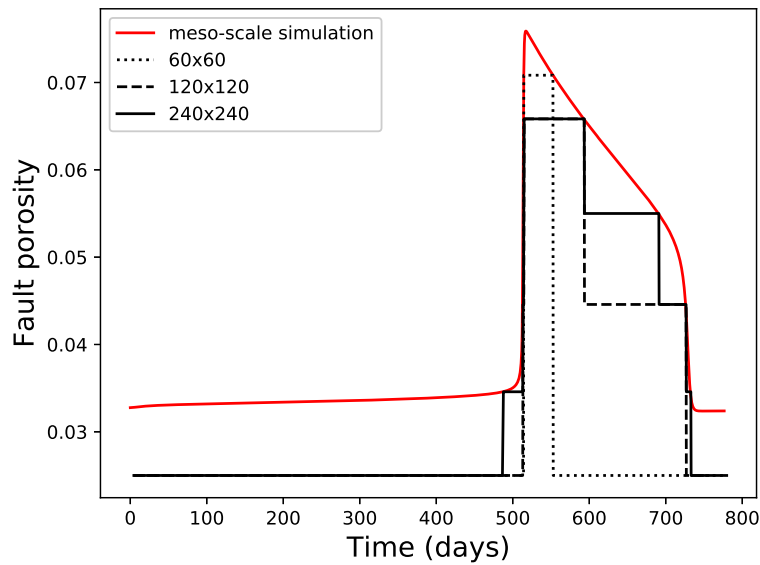


Fig. 4.3 Evolution of the downscaled porosity over time during a fault reactivation for different resolutions $n \times n$ of the micro-scale mesh. The curves are compared to the reference value ϕ computed at the meso-scale. Note that a sensitivity analysis is performed in Sec. 6.3.1 to quantify performance vs accuracy.

chemical porosity update requested by the meso-scale with the resulting (discretised) value computed by the erosion algorithm at the micro-scale, highlighting the importance of the mesh resolution for the quality of the fit.

Given the computational time associated with the simulations following that geometrical erosion algorithm, it is important to note the advantages and drawbacks of the approach. While a coarse discretisation of the porosity can potentially impact negatively the quality of the results, it also presents a considerable performance gain when porosity changes remain limited, which is the case when the fault remains locked (slow creep). Indeed, if the target chemical porosity change is smaller than the corresponding porosity obtained by updating a single layer, then the algorithm leads to no porosity update at all. In order to take advantage of this time-saving feature, we modified the *multiapp* functionality of MOOSE to add this important check at every time step and every downscaling point, before the *multiapp* runs blindly an expensive micro-scale simulation. If the target chemical porosity change is below the minimum threshold, the previous (unchanged) value of permeability gets returned instantaneously. Without a loss of results quality, this smarter multiscaling routine allows to cut down an enormous amount of computational time for two compounded reasons, temporal and spatial. Firstly, as the fault reactivation is a short event at the production time scale, the fault often remains in its slow creeping (locked) regime. Secondly, the localisation of the deformation within the fault can result in specific zones (and corresponding sampling points) experiencing very little to no chemical alteration, even when the fault reactivates.

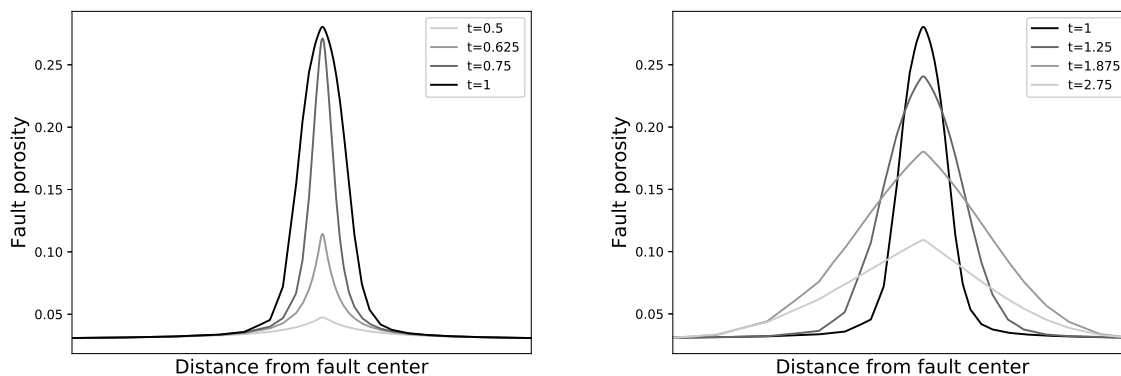


Fig. 4.4 Profiles of porosity across the fault core and damage zone at different time during reactivation (left) and deactivation (right). Times are normalised by the peak reactivation time.

4.2.2 Upscaling properties

As the meso-scale passes a chemical porosity target information to the micro-scale at N sampling points $M_{i|1 \leq i \leq N}$ where the *mutliapp* is run, the main information transferred back from the micro-scale to the meso-scale is the corresponding value of permeability computed on the eroded or dilated mesh for that timestep, explained in detail in Sec. 6. Those updated permeability values at the sampling points M_i then need to be interpolated across the full meso-scale mesh.

A common multiscale procedure consists in selecting every single Gauss point of the macro-scale mesh as sampling point (Kouznetsova, 2004). The upscaled property is then interpolated naturally on the whole mesh by following the internal finite element interpolation used, linearly for elements of first order or with higher polynomial functions for higher order elements. In comparison, the *multiapp* functionality of MOOSE provides more freedom in the multiscale procedure as the sampling points can be selected independently from the mesh discretisation. The number and position of the sampling points on the mesh are user-defined and those sampling points do not even need to be located on mesh nodes. Compromise can then be made between computational efficiency and results precision by selecting the location of the sampling points M_i appropriately, shown below. For our particular case, given the regular shape of the chemical porosity target across the fault core of the meso-scale observed in Fig. 4.4, which is essentially one dimensional and symmetrical around the centre of the fault, we can expect a similar permeability profile. This simplifying configuration allows to recreate a permeability profile with an appropriate interpolation scheme and a limited number of sampling points including:

- The middle point of the core zone. This point must be selected as it is experiencing the most drastic change of porosity.
- The far-field boundary condition. The permeability of this reference point only gets computed once at the beginning of every meso-scale simulation since this point sits at the edge of the mesh with a constant temperature boundary condition and does not experience

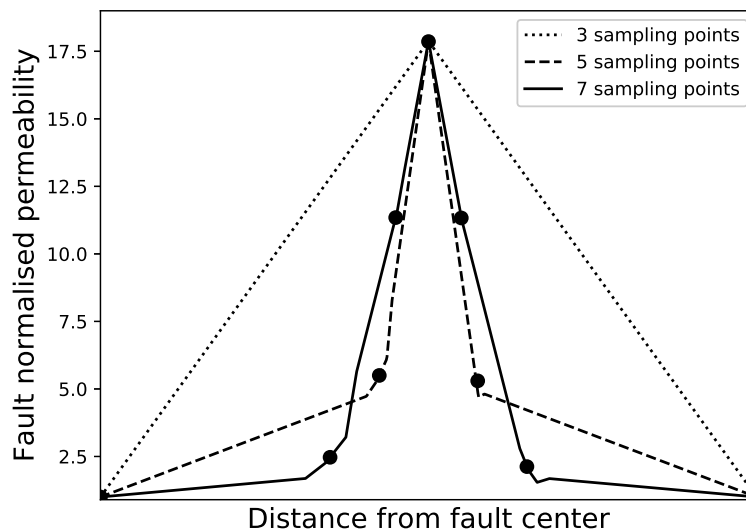


Fig. 4.5 Profiles of permeability across of the fault for increasing sampling. Note that the middle point and the boundary points are sampled in each simulation. The visible kinks on the curves are due to visualisation issues.

dissolution or precipitation. It is indeed far away from the fault core and all excess heat generated by the localised shear heating gets dissipated by that point.

- A few points in between those two. Those points are selected with higher density closer to the middle because of the expected bell curve profile, with the exact number of points depending on the precision required, as shown in Fig. 4.5.

Note that, despite the symmetrical geometry of the meso-scale mesh, the existence of a pore pressure gradient across the fault breaks the symmetry of the problem, preventing us from using sampling points on a single side of the fault and replicating the symmetrical profile across the centre of the fault. The results show, however, that this pore-pressure contribution remains negligible on the porosity profile, providing a nearly perfectly symmetrical profile nonetheless (see Fig. 4.4). Therefore, we sample only one half of the fault and we compute the other half by symmetry.

Finally, the interpolation between all sampling points can itself be done in different ways and MOOSE proposes two different options by default: inverse distance weighting and radial basis function interpolation. While those two interpolation methods are more well suited for 3D cases, for our study we implemented a Bezier interpolation to better capture the localised reactivation in the fault core. This algorithm is explained independently in Appendix A.

In addition to the macro/meso-scale framework presented in Chapter 3, this chapter presented the possibility of incorporating yet another scale of importance in the model. Indeed, the information of the rock microstructure is lost at the meso-scale where it is only reduced to the porosity parameter. The only way to retrieve this information is to incorporate the micro-scale

in the framework. We focus in this contribution on the effect of chemical alterations on the permeability. This chapter explained how the multiscale procedure was done. Because the chemical model is solved at the meso-scale, the downscaled information passed to the micro-scale is directly a chemical porosity change. If this change is small enough, we do not run an expensive upscaling of the permeability since the value would not change much. The permeability is computed on the eroded mesh and transferred back to the sampling points. By adapting the sampling positions to the shape of the expected permeability profile, we can reduce the number of sampling points while keeping a good approximation of the shape of the curve.

Part II

Examples of properties homogenised from the micro-scale

Chapter 5

Upscaling of mechanical properties: yield stress

Many studies are aiming at accounting for the micro-structural influence on rock mechanical properties, whether on elastic properties (Hashin and Shtrikman, 1963; Mackenzie, 1950), rock strength (Dunn et al., 1973; Green, 1972; Gurson, 1977; Hoshino, 1974), or plastic flow law (Green, 1972; Gurson, 1977), to cite only a few. In the context of Part I, the yield value of rocks becomes the most critical material property as it can be traced back directly to fault reactivation, when assuming that faults reactivate when reaching the Coulomb Failure Criterion, which corresponds to the notion of yield. Some models already account for the impact of microstructure on yield through quantitative measures of microstructure, the Minkowski functionals (Armstrong et al., 2018), and particularly through its original and simplest parameter: porosity (Green, 1972; Gurson, 1977; Hamiel et al., 2004). In this chapter, we extend this work on the notion of yield itself, as well as the way it is affected by porosity and the microstructure from a more general perspective.

The only unambiguous determination of mechanical yield point is possibly restricted to the simplest case of ideal non-porous linear elastic and ideally plastic materials, like metals for instance. Indeed, experimental compression tests of such materials lead to characteristic stress-strain curves displaying a sharp transition between the linear elasticity and plasticity, where strain increases at constant stress. For more complex materials, however, including real geomaterials like porous rocks, strong debates remain about the notion of yield point and its quantitative characterisation. This is well illustrated, for instance, by the various definitions of yield from the sixth edition of the McGraw-Hill Dictionary of Scientific and Technical Terms (Parker, 2003):

- **yield** [MECHANICS] *That stress in a material at which plastic deformation occurs.*
- **yield point** [MECHANICS] *The lowest stress at which strain increases without increase in stress.*
- **yield strength** [MECHANICS] *The stress at which a material exhibits a specified deviation from proportionality of stress and strain.*

The fact that there exists more than one notion of yield highlights the ambiguity of the term for complex materials, and the three points defined above only represent three of all possible concepts.

This chapter tackles the challenging problem of homogenisation of the yield, which is not unique. A convenient starting point to study the links between microstructure and yield is to consider the theoretical scenario of the simplest configuration, which consists in a single spherical pore, following the seminal work from [Gurson \(1977\)](#). Different yield surfaces identified in that configuration will then be extended to more complex microstructures. In order to do so, we introduce in this chapter a mechanical simulator, benchmarked on Gurson's study. Finally, compression experiments on 3D printed samples with a given microstructure will allow us to link the theoretical, numerical and experimental approaches on the topic to capture the yield of a real microstructure reconstructed from μ CT-scans.

5.1 Upper yield: Benchmark of Gurson's criterion

Reducing the complexity of the microstructure to the extreme, the single spherical pore system becomes simple enough that a full numerical study should not be required to derive the yield surface of the corresponding porous material. This is indeed the case when considering the yield as "*the lowest stress at which strain increases without increase in stress*" (yield point from [Parker \(2003\)](#) mentioned above), since only the limit load of the material is then needed. As such, the yield point can be determined with an analytical method called *limit analysis*.

[Gurson \(1977\)](#) used that technique to distillate the influence of the porosity on the yield surface of rocks. He considered a single spherical pore as the unit cell of a void-matrix aggregate and produced therefore a study which has since then been extensively used for more complex microstructures. To avoid any non-essential complexity and restrict the study to the influence of microstructure, he selected a rigid and ideally plastic material. The outer geometry of the unit cell was taken as spherical, like the void shape, in order to retain the geometrical isotropy benefits from the symmetry in the analysis.

Limit analysis allows to directly get the limit load state of the material without having to compute the full elasto-plastic behaviour of the system. This technique is particularly useful in geotechnical engineering which is highly interested in system stability. This technique is particularly efficient in comparison to the full elasto-plastic analysis in dealing with complex geometries and complicated loadings. An exhaustive review of limit analysis can be found in [Chen \(1975\)](#). Two methods are possible to obtain either the lower- or the upper-bound of the limit load. For the lower-bound a stress distribution needs to be identified, which respects the equilibrium equation and the boundary conditions and does not violate the yield criterion. For the upper-bound, the loads are obtained by equating the external rate of work to the internal rate of dissipation.

[Gurson \(1977\)](#) chose to follow the upper-bound method and took an approximation of the internal rate of dissipation as an infimum of the exact dissipation. With subsequent derivations

(see review from [Leblond and Morin \(2014\)](#)), Gurson obtained an approximate upper solution to the yield surface of the hollow sphere geometry, which proved to be precise enough to fit experimental data ([Springmann and Kuna, 2005](#); [Xie and Shao, 2006](#)). Extending his work, numerous studies followed which improved on the model, including derivations accounting for other shapes of voids (e.g. elliptical [Gologanu et al., 1997](#)), the interaction between voids ([Fritzen et al., 2012](#); [Tvergaard, 1981](#)), or the consideration of more complex matrix materials (e.g. viscoplasticity [Besson, 2009](#)).

Starting from Gurson's original setup, we use a Finite Element approach to derive more characteristic points associated with the yield. Retrieving first the upper-bound estimate allows us to benchmark our numerical framework, which can then show its full potential. Unlike the semi-analytical approach, it can indeed be extended easily to more advanced mechanical behaviours on more complex microstructures.

5.1.1 Geometry and material considered

We present in this subsection the meshing of the hollow-sphere geometry and the material of the matrix considered for the numerical simulation.

The hollow sphere consists in a layer of solid matrix delimited by two spheres: the outer one with a radius R_{out} and the inner one with a radius R_{in} . The porosity of the system is $\phi = (\frac{R_{in}}{R_{out}})^3$ and it can be controlled by varying R_{in} for instance. The spherical layer is meshed in spherical coordinates with hexahedra of the second order using the software Gmsh. The use of spherical coordinates allows to get a good mesh quality as can be seen on [Fig. 5.1](#) indicated by a signed inverse condition number close to one, the value for a perfectly shaped element. Note that in [Sec. 5.2](#) we are interested in the behaviour at the surface of the inner sphere so for this section, the radial thickness of the elements is varied progressively along the radius to obtain thinner elements at the centre.

To approach the limit analysis results obtained with a rigid material with an elasto-plastic Finite Element simulator, we chose a large value of Young's modulus at 200 GPa so the material stays close to rigidity, along with Poisson ratio of 0.3 and yield stress of 100 MPa. As such, a small strain formulation is sufficient since the mesh deformation remains minimal. As mentioned in the introduction of the section, in order to retrieve exclusively the effect of porosity on the behaviour of the material, the constitutive model for plasticity is taken as ideal, which implies a $J2$ (or von-Mises) rate-independent plasticity model with no hardening or softening.

5.1.2 Homogenisation: Hill-Mandel condition

Calculating the homogenisation of a microscopic field to the next scale up on a heterogeneous medium like the one described in the previous section is not straightforward. Out of the many methods available (see review from [Geers et al. \(2017\)](#)), Gurson chose the Hill-Mandel condition ([Hill, 1963](#)) which postulates that the integral of the local mechanical work should be equal to

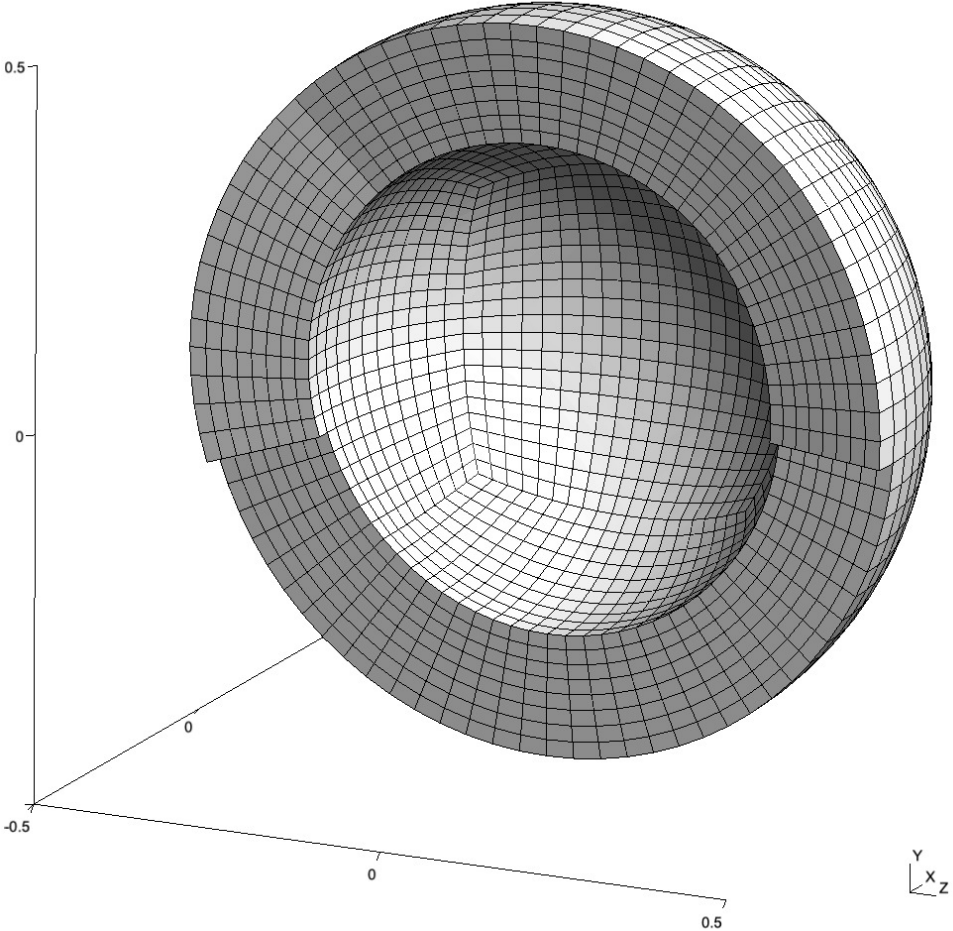


Fig. 5.1 Mesh of the hollow sphere with a porosity of 30%, showing only half for visualisation purposes. It is composed of 8 layers of elements amounting to a total of 19,200 elements. The signed inverse condition number for the mesh is higher or equal than 0.867.

the global mechanical work of the Representative Elementary Volume (REV):

$$\bar{\sigma}_{ij}\bar{\varepsilon}_{ij} = \frac{1-\phi}{|\Omega|} \int_{\Omega} \sigma_{ij}\varepsilon_{ij}dV \quad (5.1)$$

In short, this lemma describes a conservation of energy across the scales and requires conditions to hold at both scales for a system to comply. The two paragraphs below describe the setup of our specific problem for this Hill-Mandel condition to be respected in terms of strain and stress.

Regarding the strain, we first note that the loading condition is actually specific to the homogenisation theory itself, as the REV – the hollow sphere of Fig. 5.1 in our case – has to be submitted to an homogeneous macroscopic rate of deformation D_{ij} . Consequently, we impose the velocity $v_i = D_{ij}x_j \forall x \in \partial\Omega$, the external surface. As a result, we can write the homogenised strain for the structure as $\bar{\varepsilon}_{ij} = D_{ij}t$.

The corresponding macroscopic stress is defined as the average of the stress over the total volume. Since the material is considered dry, the pore space is not pressurised. This translates to a traction-free boundary at the inner surface which is directly imposed through the natural boundary conditions emerging in the weak form when using the divergence theorem on the divergence of stress. Eventually the macroscopic stress can be expressed in terms of the porosity as $\bar{\sigma}_{ij} = \frac{1-\phi}{|\Omega|} \int_{\Omega} \sigma_{ij}dV \approx \frac{1-\phi_0}{|\Omega|} \int_{\Omega} \sigma_{ij}dV$. Note that in this relation, the porosity is taken as the initial value, with the assumption that the deformations of the REV are small for our material close to rigidity. In order to visualise the yield surface of the material, we are particularly interested in the Von Mises stress of the material, defined as $\bar{q} = \sqrt{\frac{3}{2}\bar{\sigma}_{ij}\bar{\sigma}_{ij}}$ and the mean stress $\bar{p} = \bar{\sigma}_{ii}$.

5.1.3 Numerical simulation

We solve the problem presented in Sec. 5.1.1 using the Finite Element simulator described in Part I. For this purely mechanical exercise, the system of equations reduces to the momentum balance equation, which is solved without external forces (gravity).

Compared to Gurson's semi-analytical derivation of the yield surface equation, the only way for us to determine the yield surface of the material is to follow the experimental procedure. Multiple loadings of different stress paths are simulated until they reach the limit load that marks one point on the yield surface on the material. The full surface can then be interpolated from all the different points gathered.

In order to map the yield surface in the $p - q$ space, we need to impose different stress paths while still respecting a homogeneous macroscopic rate of deformation to comply with the Hill-Mandel condition. We choose to follow the loading function used by [Fritzen et al. \(2012\)](#)

Table 5.1 Different combinations of α and β values that correspond to loading paths of different triaxiality ratios following Eq. 5.4. The loadings vary from pure shear on the left to isotropic extension on the right.

Alpha	1	1	1	1	1	1	1	0.5	0
Beta	0	0.05	0.15	0.25	0.35	0.5	0.75	1	1

analysis and have the velocity imposed on the sphere expressed as:

$$v_x = \dot{\epsilon}_0(\alpha + \beta)x, \quad (5.2)$$

$$v_y = \dot{\epsilon}_0(-\alpha + \beta)y, \quad (5.3)$$

$$v_z = \dot{\epsilon}_0\beta z \quad (5.4)$$

with $\dot{\epsilon}_0$ the reference loading strain rate and α and β parameters controlling the triaxiality of the stress path, governed by the ratio $\frac{\alpha}{\beta}$. The different combinations of α and β used to map the yield surface, from pure shear to isotropic extension can be found in Table. 5.1. Note that we take $\dot{\epsilon}_0 > 0$ in order to focus our study on the yielding in extension as Gurson did.

As mentioned in Sec. 5.1.2, it is important to verify first that the Hill-Mandel condition holds, which is done by computing separately and comparing the (integrated) *microscopic* and *macroscopic* contributions of Eq. 5.1. We use the setup described above with a prescribed α and β . Fig. 5.2 shows a perfect superposition of the results, which confirms the validity of the numerical approach.

The next numerical aspect to check is the impact of the mesh discretisation on the results. We perform therefore a mesh sensitivity analysis by running the same simulation as above on various meshes of increasing density from 12,738 up to 871,038 degrees of freedom. Fig. 5.3 compares the relative error obtained on the limit load value of both invariants of the macroscopic stress, \bar{p} and \bar{q} by comparing those values for a given mesh with the corresponding value obtained on the biggest mesh. The results show the expected convergence of both invariants with respect to the mesh size. For the following simulations, we select the mesh with 489,702 degrees of freedom, for which the relative error on \bar{p} and \bar{q} remains below 0.2% (see Fig. 5.1).

Having verified the numerical approach, we perform the triaxial extension simulation for each α and β combination shown in Table. 5.1. Fig. 5.4 shows that for every simulation, both the macroscopic mean stress and Von Mises stress converge to limit load values before the normalised time reaches one.

The limit load values of \bar{p} and \bar{q} (at $t = 1$) from all simulations are then plotted on Fig. 5.5 as separate points in the $p - q$ space to indicate the yield surface obtained numerically for this hollow sphere. The results are then compared with Gurson's yield criterion, derived through limit analysis and expressed as

$$\frac{\bar{q}^2}{\bar{\sigma}_0^2} + 2\phi \cosh\left(\frac{3}{2} \frac{\bar{p}}{\bar{\sigma}_0}\right) - 1 - \phi^2 = 0 \quad (5.5)$$

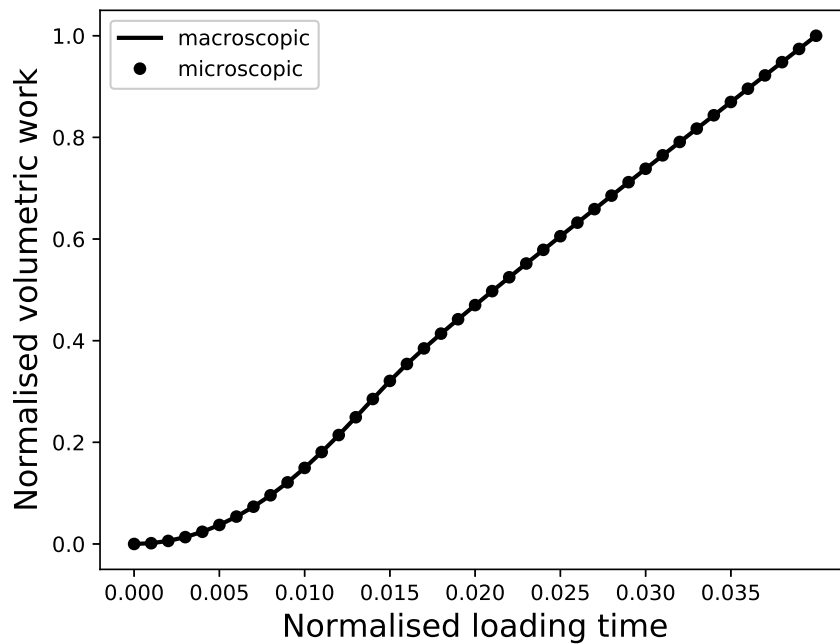


Fig. 5.2 Comparison during a prescribed loading of the hollow-sphere of the two energies defined in Eq. 5.1, local (microscopic) and macroscopic, normalised to their range of values. Note that the purpose of the figure is to show the perfect superposition of the two curves that proves Hill-Mandel condition is respected.

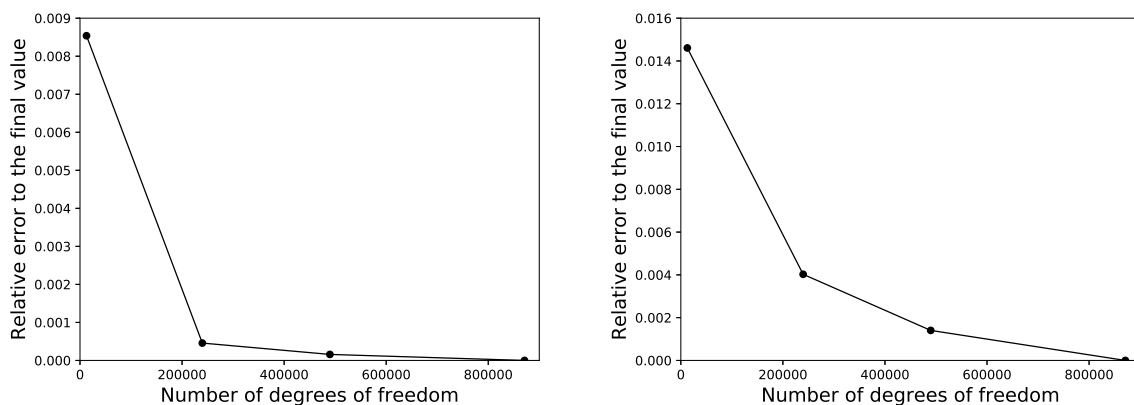


Fig. 5.3 Mesh convergence of respectively the mean (left) and Von Mises (right) stress for the hollow sphere under the loading conditions of Eq. 5.4 with $\alpha = 0.5$ and $\beta = 1$. The error is plotted against the number of degrees of freedom (DOF) of the mesh.

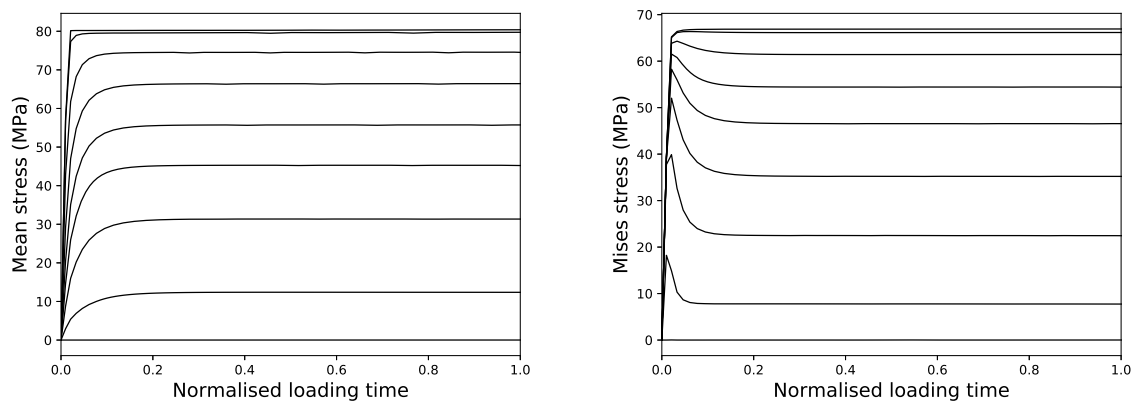


Fig. 5.4 Mean (left) and Von Mises (right) Stress vs loading time for the hollow sphere of Fig. 5.1, following the loading paths obtained for all couples (α, β) in Table. 5.1. The graph on the left-hand side goes from pure shear to isotropic compression from the bottom to the top and the other way around for the graph on the right hand side.

The whole exercise is repeated for a different value of porosity of 12.5% and the results are also plotted on Fig. 5.5.

For both scenarios ($\phi = 30\%$ and $\phi = 12.5\%$), fig. 5.5 shows reasonable matches between our numerical results and Gurson's upper bound approximation, with Gurson's curve naturally falling above the yield envelope computed numerically. Given the numerical precision of our results (see Fig. 5.3), the difference between both curves even allows us to quantify the (relatively constrained) approximation error coming from Gurson's upper bound approximation of the dissipation, since the full numerical simulations computed the exact yield surface within a very strict numerical tolerance.

Note that the porosity has a weakening effect on the material for any stress path in the $p - q$ space. Even in pure shear, Fig. 5.11 shows that, when following a vertical stress path from the origin, the porous material does not reach the value of 100 MPa input as the yield strength of the matrix.

5.2 Lower yield

After the analysis in Sec. 5.1 of an upper value of the yield, we can now study a lower value by selecting a different definition from the McGraw-Hill Dictionary of Scientific and Technical Terms: (*yield*) "That stress in a material at which plastic deformation occurs". This definition leads indeed to a lower bound as it focuses on the onset of plasticity, a concept more relevant from a mathematical point of view than an experimental perspective. This threshold is indeed nearly impossible to track experimentally on real geomaterials as it can be reached for a minimal stress value when a single minuscule part of the sample stops behaving in an elastic manner. Such events could be absolutely imperceptible in samples with heterogeneities (Desrues et al., 2017a), which is the case for rocks. This case study remains interesting nonetheless, not

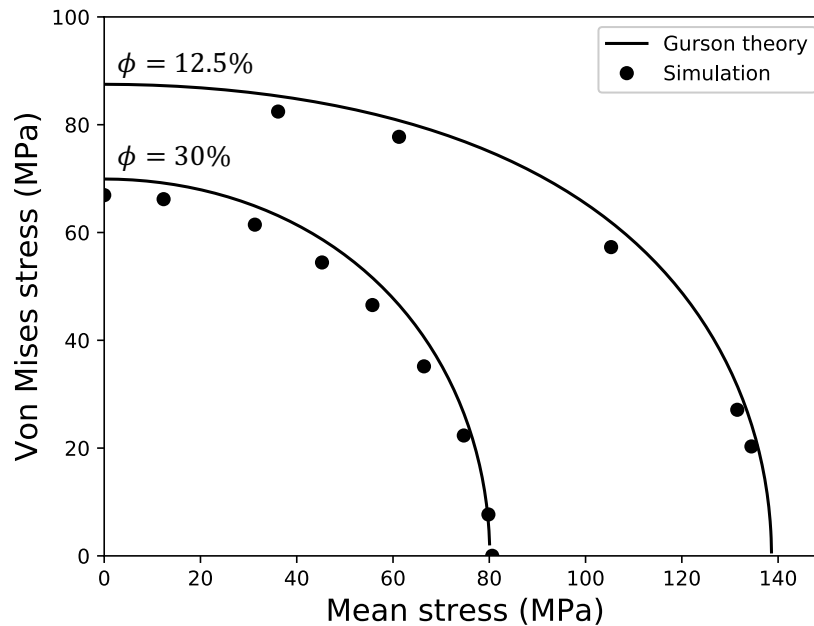


Fig. 5.5 Yield surface of the hollow sphere in the $p - q$ space for two different porosities $\phi=30\%$ and 12.5% . The results of our simulation are compared with Gurson's yield criterion.

just from a theoretical perspective but also to get an estimate of the admissible range of yield envelopes that could be obtained with any existing or new definition. Note that it can be used by itself for the development of macroscopic elastoplastic constitutive models of foams (Daxner, 2010), where the homogeneous nature of the material makes the lower yield more relevant to be used as a macroscopic yield surface.

Contrarily to the experimental viewpoint, the occurrence of the first irreversible deformation in the material is easy to compute numerically, with the timing of the event determined by the first element of the mesh that enters plasticity. In our hollow sphere model, since the pore acts as a weakness for the material, the stress concentrates around the pore and the first element to enter the plastic regime will therefore be located on the inner spherical surface of the model for any of the admissible loading paths considered. For this reason, the mesh used to determine this lower yield is modified from the one shown in Fig. 5.1, keeping the same number of elements but with a different radial distribution of element thicknesses, with finer elements towards the centre of the sphere to capture the onset of plasticity more precisely.

The results are plotted on Fig. 5.6a, which shows that this lower yield surface has a different shape from Gurson's. While the behaviour is similar for shearing stress paths, the lower yield surface becomes almost linear in $p - q$ for loadings that are more isotropic.

5.3 Experimental yield

The upper and lower values of the yield identified in Sec.5.1 and 5.2 are particularly useful as they provide bounds in between which any other definition of yield will fall. For practical purposes, however, experimentalists rely instead on the third definition of the yield stated in the

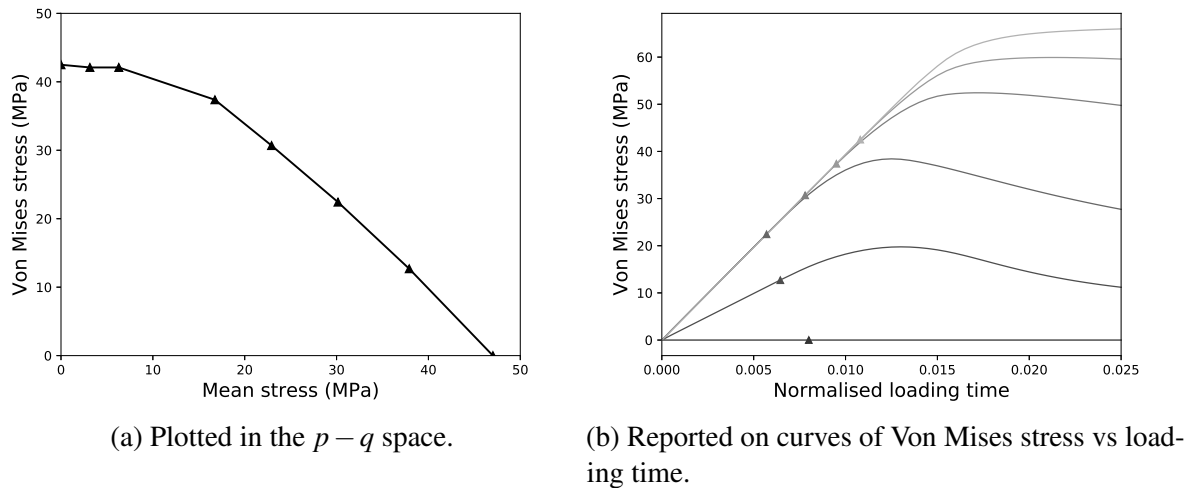


Fig. 5.6 Lower yield surface for the hollow sphere of porosity $\phi=30\%$ obtained under the loading boundary conditions of Eq. 5.4 for various triaxial ratios.

introduction of this chapter, (*yield strength*) "the stress at which a material exhibits a specified deviation from proportionality of stress and strain".

This definition, which assumes that the material behaves linearly in elasticity, is more subjective than the previous two since the *deviation from proportionality* cannot be determined in a unique manner on real measurement data. This *experimental yield* is usually identified graphically on the stress-strain curve and it requires the specification of an ad-hoc strain threshold X , given by ASTM standards and typically of 0.1, 0.2 or 0.5% (ASTM E8/E8M-16a, 2016). An offset method, often called $X\%$ proof stress (Ross, 1999), then determines the yield as the intersection of the stress-strain curve with a line parallel to the initial linear-elastic part of that stress-strain curve, shifted by the amount of strain X (see Fig. 5.7).

Since our virtual material is taken as extremely rigid and does not correspond to any ASTM standard, we will consider an arbitrarily small offset of 0.04% of plastic strain of deviation. The identified experimental yields for several loading paths on the hollow sphere are reported on Fig. 5.8b.

5.4 Energetic yield

As useful and widespread as the experimental yield is, its determination method remains empirical and dependent on an arbitrary threshold value. From a modelling perspective, it is therefore interesting to investigate other potential indicators marking the transition between elasticity and plasticity. Given the critical role of the energy in the framework presented in Part I, it is particularly attractive to identify an energetic transition, as elasticity stores energy, whereas plasticity dissipates energy. Indeed, a clear regime transition can be observed on Fig. 5.2 at approximately 0.0075 normalised time. In this specific case, the transition can be determined by the location of the maximum of the derivative of mechanical work as a function of loading time

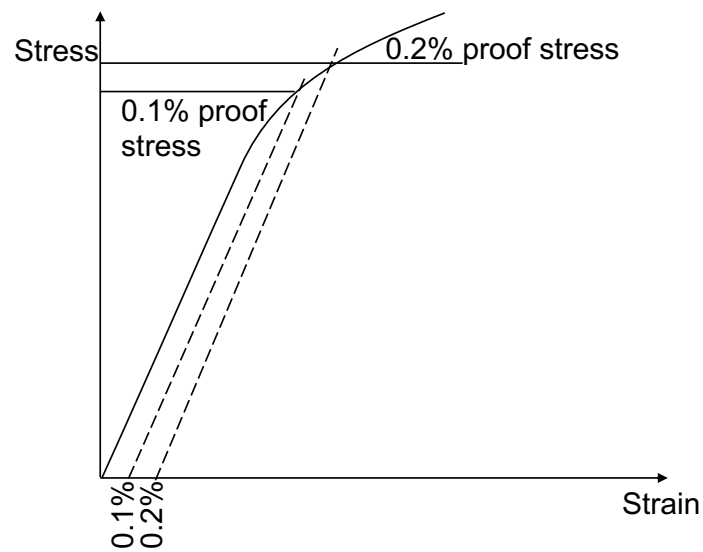
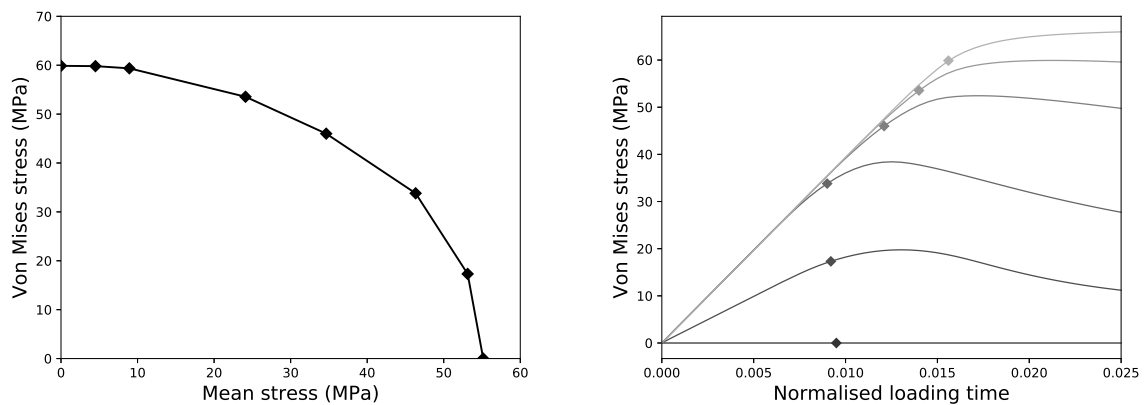


Fig. 5.7 Figure showcasing the offset method to determine the $X\%$ proof stress. Modified from Ross (1999).



(a) Plotted in the $p - q$ space.

(b) Reported on curves of Von Mises stress vs loading time.

Fig. 5.8 Experimental yield surface for the hollow sphere of porosity $\phi=30\%$ obtained under the loading boundary conditions of Eq. 5.4 for various triaxial ratios.

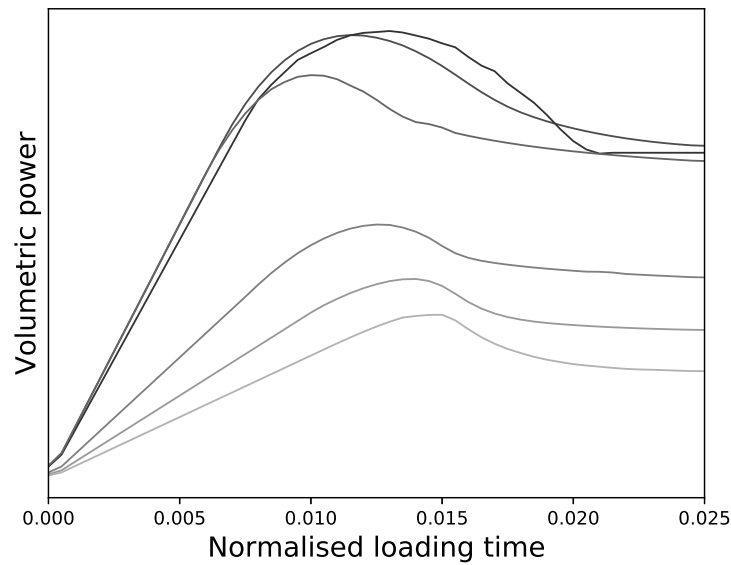


Fig. 5.9 Derivative of the energy with the loading time vs loading time for various loading paths. The energy is defined as the macroscopic stress tensor contracted with the macroscopic strain tensor. The maximum is achieved for higher values the closer we get to an isotropic extension.

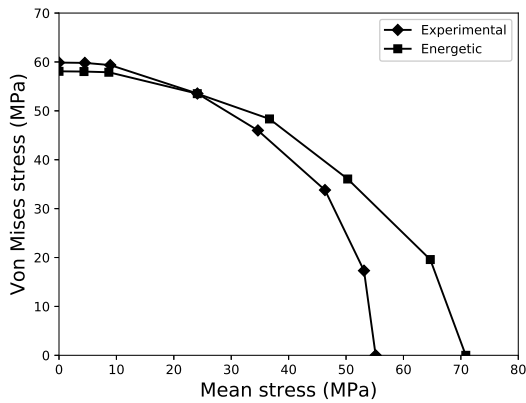
which corresponds to the maximum of mechanical power dissipated. Fig. 5.9 shows that this maximum actually does exist for each loading path ranging from pure shear to isotropic loading for our problem at hand.

We propose therefore to use this indicator – when it exists – as an *energetic yield*, which is plotted in the $p - q$ space in Fig. 5.10a. It is quite reassuring to see that this surface matches rather well with the experimental yield surface, at least in the regimes closer to pure shear. This means that in cases of uniaxial experiments, for instance, the experimental yield is also energetically meaningful. For regimes in compaction closer to isotropic compression, however, the link becomes looser and the experimental yield no longer tracks the same energetic transition.

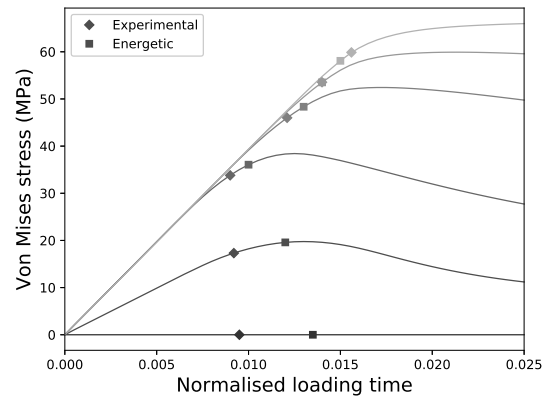
5.5 Summary of the different yield surfaces derived

The previous sections have shown that considering a unique yield point is a misconception for porous materials. Various definitions lead to different envelopes in the $p - q$ space and Fig. 5.11 superposes the four envelopes derived from the definitions considered so far. As mentioned previously, Gurson's upper bound limit load analysis (see Sec. 5.1) provides the *upper yield*, an upper bound to all possible yield envelope, while the theoretical definition (see Sec. 5.2) provides the *lower yield*, a corresponding lower bound. We see indeed that all other curves, like the *experimental yield* (see Sec. 5.3) and *energetic yield* (see Sec. 5.4), fall indeed in between.

The criterion for selecting a given yield surface has to be established for the specific motive behind the determination of this material property. For instance, most modellers use the yield to fit stress-strain curves and therefore the experimental yield becomes particularly useful because



(a) Plotted in the $p - q$ space.



(b) Reported on curves of Von Mises stress vs loading time for various triaxial ratios ranging from pure shear (light grey) to isotropic compression (dark grey).

Fig. 5.10 Energetic yield surface for the hollow sphere of porosity $\phi=30\%$ obtained under the loading boundary conditions of Eq. 5.4 for various triaxial ratios. Results are superposed with the ones obtained in Fig. 5.8.

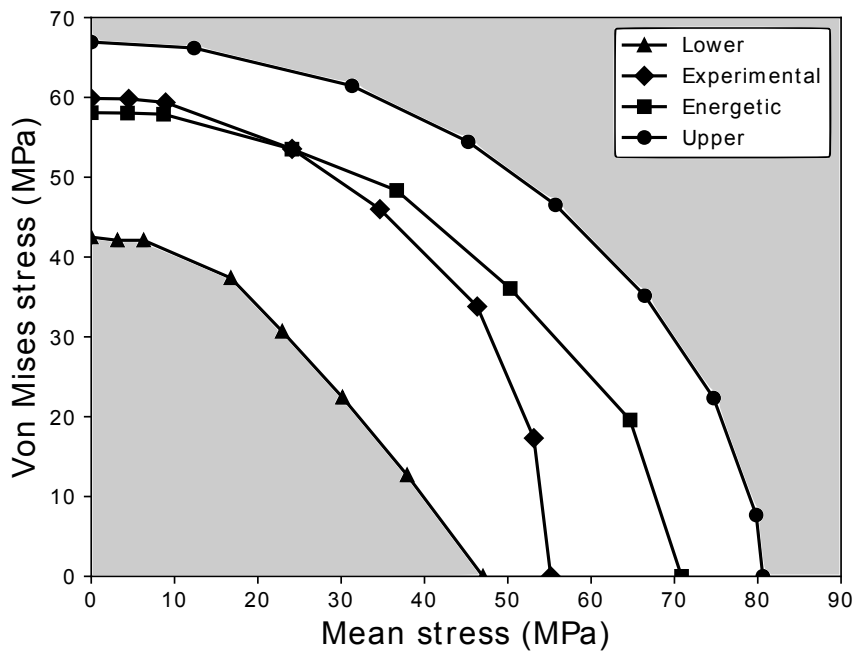


Fig. 5.11 Different yield surfaces considered in this contribution plotted in the $p - q$ space for the hollow sphere of porosity $\phi=30\%$.

that yield point accounts for the homogenisation of all processes occurring at the scale of the sample. Nevertheless, the other definitions also present their advantages and the list considered here is by no means exhaustive. [Christensen \(2007\)](#), for example, derived a yield criterion based on the maximum of the second derivative of stress with respect to strain, which characterises the inflexion point in the elasto-plastic transition. We could also mention the approach from [Lin et al. \(2019\)](#) who are inverting for a yield closer to the lower yield from experimental data.

The respective shapes of the four yield envelopes plotted on Fig. 5.11 also provide some interesting information. We observe that only the upper and energetic envelopes seem to be scaled one from another. This indicates some consistency between the two approaches based on energy considerations. The difference in shape with the other two curves also highlights that one must be careful when using a given yield envelope for another purpose than originally intended. Simple scaling coefficients are not necessarily enough to transform one yield curve into another. For example, the lower yield exhibits a quasi-linear relationship for stress paths close to isotropic compression, whereas all other curves remain elliptic. It is also worth noting that, while the experimental yield is larger than the energetic one for low mean stresses (pure shear), those two curves intersect each other and the energetic yield is above the experimental yield for deformations with stronger volumetric components. Hopefully, the comparison between those four curves will serve as a stepping stone to identify translating relationships between the various yield curves in the future.

A critical result, highlighted by Fig. 5.11, is that the presence of porosity in a pressure insensitive material causes it to become pressure sensitive and exhibit a cap in compression, regardless of the yield surface considered. As a historical anecdote, this cap was discovered by von Kármán in 1910 ([Döhne and Von Kármán, 1912](#)) using the first triaxial machine as he wanted to test the validity of the Mohr failure envelope ([Mohr, 1900](#)) on marble expecting a monotonous function of shear strength with respect to pressure. Despite its very low porosity the marble displayed nonetheless a compression cap at very high confining pressures. This fundamental point highlights, as [Green \(1972\)](#) or [Gurson \(1977\)](#) pointed out, that all natural materials, which are porous to some extent, will be subject to compaction caps. Interestingly at the early stage of subsurface exploration, the cap was hardly ever observed because the confinements were still low at shallow depth of operations. Therefore, modellers commonly used open yield surfaces such as Tresca or Mohr-Coulomb. With subsurface exploration moving deeper to higher pressure environments, compaction caps are observed more frequently and modellers turn towards closed surface models like the modified cam-clay model ([Roscoe and Burland, 1968](#)) for instance.

5.6 Validation on 3D printed material

The previous sections showed explicitly the influence of porosity on the yielding of a material with the simplest microstructure, made of a single spherical pore. By taking a virtually ideally plastic material, the relationships extracted can indeed be attributed solely to the microstructure without any interfering influence of any other material properties. That analysis was an important

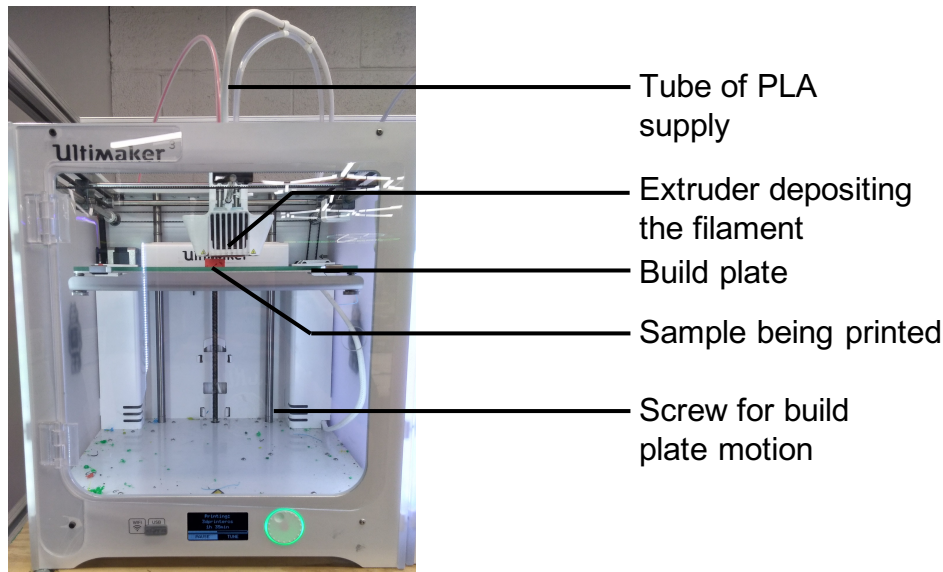


Fig. 5.12 Ultimaker 3 at the Innovation co-Lab of Duke University.

first step which allowed us to identify four different definitions of yield and observe their differences in terms of yield envelopes.

We aim now to verify how the understanding gathered above holds for physical materials, by complementing our theoretical analysis with an equivalent experimental study on a real material. To reach this objective, we run compression tests on a sample with an internal spherical void, like the hollow sphere geometry of Gurson shown in Fig. 5.1. In order to obtain a perfect control of the internal geometry of our sample, we reach out to 3D printing for the creation of our samples as it is arguably the best technique available.

3D printing is a revolutionary technique which is progressively impacting every engineering discipline, from printing planes in aerospace engineering (Marks, 2011) to printing organs with organic tissues in bioengineering (Mironov et al., 2003), to cite only a few of a long list of achievements. Its penetration in various fields remains disparate and in geomechanics, like many other areas, 3D printing is only beginning to transition from visualisation (see review from Melis et al. (2018)) to functional purposes. As such, work on characterisation of the mechanical behaviour of the printed material remains necessary to better understand, in turn, the mechanical response of printed parts (see review from Popescu et al. (2018)). Since no accepted mechanical constitutive model exists for 3D printed materials, we conduct our own analysis of the 3D printed material and propose an elasto-plastic model for it. The following section describes our printing and testing procedure before suggesting a model for the 3D printed material in the last section.

5.6.1 3D printing and mechanical testing procedure

In recent years, many 3D printing methods have been made available (see review from Dizon et al. (2018)). Without loss of generality we choose to work with the standard Fused Deposition Modeling (FDM) on the Ultimaker 3 machines of the Innovation co-Lab of Duke University, as shown in Fig. 5.12, with a nozzle of 0.4mm diameter. The machine offers the possibility to

print multiple materials (see exhaustive list¹ from the manufacturer), with polylactic acid (PLA) and acrylonitrile butadiene styrene (ABS) two of the most commonly used in mechanical testing of 3D printed materials (Dizon et al., 2018; Popescu et al., 2018). Without any preferences, we choose to work with PLA.

Many of the printing settings influence the mechanical properties of the printed sample, as can be seen in the extensive review of Popescu et al. (2018) and the references therein pointing to studies on the influence of slicing parameters, building orientation and temperature conditions. It is therefore important to keep those parameters constant for consistency purposes between all samples preparation. Starting from the default settings of the 3D printer, we keep the infill density at 100% in order to have a non-porous matrix material. For the building orientation, the samples are printed vertically and each layer is printed with a rotation of 90 degrees from the previous one in order to reduce the anisotropy of the printing that you would obtain when stacking directly the filaments on top of each other. For the temperature conditions, we follow the recommendation of the Ultimaker 3 user manual for PLA² for the extruder's temperature at 200°C and the one of the bed table at 60°C. For the slicing parameters, the wall/shell thickness of the sample is taken to be equal to the layer height in order to be printed with a single filament in size. Finally, the printing speed is set to 30 mm/s which produces a sample of good quality.

All the compression tests presented in this contribution were performed on the HM3000.3F load frame (see Fig. 5.13), manufactured by Humboldt Mfg. Co., with a maximum loading capacity of 50 kN. In order to measure the stress on top of the sample, we use the HM-2300.100 S-Type load cell (see Fig. 5.13), which has the same load capacity as the machine and is also manufactured by Humboldt Mfg. Co. The strain is measured directly from the speed of the load plate and it was verified that the deformation of the load cell, which is taken in account with this method, had a negligible effect on the results.

An important parameter to choose for compression tests is the ratio of height to diameter of the cylindrical samples, as various size ratios lead to different modes of deformations; an exhaustive list can be found in Kuhn and Medlin (2000) and is reproduced in Fig. 5.14. The two particular modes to avoid are barrelling on one end of the spectrum and buckling on the other. Barrelling, as its name implies, is the distortion of the specimen in a barrel shape during compression, as visualised on the 1:1 size ratio sample of Fig. 5.15a. It is promoted by low size ratios and primarily caused by the frictional contact on the faces of the sample in contact with the press, which restrains the lateral movement of those boundary conditions. Using lubricants at the contact reduces this effect, although it does not work for large strain/stress (Banerjee, 1985). Buckling is a mode of failure that refers also to the shape that the specimen deforms in, as visualised on the 2:1 size ratio sample of Fig. 5.15c. It is characterised by an unstable lateral material deflection and appears predominantly for elongated samples, i.e. with high size ratios. The phenomenon can be reduced by a perfect flatness, parallelism, and perpendicularity of both the sample and the loading plates, even though those conditions do not prevent systematically

¹<http://ultimaker.com/materials>

²<http://ultimaker.com/en/resources/22225-how-to-print-with-ultimaker-pla>

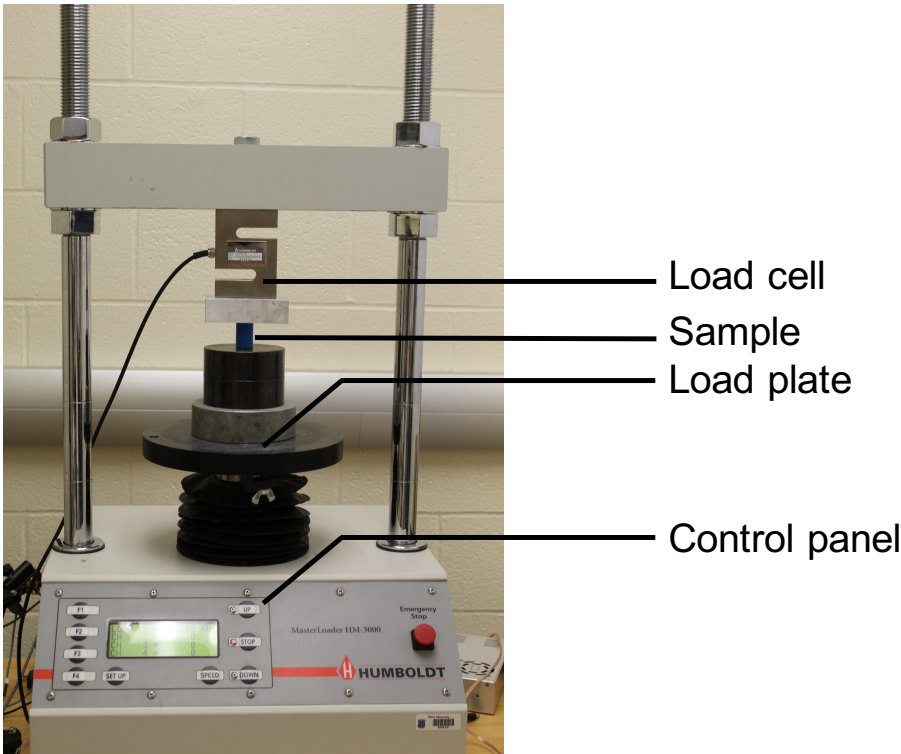


Fig. 5.13 Load frame and load cell used for the uniaxial compression testing in this contribution.

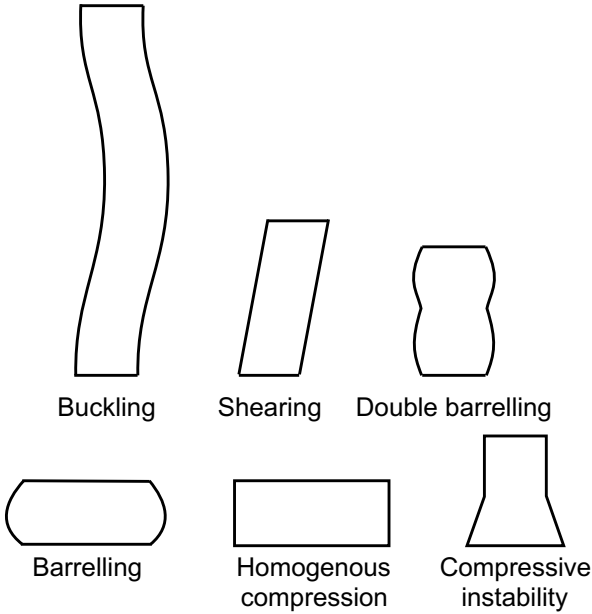


Fig. 5.14 Possible deformation modes in compression, figure modified from [Kuhn and Medlin \(2000\)](#).

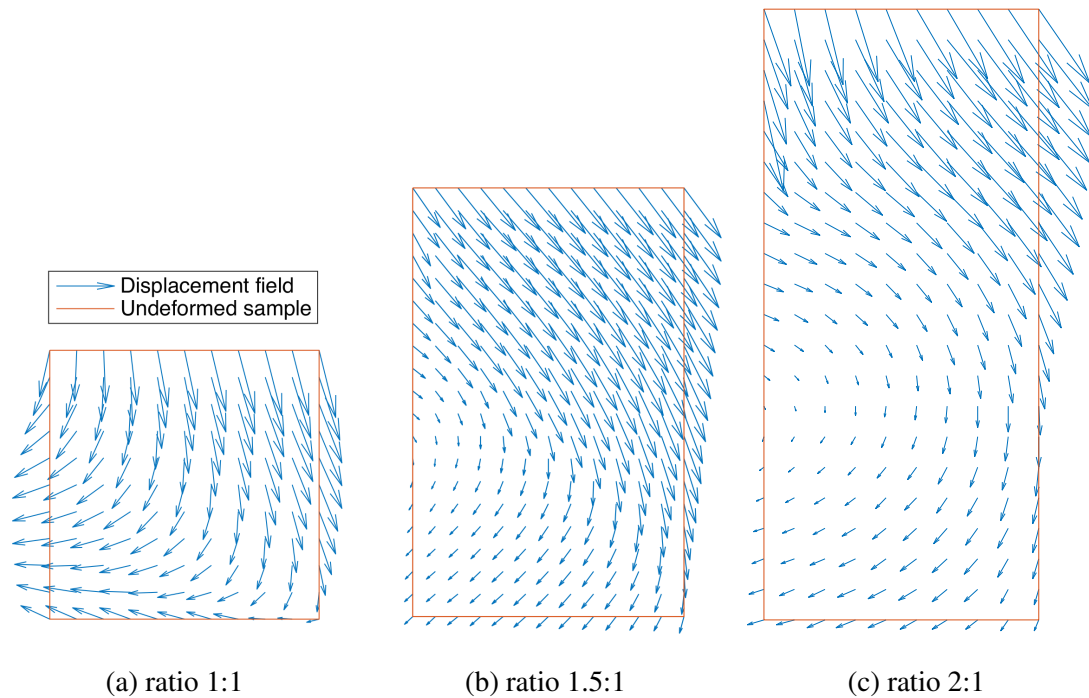


Fig. 5.15 Displacement fields for deformed sample of different size ratios. The displacement fields were obtained by Digital Image Correlation, using the evolution of speckle patterns spray painted on the sample.

the occurrence of buckling. Since both of those deformation modes result in non-uniform strain and stress distributions, we therefore try to avoid them to obtain representative results. We found out that buckling was considerably reduced for size ratios under 2:1 which is also the recommendation of the ASTM standards mentioned in [Kuhn and Medlin \(2000\)](#) for controlling this deformation mode. Eventually we choose to test samples with a size ratio of 1.5:1 in order to avoid promoting barrelling for lower ratios. Comparison tests on the effect of lubricant on such samples showed no noticeable difference and all tests presented below were therefore conducted without any lubricant. We note that for every size ratio sample, a shearband is created during compression. The shearbands are visualised as a superposition to the different modes of deformation on Fig. 5.15 or isolated on the photo of Fig. 5.16.

For a given size ratio of the samples, the absolute size itself plays a non-negligible role. Compared to injection moulding that creates a sample made of pure homogeneous material, the 3D printing method introduces a notion of internal length scale related to the filament diameter, which is also the layer height in the printer setting. Since the filaments are not fused perfectly, there exist some void gaps between them which results in a global micro-porosity of the printed material. [Huang et al. \(2015\)](#) measured that this porosity could amount to as much as 4%. This micro-porosity could explain the discrepancy observed between mechanical response of PLA samples printed and moulded ([Ahn et al., 2002](#); [Divyathej et al., 2016](#)). From our full numerical study previously, we understand that, for this reason, it is necessary to test the mechanical response of the 3D printed PLA. In order to have representative and reproducible results, we need to achieve a good scale separation between the filament size and the sample size. In other

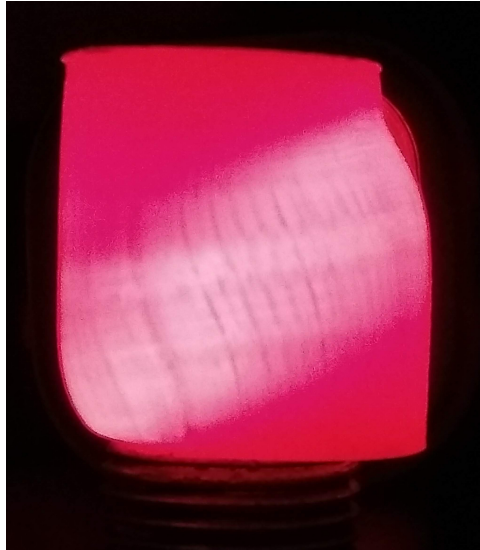


Fig. 5.16 Visualisation of the shear band of the 1.5:1 size ratio sample of Fig. 5.15b at 20% strain under red light.

words, we need to print a sample above the REV size of the 3D printed PLA. We make the hypothesis that this is achieved with a sample of diameter 22 mm and height 33 mm, considering a filament size of 0.1 mm, and we will verify this assumption after the results obtained.

One last possible parameter which could influence compression tests on 3D printed samples is the time elapsed between the impression and compression of the samples. One can indeed wonder, with the heat treatment that the polymer receives during the printing process, if there is a needed relaxation time for a sample to reach a static steady state once the impression is finished. In this regard, a study from [3D Matter \(2015\)](#) measured that the peak stress of the material increases with time after printed until it reaches a steady value after 3 days approximately. To verify and complete this analysis, we test this theory on the whole stress-strain response of our samples. The specimens are left next to the machine in the Multiphysics Geomechanics confined laboratory for different periods of time after they are printed. Note that the temperature and relative humidity are monitored to be constant at respectively $22\pm 2^\circ\text{C}$ and 58.8%. Fig. 5.17 shows the resulting stress strain curves for different times of relaxation. We observe no difference between the curves and can infer that the relaxation time has no influence on the mechanical behaviour of our samples. In addition, it is important to note the good superposition in Fig. 5.17 of the large number of curves produced for this study, demonstrating the high level of reproducibility of experiments on 3D printed samples, which cannot be easily achieved when testing rocks. This reproducibility also validates our assumption that the selected sample size is above the REV size.

5.6.2 Proposed experimental protocol to measure the macroscopic yield

Sec. 5.4 had defined a new indicator to get the value of the macroscopic yield. In this section, we verify the theory for real experiments and suggest a new experimental protocol to measure the

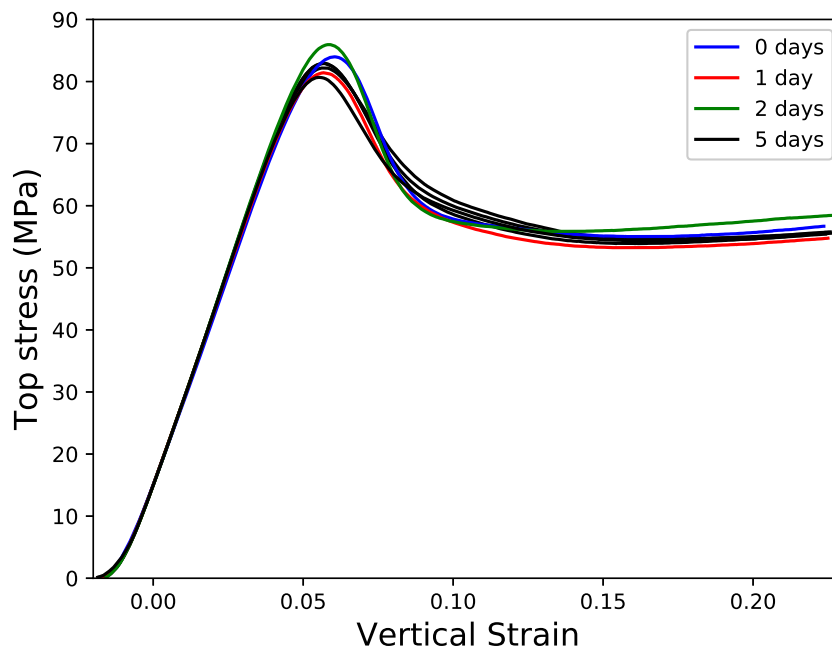


Fig. 5.17 Stress strain curves of non-porous cylindrical samples of 3D printed PLA for different relaxation times. 0 days means that the sample was tested just after being printed. 4 different curves correspond to 5 days of relaxation.

macroscopic yield. We specifically use the data of one of the previous tests performed for Fig. 5.17 to demonstrate the method.

Sec. 5.4 showed that we could define the macroscopic yield energetically as the stress corresponding to the maximum of mechanical power dissipated. In the case of uniaxial compression where only the compressive stress is non null, the expression of the mechanical work reduces to $\epsilon_{11}\sigma_{11}$. The power dissipated by this work can be derived by taking the derivative in time of the mechanical work, whose maximum can then be reported on the stress-strain curve, as showcased in Fig. 5.18.

The derivative can be roughly but directly obtained on the raw data by doing a discrete differentiation of the data. However, if the result has too much noise to be able to measure an unambiguous maximum, like in Fig. 5.18 for instance, we advise to apply numerical processing to obtain a smoother curve. Particularly in the case of Fig. 5.18, we fit a polynomial function of degree fifty on the experimental curve of mechanical work and can therefore obtain the smoother derivative shown in Fig. 5.18.

For this 3D printed full cylinder of PLA, we obtain a value of the energetic yield at 74.5 MPa. In comparison, the offset method of 0.1% strain currently used by experimentalists gives a value of 78 MPa, just a bit higher on the stress-strain curve as seen in Fig. 5.18. Once again, we would like still to point out that this 'offset method is dependent of an arbitrary threshold.'

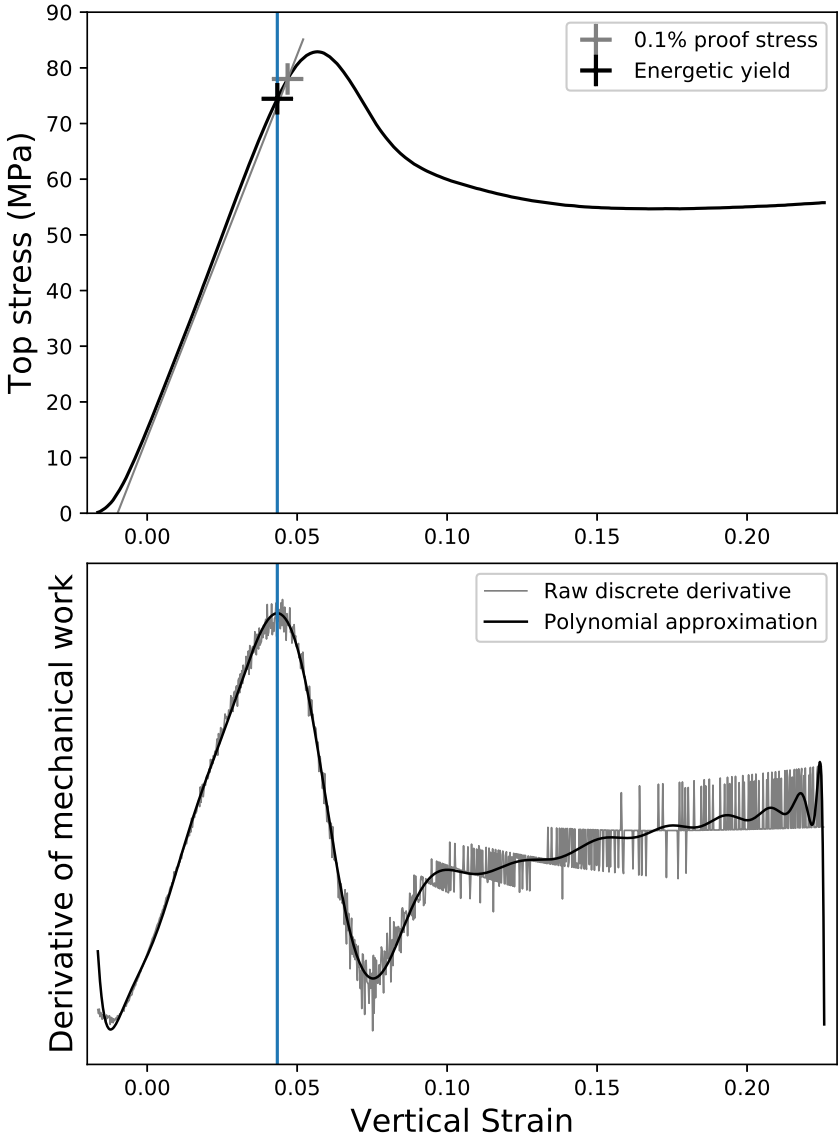


Fig. 5.18 Mechanical power dissipated during with loading time.

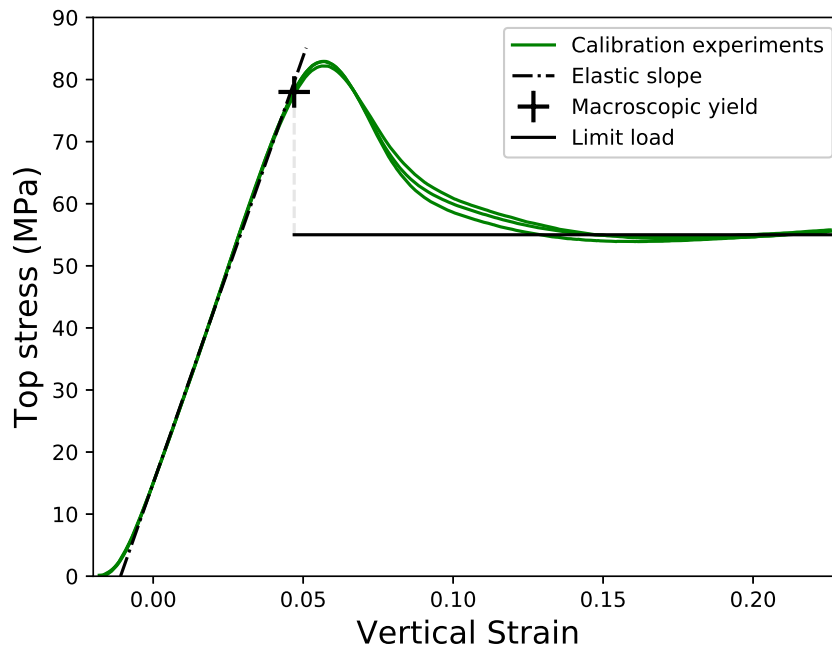


Fig. 5.19 Stress strain curves of uniaxial compression of 3D printed full cylinders of PLA. Our suggested elasto-plastic model is superposed to the curves and determined by three parameters: the slope of the linear elastic part, the yield value, and the limit load.

5.6.3 Mechanical model for 3D printed PLA

In this section we propose an elasto-plastic model to fit the stress-strain curves, plotted in Fig. 5.19, of the PLA cylinders printed as described in Sec. 5.6.1.

We can observe on that figure that the material does not behave in a linear elastic manner at first but rather displays a non-linear phase due to strain measurement errors (Jardine et al., 1984) (e.g. bedding error). Relatively quickly, however, the material follows a linear elastic response once the top stress value reaches a threshold of approximately 5 MPa, as seen on Fig. 5.19. In order to remove the inconsistent bedding error and have the elastic part of all curves superposed for assessing the reproducibility of the results, we shift the origin of vertical strain of each stress-strain curve so it corresponds to the stress value of 15 MPa, a safe arbitrary value of above which linear elasticity is fully observed.

As can be seen on Fig. 5.19, the elastic properties are extremely consistent between all samples as the elastic parts of the curves completely superpose. We can then measure a Young's modulus of 1375 MPa on the curves of Fig. 5.19 since the Young's modulus of the material is directly given by the slope of the elastic part in uniaxial compression. Since Poisson's ratio does not play a role in uniaxial compression, we do not measure it and assume the value reported in the literature of 0.45 for our numerical model, as the material is known to be quite incompressible. Note that despite the value being close to 0.5, the limit of incompressibility, no numerical instabilities were observed in the results.

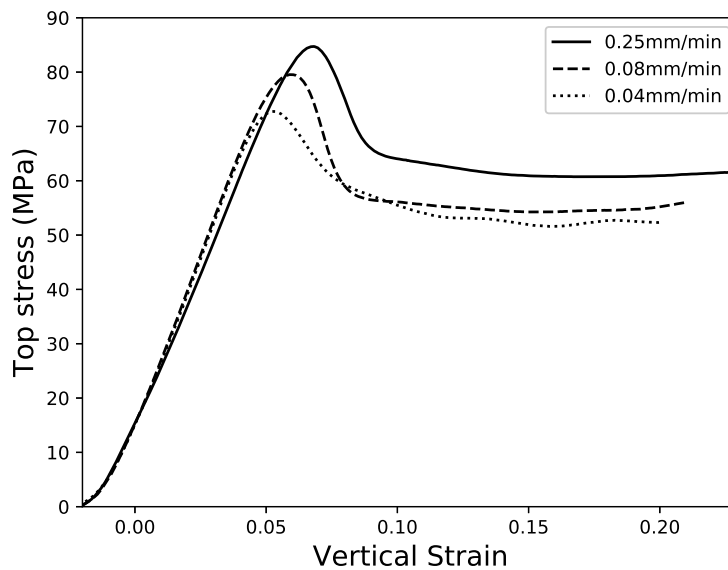


Fig. 5.20 Stress strain curves of uniaxial compression of 3D printed PLA cylinders under different loading rates.

As a polymer, PLA naturally remains viscoplastic after the printing process, as can be seen on Fig. 5.20 which shows the different responses obtained for varying loading rates. It is worth noting that the expected viscoelasticity of the PLA was not observed as the elastic part of the curves of Fig. 5.20 are superposing even at different loading rates. Since this contribution is not focused on quantifying the rate-dependency of the material, we select an arbitrary loading rate of 0.08mm/min for all experiments in this contribution.

The plastic part of the curves in Fig. 5.19 is decomposed in three different phases: Past the end of elastic behaviour, the material is hardening, which is due to the viscoplasticity of the polymer, until the peak stress is reached; after the peak stress, the material experiences softening, arguably from the shearband forming; eventually, the material converges to a limit load. Note that the curves on Fig 5.19 do not display a limit load per se as the stress increases again at large strains. The reason is that the sample is compressed above an amount of strain at which the top surface of the sample starts increasing due to the shearband, as can be seen on Fig. 5.21. As a result, even though the stress might have converged to a steady value, the load is increasing because the surface on which the stress is applied enlarges. Due to the technical difficulty to properly take this change of surface area into account, the stress plotted is calculated by accounting for the initial top surface area only, which can therefore not capture the eventual hardening at large strains. For this reason we decide to disregard the last part of the curves where the load increases and consider for the value of limit load the minimum value of stress achieved after softening.

Our contribution focuses on the influence of the microstructure on the material yield. For this reason, we do not necessarily need to capture in the model the parts of the stress strain curves that corresponds to the intrinsic behaviour of the material, i.e. the hardening from viscoplasticity



Fig. 5.21 Top view of cylinder compressed at large strains. Contacting surface has increased non-uniformly on the left side from initial surface highlighted in white.

and the softening from shearbanding. We focus instead on the two end points of the plastic behaviour: the macroscopic yield which corresponds to the onset of plasticity, and the limit load. Fig. 5.19 shows the calibration of the plasticity model for the 3D printed PLA with a value of the macroscopic yield measured at 78 MPa with the protocol of Sec. 5.6.2 and the value of the limit load at 55 MPa.

Note that the model selected here is only suggested for the specific printing settings with the testing procedure detailed in Sec. 5.6.1 and may not be applicable with other parameters as we have shown – non-exhaustively – that many parameters influence the mechanical properties of the printed PLA.

5.6.4 Forward prediction of the microstructure influence on PLA yields

The objective of this section is to verify that our numerical model is able to determine the influence of the microstructure on the yield points of a real material as it was showcased in Sec. 5.5 for an ideal material. In order to do so, we verify if the numerical model can correctly predict the yielding of printed PLA sample with a specific microstructure. Specifically, we simulate numerically a uniaxial compression test on cylindrical PLA samples with the same internal geometry as in Sec. 5.1.

Because the model presented for the printed PLA in Sec. 5.6.3 focuses only on the two end members of plasticity and does not model the hardening and softening behaviour that happens in between, we are only looking at the evolution of those two points. In order to get the evolution of each yield point we model the plastic behaviour separately with an ideal J_2 material as it is defined by our single parameter of interest, the yield point. Each simulation is run using the same model with respectively the energetic yield and the limit load value as input parameters

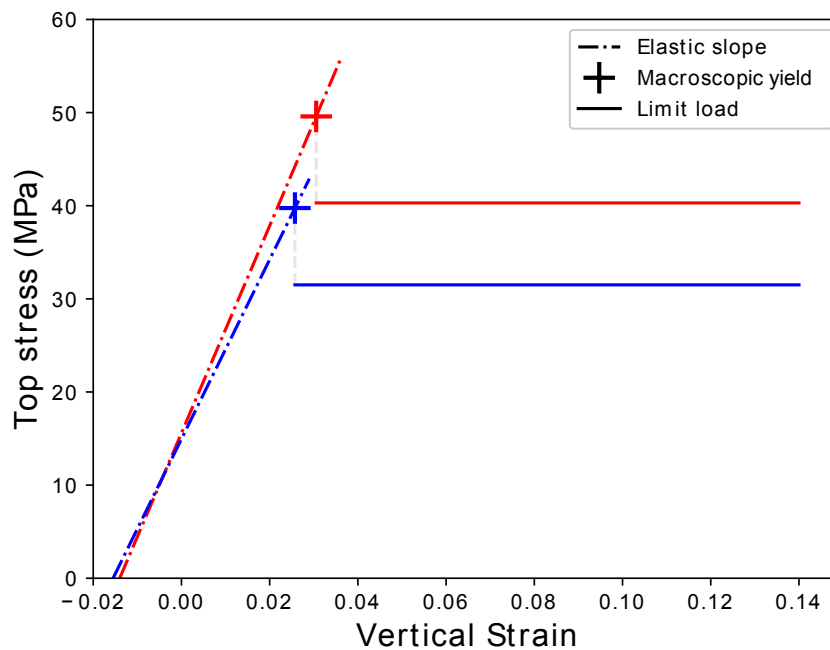


Fig. 5.22 Forward prediction of elasticity and characteristic plastic points of 3D printed PLA cylindrical samples with spherical void of varying normalised diameter: 0.6 in red and 0.7 in blue.

for plasticity. The value of the macroscopic yield of the porous system is measured using the protocol of Sec. 5.6.2 on the results of the first simulation. The value of the limit load is retrieved by taking the limit load value of the second simulation. Each computation is performed for two geometries of different hole diameter (normalised to the cylinder diameter), 0.6 and 0.7, meshed with second order tetrahedra. The results are displayed in Fig. 5.22, following the layout introduced in Fig. 5.19.

In order to validate the results of the numerical model, we run experimentally the equivalent uniaxial compression on 3D printed PLA samples that gives the exact behaviour of the porous material.

Compared to Sec. 5.6.3, the cylinders printed for this section contain a spherical void of varying diameter at their centre, which will collapse in plasticity. Due to the FDM principle of printing, the molten filament is deposited vertically on the sample, which makes it impossible for this technique to print correctly any overhanging part with an angle greater than 45° . Unfortunately, this is the case of the spherical void with the overhang going to 90° at the top of the sphere. To help the printing, FDM usually relies on printing under these overhangs some support structure that the user can remove after the print is finished. However, our overhang is fully enclosed in the structure so we would not be able to remove such a support structure and keeping it in place would increase artificially the resistance of the system. We decide therefore to print without any support structure and the resulting print is photographed in Fig. 5.23. We can see that the print remained acceptable, even though the quality is definitely affected. Fortunately,

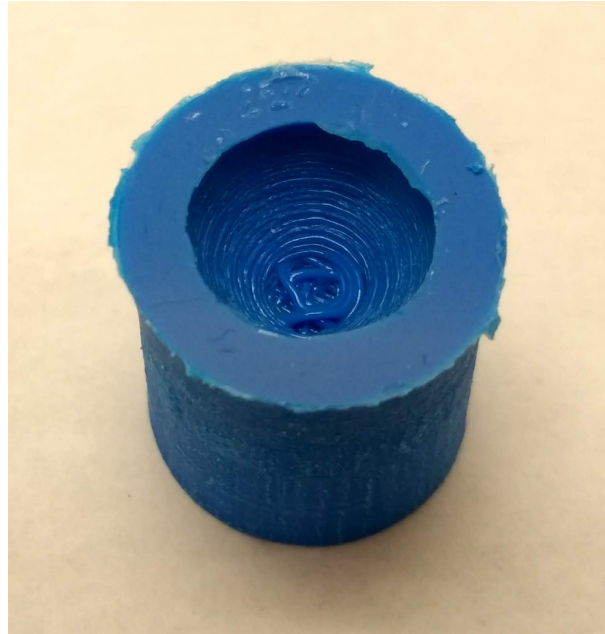


Fig. 5.23 Visualisation of the printing quality of the top of the spherical void of the hollow cylinder. Half of the cylinder was printed for visualisation purposes and the sample is displayed upside down.

during the mechanical compression, this top part of the sphere is the location which experiences the minimum of stress overall, so this quality of printing is suitable for our purposes.

The experimental results are plotted in Fig. 5.24 for two different sphere diameters, similarly to the numerical study, with each test repeated two times for reliability reasons. The good superposition of all curves shows that the results of hollow cylinders experiments are as reproducible as the full ones. The curves for the porous cylinders display sequentially a hardening and a softening phase, before converging to a limit load. As a reminder, an eventual hardening occurs artificially due to the increase of the surface area of contact, which is disregarded. All in all, the mechanical behaviours of the porous samples are very similar to the one for a full sample but with a lower and faster transition to plasticity as porosity increases. The modes of deformation, however, are different, as visualised in Fig. 5.25b. Due to the presence of the weaker sphere in the centre, the deformation localises in that area and results in a pore collapse, whereas the deformation of the full sample remains homogeneous.

The comparison of the numerical and experimental results of Fig. 5.24, quantified in Table. 5.2, shows that the simulation is matching closely the two properties of plasticity considered: the energetic yield and the limit load value. Interestingly, this perfect fit, observed in Fig. 5.24, demonstrates that the influence of the microstructure on a real material's yield could be retrieved even with an idealised model without taking into account the intrinsic behaviour of the real material. Particularly, we showed in this section that the influence of the microstructure on the yield is independent of the hardening and softening behaviour of our 3D printed PLA. This conclusion highlights the potential of the numerical approach to extract the impact of the microstructure on the yield despite an idealised modelling of the material.

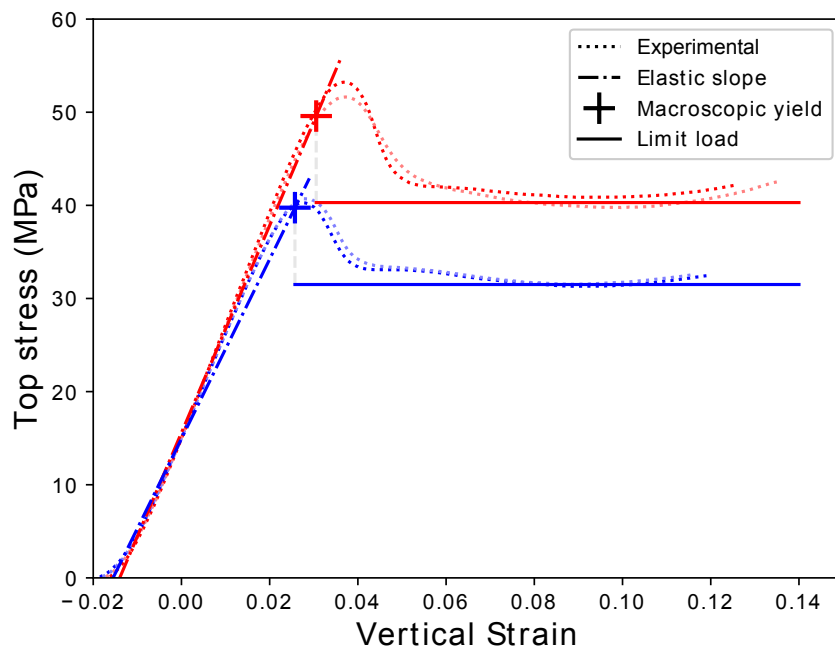
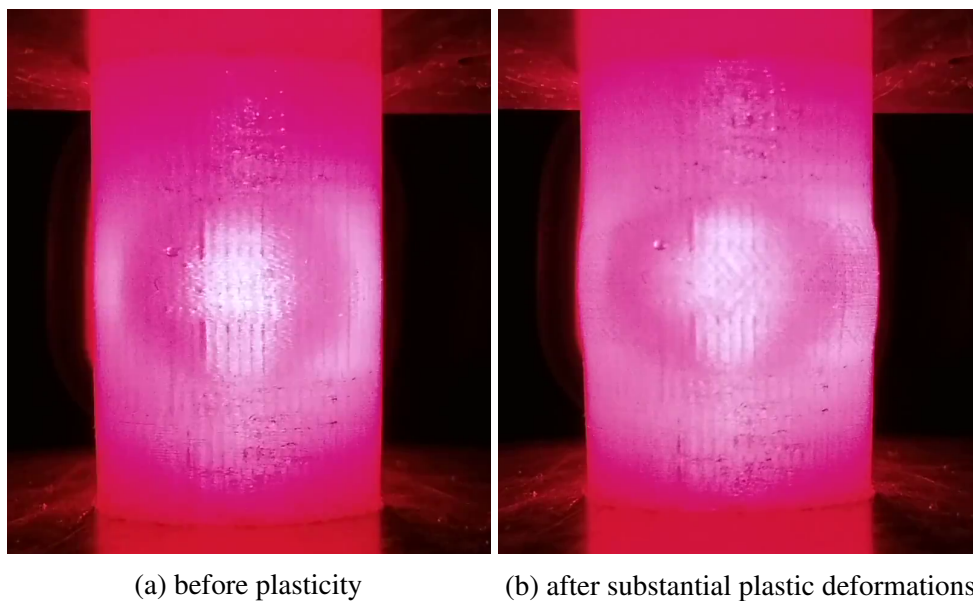


Fig. 5.24 Stress strain curves of uniaxial compression of 3D printed cylinders of PLA containing a spherical void of different normalised diameter: 0.6 in red and 0.7 in blue. The results of the simulation using the model of Sec. 5.6.3 are superposed to the experimental results.



(a) before plasticity

(b) after substantial plastic deformations

Fig. 5.25 Photos of a hollow cylinder, printed with semi-transparent PLA, in front of red light at two different stages of an uniaxial compression.

Table 5.2 Mechanical properties measured for the experimental and numerical results of the uniaxial compression of hollow cylinders.

Void diameter (normalised)	0.6			0.7		
Specimen number	exp 1	exp 2	simulation	exp 1	exp 2	simulation
Young's modulus (MPa)	1215	1181	1113	1123	1122	964
Energetic yield (MPa)	49.30	47.34	49.59	36.88	37.58	39.75
Limit load (MPa)	40.85	39.78	40.30	31.3	31.51	31.50

The advantage of studying the single pore compared to any arbitrary structure is that this geometry was designed as an idealised REV of a real rock microstructure. Therefore, our study should in principle be representative of one conducted on a real rock microstructure, which is confirmed by the fact that Gurson's theory on the hollow sphere is able to fit real data (Springmann and Kuna, 2005; Xie and Shao, 2006). We can therefore propose the hypothesis that our approach should be able to predict correctly the influence of the microstructure on the yielding of any given material, which is put to the test in the next section.

5.7 Application to real microstructure geometry

After the theoretical study on an idealised microstructure of a single spherical pore (Sec. 5.1-5.5) and its experimental validation (Sec. 5.6), we can eventually move our focus to a real rock microstructure and determine its influence on the rock's yield. As seen previously, two approaches are possible to do this analysis, numerically and experimentally. Both are detailed and compared below.

5.7.1 Experimental approach

In order to determine the rock's yield from its microstructure, we run a uniaxial compression laboratory experiment on a 3D printed reconstituted rock microstructure. The original rock selected is a 0.5 mm³ subsample of the Berea sandstone from the Imperial College Consortium On Pore-Scale Modelling (2014a). This geometry is first meshed using the method of Sec. 4.1.3 and then converted to an STL file format in order to be processed by the Ultimaker 3 machine for printing. The printer settings are detailed in Sec. 5.6.1 and the sample is printed as a cube of 22 mm³ size. The quality of the printed sample is quite remarkable in terms of details, capturing very well the overall complexity of the original rock, even though the quality of the print remains imperfect, as can be seen in Fig. 5.26-5.27, due to the 45° limit of any overhang discussed in Sec. 5.6.4.

Five printed samples are then tested in uniaxial compression following the experimental procedure of Sec. 5.6.1, with a loading speed of 0.08 mm/min. The results are plotted in Fig. 5.28. The resulting stress strain curves, plotted in Fig. 5.28, all have the same general shape, including the same elastic properties and plastic hardening, but noticeably different values of experimental

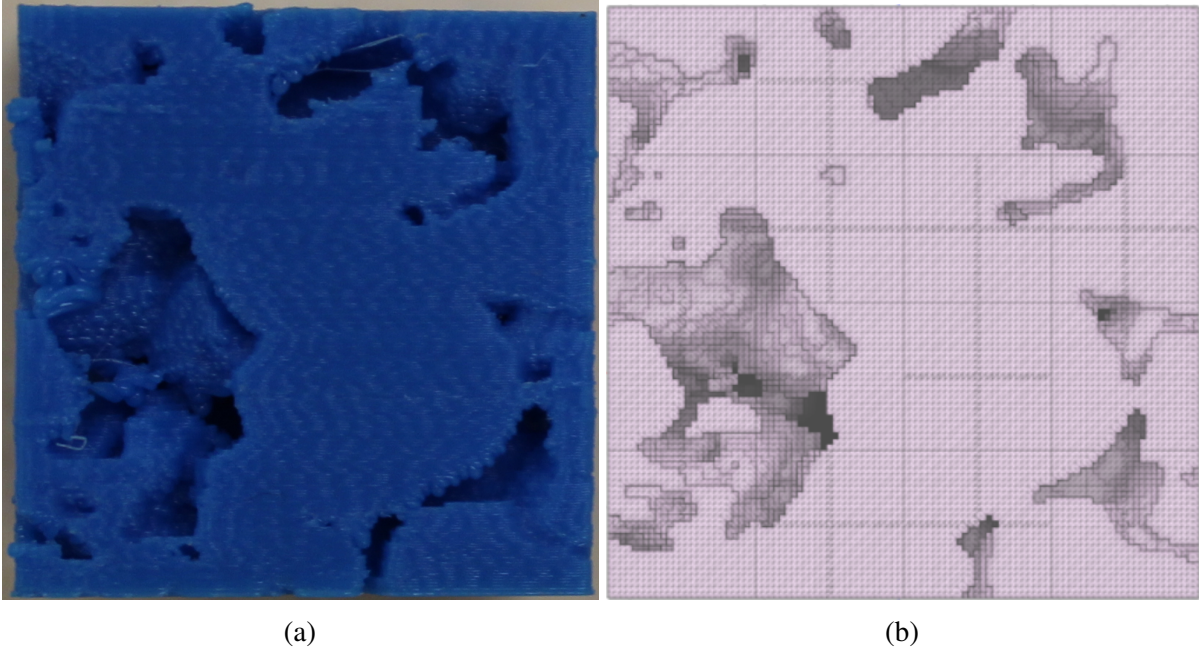


Fig. 5.26 Side face of the printed microstructure (a) compared to the digital rock (b).

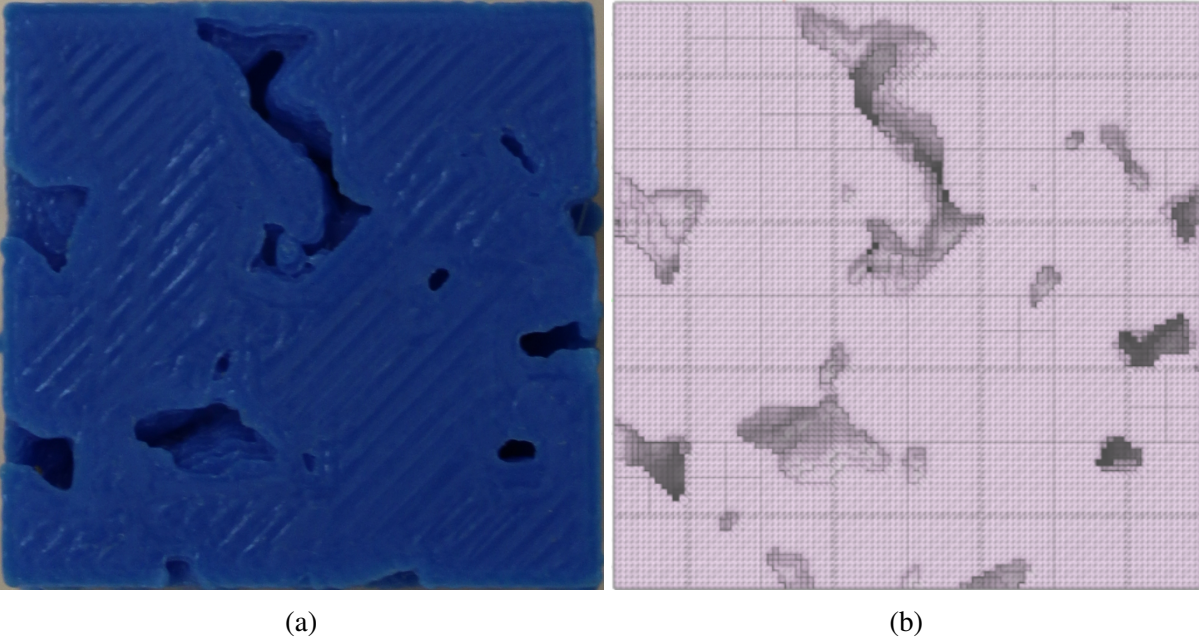


Fig. 5.27 Top face of the printed microstructure (a) compared to the digital rock (b).

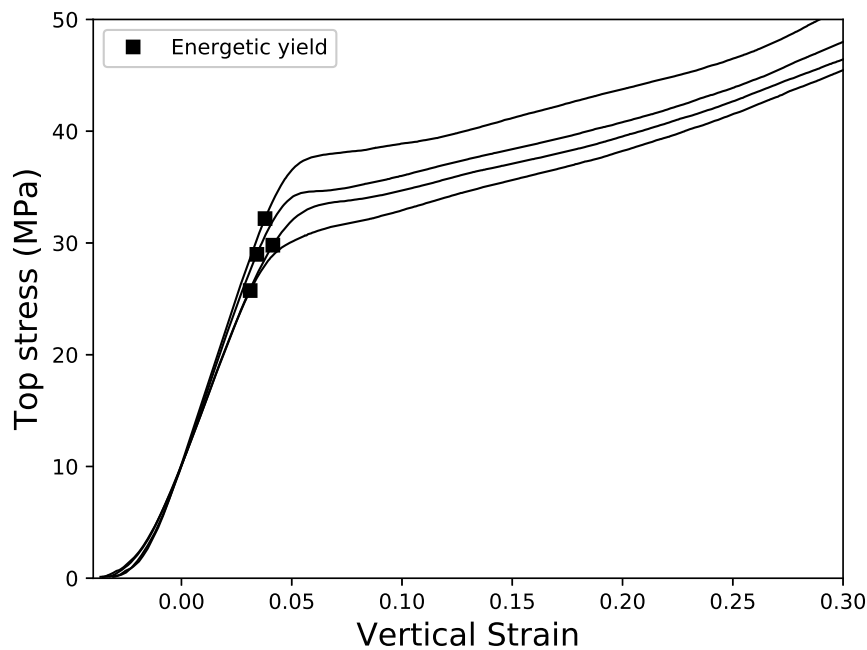


Fig. 5.28 Stress-strain curves of the uniaxial compression of 3D printed samples of digital rock.

yields. We can only infer that the lack of reproducibility is due to the poor printing quality because the curves of Fig. 5.24, whose samples' printing quality was high, superposed completely. Compared to Fig. 5.24, the complex microstructure plays a different role than the idealised single pore: the sample shows no softening nor limit load, but instead hardens continuously. The complex pore network in the μ CT-scan results in a very disperse pore collapse over the whole sample that could prevent therefore an homogeneous shearband to form which would explain the absence of softening.

Following the protocol of Sec. 5.6.2, we determine the energetic yield of the rock, as shown on Fig. 5.29. We note that the value does not match the experimental yield, found a few MPa below. The energetic yield is reported on Fig. 5.28 for each experimental curve. The error margin on the macroscopic yield, of 7 MPa, is directly correlated to the difference in magnitude of the different curves.

5.7.2 Numerical approach

In order to numerically determine the yield of this rock from its microstructure and be able to compare the results with the experimental approach in the following section, we run the same analysis as Sec. 5.6.4 on a digital version of that same microstructure, reconstructed from μ CT-scans and meshed following the method of Sec. 4.1.3. In order to retrieve exclusively the influence of the microstructure on the yield, we take an ideal $J2$ model for the plasticity of the matrix material as mentioned in Sec. 5.1.1. Still, for the sake of comparison, we calibrate this model to resemble the behaviour of the printed PLA plastic, on the response of 3D printed PLA

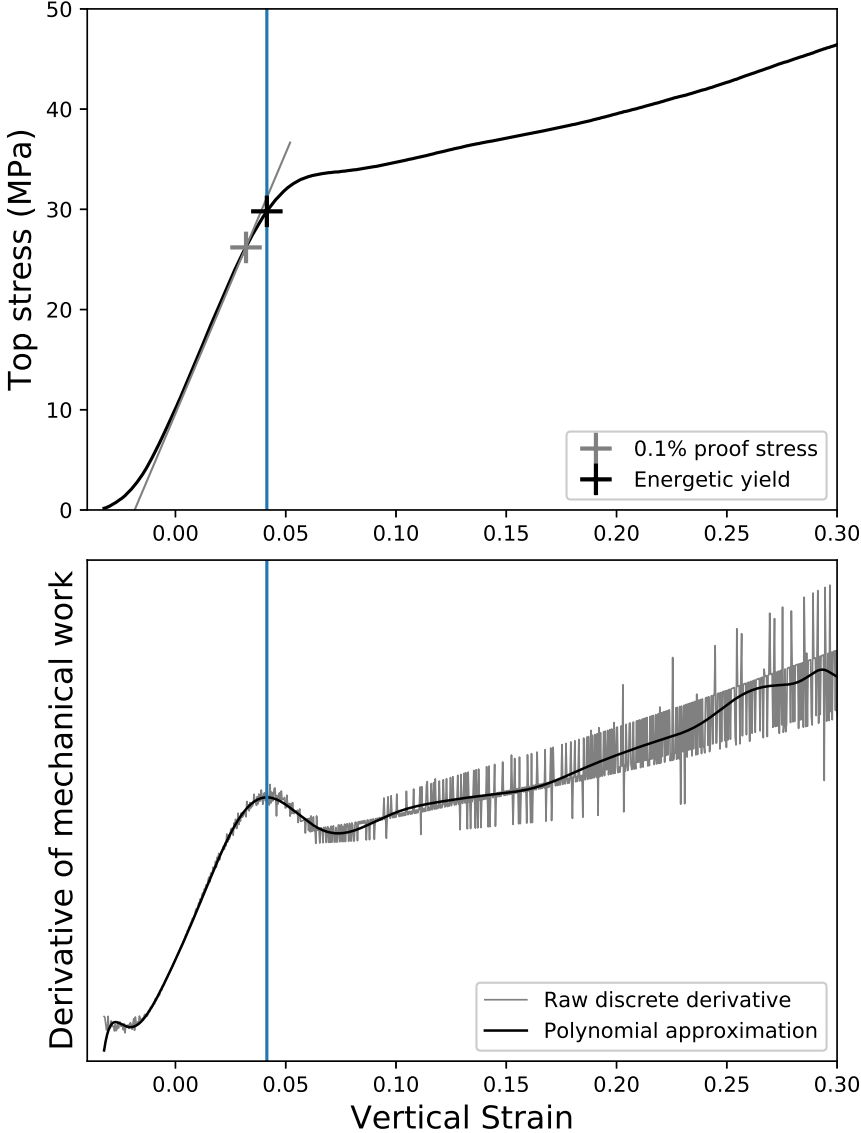


Fig. 5.29 Determination of the energetic and experimental yield of the 3D printed samples of digital rock.

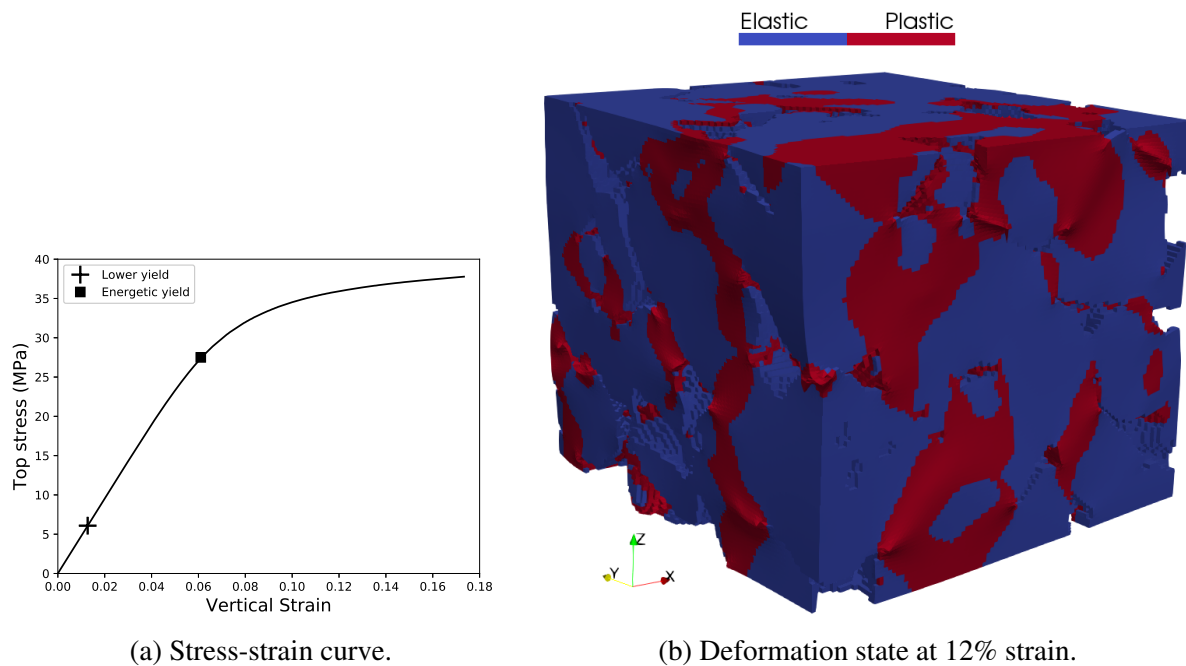


Fig. 5.30 Numerical uniaxial compression of a 0.5mm^3 subsample of the Berea sandstone from the [Imperial College Consortium On Pore-Scale Modelling \(2014a\)](#).

cubes of 22 mm size. Eventually the elasto-plastic model selected is an isotropic linear elasticity with a Young's modulus of 875 MPa and a Poisson ratio of 0.45 and a yield point of 70 MPa, calibrated on the energetic yield measured with the protocol of Sec. 5.6.2. The resulting stress strain curve is plotted in Fig. 5.30a. We can observe that we do not reach indeed a limit load like in Fig. 5.28.

Compared to the experimental approach, the advantage of the numerical one is that we can determine the lower-yield of the rock following the methodology of Sec. 5.2. Interestingly we see that the value obtained, reported on Fig. 5.30a, falls quite low on the stress-strain curve compared to the one obtained for the hollow-sphere, shown in Fig. 5.6b. This difference falls within our expectations because local stress concentration around the large number of heterogeneities present in real materials lowers the lower-yield and in comparison, the ideal hollow sphere geometry, without any heterogeneities, results in a unrealistically high value. Since the lower-yield does not represent any visible change of behaviour in the stress-strain curve, as we can see in Fig. 5.30a and even Fig. 5.6b, this is rarely the one measured in reality because, despite abiding to one of the possible definitions of yield ([Parker, 2003](#)).

5.7.3 Comparison of the two approaches

We can see that the curves obtained with both approaches, superposed in Fig. 5.31, are matching qualitatively as they all display a similar shape. However, the porous material appears to be stiffer and stronger (higher macroscopic yield) with the experimental approach. This could be explained by the reinforcement of the structure due to the existence of artificial bridges between pores that were created during the imperfect printing process. A μCT -scan of the printed sample

could possibly validate and quantify this effect but, in any case, the suboptimal printing quality adds to the uncertainty of the experimental results, which brings us more confidence in the value of elasticity and macroscopic yield determined with the numerical approach.

Despite the difference in magnitude, all curves display a similar hardening after the onset of plasticity. At large strains (past $\sim 20\%$), however, the hardening of the experimental curves is increasing, which is not the case on the simulated curve. This increase is easily explained by the creation of new contacts in the sample that occur after local pore collapses. The simulation cannot reproduce this behaviour since contacts are currently not supported in our mechanical simulator. Numerical results are therefore unrealistic passed a certain amount of strain, denoted by a dot on the numerical curve.

In conclusion, both approaches, experimental and numerical, proved able to determine able to determine one of the influences of the microstructure on a rock's yield, yet both with their own limitations. On the one side, the printing process we selected did not produce a quality high enough to obtain perfectly reproducible and therefore trustful results. On the other side, the lack of contact mechanics in the numerical simulator prevented the numerical results to be trusted at large strains. Nonetheless, those defaults remain at the technical level and one could expect improvements on both fronts in the near future: We can use 3D printing techniques more suited to print μ CT-scans with high resolution (achieved for instance in [Ishutov et al., 2015](#)); and MOOSE proposes a contact mechanics module ([Gaston et al., 2009](#)), but incorporating this functionality in our numerical model remains to be done.

It is important to note that, on top of their current abilities, both these methods present some extra capabilities which will also allow to superpose the intrinsic material behaviour of rocks to the influence of the microstructure. On the experimental side, we refer to the technology of powder bed and inkjet 3D printing technique that allows the creation of composite materials made of material powder bonded with a liquid agent. This method has been used in recent studies to replicate rocks with 3D printing ([Fereshtenejad and Song, 2016](#); [Jiang et al., 2016](#)), producing materials with the same brittle characteristics as rocks. On the numerical side, the model can be extended to capture different mechanisms and better reproduce particular rock properties. In particular, the next section showcases the extension of our mechanical simulator to the implementation of viscoplasticity.

5.7.4 Extension of the numerical model to viscoplasticity

Following on the study of a real microstructure above, this subsection presents the extension of the analysis to a matrix made of a more complex material. Specifically, we incorporate in our mechanical model the finite strain elasto-viscoplastic model used in REDBACK. The full system of equations was presented in Sec. 2.1 and the following paragraph briefly presents again the equations required for the scope of this study.

We here use an overstress (visco)plastic formulation, as described by [Poulet and Veveakis \(2016\)](#). For the simple case of the matrix modelled with associative J_2 plasticity, the flow law

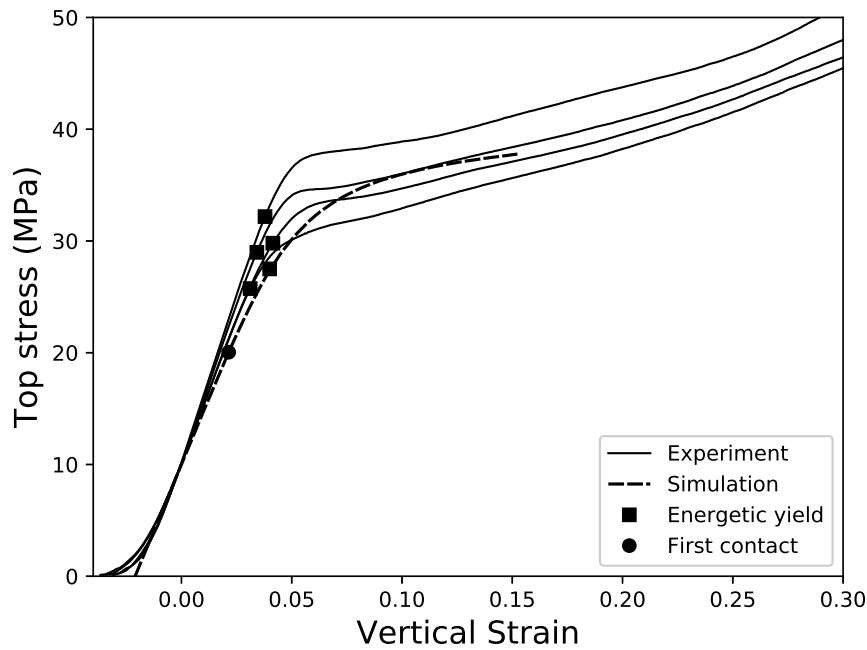


Fig. 5.31 Stress-strain curves of the uniaxial compression of 3D printed samples of digital rock.

reads:

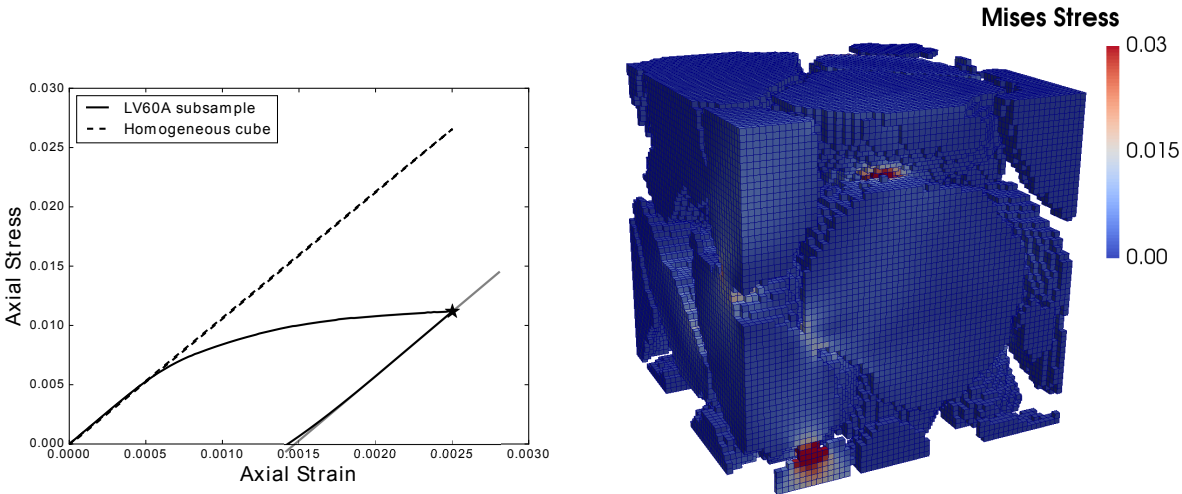
$$\dot{\boldsymbol{\epsilon}}_s^p = \dot{\lambda} \frac{\partial f}{\partial \boldsymbol{\sigma}_s} \quad (5.6)$$

$$\dot{\lambda} = \dot{\boldsymbol{\epsilon}}_{s,ref} \left\langle \frac{q}{q_Y} - 1 \right\rangle \quad (5.7)$$

In the above expressions, $f = q - q_Y$ is the yield surface, q_Y is the yield stress of the material in pure shear and $\dot{\boldsymbol{\epsilon}}_{s,ref}$ is a reference strain rate value.

To demonstrate the role of the mechanical model used in this study we simulate the uniaxial compression of the reconstructed LV60A ([Imperial College Consortium On Pore-Scale Modelling, 2014c](#)) sandpack sample, considering for simplicity a cubic subsample of 0.6 mm^3 . We consider an elasto-visco-plastic behaviour for the solid matrix with a von-Mises (i.e. pressure insensitive) yield criterion. A constant velocity is imposed to the top face of the sample. Isotropic elasticity is assumed and standard values for sandstone samples are used for the Young's modulus (10 GPa), Poisson ratio (0.3) and yield stress ($q_Y = 30 \text{ MPa}$).

Fig. 5.32a shows the results of the numerical simulation in terms of stress-strain response in solid lines, compared with the same response for a homogeneously solid cube represented in dashed lines. Fig. 5.32b shows the deviatoric stress distribution in the subsample used at peak stress, denoted by a star in Fig. 5.32a, showing the expected stress concentration and plastic zones at the grains contact. We observe and confirm an important point already stated that the pore structure induces a softening effect in the mechanical response of the sample. In addition, an extra unloading step is performed and shows that the unloading curve deviates from linearity,



(a) Normalised stress-strain curve. Grey line shows deviation from linearity in unloading.

(b) Visualisation of normalised deviatoric stress at maximum loading time (see star symbol in Fig. 5.32a)

Fig. 5.32 Simulation results of uniaxial test on a subsample of the LV60A sandpack from Imperial College Consortium On Pore-Scale Modelling (2014c) of size 0.6 mm, meshed with 138,070 elements. The normalised value of von-Mises yield stress is 0.03.

suggesting a degradation of the elastic modulus of the structure due to irreversible deformation of the pore structure, observed in the experiments of Sari (2019, Fig. 2.15-2.16).

Chapter 6

Permeability homogenisation of deforming microstructure

Having studied the influence of the microstructure on the mechanical behaviour of the material in the previous chapter, we now focus our analysis on its influence at the micro-scale on fluid flow, which gets homogenised to Darcy's law at the meso-scale through the notion of permeability. The first section (Sec. 6.1) presents our flow simulator at the micro-scale and the method to homogenise permeability at the next scale up. Using this framework, we then study the influence on the flow behaviour of both mechanical deformations (Sec. 6.2) and chemical alterations (Sec. 6.3) of the microstructure.

6.1 Flow simulator (Eulerian)

In this section, we present the underlying system of governing equations describing the flow of a fluid through a fully saturated rock pore space. We consider a porous rock at the micro-scale composed of a solid matrix and a pore space containing a single phase incompressible fluid.

6.1.1 Flow equations at the micro-scale

Generally, the flow in the pore space is governed by the Navier-Stokes equations (Batchelor, 2000). Given the geological applications targeted (see Part I), we can restrict the study to the case of low-velocity flow and consider therefore the flow to be laminar. For the purpose of computing permeability, solving the steady-state flow is even sufficient. Based on these assumptions the system is reduced to the traditional Stokes equations. To normalise the system we introduce the dimensionless variables

$$p_f^* = \frac{L_{ref}}{\mu_f v_{f,ref}} p_f, \quad (6.1)$$

$$\vec{v}_f^* = \frac{\vec{v}_f}{v_{f,ref}}, \quad (6.2)$$

where \vec{v}_f denotes the fluid velocity and p_f the fluid pressure in the pore space, μ_f is the fluid viscosity and L_{ref} and v_{ref} are respectively length and velocity references. The Stokes system can be expressed in dimensionless form as

$$-\frac{1}{Re} \nabla^2 \vec{v}_f^* + \nabla p_f^* = 0, \quad (6.3)$$

$$-\nabla \cdot \vec{v}_f^* = 0, \quad (6.4)$$

where Re is the Reynolds number. All symbols are defined in Table 1. Eq. 6.3 expresses the momentum balance in the case of laminar, steady-state flow, while Eq. 6.4 presents the simplified mass balance under the assumption of incompressibility. This set of equations requires some boundary conditions to be solved and a common approach consists in imposing no-slip at the interface between the pore space and the grains.

Darcy-Brinkman model

Imposing no-slip boundary conditions at the pore-grain interface requires the identification and tracking of that interface at every timestep, which can become a numerical challenge by itself when the interface evolves in time due to quasi-static mechanical deformation or chemical alteration of the microstructure. Fortunately, this issue can be avoided altogether using a slightly different approach and solving for the Darcy-Brinkman system of equations, which was introduced by Brinkman (1949) as an extension of Darcy's law in order to be able to simulate "the viscous force exerted by a flowing fluid on a dense swarm of particles" (Brinkman, 1949). It can be expressed in a dimensionless form as

$$-\frac{1}{Re} \nabla^2 \vec{v}_f^* + \frac{1}{Re k^*} \vec{v}_f^* + \nabla p_f^* = 0, \quad (6.5)$$

$$-\nabla \cdot \vec{v}_f^* = 0, \quad (6.6)$$

where $k^* = \frac{k}{L_{ref}^2}$ is the normalised permeability. This system is particularly useful to simulate flow in fractured porous media, for instance, as the usage of the permeability in the second term of Eq. 6.5 allows an easy handling of the flow with Darcy's law in the matrix, where the permeability value is determined, as well as in the fractures, where the permeability would be considered infinite, simply cancelling that term in the equation and reducing the system to Stokes flow. The same approach can be used on a micro-scale structure, using infinite permeability in the pore space (10^{15} in this contribution) and an arbitrary low but positive value of permeability within the solid matrix (10^{-15} in this contribution), as the grains are considered impermeable. This technique allows to simulate the flow within the pore space without having to discretise the interface boundary and impose on it no-slip boundary conditions. Instead the no-slip boundary conditions are respected automatically at the pore-grain interface delimited only in the distribution of permeability, where it jumps from infinite to infinitesimal.

6.1.2 Numerical Implementation

In this section, we introduce the implementation of the flow simulator used to model the fluid behaviour within the pore space, having drawn inspiration from the early development of the Navier-Stokes module of MOOSE (Gaston et al., 2009), now published as Peterson et al. (2018). Both models presented in the previous section are implemented as part of REDBACK (Poulet and Veveakis, 2016), within the FEM platform MOOSE. Compared to other numerical simulators specifically designed to solve such flow problems, the finite element approach selected comes at a computational price in terms of processing and memory usage, but the hybrid parallelism of MOOSE compensates for those limitations as the code is specifically designed to run on supercomputers, as needed in Sec. 6.1.6. The model equations (Eq. 6.3-6.4) and (Eq. 6.5-6.6) are introduced in the numerical platform through their variational statement, also known as weak form, which can then be solved on any provided mesh, with different mesh types being supported.

Weak form

Given the similarities between the Stokes and Darcy-Brinkman systems, we illustrate the weak formulation on Stokes' problem only. The system of equations (Eq. 6.3-6.4) in three dimensions involves four coupled variables: three variables for the fluid velocity \vec{v}_f (one for each spatial dimension) and a variable for fluid pressure p_f . For error consistency reasons, as stated by Hood and Taylor (1974), we use a polynomial interpolation of second order for the velocity and first order for the pressure. This constrains the mesh to use second order elements.

The weak form of the system is derived by introducing test functions (ψ_p , ψ_{vx} , ψ_{vy} , ψ_{vz}) for each variable, which are multiplying the system in its integral form to reduce the continuity requirements of the solution.

For the mass balance, multiplying Eq. 6.4 by ψ_p and integrating over the whole volume Ω leads to the weak form

$$\int_{\Omega} \psi_p (-\nabla \cdot \vec{v}_f^*) = 0 \quad (6.7)$$

For simplicity of notation, round parentheses are used to denote volumetric integrals, $(a, b) = \int_{\Omega} a \cdot b$, and this weak form can then be written as

$$(\psi_p, -\nabla \cdot \vec{v}_f^*) = 0 \quad (6.8)$$

Similarly, the weak form of the momentum balance for $i = (x, y, z)$ is derived from Eq. 6.3 as

$$\int_{\Omega} \psi_{vi} \left(-\frac{1}{Re} \nabla^2 v_{fi}^* \right) + \int_{\Omega} \psi_{vi} \partial_i p_f^* = 0 \quad (6.9)$$

where the Einstein notation does not apply. Using the divergence theorem to reduce the polynomial order of both the velocity and the pressure variables in the residual, this equation can be

rewritten as

$$\int_{\Omega} \nabla \psi_{vi} \cdot \frac{1}{Re} \nabla v_{fi}^* - \int_{\partial\Omega} \psi_{vi} \left(\frac{1}{Re} \nabla v_{fi}^* \cdot \vec{n} \right) - \int_{\Omega} \nabla \psi_{vi} \cdot p_f^* + \int_{\partial\Omega} \psi_{vi} (\partial_i p_f^* \cdot \vec{n}) = 0 \quad (6.10)$$

and finally, as

$$\left(\nabla \psi_{vi}, \frac{1}{Re} \nabla v_{fi}^* \right) + \langle \psi_{vi}, -\frac{1}{Re} \nabla v_{fi}^* \cdot \vec{n} \rangle + \left(\nabla \psi_{vi}, -p_f^* \right) + \langle \psi_{vi}, \partial_i p_f^* \cdot \vec{n} \rangle = 0 \quad (6.11)$$

using an angular bracket notation to express surface terms for the boundary conditions $\langle a, b \rangle = \int_{\partial\Omega} a \cdot b$.

In order to set up a pressure-driven flow, the common approach is to impose a high pressure at the inlet and a low pressure at the outlet. However, due to Stokes system formulation where the pressure variable is essentially reduced to a Lagrange multiplier of the divergence free condition on the velocity, no boundary conditions on the pressure can be prescribed. The pressure gradient has to be imposed with a Neumann boundary condition of velocity at the inlet equal to the value of the pressure gradient that needs to be imposed. One possible solution is for instance to switch the formulation to the pressure Poisson equation (see discussion by [Gresho and Sani \(1987\)](#)). In this contribution we chose a different solution that allows us to use directly Dirichlet boundary conditions of pressure to simulate a global pressure gradient. The approach consists simply in not integrating by part the pressure term of Eq. 6.9.

The system of equations is solved using a Newton solver, and as such the jacobian of the system is required in order to improve numerical convergence ([Gaston et al., 2009](#)). The jacobian formulation of Eq. 6.8 and 6.11 in its matrix form derived respectively by \vec{v}_f^* and p_f^* is expressed as

$$J = \begin{pmatrix} \left(\nabla \psi_{vx}, \frac{1}{Re} \partial_{v_{fx}^*} (v_{fx}^* \nabla \Phi_{vx}) \right) & 0 & 0 & \left(\psi_{vx}, \partial_{p_f^*} (v_{fx}^* \nabla \Phi_{vx}) \right) \\ 0 & \left(\nabla \psi_{vy}, \frac{1}{Re} \partial_{v_{fy}^*} (v_{fy}^* \nabla \Phi_{vy}) \right) & 0 & \left(\psi_{vy}, \partial_{p_f^*} (v_{fy}^* \nabla \Phi_{vy}) \right) \\ 0 & 0 & \left(\nabla \psi_{vz}, \frac{1}{Re} \partial_{v_{fz}^*} (v_{fz}^* \nabla \Phi_{vz}) \right) & \left(\psi_{vz}, \partial_{p_f^*} (v_{fz}^* \nabla \Phi_{vz}) \right) \\ \left(\psi_p, \partial_{v_{fx}^*} (p_f^* \nabla \Phi_p) \right) & \left(\psi_p, \partial_{v_{fy}^*} (p_f^* \nabla \Phi_p) \right) & \left(\psi_p, \partial_{v_{fz}^*} (p_f^* \nabla \Phi_p) \right) & 0 \end{pmatrix}$$

where Φ_i denotes the trial functions for each variable. The implementation of all jacobians is indeed essential for the convergence of a Newton scheme, however the numerical problem in this case remains stiff and requires a good preconditioning scheme. The scheme used in this study is detailed in the following section.

Divergence-free condition

In order to respect the divergence-free condition from Eq. 6.4 we need to ensure that the number of velocity unknowns will be greater than the number of pressure unknowns for the equation to be numerically consistent. This can be obtained for example by using admissible elements as stated by the Brezzi-Babuška condition ([Brezzi, 1974](#)). Taylor-Hood elements ([Taylor and Hood, 1973](#)) respect this condition and have been shown to be more accurate than regular second-order

elements (Huyakorn et al., 1978). In 2D these are Taylor-Hood quadrangle (QUAD9) elements, using nine nodes for the interpolation of the flow velocity and four nodes for the fluid pressure. In 3D these are Taylor-Hood hexagonal (HEX27) elements with 27 nodes for the velocity and eight for the pressure. Note that the divergence-free condition can still be respected without the Brezzi-Babuška condition by using a Petrov-Galerkin method of stabilisation that introduces a stabilising term in the system. In this contribution we use the pressure-stabilising/Petrov-Galerkin formulation (Tezduyar et al., 1992) or Taylor-Hood elements, depending on the application at hand.

6.1.3 Preconditioner

The Stokes problem (Stokes, 1845) has been extensively studied (see review from Blunt et al., 2013) already and as such a lot of research is focusing on improving the robustness of the underlying solvers. This research field falls outside the scope of this contribution and we limit ourselves to existing numerical solutions available in the PETSc (Portable, Extensible Toolkit for Scientific Computation) library (Balay et al., 2016b). We are using a suitable preconditioner to fit the block definition of the underlying system of equations, which can be written in matrix form as

$$\begin{pmatrix} A & B \\ B^T & 0 \end{pmatrix} \begin{pmatrix} \vec{v}_f^* \\ p_f^* \end{pmatrix} \quad (6.12)$$

with

$$\begin{aligned} A [\vec{v}_f^*] (\psi) &= (\nabla \psi, \frac{1}{Re} \nabla \vec{v}_f^*) \\ B [p_f^*] (\psi) &= (\nabla \psi, p_f^*) \\ B^T [\vec{v}_f^*] (\psi) &= (\psi, \nabla \cdot \vec{v}_f^*) \end{aligned}$$

The matrix in Eq. 6.12 presents a saddle point problem since the mass balance equation does not depend on fluid pressure, leading to zero entries on the diagonal. As a result it is numerically challenging to solve without adapted preconditioning. Following Elman et al. (2008), the Schur method is used to precondition the system. We follow a prescribed solution from Balay et al. (2016a) and use a Jacobi preconditioner for the fluid pressure subsystem and the algebraic multigrid method (BoomerAMG (Henson and Yang, 2002)) from HYPRE for the fluid velocity subsystem.

6.1.4 Verification of flow simulator

To test the validity of the flow simulator presented in this section, we present some benchmark applications, including the Poiseuille flow in a tube and some permeability computations, before applying it to realistic geometries with tortuous flow paths in the following section.

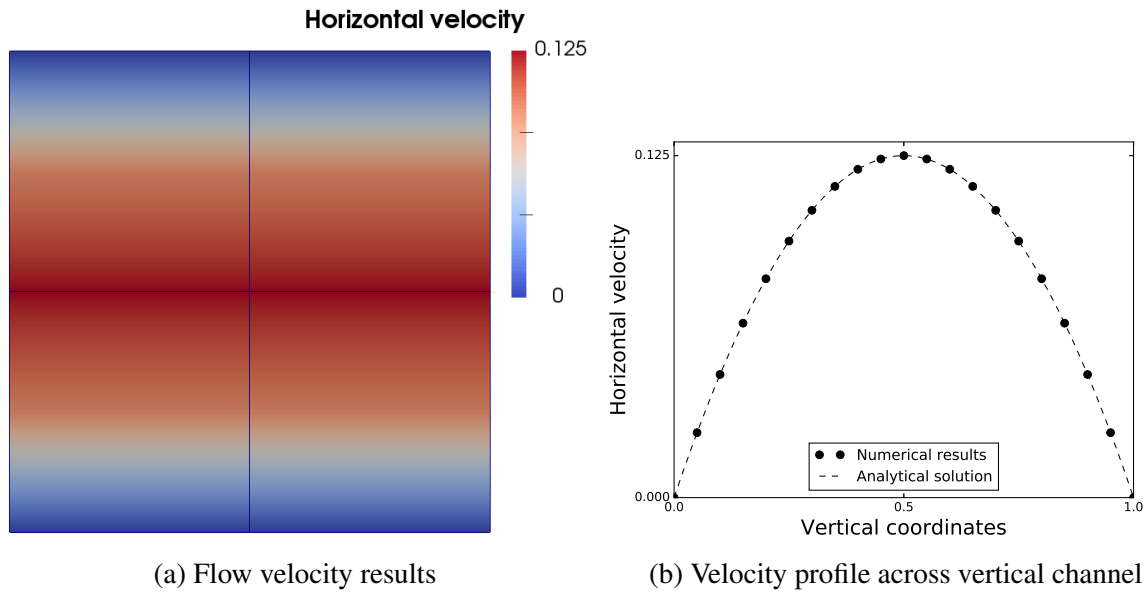


Fig. 6.1 Dimensionless velocity profile on the outlet for Poiseuille flow for the coarsest mesh, 2×2 Taylor-Hood elements, leading to a machine-precision match between the numerical results and the analytical solution $v_{fx,max} = \frac{h^2 \Delta p_f}{8 \mu_f L} = 0.125$.

The simplest application to benchmark a numerical flow simulator is the traditional Poiseuille flow, a pressure-driven flow in a constant diameter tube, because of its simple analytical solution. The expected velocity field in 2D in cartesian coordinates is expressed as

$$v_{fx} = \frac{\Delta p_f}{2 \mu_f L} y(h-y) \quad (6.13)$$

with h the height of the tube following the y -direction, μ_f the fluid viscosity and L the length of the tube in the x -direction. The vertical velocity is equal to 0.

The problem is setup numerically by using a square domain of size 1 m, using the left hand side as a flow inlet and the right hand side as the corresponding outlet. The fluid considered is characterised by a viscosity $\mu_f = 1$ Pa.s and the overall problem is described by a Reynolds number $Re = 1$. A pressure gradient of 1 Pa is applied horizontally over the domain by setting $p_f = 1$ Pa on the inlet and $p_f = 0$ Pa on the outlet. No-slip boundary conditions are imposed at the top and bottom boundaries. Vertical velocity is also forced to zero on the inlet to ensure horizontal flow, in compliance with Poiseuille flow.

The obtained velocity profile matches the analytical solution from equation 6.13 at machine precision, as illustrated in Fig. 6.1, using any number $N \geq 2$ of elements across the channel because of the second-order nature of the elements used (QUAD9).

Since Darcy-Brinkman is used specifically to simulate flow in porous media, in order to validate the implementation presented in Sec. 6.1.1, we place the Poiseuille flow channel of Fig. 6.1a in the middle of a solid phase layer. The flow in the fluid channel follows the Poiseuille law and therefore we can compare the numerical result to the analytical solution. Fig. 6.2 shows the mesh convergence of the simulation for the value of the horizontal velocity in the middle

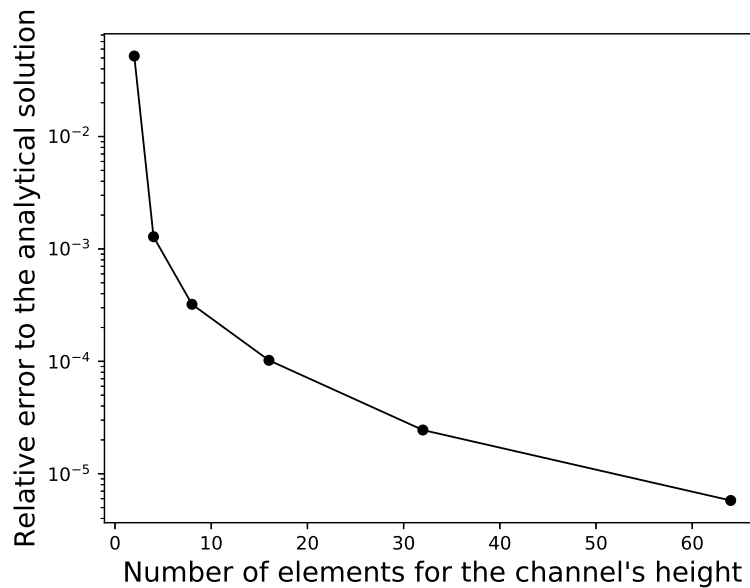


Fig. 6.2 Mesh convergence of the horizontal velocity in the middle of a Poiseuille flow channel, simulated with the Darcy-Brinkman formulation. At each point, the mesh is refined following the octree method.

of the channel. Compared to Stokes benchmark of Poiseuille flow that converges exactly to the analytical solution even for the coarsest mesh, it takes a high resolution for Darcy-Brinkman to converge. This study points out that Darcy-Brinkman's simplicity of dealing with porous media is counterbalanced in the precision of the results compared to Stokes. However, given the large permeability evolution due to mechanical and chemical deformations (see Fig. 2.2) considered in the following sections, a precision of 10^{-3} for the less accurate method, Darcy-Brinkman, is acceptable. Therefore, both methods are suitable for this problem.

6.1.5 Validation of permeability computation

One of the principal applications of flow simulations at the pore-scale resides in the numerical computation of permeability. As a second type of applications, we propose therefore to compute permeability for porous samples in different configurations.

Permeability computation scheme

The steady-state flow is computed using no-slip boundary conditions at the fluid-rock interface and the sample boundaries. A pressure-driven flow is imposed across the whole sample by setting a higher pressure at a chosen inlet and a lower pressure at the corresponding outlet. All samples used in this contribution are cubic and the inlet and outlet are considered on opposite faces. A pressure difference $\Delta p^* = 1$ is selected to remain in the laminar regime.

The concept of permeability was first introduced by [Darcy \(1856\)](#) as an empirical quantity k relating the superficial fluid flow v_{fs} with the applied pressure gradient across the sample, in

order to quantify the value of hydraulic conductivity.

$$k = \mu_f L_{ref} \frac{v_{fs}}{\Delta p_f} \quad (6.14)$$

Darcy's law was first derived empirically but eventually proven to be a homogenisation of the Stokes formulation (Whitaker, 1986) under a strict set of conditions.

The velocity v_{fs} used in Darcy's law is the superficial velocity, defined by the flow rate through a cross-section. This velocity is different from the variable \vec{v}_f used in the Stokes formulation, representing local velocities. In a porous medium, the superficial velocity and the local velocity are linked by the relationship

$$v_{fs} = \phi \vec{v}_f \cdot \vec{n}$$

Note that the superficial velocity is not the norm of the local velocity vector, but its projection on a selected flow direction defined by a unit vector \vec{n} .

Using the dimensionless variables of Eq. 6.1-6.2, the permeability definition becomes

$$k = \frac{\phi \vec{v}_f^* \cdot \vec{n}}{\Delta p_f^*} L_{ref}^2 \quad (6.15)$$

Note that the reference length L_{ref} used in this contribution is the length of the sample's considered. This equation provides a value for a given direction by averaging over the whole volume, in line with the homogenised nature of permeability. This computation of permeability is used to test the flow simulator on a series of usual configurations presented below.

Kozeny-Carman law

One of the most commonly used formulas to calculate permeability of granular porous media is the Kozeny-Carman model. Modelling originally a granular bed with an equivalent array of Poiseuille channels, it provides a relationship between permeability k , porosity ϕ and average grain size d_s , and as such is well suited for permeability calculation for undeformed granular rocks. The equation derived by Carman (1937) reads

$$k = \frac{d_s^2}{36K} \frac{\phi^3}{(1-\phi)^2} \quad (6.16)$$

The parameter K represents the Kozeny's constant and has been experimentally calibrated by Carman to an approximate value of 5 for uniform sphere packing, which is the case in this section.

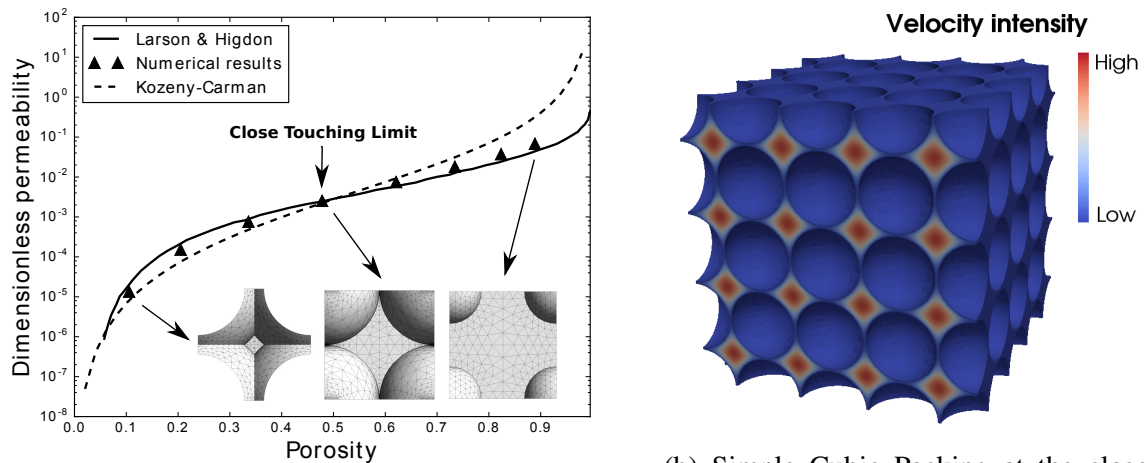
This relationship was originally obtained by studying a head of water filtering through a sand bed by gravity. Starting from the analytical Poiseuille law, the model was derived semi-analytically and calibrated with experimentation on real samples. One of the main assumptions of this model is the consideration of spherical grains, which is suitable for unconsolidated sand

(Taylor, 1948) on which the model was built. For this reason we are testing firstly the numerical calculation of permeability with the flow simulator on beds of packed spheres and comparing the results with the Kozeny-Carman relationship. The meshes required for such a configuration are created in the meshing software SALOME (Ribes et al., 2017), using the NETGEN meshing algorithm which was selected for its ability to handle topological operations. This functionality is particularly important as the medium is consolidated and grains are touching. A Python script for SALOME was developed which takes as input parameters the spheres distribution defined by all centres coordinates and corresponding radii. The resulting meshes are unstructured and capture the interface of the spheres, accordingly to the level of refinement selected. Grouping of elements is performed to define the boundaries and pore-grain interface needed for the flow simulation. Note that this workflow generates unstructured second-order but not Taylor-Hood elements (see Sec. 6.1.2), so the divergence-free condition is not strictly enforced. This limitation however does not affect the results for the benchmarks presented in this section.

Regular packing We consider a Simple Cubic Packing, the simplest regular sphere packing, where spheres of diameter d_s are located at the corners of a cubic periodic pattern of length L . We compute the permeability of the whole packing (Fig. 6.3b) for a single pattern geometry by applying periodic boundary conditions for the flow. In this configuration, the close touching limit of the spheres happens for $d_s = L$, which corresponds to a value of 47.6% porosity. We can see in Fig. 6.3a that in this case the permeability is very close to the one calculated with the Kozeny-Carman relationship. This comparison is repeated for various values of porosity, following the configuration described by Zick and Homsy (1982) by varying d_s . Since the porosity variation is obtained through changes of the sphere radius, the dimensionless permeability k/d_s^2 is plotted in Fig. 6.3b as it is independent of the grain size. The result matches previous results from Larson and Higdon (1989). Note that this packing is not expected to reproduce precisely the Kozeny-Carman results away from the Close Touching Limit when Carman's underlying assumption of touching spherical grains is no longer respected.

Random Close Packing The perfectly periodic packing presented above (Sec. 6.1.5) is not particularly representative for rocks and we now consider a more realistic scenario for granular media with Random Close Packing (RCP).

To create such a distribution of spheres, we use the YADE (Smilauer et al., 2015) package and its *randomDensePack* function. The center coordinates and radii of all spheres are then extracted to feed the meshing script presented above. The lack of periodicity for this configuration, unlike the Simple Cubic Packing, adds an extra step to identify the permeability of such a packing. The identification of a representative elementary volume (REV) for this parameter is indeed required. It can be obtained by computing the evolution of the overall permeability (see Fig 6.4) for a given flow direction as a function of the sample size, which we monitor via the number of spheres considered. The choice of flow direction should not affect the final convergence value of permeability since the overall packing remains isotropic for a large enough number of



(a) Permeability vs porosity. The geometry of the pore touching limit. Pressure gradient is imposed from the inlet and the pressure gradient in the space seen from the inlet is shown for different values of sphere radius.

(b) Simple Cubic Packing at the close touching limit. Pressure gradient is imposed from the inlet and the pressure gradient in the space seen from the inlet is shown for different values of sphere radius.

Fig. 6.3 Comparison of permeability vs porosity evolution against Kozeny-Carman and results from Larson and Higdon (1989) for a Simple Cubic Packing.

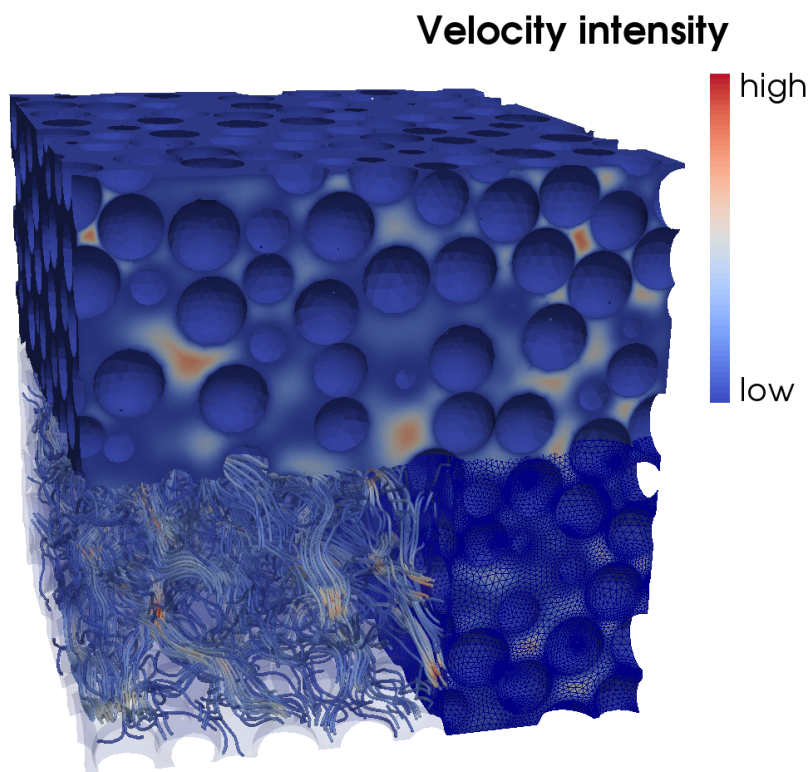
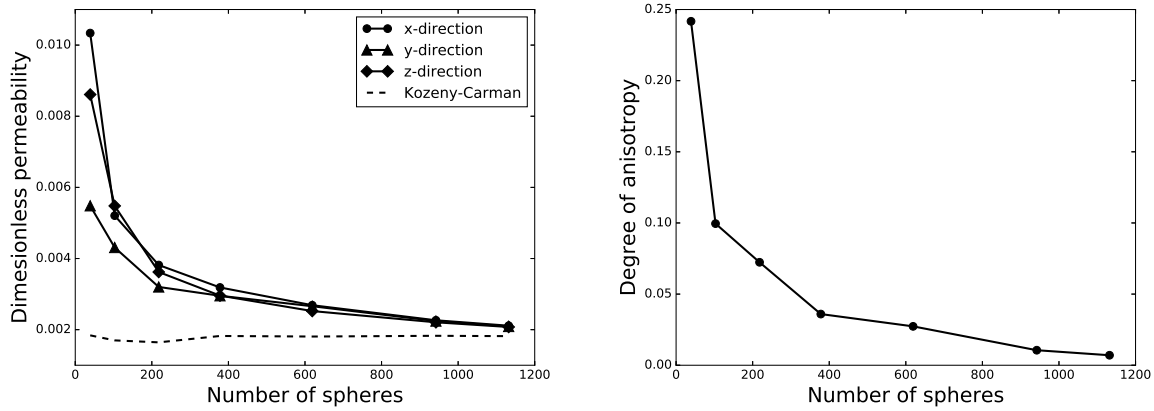


Fig. 6.4 Simulation results on RCP with 942 spheres, showing the flow intensity, streamlines, and mesh elements in parts of the model. The mesh contains 1,521,836 elements.



(a) Directional permeabilities converging to the (b) Corresponding anisotropy degree convergence Kozeny-Carman limit

Fig. 6.5 Permeability evolution as a function of the number of spheres for RCP.

spheres. As such we compute the permeabilities k_x , k_y , k_z in all three axis directions to monitor an anisotropy degree I convergence to zero. This index is inspired by the definition from [Clavaud et al. \(2008\)](#) and is defined as

$$I = \left[\frac{(k_x - k_{iso})^2 + (k_y - k_{iso})^2 + (k_z - k_{iso})^2}{k_x^2 + k_y^2 + k_z^2} \right]^{1/2} \quad (6.17)$$

where

$$k_{iso} = (k_x k_y k_z)^{1/3} \quad (6.18)$$

Fig. 6.5 shows the evolution of permeability and anisotropy index with the number of spheres. The index I reaches a value below 1% for the final simulation with 1132 spheres and seems to converge towards zero, the limit of perfect isotropy, from the shape of the plotted curve. The same convergence rate can be observed for each directional permeability (k_x , k_y , k_z), all converging towards the predicted value by Kozeny-Carman. The total number of spheres was capped for numerical reasons as the simulations were computationally too expensive in memory for the currently unoptimised version of the code used (see Sec. 6.1.3).

6.1.6 Flow on μ CT-scans

A last validation test is performed on a digital rock to demonstrate the ability of the flow simulator to work on real samples.

We run a flow simulation on the LV60A ([Imperial College Consortium On Pore-Scale Modelling, 2014c](#)) sandpack shown in Fig. 6.6, which has already been used to evaluate other codes (e.g. [Dong and Blunt, 2009](#); [Mostaghimi et al., 2012](#)). The total size of the sandpack sample is 3 mm^3 and it has been scanned with a resolution of $10.002 \mu\text{m}$. The quality of the

simulations is assessed by comparing the computed values of permeability with the reported value of 35.3 D in the original online database for that sample (Dong and Blunt, 2009), computed on both voxelated images and pore networks. Note that this reference permeability is itself the result of numerical simulations and does not match exactly the value of 32.2 ± 0.3 D obtained experimentally on that sample by Talabi and Blunt (2010) for example. This difference highlights the fact that significant uncertainties remain at all levels, both from physical assumptions on the numerical side and from practical limitations on the experimental side. Uncertainty arises from laboratory measurements due to the lack of resolution when capturing micro- and mesoporosities, cumulated to errors arising from the signal treatments and the binarisation process (Guibert et al., 2015). Both of these uncertainties affect the digital reconstruction of the real pore space and consequently the computation of transport properties, which is why the reference permeability value is selected as the value obtained from numerical experiments and reported officially on the online database.

We use the previous REV study from Mostaghimi et al. (2012), not based on the number of grains, to evaluate the minimum sample size required for permeability REV at around 100 pixels per dimension. The process consists in progressively increasing the sample size considered for the flow simulation to compute the permeability until convergence occurs, starting from a subsample at the centre ($x = 0$). For each subsample size considered, the permeability is evaluated at random locations within the global sample, including one centred on the center of the image displayed in Fig. 6.7. This procedure improves on the approach from Guibert et al. (2015) who only computes permeability at the center of the sample and is therefore not conclusively addressing the representativeness of the sampling. Given the identified minimum size $N \approx 100$ of pixels per dimension (corresponding to 1 mm^3) to define a REV for that sample, as well as the numerical cost of the flow simulator, we limit our analysis to a maximum of $N = 150$ pixels per dimension, obtained using supercomputer computational power and display the results of this analysis in Fig. 6.7. Results show a good match with the study of Mostaghimi et al. (2012), with permeability converging for $N \geq 100$ to a value of 37.9 D, in between the respective values of 39 D and 35.3 D reported by Mostaghimi et al. (2012) and Dong and Blunt (2009). Even more precision could have been achieved by adding periodic boundary conditions.

This successful study concludes the validation of our Eulerian simulator for permeability computation on μ CT-scan data. In the following section, we briefly present the solid mechanics (Lagrangian) simulator, used to deform mechanically the grain skeleton.

6.2 Fluid-microstructure coupling scheme (Eulerian-Lagrangian)

When studying multiphysics phenomena, coupled effects between the different physics have to be recognised and considered. In the case of hydro-mechanical simulations in porous media at the micro-scale, the main interaction is the direct transfer of force between the fluid and the grains at their interface, with the two following opposite couplings.

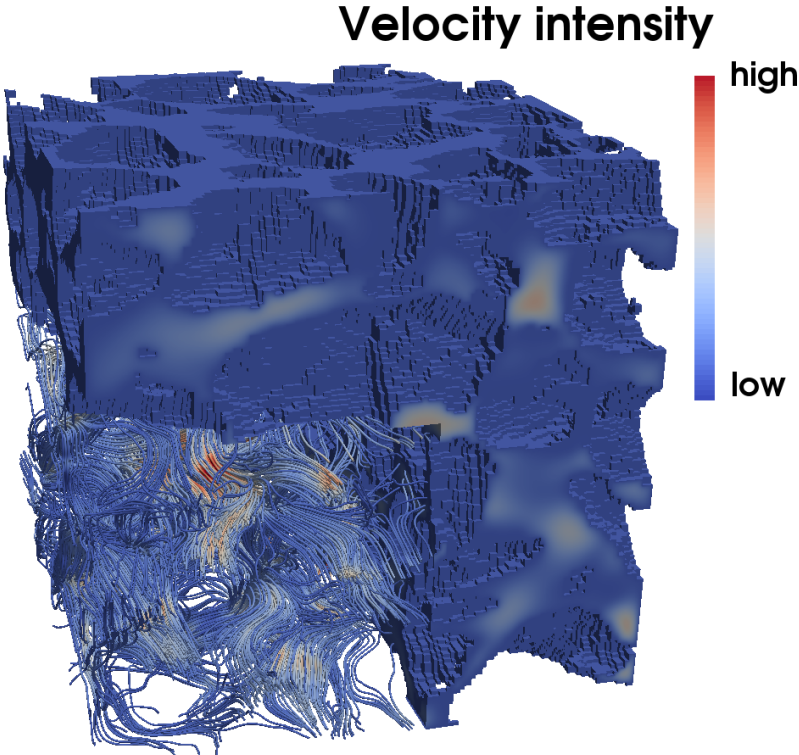


Fig. 6.6 Visualisation of pore space and flow intensity and streamlines on a 1.5 mm³ subsample of LV60A meshed with 1,237,177 elements.

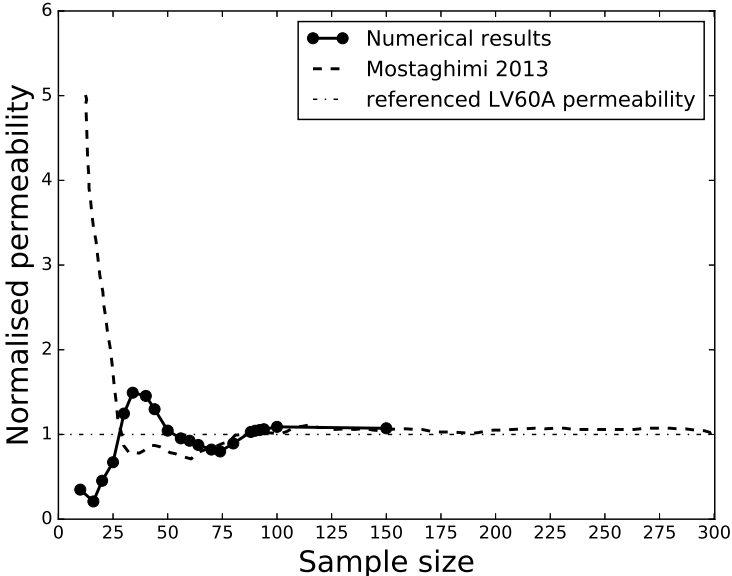


Fig. 6.7 Evolution of permeability with increasing subsample size.

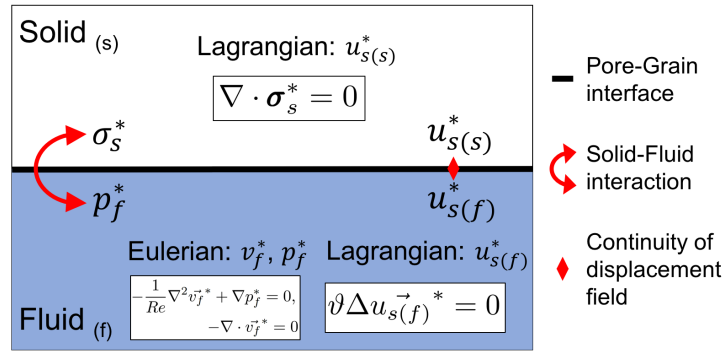


Fig. 6.8 Illustration of the FSI scheme presented in detail in Sec. 6.2.

The first one accounts for the effect of the fluid pressure on the solid stress, as documented by [Terzaghi \(1923\)](#) at the macro-scale through the concept of effective stress, defined as $\sigma'_s = \sigma_s - p_f \mathbf{I}$. The second and opposite coupling accounts for the effect of mechanical deformation on the flow through geometrical changes of the pore space due to the displacement of the fluid-rock interface. This last coupling triggers a permeability variation due to flow path changes imposed by grain movements. In certain scenarios this variation can be significant, potentially ranging orders of magnitude when pore throats are closing for example. The following subsections explain in detail the scheme used in this contribution, conceptually summarised in Fig. 6.8.

6.2.1 Mathematical framework

The model formulation for the fluid flow within the pores can be coupled with a mechanical deformation of the solid matrix (described in Chapter 5, using the specific material of Sec. 5.7.4) by considering the fluid-microstructure interaction (hereinafter simplified to fluid-structure interaction (FSI)). The pore-grain boundary movement and the fluid pressure on the grains represent the two main couplings between the fluid and solid presented above.

Impact of mechanical deformations on the flow

Following the mechanical displacement computed on the solid matrix, the evolution of the pore-grain boundary is taken as a boundary condition constraint for the flow problem resolution within the pores. The fluid flow equations, however, are described in an Eulerian framework while the existing mechanics is a Lagrangian description, leading to difficult implementation task as we need a mesh that is suitable for both problems. In this contribution we propose to adapt the mesh within the pore space at each timestep to account for the pore-grain boundary movement arising from the mechanical deformation of the solid matrix. This re-meshing procedure is implemented as part of the simulation itself by solving a diffusion problem for the (solid) displacement variables within the pore space:

$$\vartheta \Delta u_{s(f)}^* = 0 \quad (6.19)$$

with its weak form and jacobian respectively written as

$$(\nabla \psi_{ui}, \vartheta \nabla u_{s(f)i}^*) \quad (6.20)$$

$$(\nabla \psi_{ui}, \vartheta \partial_{u_{s(f)i}^*} (u_{s(f)i}^* \nabla \Phi_{ui})) \quad (6.21)$$

Note that a relaxation factor $\vartheta \ll 1$ is introduced, to be discussed in the following paragraphs.

The idea of this diffusion term is to adapt the mesh smoothly in the pore space without any interaction with the mechanical problem, solved within the solid matrix only. The displacements of the pore-grain interface, resulting from the mechanical deformation within the solid matrix, should be imposed as boundary conditions for the diffusion within the pore space. However, the mesh nodes at the pore-grain interface belong to different mesh elements where both the mechanics (on one side) and the fluid flow (on the other side) are being solved. This results in an unwanted coupling of the diffusion for the displacement variables at those nodes, expressed through the following interface boundary condition:

$$\langle \psi_{ui}, \vartheta \nabla u_{i(f)}^* \cdot \vec{n} \rangle + \langle \psi_{ui}, (\boldsymbol{\sigma}_s^* \cdot \vec{n})_i \rangle = 0 \quad (6.22)$$

The second term is the natural boundary condition coming from the mechanical system solved in the solid domain. The first term is the contribution of the re-meshing diffusion approach. As such, we seek for a minimisation of this term in order to retrieve unaffected the mechanical displacement of the solid-fluid interface.

To this end, we introduce a relaxation factor $\vartheta \ll 1$ to multiply the diffusion term, so that its effect on the mechanical deformation becomes negligible, while the diffusion gets solved identically within the pore space. This implementation allows the nodes in the pore space to be smoothly displaced without having any interaction with the mechanical problem for values of $\vartheta \ll 1$. To confirm this statement we run a suite of simulations for different values of ϑ on a synthetic pore channel of a rock subjected to external compressive displacement. The 2D rectangular model is composed of only two horizontal layers, a fluid channel at the bottom and a rock layer at the top, as shown in Fig. 6.9a. This geometry of length to height ratio of 1.5 is meshed regularly with 1,536 QUAD9 elements. An external mechanical force is applied on the right hand side of the model as a displacement boundary condition with the left hand side being fixed horizontally. The top surface is fixed vertically.

The results of Fig. 6.9b show the convergence of the proposed framework towards the reference Lagrangian scheme where only the mechanical deformation is computed. A numerical resistance to the compression $\sigma_{BC} = \vartheta \nabla \vec{u}_f^*$ can be noticed for higher values of ϑ , where the gradient of displacement $\nabla \vec{u}_f^*$ is computed on the pore space, and is therefore constant in our selected example. As such, the value of ϑ is selected for a given numerical tolerance tol as:

$$\vartheta \leq \frac{tol}{tol + \max \|\nabla \vec{u}_f^*\|} \quad (6.23)$$

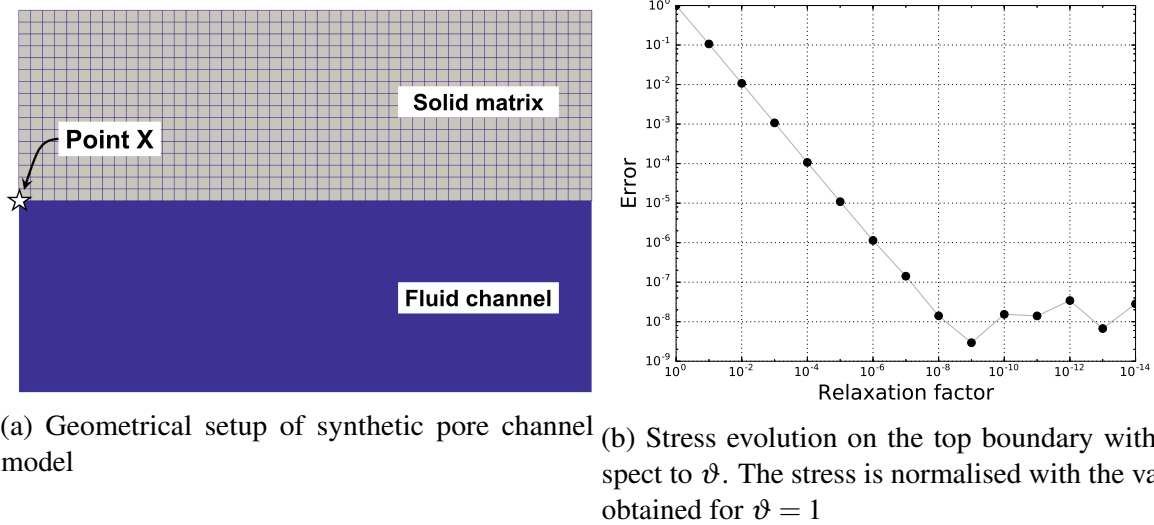


Fig. 6.9 Benchmark of Eulerian-Lagrangian scheme and selection of numerical value for relaxation parameter ϑ .

For a tolerance of 10^{-8} and an imposed dimensionless horizontal displacement of 0.1 (leading to a vertical gradient of displacement of 0.0146 through the Poisson effect), we can observe in Fig. 6.9b the linear dependency between the stress at the pore-grain interface and ϑ , until a value of $\vartheta \approx 10^{-8}$ low enough to reach the numerical tolerance. These results highlight the importance of considering this parameter ϑ as a value of $\vartheta = 1$ yields an error on displacement of about 7%. In the following examples of this section, we selected the ultra-conservative value $\vartheta = 10^{-14}$ in order to avoid any influence of the diffusion even for large displacements.

The resulting geometrical changes of the pore space represent the first part of the fluid-structure interaction by expressing the impact of the mechanical deformation on the flow path at the fluid-rock interface.

Impact of fluid pressure on the grains

The second part of the fluid-structure interaction consists in accounting for the feedback of the fluid pressure on the solid matrix at the same interface, by considering the fluid pressure as a boundary stress for the rock. Since the mechanical problem solved involves displacement variables, this external stress is expressed as a Neumann boundary condition for the displacement. The weak formulation is written as

$$\langle \Psi_{ui}, -p_f^* n_i \rangle \quad (6.24)$$

as an additional term to the boundary condition for the solid matrix stress equilibrium equation (Eq. 6.22).

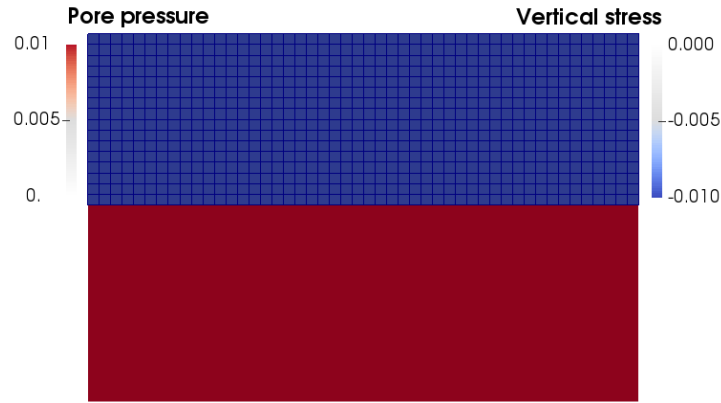


Fig. 6.10 Validation of Terzaghi's effective stress principle. The box has zero displacement on all boundaries, and the normalised vertical stress of the solid domain equilibrates to the imposed value of the normalised fluid pressure.

The jacobian of this term is introduced in the mechanical system of equation, which corresponds to an off-diagonal jacobian term of the system, for the fluid pressure variable.

$$\langle \psi_{ui}, -\Phi_{ui} n_i \rangle \quad (6.25)$$

The final coupled scheme should be validated against Terzaghi's concept of effective stress ($\boldsymbol{\sigma}'_s = \boldsymbol{\sigma}_s - p_f \mathbf{I}$). In Fig. 6.10 we show the validation of this concept on the same channel setup shown in Fig. 6.9a, when displacement is kept fixed on all sides. Since the fluid-solid boundary is allowed to move, zero displacement boundary conditions correspond to zero total stress. This means that the solid-fluid boundary accommodates all the stress variations between the fluid and the solid domains. We observe in Fig. 6.10 that -as expected- the system equilibrates the stress on the solid domain with the pressure of the fluid, which is the main coupling that needs to be satisfied in this hydromechanical study (see Fig. 6.8).

6.2.2 Tight vs. sequential coupling

The fluid-structure interactions presented in Sec. 6.2.1 can be used to numerically couple the hydraulic and mechanical components of the simulation either in sequential or in a tightly coupled manner.

We initially implement a loose coupling, where the mechanical and hydraulic simulations are run as separate simulations in a sequential manner. At each timestep, a mechanical simulation updates the displacement field within the whole mesh, using a proper mechanical model within the solid matrix and a simple diffusion within the pore space. The mechanically deformed mesh is then used for the following substep where the fluid flow is computed within the pore space. The resulting fluid pressure field is then used to apply a pressure boundary condition at the pore-grain interface for the next mechanical simulation as part of the following timestep.

Alternatively, the mechanical and hydraulic components can be solved simultaneously as a tightly coupled system of equations with non-linear feedbacks stemming from the fluid-structure interactions presented above.

The sequential coupling has a major advantage in terms of computational cost, as the two subsystems are both smaller and easier to solve than the full system since they are solved separately. This numerical efficiency easily explains the popularity of this approach (e.g. [Jasinski et al., 2015](#)) in scenarios where the influence of the coupling terms remains reasonably small. This is particularly interesting when coupling physical processes between different length-scales for example.

The sequential approach however starts losing its validity when the coupling terms exert a strong influence on the response of the global system, as illustrated in the following example. A comparison between the two coupling strategies is performed on a flow simulation through the synthetic pore channel shown in [Fig. 6.9a](#), this time with the rock subjected to an external compressive stress. This scenario is characteristic of fluid flow in deeper unconventional petroleum reservoirs (e.g. shale), but is limited here to its simplest geometry for clarity. A Young's modulus $E^* = 1$ is selected for the solid matrix. An external mechanical force $\sigma_{top}^* = 0.8$ is applied to the top of the model to simulate some particular confinement condition, while a fixed velocity flow $v_{fx}^* = 0.01$ is applied from the left hand side of the channel, with a fluid pressure of $p_f^* = 0$ imposed on the right hand side. The hydro-mechanical simulation is solved using both approaches with the same PETSc options, an ASM (Additive Schwarz Method) preconditioner with GMRES (Generalized Minimal RESidual) method and LU (Lower Upper) decomposition.

Under normal conditions, any simulation would be run in a single step to compute the quasi-static rock deformation and steady-state fluid flow. The value of σ_{top}^* however is chosen on purpose to be sufficiently large for the coupling interactions to be significant enough, and several computational steps are repeated, keeping the boundary conditions unchanged, until the system finally reaches a perfect equilibrium after an oscillatory behaviour (see [Fig. 6.11](#)). [Fig. 6.11b](#) shows that after a single step of mechanical deformation and fluid flow, the fluid pressure feedback on the mechanics is not yet taken into account and the solid matrix remains horizontal. [Fig. 6.11c](#) shows the simulation results after the second step, where that feedback is considered for the first time. The constant flow velocity boundary condition forces a fluid pressure increase on the reduced channel, pushing back the solid matrix upwards on the left hand side of the model. [Fig. 6.11d](#) shows the configuration after 24 steps, where convergence is visually obtained.

To quantify the convergence rate of this simulation we track the displacement of point X in [Fig. 6.9a](#) and display its evolution in [Fig. 6.12a](#). The displacement is normalised by its final value when convergence is reached and plotted as a function of the computational time used to solve the problem, normalised by the time taken to solve the problem in a tightly coupled manner. A star at coordinates (1,1) shows the reference of the tightly coupled approach. The solid line shows the results for the sequential approach, highlighting the oscillatory response of the system imposed by the lagging application of the fluid-structure interactions as boundary conditions

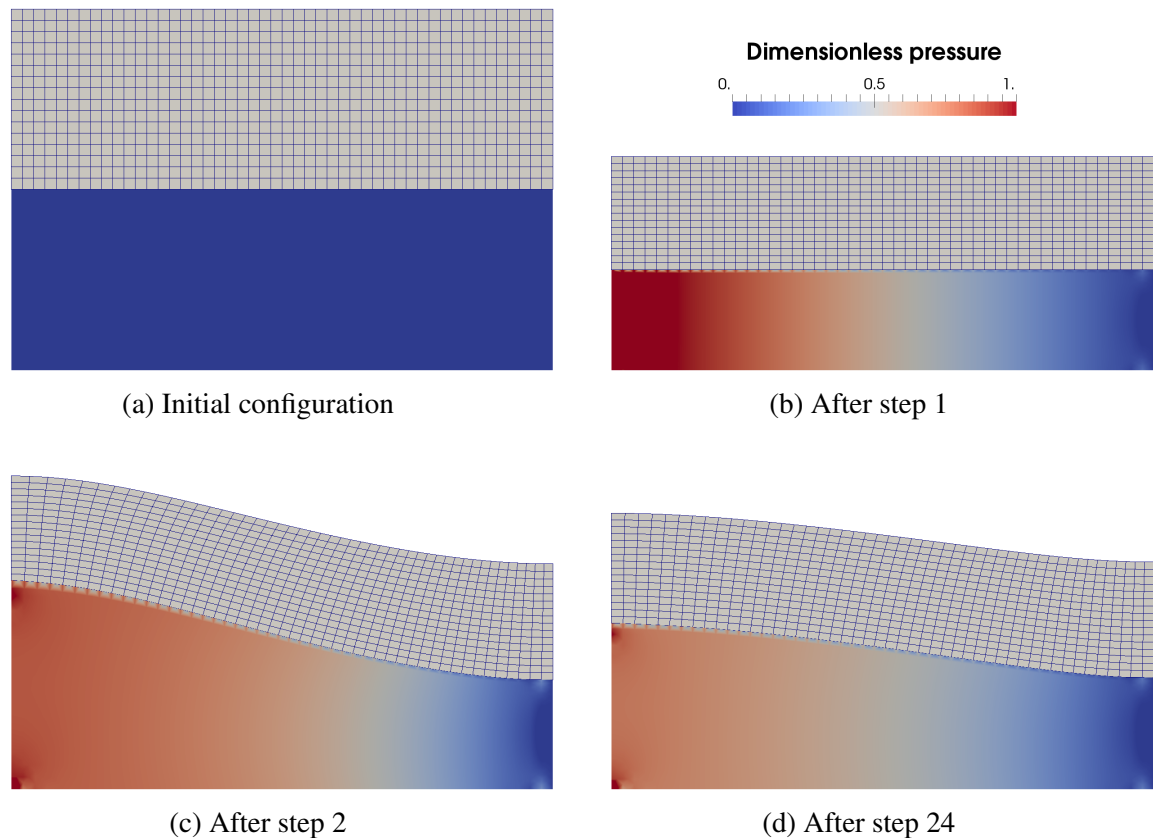


Fig. 6.11 Step by step evolution of sequentially coupled hydro-mechanics. No magnification was applied for visualisation

from one step to the next. The x-coordinate of the star highlights the fact that the tightly coupled approach is computationally more expensive, as more than three loosely coupled steps have been computed during a single tightly coupled step. Looking at the y-axis however reveals the slow convergence of the loosely coupled approach, with the error presented in Fig. 6.12b in logarithmic scale. This figure shows that the tightly coupled approach gets computed to the imposed numerical tolerance of 10^{-8} in a single iteration, while the loosely coupled simulation reduces its error at a very slow pace, only reaching an error of 10^{-5} after a computational time four times longer. The tightly coupled strategy is therefore the much preferred solution in this instance when convergence accuracy is taken into account.

6.2.3 Fluid-microstructure interaction under oedometric compression

In order to illustrate the physical and numerical coupling scheme, we subject the digital rock sample previously studied (LV60A) to an oedometric compression simulation. We therefore confine the sample in a fixed container (i.e. zero lateral displacement) and increase the axial load under constant velocity. We then record the average axial stress at the top of the sample, and the axial strain experienced by the digital rock. The same loading protocol on the same digital rock sample is used in two different scenarios, with and without fluid flow in the pore space (see Fig. 6.13). In the case where fluid flow is present, the inlet and outlet pressures are being

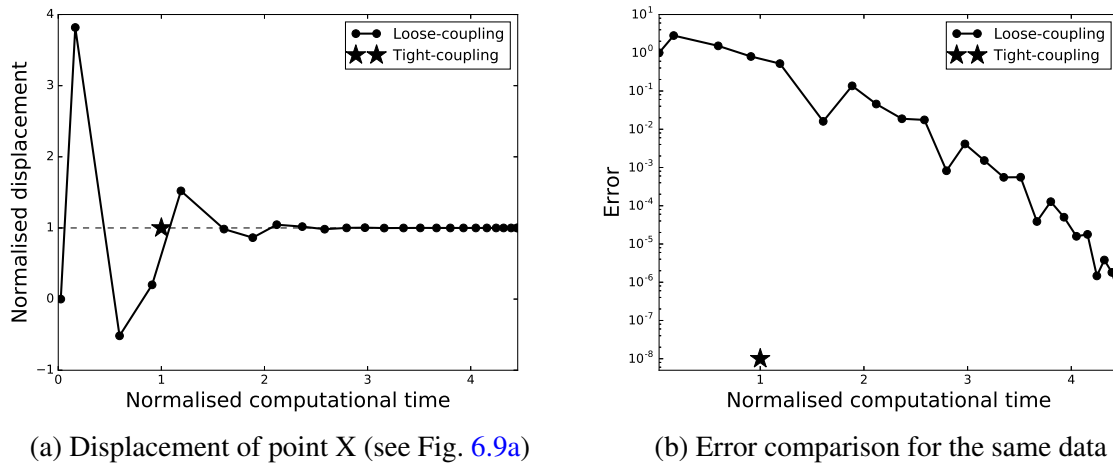


Fig. 6.12 Comparison of convergence between the loose and tight coupling schemes

controlled and the fluid velocity is monitored. On all other sides of the sample, no slip boundary conditions are imposed for the flow. On a computational perspective, this particular simulation which results are exhibited in Fig. 6.13 and Fig. 6.14, was performed on a 2.7 GHz CPU with 20 processors (the number was chosen for scalability reasons) and took 33 hours to iterate 48 timesteps.

The first target is to showcase how Terzaghi's effective stress concept is recovered when the micro-scale of the digital rock is taken into account. To this end, we plot in Fig. 6.14a the average axial stress at the top of the sample vs the corresponding axial strain for both the dry and wet cases. We notice that both curves are identical, shifted by a constant which is interpreted as the macroscopic value of the pore pressure at the top of the sample. This means that through the numerical experiment, an equivalent value of the macroscopic pore pressure is derived. As the calculated macroscopic pore pressure varies within 10% of the average of the microscopic fluid pressure, we believe that this macroscopic pore pressure represents not only the microscopic fluid pressure but also incorporates an homogenisation of the microstructure that could explain the discrepancy, sometimes accounted for by the Biot coefficient (Biot and Willis, 1957). Deriving a conclusive relationship between the macro- and micro-scopic fluid pressures requires a thorough homogenisation step. Since -as already mentioned- the current sample was not tested for representativeness as an REV of the coupled hydro-mechanical problem, this homogenisation step falls outside the scope of this work. This implies that even though the calculated macroscopic pore pressure is comparable to the average of the microscopic fluid pressure (computed on the model of Fig. 6.13 at less than 10% discrepancy) in this example, those values cannot be conclusively linked.

The second target of this exercise is to monitor the macroscopic mechanical response of the material and evaluate the permeability evolution of a real digital rock with increasing axial deformation. Although the matrix was assumed to obey a pressure insensitive (von-Mises) criterion, we observe in Fig. 6.14b a residual (plastic) volumetric strain after unloading. This

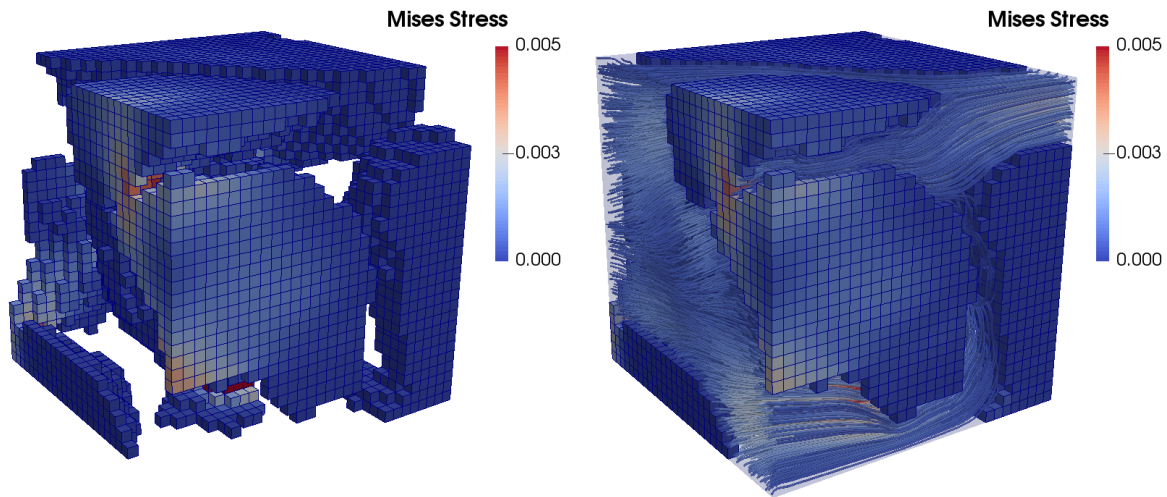


Fig. 6.13 Oedometric compression for a dry (left) and a saturated (right) digitised rock sample at the peak stress of Fig. 6.14a. Normalised yield stress is 0.005

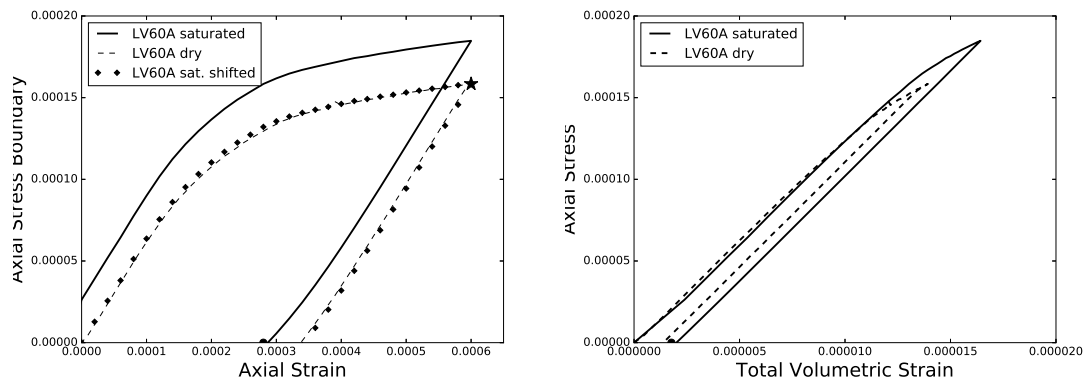
indicates that pressure sensitivity is arising from the geometry of the digital rock, which is also amplified by the presence of fluids.

The residual volumetric strain also suggests permanent changes in permeability. In the literature, a linear reduction of permeability with increasing strain is reported for sandstones (Ngwenya et al., 2003) in the relatively high confinement compaction regime. Since the oedometric test performed here corresponds to this compaction regime, we indeed observe in Fig. 6.14c a linear relationship between permeability and axial strain. The current framework also provides the computation of cross-flow in all direction, leading to the full permeability tensor. Fig. 6.14c shows for example the permeabilities in all three (X, Y, Z) directions for a given imposed flow along the X-axis. In this case, the magnitude of the cross-flow along the Y and Z axes is negligible (maximum permeability value reached in y and z is respectively 3 and 6% of the maximum value in x) and yet the linear relationship between permeability and compression is preserved in cross-flow.

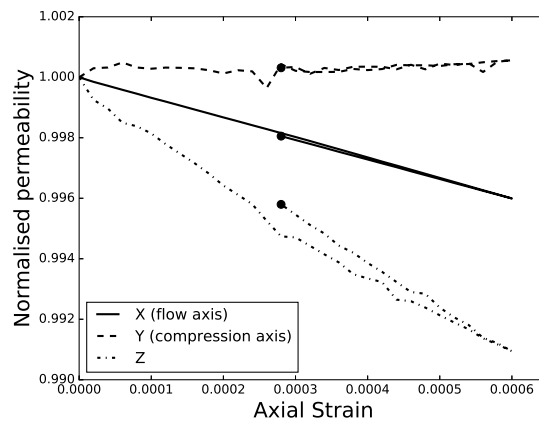
6.3 Influence of chemical dissolution on permeability

In the context of fault reactivation in a low permeability chemical shear zone (see Chapter 2), chemical dissolution and precipitation can be responsible for permeability evolution of orders of magnitude (Poulet et al., 2017). In comparison the change of permeability induced by the hydromechanical mechanism described in the previous section is negligible. For this reason we will focus in this section specifically on the chemical alteration of the rock microstructure. The upscaled permeability evolution with erosion is compared to the common empirical porosity-permeability relationship of Kozeny-Carman.

Chemical dissolution at the pore level is an active field of research which can involve different coupled processes with various effects (see review from Xiong et al. (2016) and the references



(a) Normalised stress-strain curve responses for (b) Normalised axial stress vs normalised volumetric strain
dry and saturated digital rock samples.



(c) Permeability evolution with respect to normalised axial strain in all three directions. Permeability was normalised separately with the initial value of each direction.

Fig. 6.14 Comparison between purely mechanical and hydro-mechanical simulations. In (a), the dry curve is retrieved when the saturated response is shifted by the pore pressure. The black dot on each figure marks the end of the numerical simulation.

therein). In general, dissolution can be related to the flow velocity inside the pore space, the spatial distribution of chemical composition of the grains, and the stress on the solid skeleton, just to cite a few. The focus of our study, however, is not to present the most accurate model at the micro-scale, but to demonstrate how the effects at that scale can be linked to the next scale up. As such, we restrict ourselves to the simplest case where the dissolution only depends on the microstructure geometry, independently from the distribution of flow velocity, stress or other properties. This choice also fits nicely with the application of fault reactivation selected in this contribution where the flow remains low and host rocks like carbonates can be quite homogeneous mineralogically. The dissolution can be assumed to be decoupled from the flow and both computed sequentially. As explained in Chapter 4, the chemical porosity change $\Delta\phi_{chem}$ is computed at the meso-scale (see Chapter 2) and fed to the micro-scale where its spatial distribution is evaluated in order to update the permeability from a flow simulation. The first section focuses on explaining the erosion/dilation algorithm used for accommodating $\Delta\phi_{chem}$ at the micro-scale and the last section compares this algorithm with the Kozeny-Carman law, to validate the common usage of this law for problems involving precipitation.

6.3.1 Erosion/dilation algorithm

The effective chemical reaction considered in our model is a dissolution of the solid skeleton (see Sec. 2.1), triggered by the rise of temperature of the fault's core due to shear heating. Assuming uniform temperature at the micro-scale and chemical homogeneity of the sample, we consider at first order the dissolution to happen homogeneously at the surface of the pore space. Given the target change $\Delta\phi_{chem}$ of porosity imposed by the meso-scale, we implemented a geometrical erosion/dilation algorithm which switches the nature of layers of voxels between pore space and solid matrix at the interface. Since a dilation of the pore space is equivalent to an erosion of the solid space, we only need to describe the erosion algorithm. The target change $\Delta\phi_{chem}$ is converted to a target volume ΔV and the algorithm evaluates successively whether a k^{th} layer of volume V_k should be converted from pore to solid, in order to approach the volume target as closely as possible without exceeding it.

$$\sum_{k=1}^n V_k \leq \Delta V < \sum_{k=1}^{n+1} V_k \quad (6.26)$$

Removing a discrete number of layers introduces a numerical discretisation of the porosity evolution, which can be kept monotonous by approaching ΔV with its infimum value (Eq. 6.26). This approach also captures well the general behaviour of the fault which is creeping slowly during most of the simulation, with barely any change in porosity, and evolving quickly during slip events marked by large porosity changes. The computed porosity remains thereby identical to its initial value until a slip event becomes perceptible, after which the porosity jumps by steps controlled by the mesh resolution. The erosion of each successive layer (of index k) is done by the function *BoundaryElements* described hereunder.

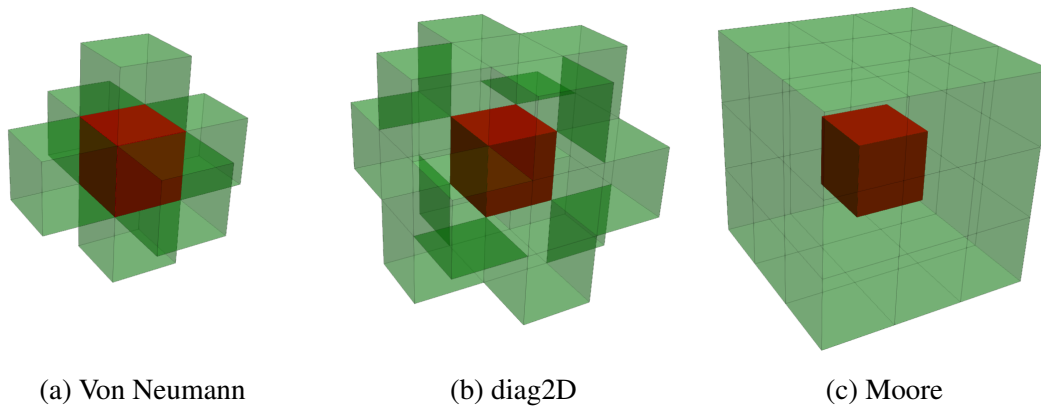


Fig. 6.15 Visualisation of the three types of neighbourhoods.

BoundaryElements This function is used to find all elements at the pore-grain interface and computes the volume of the next layer to be eroded. It parses all mesh elements and queries each *SubdomainID* to compare it with those of its neighbours. Each element identified as grain (*SubdomainID* = 1) with at least one of its neighbours representing a pore (*SubdomainID* = 0) is added to the list of interface elements, whose *SubdomainID* is switched from 1 to 0 once the whole mesh is parsed. The corresponding volume V_k is then used to assess the termination of the iterative algorithm (Eq. 6.26) before the next iteration ($k + 1$) can start if need be.

Elements neighbourhoods

For a regular grid, there exist three types of element neighbourhood. The simpler one considers only the elements sharing a common face with the element queried and this neighbourhood is referred as *von Neumann*, as commonly done in the field of cellular automata. The *diag2D* type considers elements sharing common edges as well, and the *Moore* type considers elements sharing any corner point. These three neighbourhoods are visualised in Fig. 6.15. In order to select the most appropriate type for our model, we first check the erosion of some of the fundamental shapes that are found in segmented μ CT-scans of rocks.

The first shape that we erode is the cube since the mesh of the rock microstructure is a reconstruction of μ CT-scans images, that are naturally pixelated. From the initial cube displayed in Fig. 6.16, we apply a high level of erosion using the three type of neighbourhood presented above. We can see in Fig. 6.16 that using the von Neumann neighbourhood erodes the cube in a spherical manner, as a small rhombicuboctahedron, whereas with the Moore neighbourhood we retain a perfect cubic shape. With the *diag2D* neighbourhood we obtain an eroded shape in between the two, a truncated cube. It is important to note that we do not necessarily want to retain the cubic shape of the pixel since the discretisation is a distortion of the real microstructure. In this case the Moore neighbourhood is less attractive.

The second shape that we erode is the sphere since we are mostly dealing with granular materials. Indeed, if the resolution of the μ CT-scan is high enough, we should see more or less spherical grains. In this case we can see in Fig. 6.16 that the von Neumann neighbourhood creates

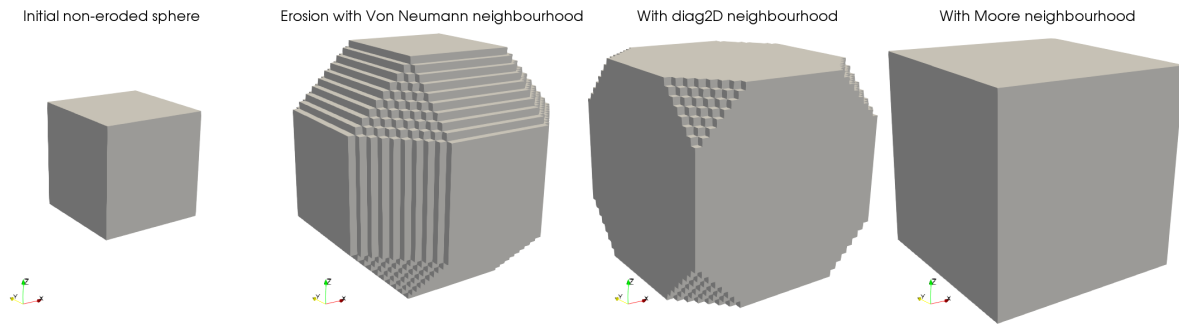


Fig. 6.16 Erosion of a cube by considering three different types of neighbourhood.

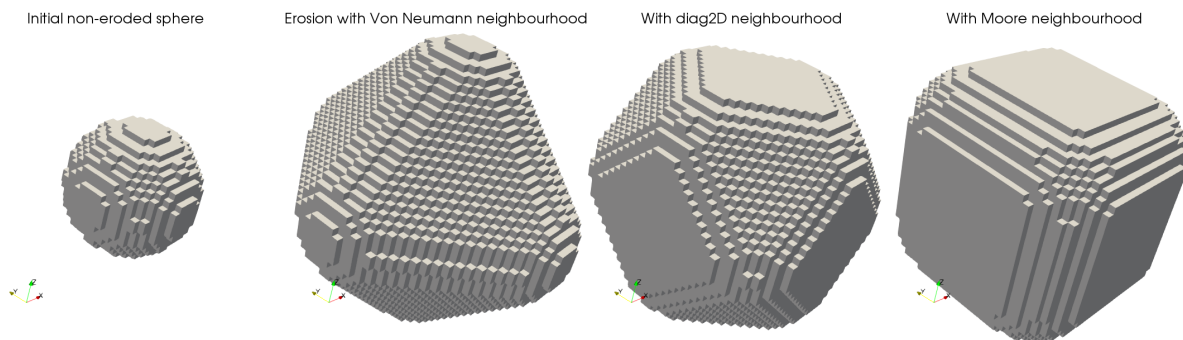


Fig. 6.17 Erosion of a sphere by considering three different types of neighbourhood.

a regular octahedron, which differs a lot from the initial sphere. On the other hand, the Moore neighbourhood will erode the sphere into a cube-like shape. It is the diag2D neighbourhood that approaches a spherical erosion the most. It is more adapted to our hypothesis of homogeneous dissolution which brings us to select the diag2D neighbourhood for the rest of the contribution, in agreement with the study on the cube shape.

Still, we can note from Fig. 6.18 that the different implementations do not change much the geometry of the microstructure for reasonable levels of dissolution/precipitation.

Mesh resolution sensitivity on porosity evolution

The mesh resolution of this approach has obviously a direct impact on the discretisation of the porosity evolution with the erosion level, leading to the usual compromise between precision and computational time. Fig. 6.19a shows the porosity evolution with the number of eroded layers for two different initial mesh resolutions, highlighting the expected gain in porosity resolution with increased refinement. Given the good resolution of the initial mesh, those porosity curves are particularly smooth and a different behaviour can be expected for the corresponding permeability evolution. The results of Fig. 6.19 will be used in Chapter 7 to decide on the resolution to balance precision and computational time.

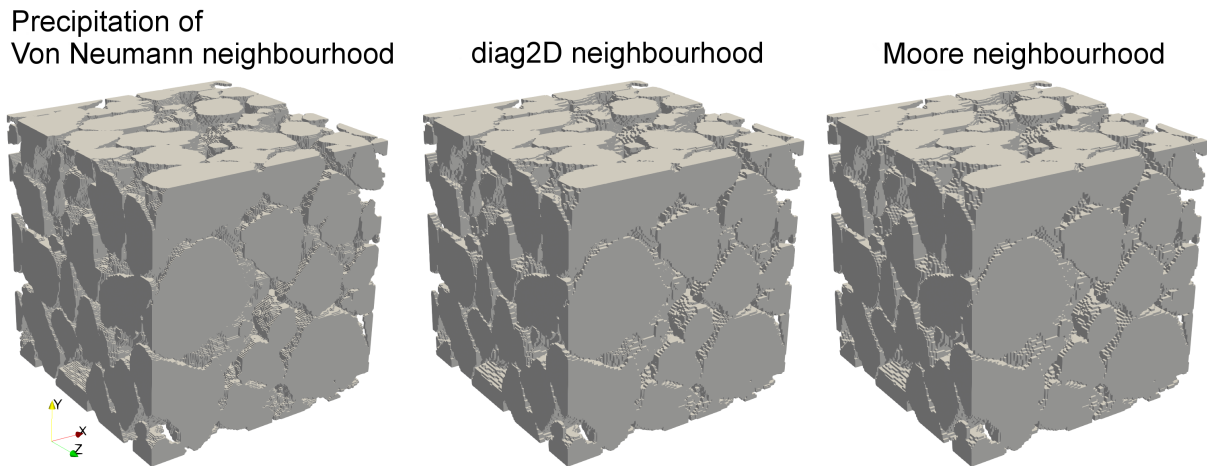
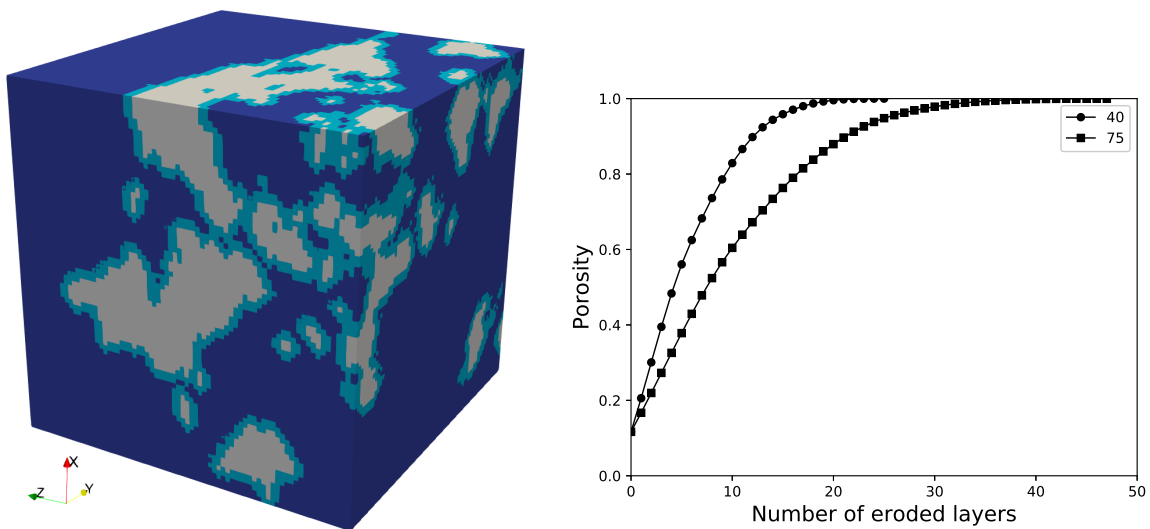


Fig. 6.18 Comparison of the three types of element neighbourhood during the precipitation of a 1.2 mm^3 size sample of the LV60A sand pack from its initial porosity of 37% to a target value of 27%.



(a) Visualisation of a few eroded layers in bright blue. In white is the pore space; In dark blue are the grains.
(b) Evolution of layers volume at different resolutions. The graphs entitled n have a resolution of $n \times n \times n$.

Fig. 6.19 Study on the error made on $\Delta\phi$ using the erosion algorithm at different resolutions on a 0.2 mm^3 subsample of the carbonate rock C1 from [Imperial College Consortium On Pore-Scale Modelling \(2014b\)](#).

6.3.2 Deviation of Kozeny-Carman equation due to precipitation

The algorithm described in this section combined with the flow simulator of Sec. 6.1 allows to study the evolution of permeability during homogeneous dissolution/precipitation for any type of rock microstructure. When used in the multiscale framework of Chapter 4, this model is meant to replace empirical laws of permeability evolution by a dynamic physical upscaling. The most commonly used empirical law to estimate permeability from changes in the microstructure is the Kozeny-Carman law, which links permeability to porosity. A multitude of rocks have been calibrated to respect the Kozeny-Carman law (Chapuis and Aubertin, 2003; Heijs and Lowe, 1995) but most studies focus on static porosity (Doyen, 1988) and few have been made on the validity of the law after precipitation, which is what we verify in this section.

The material selected for this study is a sand pack, which should respect the Kozeny-Carman law particularly well because of its granular structure, due to non-consolidation. The Kozeny-Carman law chosen for this section is the more general form of Eq. 6.16, originally established before making the hypothesis that the media is represented by a packing of spheres. Indeed, although the grains of this natural sand pack are as spherical as can be found in a geomaterial, they are not perfect spheres like the ones used in Sec. 6.1.5. This formulation of the law reads as

$$k = \frac{1}{K} \frac{\phi^3}{S^2}, \quad (6.27)$$

where a new variable is introduced, the specific surface area S , in m^{-1} , denoting the area of the pore space divided by the bulk volume of the rock sample.

The size of the subsample is taken at 1.2 mm^3 , larger than the REV size of permeability which was computed to be $\approx 1 \text{ mm}^3$ in Sec. 6.1.6. The unprecipitated sand pack's permeability was calibrated to match the Kozeny-Carman law for the corresponding initial porosity of 37.6%, as shown on Fig. 6.20 by the superposition of the points on the far right hand side. This fit was obtained by taking a value of the Kozeny constant $K = 3.915$, which falls close to the value of 5 proposed by Ergun and Orning (1949) for a packed bed of spheres, as predicted, and was kept constant for the rest of the simulation.

The rest of the figure shows the evolution of this sand pack's permeability during precipitation, running through the graph from right to left, with porosity values decreasing from the initial 37.6% to 5%. we observe that the higher the precipitation level, the further the deviation from the Kozeny-Carman law. This can be explained by the fact that precipitation creates thicker bonds at the grains contact which were initially perfect. The porous medium can no longer be assimilated to a packing of spheres and this deviation from the hypothesis of the model justifies the difference in behaviour. This is confirmed by the similar study of Beckingham (2017). As mentioned in Sec. 6.3.1, we note that the porosity-permeability relationship is not affected much by the different types of neighbourhood considered, since all three types of erosion fall approximately on the same interpolated curve in Fig. 6.20.

Fig. 6.21a shows that in addition to losing the grain's spherical shape with precipitation, we are losing the REV convergence of the sample. This is visually highlighted on Fig. 6.21b where

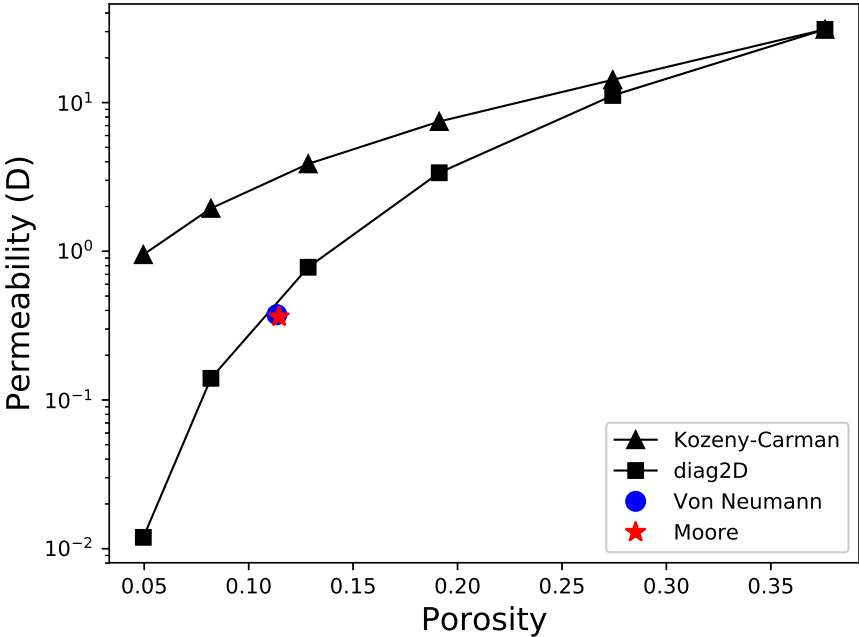
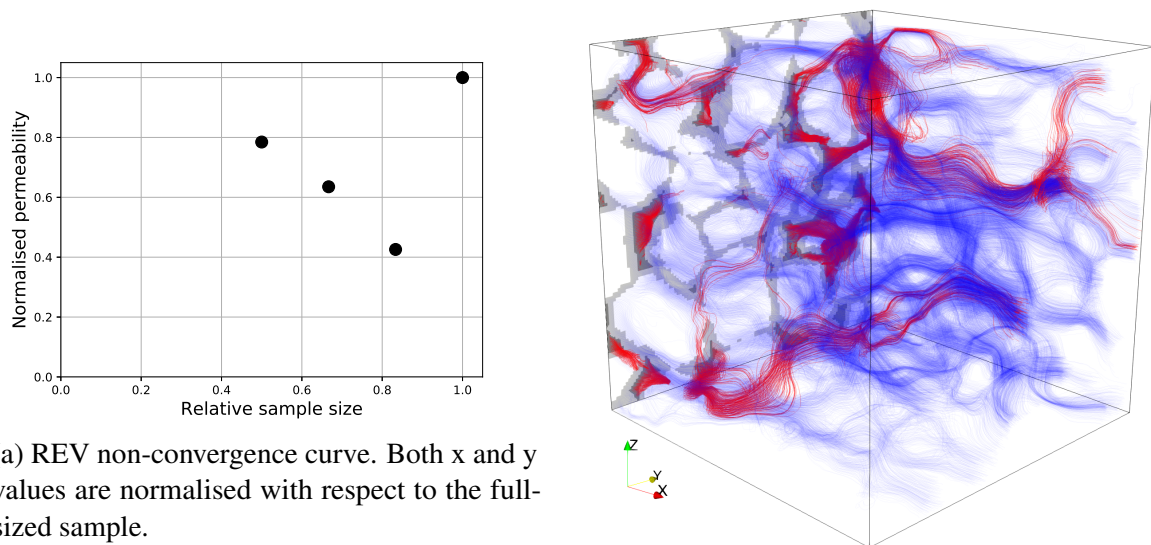


Fig. 6.20 Permeability evolution (solid line with squares) during the precipitation of a 1.2 mm³ subsample of the LV60A sand pack from an initial 37.6% porosity down to 5%. Superposed is the permeability (solid line with triangles) calculated using the Kozeny-Carman law of Eq. 6.27, calibrated to the unprecipitated state using $K = 3.915$. In comparison to the diag2D neighbourhood, we plot one advanced state of precipitation of the same sample using separately the Von Neumann (blue circle) and the Moore (red star) neighbourhood.



(a) REV non-convergence curve. Both x and y values are normalised with respect to the full-sized sample.

(b) Visualisation of the flow streamlines of both the initial (blue) and the precipitated (red) sample.

Fig. 6.21 Assessment of the REV non-convergence of the LV60A sample of Fig. 6.20, precipitated to 8% of porosity.

we can see that the very homogeneous flow in the initial sample has been reduced to two major flow paths after precipitation. If the precipitation ends up closing flow channels, the flow has high chances to become heterogeneous and as such, the size of the REV increases.

An REV analysis was performed on that sample by increasing the sample size from 0.6 mm^3 to its full size of 1.2 mm^3 and computing the permeability in each case. Fig. 6.21a plots the evolution of normalised permeability with the relative sample size and shows that precipitation not only affects the grains' sphericity but the REV convergence altogether. This is visually highlighted on Fig. 6.21b where we can see that the very homogeneous flow in the initial sample has been reduced to two major flow paths after precipitation. With precipitation closing flow channels, the flow naturally become more heterogeneous and, as such, the size of the REV increases, explaining the non-convergence observed in Fig. 6.21a.

In conclusion, this chapter presented a flow simulator on digital rock samples reconstructed from segmented μCT -scan images (Fig. 4.1), where permeability can be directly computed from the fluid flowing through a deformed sample. It has been verified against both analytical formulas (Fig. 6.1) and other numerical approaches (Fig. 6.3 and 6.7). The flow simulator can be coupled to either a Lagrangian solid mechanics simulator or an erosion algorithm in order to determine permeability evolution with microstructure deformations. Incorporated in our multiscale framework, the model become more specific of the rock considered and its microstructure, in contrast with the previous use of generic laws like Kozeny-Carman.

Part III

Influence of multiphysics couplings across scales

Chapter 7

Application to induced fault reactivation

Part I presented three separate length scales of importance in the problem of fault reactivation, with the couplings between those scales detailed in Chapters 3 and 4. Part II showed in particular the challenge to upscale two critical properties, yield and permeability, from the micro- to meso-scale. Building on the theoretical presentation of this multiscale multiphysics framework, with all components introduced in the previous chapters, we present now one particular application of this approach for a fluid production-induced chemical fault reactivation. The first subsections present chronologically the different phases of this complex phenomenon (reactivation, propagation, deactivation) which displays a particularly strong interplay between the meso-scale and the macro-scale and is therefore modelled only with the macro/meso scale model. In the second section, we compare our framework with the empirical rate and state law, used to describe frictional interfaces, and show that our model not only matches this empirical law but provides in addition a physical description of the input parameters of the rate and state law. The third section demonstrates the importance of the micro-scale and how a change in the microstructure can directly affect multiple physical mechanisms at the macro-scale, using the full multiscale framework.

7.1 Simulation using the macro/meso-scale model

7.1.1 Geological setup

We focus on the problem of a chemically active sealing fault near criticality embedded in a carbonate reservoir under extension as depicted in Figure 3.1. In accordance with the Andersonian depiction of a typical extensional setting, the fault is dipping at 60° (Anderson, 1905). The reservoir, located at four kilometres depth, measures two hundred metres in height and stretches horizontally far beyond the fault. We select therefore a zone of 1 km centred on the fault of interest. With the cap rock above and an impermeable layer below, the reservoir is hydraulically sealed at the top and bottom boundaries. In comparison to the 10% porosity and 10 mD permeability of the reservoir, the pre-existing carbonate fault act as a seal with a porosity of 3% (Sulem and Famin, 2009) and a permeability of 0.01 mD. The fault core has a thickness of 1

Table 7.1 Parameters for the chemical shear zone model (refer to Sec. 2.1) in the geological environment of Sec. 7.1.1. We take inspiration from [Alevizos et al. \(2014\)](#); [Veveakis et al. \(2014\)](#) and the references therein as well as [L'vov \(2007\)](#) particularly for the calcite decomposition.

Name	Symbol	Value	Unit
Activation energy of calcite decomposition	E_+	52	$kJ.mol^{-1}$
Activation energy of calcite precipitation	E_-	33	$kJ.mol^{-1}$
Arrhenius number of the mechanics	Ar_m	7	-
Fluid compressibility	β_f	5×10^{-10}	Pa^{-1}
Fluid viscosity	μ_f	0.00023	Pa.s
Molar mass of fluid specy B	M_B	0.018	$kg.mol^{-1}$
Molar mass of solid species A and AB	M_{AB}	0.35	$kg.mol^{-1}$
Pre-exponential factor of forward reaction	A_+	1.4	s^{-1}
Pre-exponential factor of reverse reaction	A_-	0.0014	s^{-1}
Solid density (A and AB)	ρ_s	2700	$kg.m^{-3}$
Taylor-Quinney coefficient	χ	0.6	-
Thermal conductivity of the mixture	α_m	2.7	$kg.m.K^{-1}.s^{-3}$
Thermal diffusivity of the mixture	c_{th}	10^{-6}	$m^2.s^{-1}$

cm and is modelled at the meso scale (Fig. 2.1) within 1m of its surroundings. We model the pre-existence of this fault core with a lower strength (16 MPa) than the reservoir (80 MPa). All other properties than the strength and permeability are taken equal within the reservoir and the fault. The reservoir is modelled as an elastic medium with a Young modulus of 20 GPa and a Poisson ratio of 0.2. In order to apply the chemical shear zone model (see Sec. 2.1), we list in addition the specific set of parameters from Table 7.1.

We impose on the layer the lithostatic overburden stress corresponding to four kilometres depth and we select a vertical to horizontal stress ratio of 2.3 for the reservoir to be in the extensional regime. The pore pressure is initialised with the weight of the hydrostatic column. Given the low background geological strain rate, we assume no lateral displacement of the reservoir during the relatively short time scale of production of a few years. This common hypothesis results in a uniaxial strain loading condition for the reservoir ([Jaeger, 2007](#)). Note that the lateral displacements are fixed only after the stress initialisation of the domain in Fig. 7.1a in order to still capture the extensional nature of the reservoir as can be seen in the setting of Fig. 7.1b.

Vertical uplift from a fault slip can propagates far away from the source, sometimes hundreds of kilometres as [Scholz \(2002, Fig. 5.3\)](#) showed for the Nankaido earthquake of 1946. Since this contribution focuses on the local repercussions of the fault reactivation on its environment, we choose to model only a 1 km long section of the reservoir and the vertical slip of the fault is accommodated uniformly across the bottom boundary of the domain on either side of the fault as can be seen in the setting of Fig. 7.1c. Capturing the effects of the fault slip at the larger scale would require further specific assumptions about the fault surroundings and falls outside the scope of this generic study.

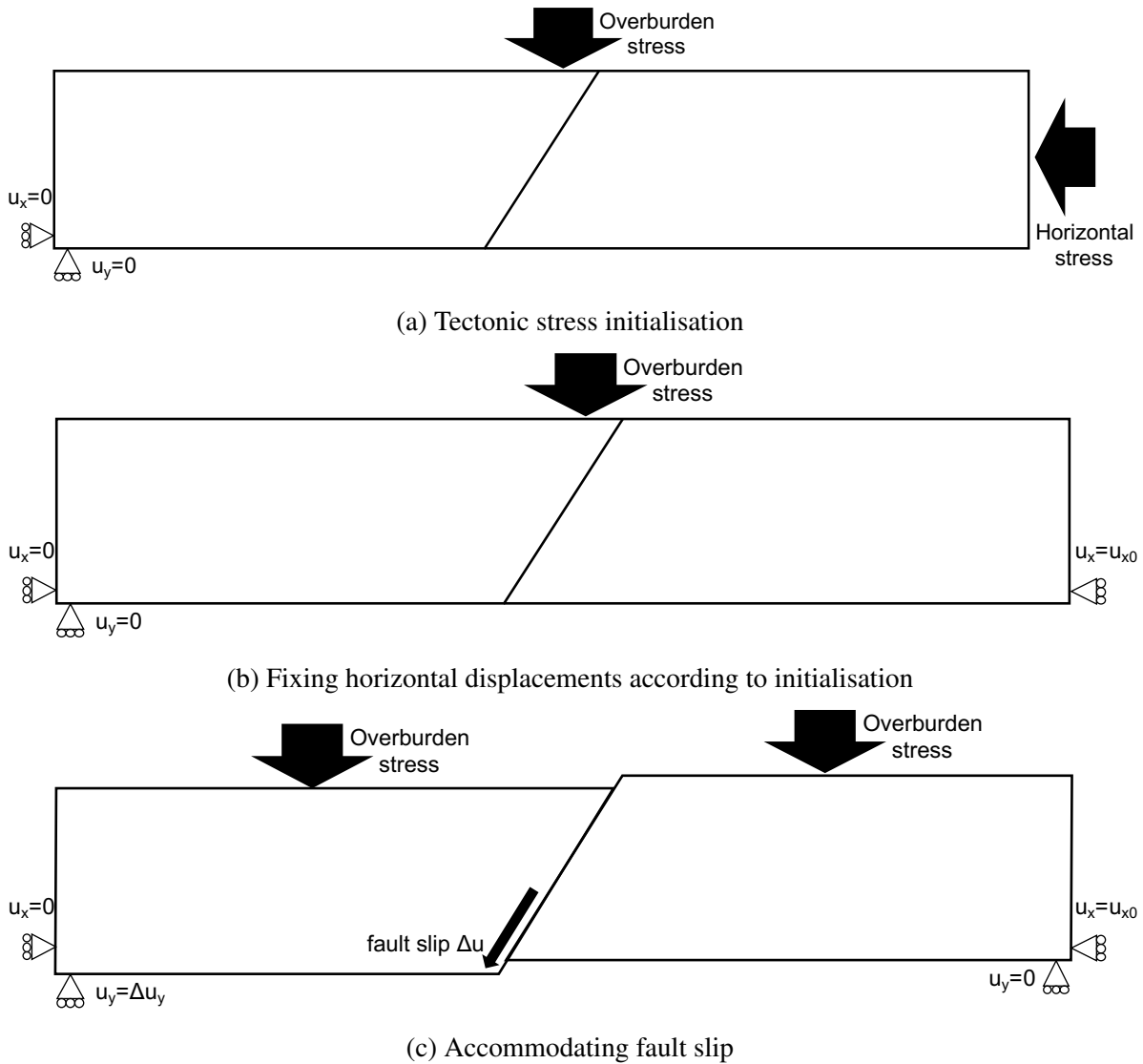


Fig. 7.1 Schematic of boundary conditions. The reservoir, compartmented by a normal fault, is in extension. Note that the stress imposed is total, with the effective stress retrieved with the addition of the pore pressure boundary conditions (initialised with a hydrostatic oil gradient on reservoir sides). The figure is purposely schematic in order to keep the focus of the reader on the boundary conditions imposed. The pore pressure values are shown indicatively by the colouring of the reservoir in those three chronological steps, only to help the comprehension of the boundary conditions (see full results in the following sections).

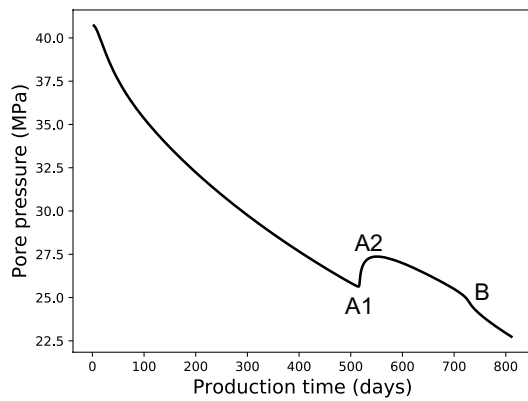
The reservoir is filled with overpressurised oil, of density 0.8, at an initial pore pressure of 40 MPa. Even though the fault permeability is very low, geological times have allowed for the reservoir to equilibrate the pressure on both sides of the fault. From this initial state, we are investigating the fault reactivation scenario in the case of the production from a well drilled through the reservoir located very close to the fault. This section presents the results of the reactivation scenario due to production from a well located next to the sealing fault, as presented in Sec. 7.1.1. The system displays three important phases: the reactivation of a first fault segment, the propagation of the slip along the fault and finally, the fault deactivation and healing.

7.1.2 Production-induced fault reactivation

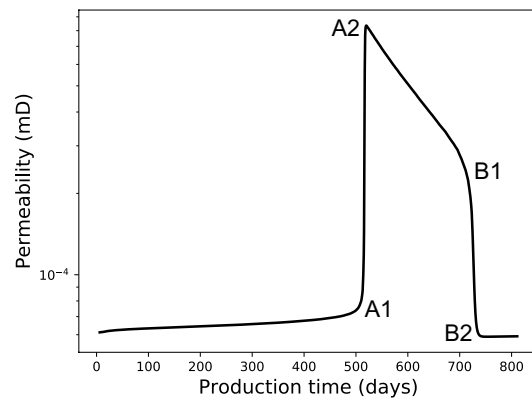
We consider a production well located at 50 m from the fault, as seen on Fig. 3.1. Initially, the pore pressure is equilibrated on both sides of the fault, despite its low permeability. The simulation starts when oil production begins from the well with a prescribed flow rate. Initially, the pressure starts decreasing on the left compartment of the reservoir only, as the fault acts as a seal. Fig. 3.1 shows the undisturbed pressure distribution across the fault at this early stage of production.

This decrease in pore pressure can potentially lead to fault reactivation, under certain conditions linked to the stress path followed during production and material properties, which can easily be understood with a simple analytical approach. Following the uniaxial strain conditions of the setup considered, known to match field observations of reservoir stress paths (Engelder and Fischer, 1994), the evolution of shear stress $\Delta\tau$ in elasticity can be analytically computed from the variation of pore pressure Δp_f as $\Delta\tau = -\Delta p_f \frac{1-K}{2}$, with $K = \frac{\Delta\sigma_H}{\Delta\sigma_V}$. This ratio K was introduced by Teufel et al. (1991) to characterise field observations of reservoir stress paths and is expressed as $K = \frac{\nu}{1-\nu}$. For the common model of Coulomb failure criterion used to describe the reactivation of faults, $\tau = c + \mu(\bar{\sigma} - p_f)$. Therefore, if $\frac{1-K}{2}$ is greater than the friction angle of the fault, then reactivation will ultimately occur (Nacht et al., 2010). Our scenario falls under such a case where the shear stress augments with production as pore pressure drops, as seen on Fig. 7.2d before point A.

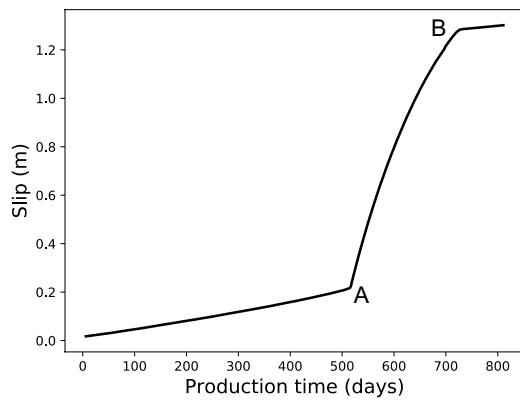
This increase of shear stress on the fault links to the generic scenario described in Sec. 2.2 and explains the reactivation of the fault around $t \approx 500$ days, jumping from point A1 to A2 on Fig. 2.3 which are correspondingly reported on the transient evolution of pore pressure, fault permeability, slip, shear stress and slip velocity plotted in Fig. 7.2. The jumps in velocity and permeability follow the expected behaviour described in Sec. 2.2. The permeability increase leads to a loss of sealing capability of the fault and lets fluid invade the reservoir. Consequently, the pore pressure on the left-hand side of the fault suddenly jumps (see Fig. 7.2a), as a result of pressure equilibration to a lower differential across the fault.



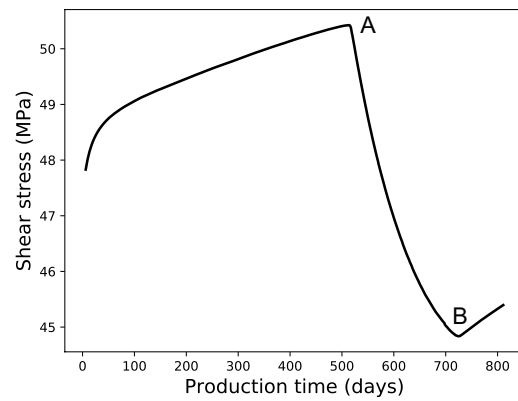
(a) Evolution of pore pressure on the left side of the fault.



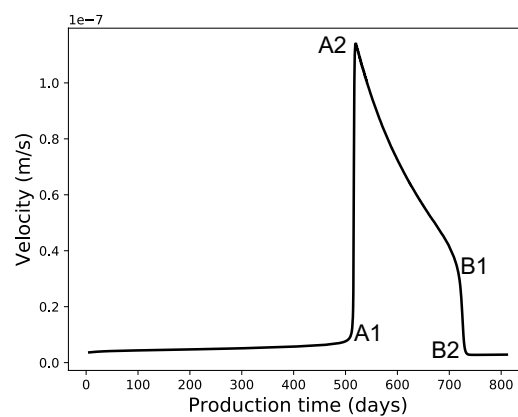
(b) Evolution of the fault permeability.



(c) Evolution of the fault slippage.



(d) Evolution of the fault shearing stress (Von Mises stress).



(e) Evolution of the fault slip rate.

Fig. 7.2 Outputs of an event of chemical fault reactivation induced by reservoir production, following the setup of Sec. 7.1.1.

7.1.3 Slip propagation and synchronisation along the fault

The reactivation of the first fault segment occurs at a specific location determined by the heterogeneous stress distribution along the fault, due to the radial diffusion of pressure depletion around the well coupled with gravitational effects. This first slip triggers a cascading chain of events, as the slip of one point of the fault directly impacts the stress state of the neighbouring fault segments. The propagation of slip events is an active field of research (e.g. [Lapusta and Rice, 2003](#); [Reches and Lockner, 1994](#); [Segall and Pollard, 1983](#)) and the exhaustive study of all possible scenarios falls outside the scope of this thesis. In our particular example, the slip propagates along the whole fault, leading to a complete synchronisation of the fault slippage.

The location of the first slip event corresponds to the zone of highest stress, but, interestingly, it is not directly linked to the pressure depletion profile. Fig. 7.3 shows this pore pressure profile evolution in time from the start of the simulation as fluid production occurs. It highlights the homothetic transformation of those series of curves and shows that, quickly after the start of production, the minimum of pore pressure shifts from the shallowest point of the fault to the approximate middle of the fault (mid-height of the reservoir), where it remains from that time onwards. Using the stress path explained above, this translates to a maximum shear stress around the middle of the fault, which can be taken as proxy for fault stability, as usually done to assess slip tendency for faults in the brittle regime ([Morris et al., 1996](#)). We can then see that the middle of the fault, where the pressure depletion is the highest, has the highest tendency of reactivating. Yet, the multiscale couplings between the fault and the reservoir lead to a more complex problem of interferences between all segments of the fault and we actually observe an initial reactivation of the fault at the top of the model, as can be seen on the timelapse of reactivation from the simulation results shown in Fig. 7.4.

Once the first fault segment reactivates, the fault starts slipping, i.e. creeping at a faster rate. The same couplings responsible for the initial reactivation remain at play afterwards and lead to a cascading transfer of forces from that location to the neighbouring fault segments, causing a sequential reactivation of those segments. Slippage is indeed known to propagate much further away than just the surroundings the fault ([Scholz, 2002](#)). In order to numerically obtain this phenomenon of propagation, we select some points of interest along the fault where the multiscale couplings stated in Sec. 3.2 are computed, keeping this number as small as possible for computational purposes, since the full study of the fault slip propagation is out of scope for this contribution. A sensitivity analysis on the number of upscaling points is presented below in Sec. 7.1.5. In the rest of the section, we still refer to Fig. 7.2 for clarity, which presents the simulation results with one sampling point taken in the middle of the fault. Following the phase of propagation that ends with the last reactivation event at the bottom of the reservoir, we observe in Fig. 7.4 a synchronisation of the whole fault.

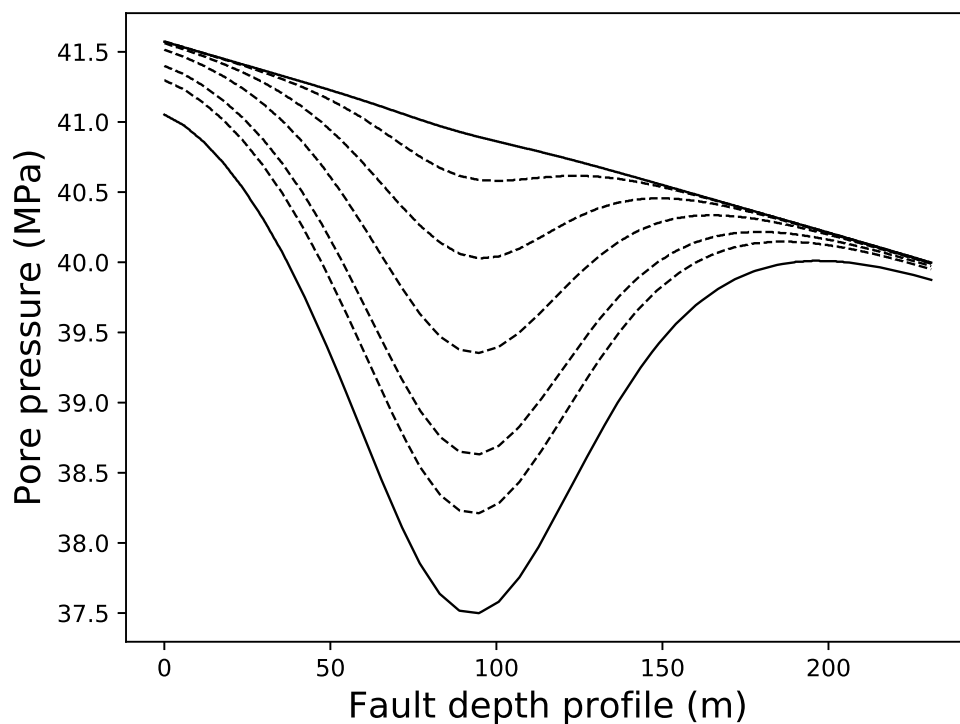


Fig. 7.3 Profile of pore pressure along the fault reaching a steady shape during early production.

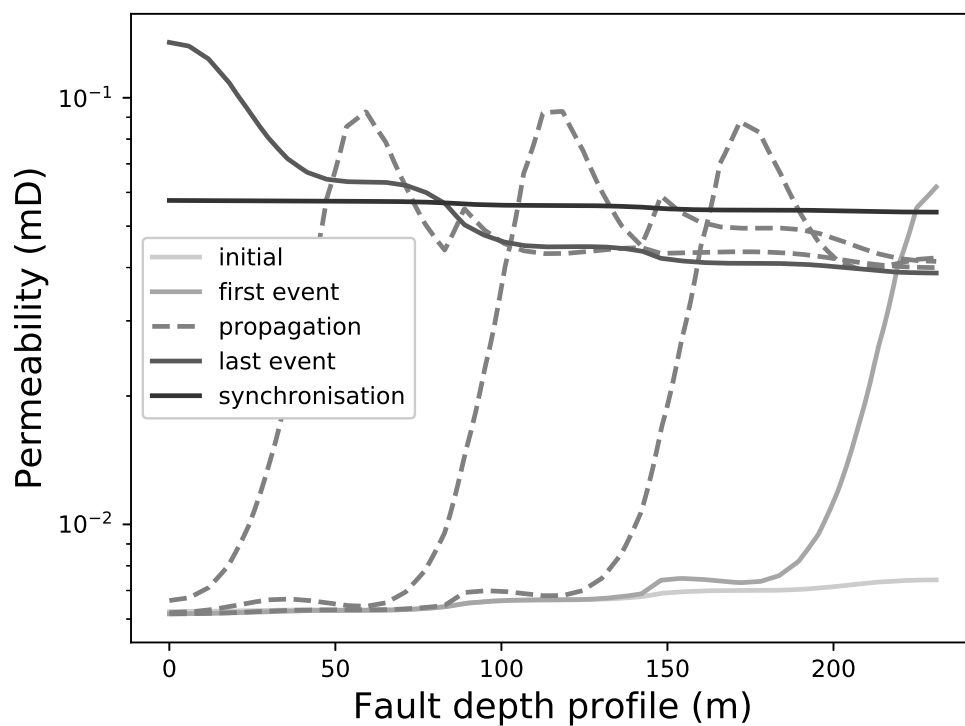


Fig. 7.4 Profile of permeability along the fault before the first slip event until the full synchronisation of the fault. The five curves show the chronological evolution of this profile at key stages of the simulation.

7.1.4 Fault deactivation and healing

The slippage of the fault results at the macro-scale in a horizontal elastic relaxation of the reservoir. Indeed, in the context of a normal fault, with the reservoir in extension, the fault slippage results in the hanging wall moving downwards. Due to the fixed lateral boundaries of the reservoir, this movement translates in a shortening of both compartments of the reservoir, relieving part of the extensive stress of the reservoir. This stress drop tends to bring back the fault towards a deactivated state, competing with the pressure depletion which keeps it activated. Given the difference of rates of those two processes, with pressure diffusing much slower than the fault slips, the stress decreases faster than the strain rate increases. This relaxation decreases the shearing stress at the fault, which corresponds to tracing downwards the highest branch of Fig. 7.2d from the reactivated state (point A2). After a sufficient decrease, the stress reaches a low enough value (point B1) where the fault cannot remain in its activated state and returns to the lower branch of the S-curve (drop from point B1 to B2). The temperature and slip velocity return to their initial value (see Fig. 7.2e) and the fault goes back to its initial slow creep regime. Correspondingly, the permeability goes back to its initial low value (see Fig. 7.2b) as the reversible temperature-activated calcite decomposition reaction switches from forward to reverse direction. The chemical dissolution responsible for the large increase of permeability gives way to its opposite reaction, which heals the fault by precipitating calcite at its core.

For the generic scenario selected, the whole reactivation event lasts for 250 days. Note the small thickness of reservoir leads the slip to propagate to the limits of the domain and the whole reservoir therefore accommodates the same vertical displacement jump as the fault. The fact that the reactivated fault splits the whole reservoir leads to an artificially increased period of slip. Considering a much deeper section of the reservoir, as well as its 3D nature, would be required to model appropriately a more precise duration of the whole slip event. This example illustrates nonetheless the ability of the approach to capture the physical couplings responsible for the activation, permeability increase and deactivation. Nonetheless, we expect a longer opening compared to a brittle fault slip, characteristic of ductile faults, along with an aseismic slip (velocity of $10^{-11}\text{m}\cdot\text{s}^{-1}$ in Fig. 7.2e) as detailed in Chapter 2.

7.1.5 Sensitivity analysis on upscaling points sampling

We investigate the sparsest sampling of upscaling points required to approach the full solution where all mesh points of the faults would be used to compute the macro/meso-scale coupling. Fig. 7.5 shows the results of different configurations used to run the same simulation with 1, 2, 3 and 5 upscaling points at different positions along the fault. The property used to visualise the convergence of the solution with the number of upscaling points is both the reactivation onset and the opening time of the fault. Note that all configurations led to the same qualitative result, with the top segment of the fault reactivating first and a synchronisation of slippage for the whole fault across the full thickness of the reservoir.

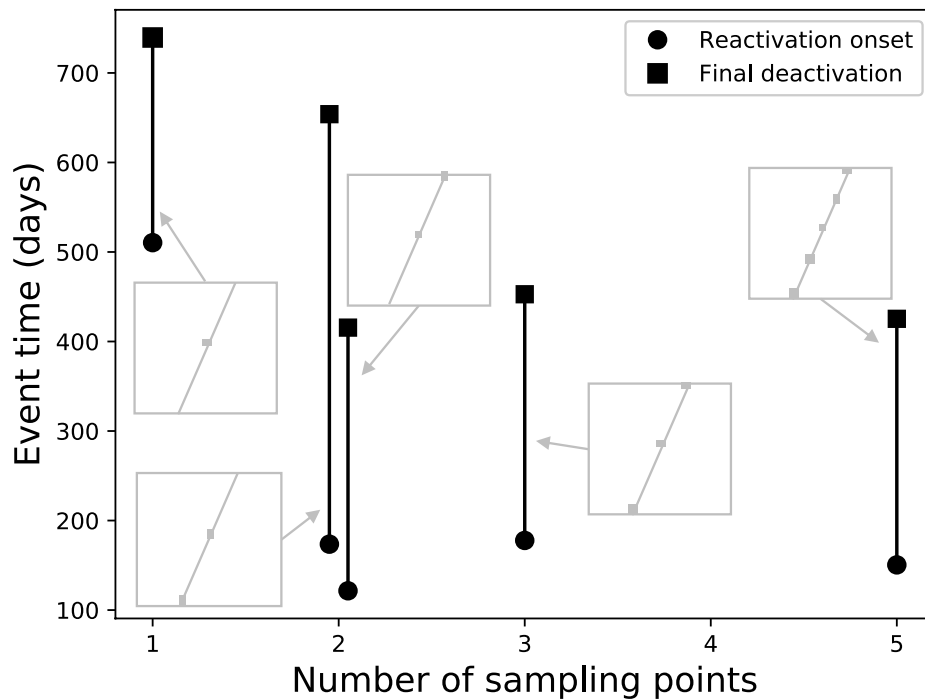
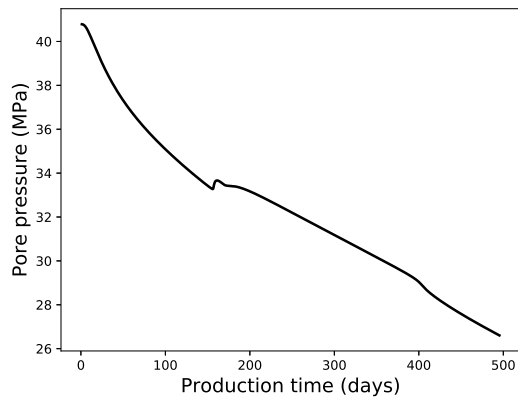


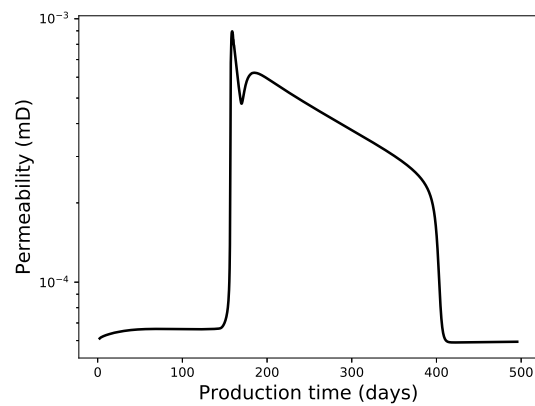
Fig. 7.5 Fault reactivation occurrence and duration depending on number of sampling points considered. The bars lengths represent the reactivation duration. Points location along the fault are visualised in grey. Note that for the one sampling point simulation, only the middle point configuration leads to the fault reactivation.

We can see that our reduced system respects the full system behaviour as long as the top and middle segments are included in the upscaling, for which the reactivation onset happens at ≈ 150 days and the fault stays active for ≈ 300 days. Increasing furthermore the number of points shows that it increases slightly the precision of the solution but the relative error on the solution has already qualitatively converged for 3 points of upscaling.

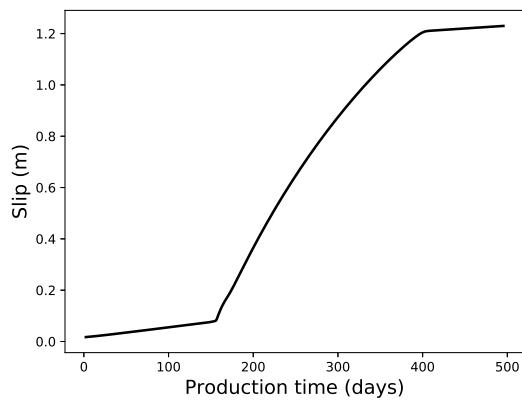
Results of the simulation using a representative number of sampling points (five) are visualised in Fig. 7.7, displaying all phases of the reactivation event as a visual summary of this section. Fig. 7.7a displays the sealing characteristic of the fault through the pressure discontinuity at the interface and the small arrows of fluid velocity in the right-hand side compartment of the reservoir. After a first reactivation event, at the top of the fault, the reactivation propagates downwards. Particularly, we visualise in Fig. 7.7b the moment when the propagation reaches the middle of the fault. The large arrows of fluid velocity indicate that the top segment has already reactivated, whereas the bottom segment remains sealed. The peak of fluid velocity located at the middle of the fault corresponds to the peak observed during propagation in Fig. 7.4. Following the phase of propagation, the synchronisation of the whole fault is observed in Fig. 7.7c, characterised by visible fault slippage and large arrows of fluid velocity along the whole fault. Healing occurs as the last phase and Fig. 7.7d displays a similar state as Fig. 7.7a with, however, an advanced stage of pressure depletion and the fault slippage accumulated during the reactivation event.



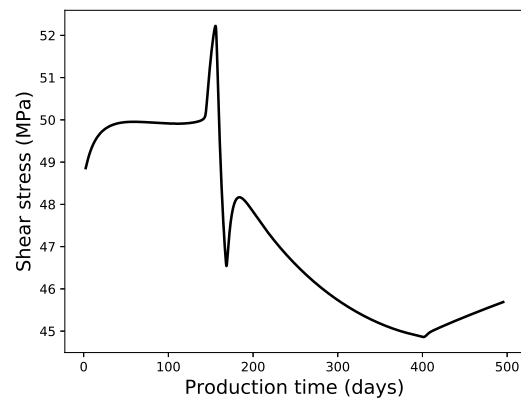
(a) Evolution of pore pressure on the left side of the fault.



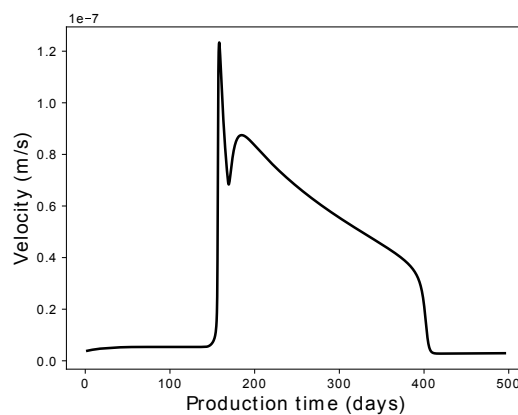
(b) Evolution of the fault permeability.



(c) Evolution of the fault slippage.

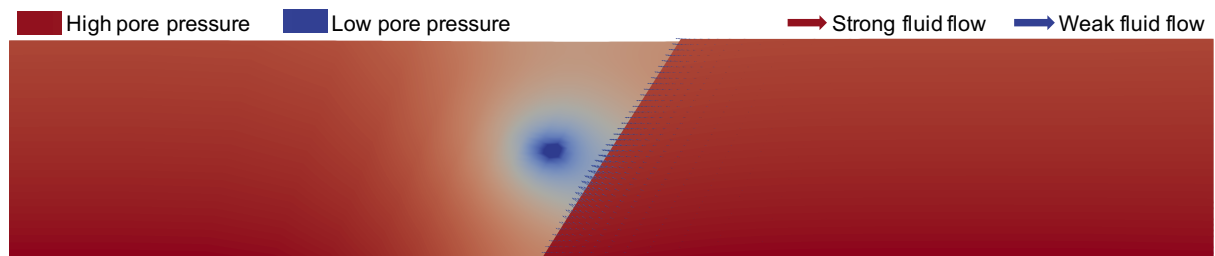


(d) Evolution of the fault shearing stress (Von Mises stress).

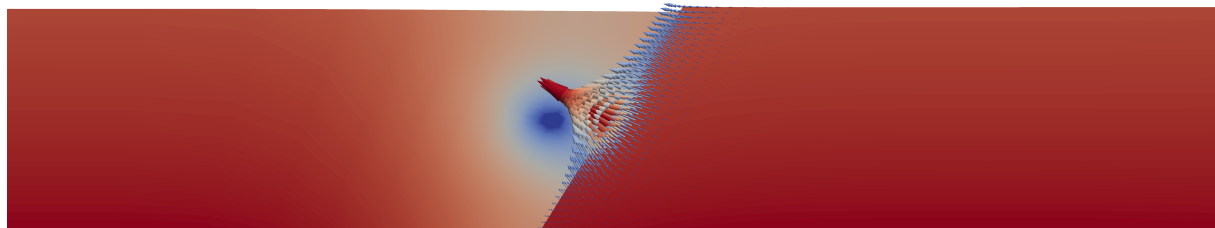


(e) Evolution of the fault slip rate.

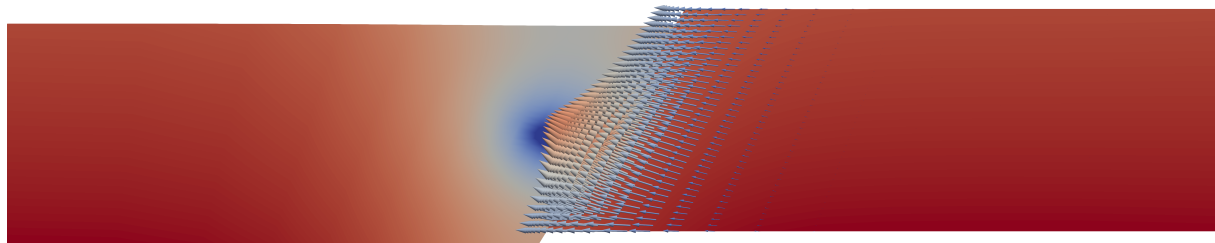
Fig. 7.6 Monitoring of the middle of the fault during a chemical fault reactivation induced by reservoir production, following the setup of Sec. 7.1.1 with five sampling points along the fault, referring to the final case of Fig. 7.5.



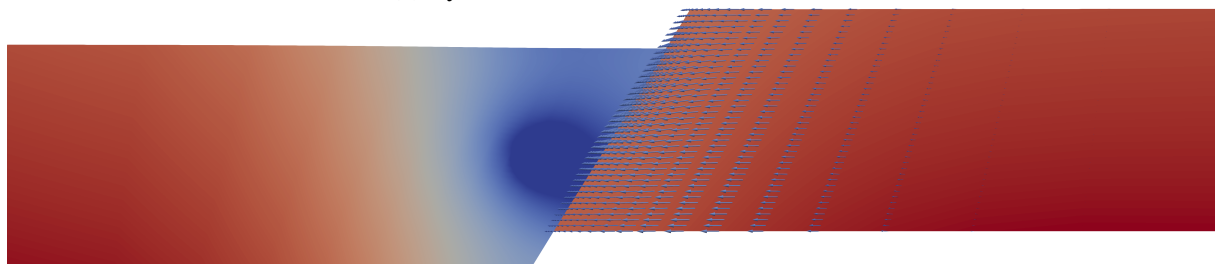
(a) Early stages of production



(b) Propagation to the middle of the fault. Contrary to the bottom segment, the top segment has already reactivated as shown by the difference of fluid velocity arrows size.



(c) Synchronisation of the whole fault



(d) Final state after fault deactivation and healing

Fig. 7.7 Schematic interpretation of numerical results showing the pressure distribution in the reservoir and fluid velocity in the right-hand-side compartment at different times during the reactivation event. The arrows size is proportional to the magnitude of the fluid velocity. Displacements are magnified by 30 times for visualisation purposes. The effect of the reactivation and corresponding permeability increase is observed on the pressure depletion across the fault. Note the pressure drop in the right compartment of the reservoir indicating fluid invasion.

Interestingly, when considering multiple points of upscaling and obtaining this event of propagation, the whole behaviour of the fault is different from the one obtained with a single point, as the phenomenon becomes one dimensional in space along the fault. If we do monitor the point in the middle of the fault, see Fig. 7.6, we can observe the interferences from other fault segments during the propagation event. They are visible on the plots of Fig. 7.6 as a perturbation of the curves of Fig. 7.2 around point A. This noise lasts for $\approx 15\%$ of the full event and after synchronisation, the behaviour becomes similar to the solution with one sampling point. Therefore, in order to keep a clear visualisation of the phenomena for the purpose of theoretical understanding, we display later in the contribution cases computed with only one sampling point in the middle of the fault.

7.2 Comparison with the rate and state law

The approach presented above is not particularly common to model the process of fault reactivation and a large proportion of modellers usually chose instead to describe the mechanical behaviour of faults directly as an interface, imposing a weakening mechanism at reactivation time to simulate the stress drop observed during the reactivation of the fault (e.g. Cueto-Felgueroso et al., 2018; Dieterich, 1992; Lapusta and Rice, 2003; Lapusta et al., 2000; Tse and Rice, 1986). Our multiscale framework, however, is meant to replace such artificial imposition of an empirical law by an upscaled law deriving from an enriched model at the meso-scale, leading to the same stress drop, as observed in Fig. 7.2d from point A to B, but providing at the same time a physics-based explanation for the reactivation of the fault and its temporary loss of sealing capability. This section focuses on the comparison of the two approaches by taking advantage of the capability of the macro-scale model of Chapter 3 to implement any constitutive model for the interface laws. Specifically, our macro/meso-scale approach is compared with a macro-scale only model implementing representative (but artificially imposed) interface laws, as detailed below.

Fault stability is commonly assessed from a purely mechanical perspective using the Coulomb Failure Criterion (e.g. Cappa and Rutqvist, 2011; Rutqvist et al., 2007; Zoback and Zinke, 2002), which monitors the distance to the yield/failure envelope of the fault in stress space and leads to reactivation when the stress state of the fault reaches this surface. Note that for the more complex case of frictional interfaces, the strength of the fault depends on the normal stress, due to asperities contacts at the interface, and the fault is then characterised by a friction coefficient. For the purpose of reducing the complexity of material properties and focus on multiphysics couplings of mechanisms, we choose, however, a pressure insensitive material for the fault which nullifies the friction coefficient and justifies looking directly at the shear strength q_y instead. For the inclusion of the pressure sensitivity, we refer to Poulet et al. (2017). Fig. 7.2d shows that the shear stress of the fault increases until it reaches point A, which is the reactivation onset. This point corresponds in addition to a peak value of shear stress, which correlates well with the theory that point A has reached the unexceedable strength of the fault, q_y , initiating rupture. We

calibrate therefore the value of q_y to the shear stress value of point A, 50.4 MPa for this specific example.

Despite not considering surface roughness, Chapter 2 showed that by including instead multiphysical mechanisms, namely shear heating and chemical dissolution, the chemical shear zone model is able to describe a fault reactivation behaviour described similarly by the theory of frictional contacts, where the fault slip is first initiated when exceeding the value of static friction. In that theory, the object then slides continuously, with a different friction called dynamic friction. In the context of fault reactivation, however, the process is too complex to be captured by a constant dynamic friction coefficient, which has been shown to depend on many parameters, see review from [Scholz \(2002\)](#). [Dieterich \(1979\)](#) introduced therefore the rate and state law, which models the two phases of the evolution of this dynamic friction coefficient. It first captures the transient transition from the static (locked) state to the dynamic (active) state achieved when the system reaches quasi-static values of friction and velocity. As observed on Fig. 7.2, this event corresponds to the transition from point A1 to A2. Since it is negligible in time, we focus instead on the second phase, which models the following quasi-static behaviour. This steady-state rate and state law can be expressed (for q in our contribution) as

$$q = q_y + (a - b) \ln\left(\frac{v}{v_0}\right) \quad (7.1)$$

where a and b are experimentally calibrated constants. As mentioned earlier, the quasi-static value of velocity v_0 is achieved at point A2, calibrated at $1.1 \times 10^{-7} \text{ m.s}^{-1}$. This law is then used as the mechanical interface law of the fault implemented in the macro-scale model and calibrated, for the sake of comparison, to the results of the macro/meso-scale model. To do so, we select $(a - b) = 0.2$ so that the slope of the macro-scale model using the rate and state law (in dashed line) matches the tangent of the simulation results (in solid line) at point A2 on Fig. 7.8. We notice that the fitted law actually matches the slip-weakening for most of the reactivated state of the fault. This weakening is commonly capped at a critical velocity ([Cueto-Felgueroso et al., 2018](#)), v_c , below which the fault is assumed locked again. This corresponds in our simulation to point B1, which represent the deactivation of the fault, when v_c reaches $0.6 \times 10^{-7} \text{ m.s}^{-1}$.

We can observe a deviation between our model and the fitted rate and state law right before the deactivation of the fault. As seen in Fig. 7.8, our model displays a smooth transition to the deactivated state compared to the rate and state law that relies on a hard threshold of velocity to return the fault to a locked state. This difference highlights the radically distinct concept of our model, in which the fault evolution is a continuous process, compared to the discrete nature of the reactivation and deactivation with the rate and state approach. We can see that the two approaches are matching perfectly for the reactivation onset because of its abrupt nature, as seen in Fig. 7.8. For the deactivation, however, the gradual decrease of velocity is arguably more realistic with our framework, since it results from physical mechanisms like precipitation gradually compensating competing mechanisms keeping the fault activated. In that respect, we see this discrepancy in the deactivation phase as an improvement on the empirical law.

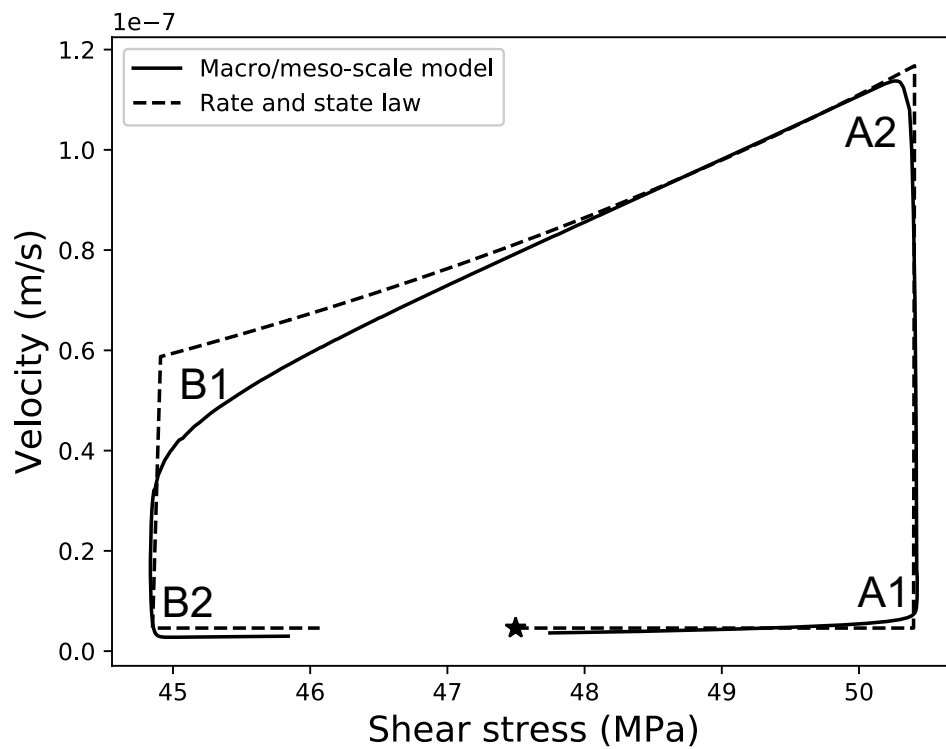


Fig. 7.8 Velocity vs shear stress of the fault. The simulation results are taken from the case study of Sec. 7.1.1 and represent an additional output of Fig. 7.2. The macro/meso-scale model is compared with the macro-scale only model implementing a rate and state law for the mechanical fault interface. The star denotes the start of fluid production.

The good match overall of Fig. 7.8 represents an extended validation of our model, since the rate and state law has itself been extensively fitted already against experimental and natural data on fault reactivation (see review from Marone, 1998). Furthermore, our model goes beyond a simple fit and actually retrieves the constitutive law as an output of the simulation. This means that q_y , v_0 , $(a - b)$ and v_c are not just calibrated, like for the rate and state law, but depend naturally on material properties of both the fault and the reservoir, involved in the physical processes described by the meso-scale model of Chapter 2.

On top of the fault slip, our model computes the permeability evolution during the reactivation and this can also be taken into account in the macro-scale only model. For illustration purposes, we select a simple arbitrary model which assumes the fault to be sealing when locked with a permeability of 0.0065 mD and to become more permeable when active with a permeability of ≈ 0.08 mD, as displayed in Fig. 7.9b. Note that the permeability plotted in this figure is $k^{(F)}$ introduced in Eq. 3.16. Using these two constitutive interface laws, we can compare the outputs of the macro/meso-scale model with the macro-scale model in Fig. 7.9. We observe that by matching the law of velocity vs shear stress and the evolution of permeability, we also match other additional outputs of the models, including the pore pressure evolution.

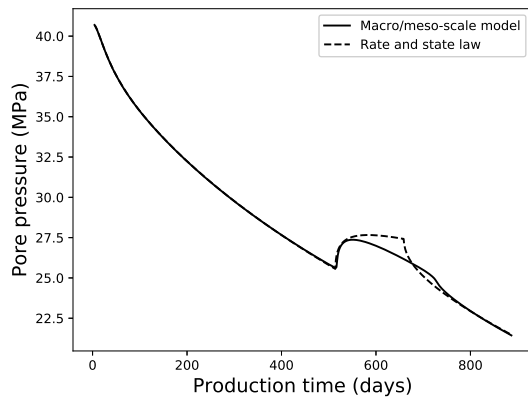
Note that the calibrated value for $(a - b)$ is positive, which corresponds as expected to a velocity-hardening behaviour, specific to stable fault slips. This stable character is nicely illustrated in our simulation where we can see that, even though production has pushed the fault to reactivate, the activated fault tends naturally to go back towards stability and deactivate. The reason behind this behaviour is that, qualitatively, the fault slippage leads to an elastic stress relaxation which in turn decreases the shear heating and thus the velocity of the fault.

7.3 Influence of the microstructure on the system

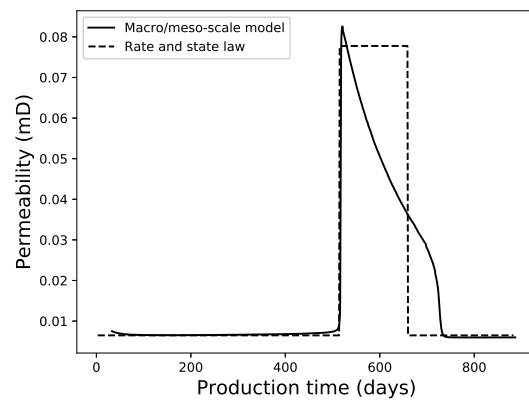
The coupled macro/meso-scale framework of Sec. 3.2 was used in the previous section to simulate an induced chemical fault reactivation event. Having understood the complex interplay between the macro- and meso-scales, we add to the framework the micro-scale couplings described in Sec. 4.2 and summarised by Fig. 4.2, in order to refine the evolution of the permeability of the fault. As the study is not quantitative, note that we use a 2D linear interpolation between the sampling points, that we implemented in MOOSE, instead of the Bezier interpolation algorithm, for simplicity. The consideration of the micro-scale allows us to study the influence of the microstructure on the whole multiscale phenomenon, which is done in this section by comparing the effect of two different microstructures.

7.3.1 Permeability hysteresis

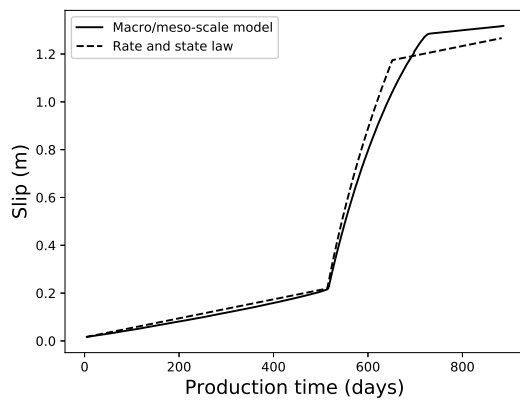
We consider two different synthetic microstructures, α and β , idealised to tortuous microscopic flow channels, whose flow paths are shown respectively in Fig. 7.10a and Fig. 7.10d. Both microstructures have the same porosity and tortuosity (the flow path has the same length),



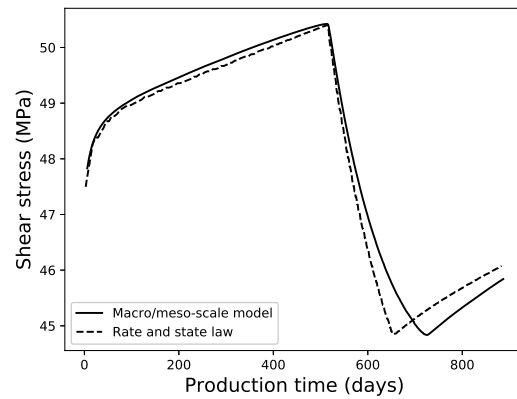
(a) Evolution of pore pressure on the left side of the fault.



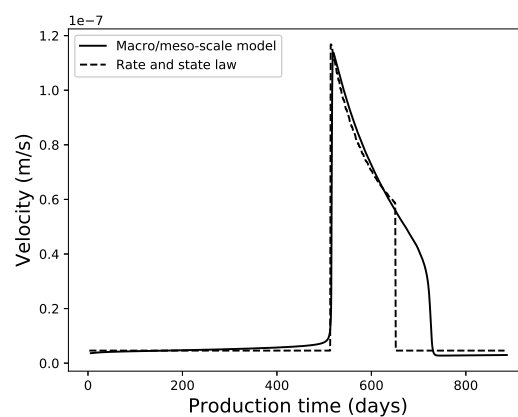
(b) Evolution of the fault zone permeability.



(c) Evolution of the fault slippage.



(d) Evolution of the fault shearing stress (Von Mises stress).



(e) Evolution of the fault slip rate.

Fig. 7.9 Outputs of an event of chemical fault reactivation, following the setup of Sec. 7.1.1, obtained with our multiscale model and with a model implementing a rate and state law for the fault and an empirical permeability evolution.

therefore the same permeability. As such, these two configurations would be strictly identical at the meso-scale if the porosity and permeability were the only properties considered in the upscaling process. Yet, we can show a major difference of behaviour between those two microstructures when subjected to the same arbitrary cycle of dissolution and re-precipitation, as induced by fault reactivation and deactivation events. Fig. 7.10b (resp. 7.10e) shows the eroded microstructure α (resp. β) after dissolution and Fig. 7.10c (resp. 7.10f) the final dilated configuration after the re-precipitation step. We observe that the narrow gap between the vertical channels of microstructure β gets completely eroded during the dissolution process when the porosity reaches a value of $\approx 18\%$, connecting the two horizontal channels and leading to a shorter flow path.

Fig. 7.11 showcases this interesting phenomenon very clearly by plotting a graph of permeability vs porosity. While both microstructures follow the same curve at first, the opening of the new channel renders the flow path less tortuous and the permeability of the microstructure β jumps to a higher value, following a new path on the permeability-porosity graph and remaining permanently on that new path from that point on, not only for the rest of the dissolution process but also for the whole re-precipitation phase. This channel creation has indeed a consequence on the final state of the structure, after the fault has healed by re-precipitation. As illustrated in Fig. 7.10f, even though the porosity goes back to its initial value, microstructure β ends up with a different permeability than its initial state. We note that the hysteresis can only be taken into account through the ability of the erosion algorithm of Sec. 6.3.1 to open flow channels during dissolution, which is not possible with a standard algorithm of skeletonization. This important permeability hysteresis phenomenon can only be observed when using the dynamic coupling between the scales because the dissolution history needs to be taken into account. Indeed, if for the case study of Fig. 7.11 the maximum of dissolution reached had remained under the critical threshold of $\approx 18\%$ then a new channel would not have been created and the permeability of the two different microstructures would have remained the same.

Interestingly we observe that both dissolution curves in Fig. 7.11 follow a cubic law of porosity. Since both configurations represent simple tortuous channels, they can indeed be described by Poiseuille's law, with the flow rate Q is given by:

$$Q = -\frac{D^3}{12\mu} \frac{dP}{dx} \quad (7.2)$$

with D the diameter of the channel and x the length of the tortuous path. We can recognize here Darcy's Law, $Q = -\frac{k}{\mu} \frac{dP}{dx}$, and therefore retrieve the cubic evolution of the permeability for a widening Poiseuille channel. The porosity is directly linked to the diameter of the channel, which explains why Fig. 7.11 shows a match with a cubic law. The match is not perfect, however, as the microstructure cannot be completely assimilated to an ideal Poiseuille channel due both to the corner effects and heterogeneity of channel height along the path.

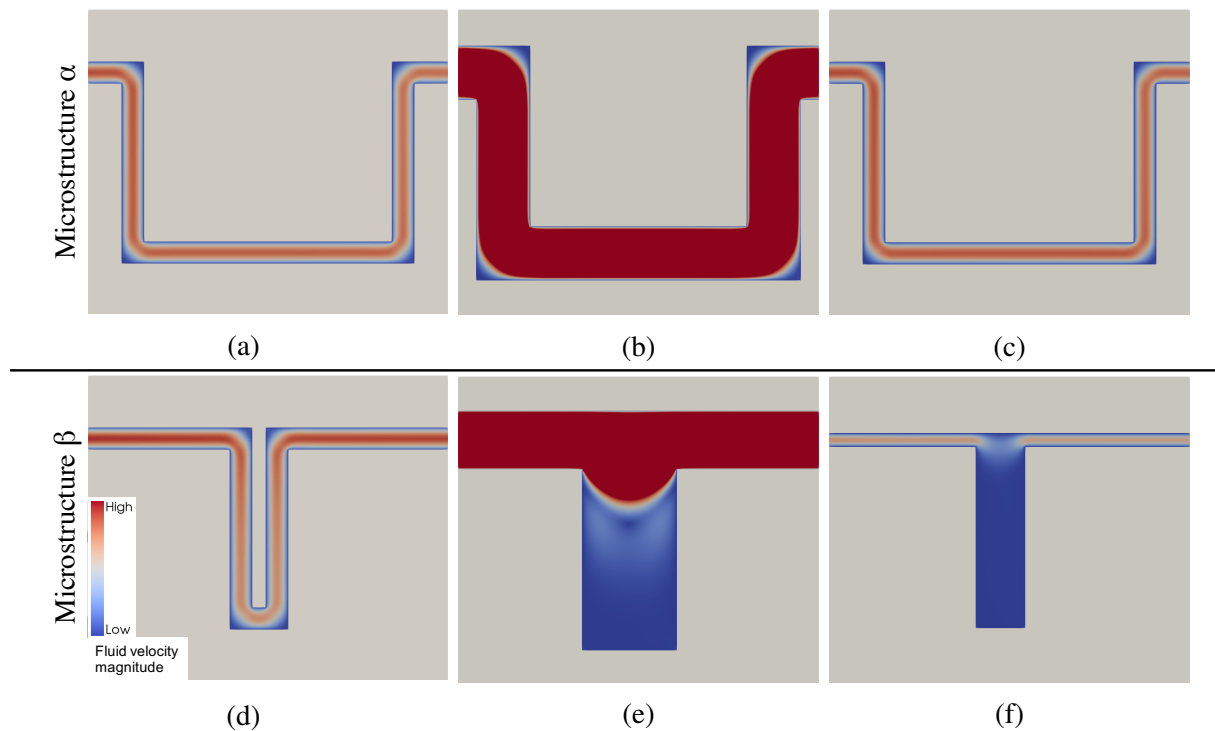


Fig. 7.10 Visualisation of fluid velocity magnitude at the initial state, peak dissolution and final reprecipitation (left to right respectively) of two different microstructures (α on top and β at the bottom) for the case study of Sec. 7.1.1.

7.3.2 Influence at the macro-scale

The two microstructures α and β are now linked to the meso- and macro-scales simulations of the case study of Sec. 7.1.1 and the outputs are plotted on Fig. 7.12 for the pore pressure, permeability, slip, shear stress and slip velocity, in blue (resp. red) for microstructure α (resp. β). Until the reactivation, both sets of curves superpose perfectly since the initial permeabilities of the two microstructures are equal.

At the peak of reactivation, however, microstructure β has reached a higher permeability from the new channel opening (see Fig. 7.10e). This higher permeability results in a more pronounced pressure equilibration, as seen in Fig. 7.12a for microstructure β ($t \approx 300$ days). Following the stress path described in Sec. 7.1.4, a higher pore pressure translates to an increase in Von Mises stress, which keeps the fault activated for a longer period as observed in Fig. 7.12e-7.12c.

This comparative study shows clearly that a change of geometry at the micro-scale, unnoticeable with the restrictive characterisation of microstructure through the notions of porosity and permeability only, affects different physical aspects of the behaviour at the macro-scale. The dependency on the microstructure is achieved with our framework through a complex coupling effect of scales and physical mechanisms, as visualised in the simplified diagram of Fig. 7.13. Pressure depletion due to production increases the shear stress at the fault due to the stress path. Past a stress threshold, the fault reactivates and slips. Simultaneously, chemical dissolution is triggered and the two microstructures reach a different permeability. This permeability feeds

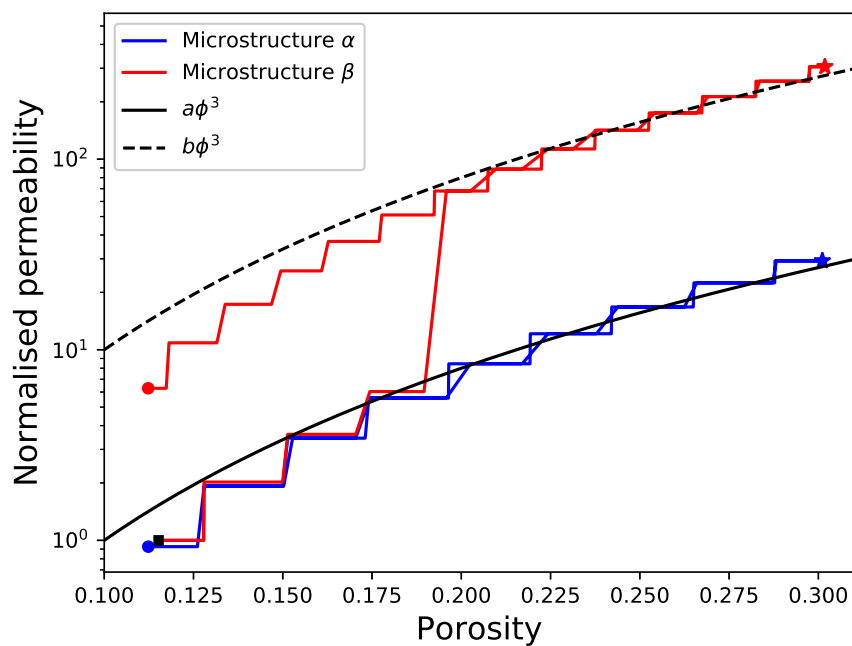
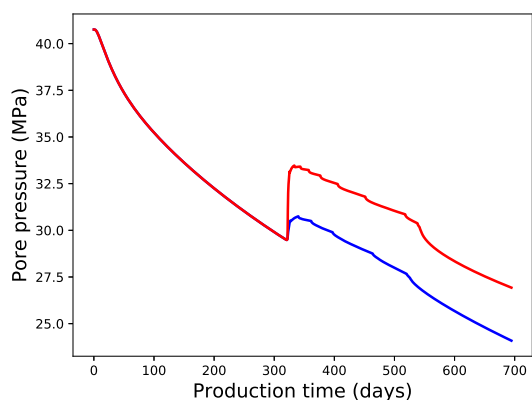
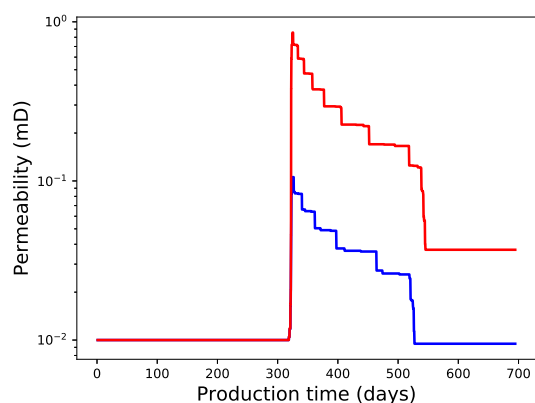


Fig. 7.11 Evolution of permeability of the two different microstructures with respect to porosity. The permeability is normalised with the value of the initial state. The two curves follow a cubic law as shown by the black curves ($a=1000$ and $b=10000$). The square point corresponds to the same initial state for both microstructures, Fig. 7.10a-7.10d ; The stars correspond to the different peak of reactivation, Fig. 7.10b-7.10e ; The dots correspond to the different final states, Fig. 7.10c-7.10f.

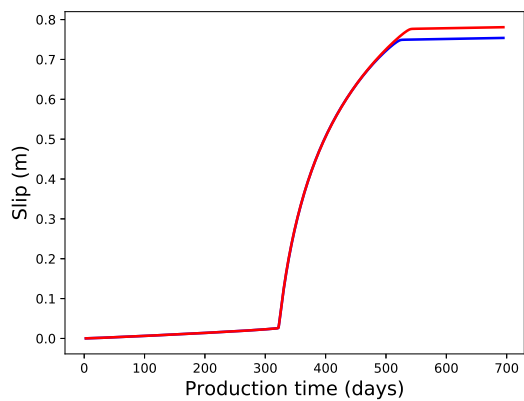
back into Darcy's law at the macro-scale and leads to a different pressure equilibration, which in turns changes the fault deactivation time due to the stress path.



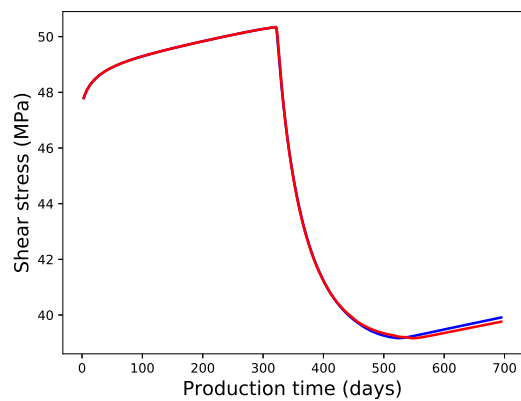
(a) Evolution of pore pressure on the left side of the fault.



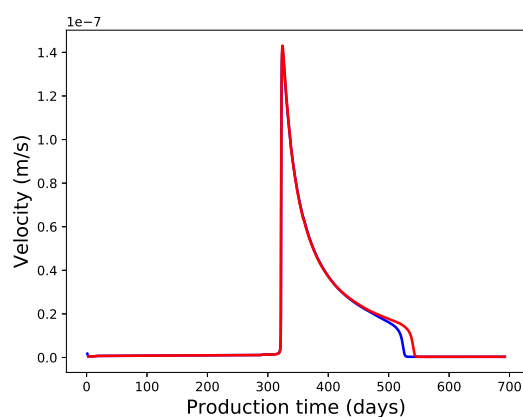
(b) Evolution of the fault permeability.



(c) Evolution of the fault slippage.



(d) Evolution of the fault shearing stress (Von Mises stress).



(e) Evolution of the fault slip rate.

Fig. 7.12 Outputs during a reservoir production following the setup of Sec. 7.1.1. Blue curve corresponds to the microstructure A and red curve to microstructure B.

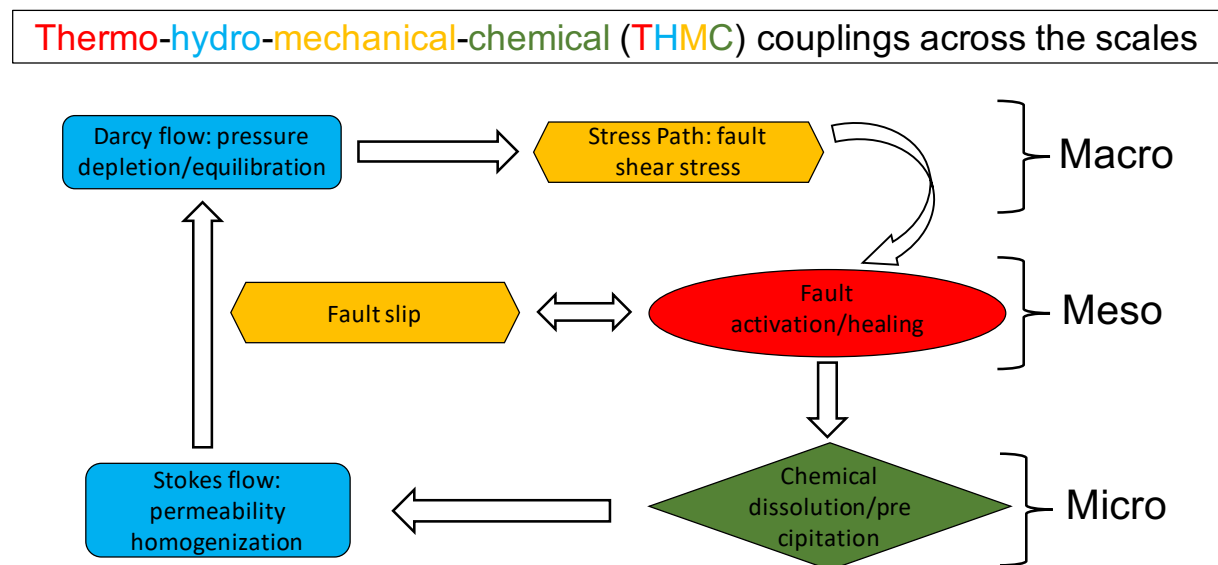


Fig. 7.13 Diagram showing a simplified loop of coupled scales and physics allowing for fault reactivation and healing. A blue box represents a hydraulic mechanism; yellow is mechanical; red is thermal; green is chemical.

Chapter 8

Summary and conclusions

This contribution focuses on the special phenomenon of chemical fault reactivation. On this aspect, the contribution warns about the potential hazard of fluid production next to a sealing fault in particular conditions. Indeed, we have shown that the phenomenon concerns chemically active faults (e.g. carbonate) and is more likely to happen with increasing depth and background velocity. If this type of fault reactivates from a pressure perturbation, the seal can be temporarily broken because of thermally activated chemical dissolution, resulting in reservoir leakage or fluid invasion, yet undetectable by classical seismic monitoring. The phenomenon of permeability increase during such a fault reactivation was shown to be complex, because of the strong couplings between all physical mechanisms at play, such as chemical dissolution, shear heating, mechanical deformation and pressure diffusion occurring across the various scales of the system. Part I and II introduced the components and framework required to couple all physical processes at their appropriate scales of interest. All elements were then used together in Part III to model a generic geological scenario, reproducing in a single simulation all characteristic aspects expected for such a phenomenon: material instability, aseismic slip, permeability increase, elastic stress relaxation, deactivation, healing and permeability hysteresis. This three-scale multiphysics approach successfully simulated a chemical fault reactivation and showed the importance of dynamically-upscaled laws, when the use of empirical laws can be too specific to a particular configuration and lack information from the lower scales. The commonly used relationships between porosity and permeability, for instance, do not allow to retrieve the permeability hysteresis. On top of those overall conclusions, we list hereunder some additional results derived for each independent component of the framework.

An important particularity of this multiscale framework is the master role of the meso (m) scale, which corresponds to the physical length scale of the chemical fault reactivation phenomenon. This approach contrasts from the common fault reactivation modelling done at the reservoir scale (e.g. [Cappa and Rutqvist, 2011](#)) and the mechanical studies on localisation purely upscaled from the micro-scale (e.g. [Nitka et al., 2011](#)). The meso-scale was shown to capture adequately the chemical shear zone behaviour, which is applicable to high P,T environments, where chemistry becomes more active. While fault reactivation in such deep environments might suffer from a lack of data compared to brittle faults found at shallower depths, their study is

actually more tractable because of the driving influence of the physics governing the system, compared to shallower systems which are more strongly influenced by geometrical and material heterogeneities. For a given setup, the stability of a ductile system depends solely on its material properties and can be derived using an arc length continuation method (Sec. 2.2), which provides a full description of the possible states of the fault. For instance, this analysis had previously helped validate the chemical shear zone (CSZ) model against real data in drastic environments like subduction zones (Alevizos et al., 2014; Poulet et al., 2014a; Veveakis et al., 2014) or megathrusts (Poulet et al., 2014b), identifying an episodic oscillatory behaviour of such stick-slip faults. In this contribution, the model was further validated by replicating the behaviour of slip-weakening laws that are commonly applied to match real fault reactivation events (Sec. 7.2). The study of historical cases is now necessary to validate and calibrate the model against real data.

This framework extends the CSZ model's range of applications to more complex behaviours at the macro-scale where the boundary conditions at the fault evolve with time. Previous applications of that model had indeed been limited to static boundary conditions corresponding to tectonic forces (e.g. Alevizos et al., 2014; Poulet et al., 2014a; Poulet and Veveakis, 2016; Poulet et al., 2014b; Veveakis et al., 2014). However, in the case of fluid production in the reservoir, the stress state of the fault depends strongly on the level of depletion of the reservoir. To take this into account, we introduced the reservoir scale (macro, Chapter 3) to simulate through poromechanics the stress changes along the fault stemming from fluid production. The macro-scale is used to provide the boundary conditions of stress and pressure to the meso-scale at every time step. Due to the clear scale separation, the fault can be treated as an interface at the macro-scale. Compared to common cases where the fault is either treated as a channel or a seal, we need to be able to treat both states and the continuous transitions in-between. Our interface law presented in Sec. 3.1.2 handles all configurations by directly resolving the flow through the fault. After the meso-scale resolution, changes of permeability and increase of slippage are fed back to the interface law of the meso-scale. By doing so, the consequences of fault reactivation such as fluid invasion can be studied at the macro-scale. Particularly, we showed in Chapter 7 that the increasing slippage results in an elastic stress relaxation of the reservoir and leads to the fault deactivation which was previously only artificially taken into account for empirical laws (e.g. Cueto-Felgueroso et al., 2018).

Chapter 7's case study displayed the model's ability to predict the occurrence of the reactivation, which is the critical parameter needed for safe subsurface operations. By coupling strongly all the physical mechanisms at play, our model is able to resolve continuously the instability of temperature that controls the phenomenon. The transition between locked and active regimes of the fault happens therefore smoothly, yet in a very short amount of time, matching nicely an artificial switch between regimes used more commonly in fault reactivation models (Sec. 7.2). This same smooth but sharp transition occurs in the deactivation stage.

We suggest that the extraordinarily high permeability increase observed during some fault reactivation can be physically modelled with the consideration of chemical dissolution, which

is active for deep carbonate rocks. Instead of a difficult calibration of an empirical law, with the aperture of the fractures vs the shear strain for example, the permeability increase can be quantified in our model using the chemical properties of the fault gouge which could be measured from cores. Coupled with the finite duration of the reactivation event, the change of permeability results in a temporary loss of the fault seal. Consequently, the model could compute the amount of fluid that leaked through the fault which provides a good assessment of the consequences of the reactivation event.

The consideration of the micro-scale in the multiscale framework (Chapter 4) allowed to capture the phenomenon of permeability hysteresis stemming from flow channel creation during chemical dissolution of the fault (Chapter 7). This effect can only be modelled with the consideration of the rock microstructure evolution at this scale. This extension of the framework also comes as an effort to link the field of data-driven science to physics-based modelling in the sense that the microstructural data, collected to characterise rock properties, is used quantitatively for physical modelling in this contribution, in a dynamical hydro-chemical simulation to simulate the transient evolution of permeability with deformation. For that purpose, Chapter 6 presented a flow simulator on meshed μ CT-scans in order to homogenise the permeability of rock microstructure. To apply that process on deformed microstructure, the simulator was coupled to either a solid mechanics module (Sec. 6.2) which required the handling of an Eulerian-Lagrangian system, and an erosion algorithm (Sec. 6.3) to simulate chemical dissolution or precipitation. The latter was incorporated into the macro-meso multiscale framework in Chapter 7, which led to some hysteresis due to the dissolution/precipitation path as new flow channels could be created. This study showcased strongly the influence of multiphysics couplings across scales and highlighted how to account for simple changes in the microstructure from μ CT-scans and quantitatively assess the resulting impact on the duration of the reactivation event at the macro-scale.

The framework introduced in this thesis is particularly rich in applications and opened the door to further exciting studies. For instance, while the study of Chapter 7 focused mainly on chemical alterations as the preponderant deformation mechanism of the microstructure, mechanical deformations remain non-negligible during fault reactivation, especially for the shear component, and affect as well the geometry of the microstructure. The permeability upscaling of Chapter 7 could therefore be further refined when linked with the hydro-mechanical simulator of Chapter 6 to capture other effects and link microstructural geological observations to the overall fault reactivation process.

Similarly, the micro-scale model could be extended to upscale for mechanical properties, which is an important feature since Chapter 5 confirmed that the presence of pore space is the cause of pressure sensitivity in rocks. Mechanical simulations on digital rock microstructures allow to go one step further and plot the entire yield envelope, with the compression cap, by identifying homogenised yield stress values on the computed stress-strain curves for different stress paths. Chapter 5 clarified the ambiguity around the notion of yield, revealing different homogenised values when considering different definitions. For this reason, we suggested a new protocol to measure the macroscopic yield of a rock based on energy considerations (Sec. 5.4-

5.6.2), which was validated both numerically and experimentally. We believe that this method could yield more valuable results than the classic experimental method in a modelling context, because it corresponds physically to a transition of energy regimes, from elastic energy storage to plastic dissipation, instead of a geometrical deviation of linear elasticity.

The upscaling of micro-scale properties is not limited to numerical modelling and Chapter 5 demonstrated that the various yields identified could either be computed numerically or measured experimentally, with relatively good agreement between the two approaches when both are based on μ CT-scans. While these images are more commonly used to reconstruct 3D models as inputs of the numerical simulations (Chapters 5-6), this contribution explored their potential in generating 3D printed samples for laboratory experiments (Sec. 5.6). The use of 3D printing is quite novel in geomechanics and we demonstrated its particular value in retrieving the geometrical influence of the microstructure on the rock yield (Sec. 5.7.1), as the only method able to recreate a physical sample from a given microstructure. Sec. 5.6 showed that this promising technique has already reached a satisfactory level of precision for geomechanical testing, extending its usage from visualisation to the modelling field.

The overall modelling framework was illustrated on a specific application to production-induced fault reactivation, yet it remains much more generic and flexible to capture numerous other scenarios linked to fault reactivation. Within the context of petroleum engineering, fluid injection is actually the most common cause for fault reactivation and could just as well be modelled with this approach. Implementing more physics at the macro-scale could also easily diversify the range of applications, including geothermal exploration, enhanced oil recovery or CO₂ storage. At even larger length scales and geological timescales, this framework is also applicable to plate tectonics theory looking at purely tectonic perturbations of faults. In this context, the framework can also be applied to mineral exploration, extending preliminary results from Poulet et al. (2018a,b) where fault openings are inferred to cause the episodic propagation of mineralising fluids, responsible for giant ore deposits when they reach lower P,T environments. This modelling framework captures the evolution of multi-physical processes across scales in a way that was unforeseeable previously and opens the door to truly exciting studies in a wide range of fields.

References

- 3D Matter (2015). What is the influence of color, printing speed, extrusion temperature and ageing on my 3D prints? <http://my3dmatter.com>.
- Ahn, S.-H., Montero, M., Odell, D., Roundy, S., and Wright, P. K. (2002). Anisotropic material properties of fused deposition modeling ABS. *Rapid Prototyping Journal*, 8(4):248–257. doi:[10.1108/13552540210441166](https://doi.org/10.1108/13552540210441166).
- Alevizos, S., Poulet, T., and Veveakis, E. (2014). Thermo-poro-mechanics of chemically active creeping faults. 1: Theory and steady state considerations. *Journal of Geophysical Research: Solid Earth*, 119(6):4558–4582. doi:[10.1002/2013JB010070](https://doi.org/10.1002/2013JB010070).
- Anderson, E. M. (1905). The dynamics of faulting. *Transactions of the Edinburgh Geological Society*, 8(3):387–402. doi:[10.1144/transed.8.3.387](https://doi.org/10.1144/transed.8.3.387).
- Andrä, H., Combaret, N., Dvorkin, J., Glatt, E., Han, J., Kabel, M., Keehm, Y., Krzikalla, F., Lee, M., Madonna, C., Marsh, M., Mukerji, T., Saenger, E. H., Sain, R., Saxena, N., Ricker, S., Wiegmann, A., and Zhan, X. (2013). Digital rock physics benchmarks—part II: Computing effective properties. *Computers & Geosciences*, 50:33–43. doi:[10.1016/j.cageo.2012.09.008](https://doi.org/10.1016/j.cageo.2012.09.008).
- Andrews, D. J. (1976). Rupture velocity of plane strain shear cracks. *J. Geophys. Res.*, 81(32):5679–5687. doi:[10.1029/jb081i032p05679](https://doi.org/10.1029/jb081i032p05679).
- Armstrong, R. T., McClure, J. E., Robins, V., Liu, Z., Arns, C. H., Schlüter, S., and Berg, S. (2018). Porous Media Characterization Using Minkowski Functionals: Theories, Applications and Future Directions. *Transport in Porous Media*, 130(1):305–335. doi:[10.1007/s11242-018-1201-4](https://doi.org/10.1007/s11242-018-1201-4).
- Arns, C. (2009). *Structure-property Relationships from Digital Images*. VDM Verlag.
- ASTM E8/E8M-16a (2016). Standard Test Methods for Tension Testing of Metallic Materials. Technical report, ASTM International. doi:[10.1520/e0008_e0008m-16a](https://doi.org/10.1520/e0008_e0008m-16a).
- Balay, S., Abhyankar, S., Adams, M. F., Brown, J., Brune, P., Buschelman, K., Dalcin, L., Eijkhout, V., Gropp, W. D., Kaushik, D., Knepley, M. G., McInnes, L. C., Rupp, K., Smith, B. F., Zampini, S., and Zhang, H. (2016a). PETSc Users Manual. Technical Report ANL-95/11 - Revision 3.7, Argonne National Laboratory.
- Balay, S., Abhyankar, S., Adams, M. F., Brown, J., Brune, P., Buschelman, K., Dalcin, L., Eijkhout, V., Gropp, W. D., Kaushik, D., Knepley, M. G., McInnes, L. C., Rupp, K., Smith, B. F., Zampini, S., and Zhang, H. (2016b). PETSc Web page. <http://www.mcs.anl.gov/petsc>.
- Bandis, S., Lumsden, A., and Barton, N. (1983). Fundamentals of rock joint deformation. *International Journal of Rock Mechanics and Mining Sciences & Geomechanics Abstracts*, 20(6):249–268. doi:[10.1016/0148-9062\(83\)90595-8](https://doi.org/10.1016/0148-9062(83)90595-8).
- Banerjee, J. K. (1985). Barreling of Solid Cylinders Under Axial Compression. *J. Eng. Mater. Technol.*, 107(2):138–144. doi:[10.1115/1.3225789](https://doi.org/10.1115/1.3225789).

- Batchelor, G. K. (2000). *An Introduction to Fluid Dynamics*. Cambridge University Press. doi:[10.1017/CBO9780511800955](https://doi.org/10.1017/CBO9780511800955).
- Bear, J. (1972). *Dynamics of fluids in porous media (Environmental science series)*. American Elsevier Publishing.
- Beckingham, L. E. (2017). Evaluation of Macroscopic Porosity-Permeability Relationships in Heterogeneous Mineral Dissolution and Precipitation Scenarios. *Water Resources Research*, 53(12):10217–10230. doi:[10.1002/2017wr021306](https://doi.org/10.1002/2017wr021306).
- Besson, J. (2009). Damage of ductile materials deforming under multiple plastic or viscoplastic mechanisms. *Int. J. Plast.*, 25(11):2204–2221. doi:[10.1016/j.ijplas.2009.03.001](https://doi.org/10.1016/j.ijplas.2009.03.001).
- Biot, M. A. and Willis, D. G. (1957). The Elastic Coefficients of the Theory of Consolidation. *Journal of Applied Mechanics*, 15:594–601.
- Blunt, M. J., Bijeljic, B., Dong, H., Gharbi, O., Iglauer, S., Mostaghimi, P., Paluszny, A., and Pentland, C. (2013). Pore-scale imaging and modelling. *Adv. Water Resour.*, 51:197–216. doi:[10.1016/j.advwatres.2012.03.003](https://doi.org/10.1016/j.advwatres.2012.03.003).
- Borujeni, A. T., Lane, N. M., Thompson, K., and Tyagi, M. (2013). Effects of image resolution and numerical resolution on computed permeability of consolidated packing using LB and FEM pore-scale simulations. *Computers & Fluids*, 88:753–763. doi:[10.1016/j.compfluid.2013.05.019](https://doi.org/10.1016/j.compfluid.2013.05.019).
- Bratu, G. (1914). Sur les équations intégrales non linéaires. *Bulletin de la Société Mathématique de France*, 42:113–142. doi:[10.24033/bsmf.943](https://doi.org/10.24033/bsmf.943).
- Brezzi, F. (1974). On the existence, uniqueness and approximation of saddle-point problems arising from lagrangian multipliers. *Revue française d'automatique, informatique, recherche opérationnelle. Analyse numérique*, 8(R2):129–151. doi:[10.1051/m2an/197408r201291](https://doi.org/10.1051/m2an/197408r201291).
- Brinkman, H. C. (1949). A calculation of the viscous force exerted by a flowing fluid on a dense swarm of particles. *Flow, Turbulence and Combustion*, 1(1):27. doi:[10.1007/bf02120313](https://doi.org/10.1007/bf02120313).
- Burchette, T. P. (2012). Carbonate rocks and petroleum reservoirs: a geological perspective from the industry. *Geological Society, London, Special Publications*, 370(1):17–37. doi:[10.1144/sp370.14](https://doi.org/10.1144/sp370.14).
- Cappa, F. and Rutqvist, J. (2011). Modeling of coupled deformation and permeability evolution during fault reactivation induced by deep underground injection of CO₂. *Int. J. Greenhouse Gas Control*, 5(2):336–346. doi:[10.1016/j.ijggc.2010.08.005](https://doi.org/10.1016/j.ijggc.2010.08.005).
- Carman, P. C. (1937). Fluid flow through granular beds. *Trans. Inst. Chem. Eng.*, 15:150–166.
- Chapuis, R. P. and Aubertin, M. (2003). On the use of the Kozeny–Carman equation to predict the hydraulic conductivity of soils. *Canadian Geotechnical Journal*, 40(3):616–628. doi:[10.1139/t03-013](https://doi.org/10.1139/t03-013).
- Chen, W.-F. (1975). *Limit Analysis and Soil Plasticity*, volume 7 of *Developments in Geotechnical Engineering*. Elsevier Scientific Pub. Co.
- Christensen, R. M. (2007). Observations on the definition of yield stress. *Acta Mech.*, 196(3–4):239–244. doi:[10.1007/s00707-007-0478-0](https://doi.org/10.1007/s00707-007-0478-0).
- Clavaud, J.-B., Mainault, A., Zamora, M., Rasolofosaon, P., and Schlitter, C. (2008). Permeability anisotropy and its relations with porous medium structure. *J. Geophys. Res.*, 113(B01202). doi:[10.1029/2007jb005004](https://doi.org/10.1029/2007jb005004).

- Cleary, P. W., Pereira, G. G., Lemiale, V., Delle Piane, C., and Clennell, M. B. (2015). Multiscale model for predicting shear zone structure and permeability in deforming rock. *Computational Particle Mechanics*, 3(2):179–199. doi:[10.1007/s40571-015-0073-4](https://doi.org/10.1007/s40571-015-0073-4).
- Correa, A. C. F., Newman, R. B., Naveira, V. P., Serra de Souza, A. L., Araujo, T., da Silva, A. A. C., Soares, A. C., Herwanger, J. V., and Meurer, G. B. (2013). Integrated Modeling for 3D Geomechanics and Coupled Simulation of Fractured Carbonate Reservoir. In *OTC Brasil. Offshore Technology Conference*. doi:[10.4043/24409-ms](https://doi.org/10.4043/24409-ms).
- Cueto-Felgueroso, L., Vila, C., Santillán, D., and Mosquera, J. C. (2018). Numerical Modeling of Injection-Induced Earthquakes Using Laboratory-Derived Friction Laws. *Water Resour. Res.*, 54(12):9833–9859. doi:[10.1029/2017wr022363](https://doi.org/10.1029/2017wr022363).
- Darcy, H. P. G. (1856). Détermination des lois d'écoulement de l'eau à travers le sable. In *Les fontaines publiques de la ville de Dijon*, pages 590–594. V. Dalamont.
- Daxner, T. (2010). Finite Element Modeling of Cellular Materials. In *CISM International Centre for Mechanical Sciences*, pages 47–106. Springer Vienna. doi:[10.1007/978-3-7091-0297-8_2](https://doi.org/10.1007/978-3-7091-0297-8_2).
- Desrues, J., Andò, E., Bésuelle, P., Viggiani, G., Debove, L., Charrier, P., and Toni, J. B. (2017a). Localisation Precursors in Geomaterials? In *Springer Series in Geomechanics and Geoengineering*, pages 3–10. Springer International Publishing. doi:[10.1007/978-3-319-56397-8_1](https://doi.org/10.1007/978-3-319-56397-8_1).
- Desrues, J., Argilaga, A., Pont, S. D., Combe, G., Caillerie, D., and kein Nguyen, T. (2017b). Restoring Mesh Independency in FEM-DEM Multi-scale Modelling of Strain Localization Using Second Gradient Regularization. In *Springer Series in Geomechanics and Geoengineering*, pages 453–457. Springer International Publishing. doi:[10.1007/978-3-319-56397-8_57](https://doi.org/10.1007/978-3-319-56397-8_57).
- Dieterich, J. H. (1979). Modeling of rock friction: 1. Experimental results and constitutive equations. *J. Geophys. Res.*, 84(B5):2161–2168. doi:[10.1029/jb084ib05p02161](https://doi.org/10.1029/jb084ib05p02161).
- Dieterich, J. H. (1992). Earthquake nucleation on faults with rate-and state-dependent strength. *Tectonophysics*, 211(1-4):115–134. doi:[10.1016/0040-1951\(92\)90055-b](https://doi.org/10.1016/0040-1951(92)90055-b).
- Divyathej, M. V., Varun, M., and Rajeev, P. (2016). Analysis of mechanical behavior of 3D printed ABS parts by experiments. *International Journal of Scientific & Engineering Research*, 7(3):116–124.
- Dizon, J. R. C., Espera, A. H., Chen, Q., and Advincula, R. C. (2018). Mechanical characterization of 3D-printed polymers. *Addit. Manuf.*, 20:44–67. doi:[10.1016/j.addma.2017.12.002](https://doi.org/10.1016/j.addma.2017.12.002).
- Dong, H. and Blunt, M. J. (2009). Pore-network extraction from micro-computerized-tomography images. *Physical Review E*, 80(3):036307. doi:[10.1103/physreve.80.036307](https://doi.org/10.1103/physreve.80.036307).
- Dos Santos, M. D. L. and Oliveira, F. R. (2014). Fault Reactivation as Mechanism of Early Water Production in Unconsolidated Sandstones Reservoirs. In *SPE Annual Technical Conference and Exhibition*. Society of Petroleum Engineers. doi:[10.2118/170850-ms](https://doi.org/10.2118/170850-ms).
- Doyen, P. M. (1988). Permeability, conductivity, and pore geometry of sandstone. *J. Geophys. Res.*, 93(B7):7729. doi:[10.1029/jb093ib07p07729](https://doi.org/10.1029/jb093ib07p07729).
- Dunn, D. E., LaFountain, L. J., and Jackson, R. E. (1973). Porosity dependence and mechanism of brittle fracture in sandstones. *J. Geophys. Res.*, 78(14):2403–2417. doi:[10.1029/jb078i014p02403](https://doi.org/10.1029/jb078i014p02403).
- Döhne, F. and Von Kármán, T. (1912). *Ueber Druckwechsel und Stöße bei Maschinen mit Kurbeltrieb*. Springer Berlin Heidelberg.

- Elman, H., Howle, V. E., Shadid, J., Shuttleworth, R., and Tuminaro, R. (2008). A taxonomy and comparison of parallel block multi-level preconditioners for the incompressible Navier–Stokes equations. *J. Comput. Phys.*, 227(3):1790–1808. doi:[10.1016/j.jcp.2007.09.026](https://doi.org/10.1016/j.jcp.2007.09.026).
- Engelder, T. and Fischer, M. P. (1994). Influence of poroelastic behavior on the magnitude of minimum horizontal stress, S_h in overpressured parts of sedimentary basins. *Geology*, 22(10):949–952. doi:[10.1130/0091-7613\(1994\)022<0949:iopbot>2.3.co;2](https://doi.org/10.1130/0091-7613(1994)022<0949:iopbot>2.3.co;2).
- Ergun, S. and Orning, A. A. (1949). Fluid Flow through Randomly Packed Columns and Fluidized Beds. *Industrial & Engineering Chemistry*, 41(6):1179–1184. doi:[10.1021/ie50474a011](https://doi.org/10.1021/ie50474a011).
- Eyre, T. S., Eaton, D. W., Garagash, D. I., Zecevic, M., Venieri, M., Weir, R., and Lawton, D. C. (2019). The role of aseismic slip in hydraulic fracturing–induced seismicity. *Science Advances*, 5(8):eaav7172. doi:[10.1126/sciadv.aav7172](https://doi.org/10.1126/sciadv.aav7172).
- Faulkner, D., Jackson, C., Lunn, R., Schlische, R., Shipton, Z., Wibberley, C., and Withjack, M. (2010). A review of recent developments concerning the structure, mechanics and fluid flow properties of fault zones. *J. Struct. Geol.*, 32(11):1557–1575. doi:[10.1016/j.jsg.2010.06.009](https://doi.org/10.1016/j.jsg.2010.06.009).
- Fereshtenejad, S. and Song, J.-J. (2016). Fundamental Study on Applicability of Powder-Based 3D Printer for Physical Modeling in Rock Mechanics. *Rock Mech. Rock Eng.*, 49(6):2065–2074. doi:[10.1007/s00603-015-0904-x](https://doi.org/10.1007/s00603-015-0904-x).
- Fritzen, F., Forest, S., Böhlke, T., Kondo, D., and Kanit, T. (2012). Computational homogenization of elasto-plastic porous metals. *Int. J. Plast.*, 29:102–119. doi:[10.1016/j.ijplas.2011.08.005](https://doi.org/10.1016/j.ijplas.2011.08.005).
- Gaston, D., Newman, C., Hansen, G., and Lebrun-Grandié, D. (2009). MOOSE: A parallel computational framework for coupled systems of nonlinear equations. *Nucl. Eng. Des.*, 239(10):1768–1778. doi:[10.1016/j.nucengdes.2009.05.021](https://doi.org/10.1016/j.nucengdes.2009.05.021).
- Geers, M. G. D., Kouznetsova, V. G., Matouš, K., and Yvonnet, J. (2017). *Homogenization Methods and Multiscale Modeling: Nonlinear Problems*, pages 1–34. American Cancer Society. doi:[10.1002/9781119176817.ecm2107](https://doi.org/10.1002/9781119176817.ecm2107).
- Gologanu, M., Leblond, J.-B., Perrin, G., and Devaux, J. (1997). Recent Extensions of Gurson’s Model for Porous Ductile Metals. In *Continuum Micromechanics*, pages 61–130. Springer Vienna. doi:[10.1007/978-3-7091-2662-2_2](https://doi.org/10.1007/978-3-7091-2662-2_2).
- Green, R. J. (1972). A plasticity theory for porous solids. *Int. J. Mech. Sci.*, 14(4):215–224. doi:[10.1016/0020-7403\(72\)90063-x](https://doi.org/10.1016/0020-7403(72)90063-x).
- Gresho, P. M. and Sani, R. L. (1987). On pressure boundary conditions for the incompressible Navier-Stokes equations. *Int. J. Numer. Methods Fluids*, 7(10):1111–1145. doi:[10.1002/fld.1650071008](https://doi.org/10.1002/fld.1650071008).
- Guibert, R., Nazarova, M., Horgue, P., Hamon, G., Creux, P., and Debenest, G. (2015). Computational Permeability Determination from Pore-Scale Imaging: Sample Size, Mesh and Method Sensitivities. *Transp. Porous Media*, 107(3):641–656. doi:[10.1007/s11242-015-0458-0](https://doi.org/10.1007/s11242-015-0458-0).
- Gurson, A. L. (1977). Continuum Theory of Ductile Rupture by Void Nucleation and Growth: Part I—Yield Criteria and Flow Rules for Porous Ductile Media. *J. Eng. Mater. Technol.*, 99(1):2–15. doi:[10.1115/1.3443401](https://doi.org/10.1115/1.3443401).
- Hamiel, Y., Lyakhovskiy, V., and Agnon, A. (2004). Coupled evolution of damage and porosity in poroelastic media: theory and applications to deformation of porous rocks. *Geophys. J. Int.*, 156(3):701–713. doi:[10.1111/j.1365-246x.2004.02172.x](https://doi.org/10.1111/j.1365-246x.2004.02172.x).

- Han, R., Shimamoto, T., Hirose, T., Ree, J.-H., and i. Ando, J. (2007). Ultralow Friction of Carbonate Faults Caused by Thermal Decomposition. *Science*, 316(5826):878–881. doi:[10.1126/science.1139763](https://doi.org/10.1126/science.1139763).
- Hashin, Z. and Shtrikman, S. (1963). A variational approach to the theory of the elastic behaviour of multiphase materials. *J. Mech. Phys. Solids*, 11(2):127–140. doi:[10.1016/0022-5096\(63\)90060-7](https://doi.org/10.1016/0022-5096(63)90060-7).
- Heijs, A. W. J. and Lowe, C. P. (1995). Numerical evaluation of the permeability and the Kozeny constant for two types of porous media. *Physical Review E*, 51(5):4346–4352. doi:[10.1103/physreve.51.4346](https://doi.org/10.1103/physreve.51.4346).
- Henson, V. E. and Yang, U. M. (2002). BoomerAMG: A parallel algebraic multigrid solver and preconditioner. *Applied Numerical Mathematics*, 41(1):155–177. doi:[10.1016/s0168-9274\(01\)00115-5](https://doi.org/10.1016/s0168-9274(01)00115-5).
- Hill, R. (1963). Elastic properties of reinforced solids: Some theoretical principles. *J. Mech. Phys. Solids*, 11(5):357–372. doi:[10.1016/0022-5096\(63\)90036-x](https://doi.org/10.1016/0022-5096(63)90036-x).
- Holland, A. A. (2013). Earthquakes Triggered by Hydraulic Fracturing in South-Central Oklahoma. *Bull. Seismol. Soc. Am.*, 103(3):1784–1792. doi:[10.1785/0120120109](https://doi.org/10.1785/0120120109).
- Hood, P. and Taylor, C. (1974). Navier-Stokes equations using mixed interpolation. *Finite Element Method in Flow Problems*, pages 121–132.
- Hoshino, K. (1974). Effect of porosity on the strength of the clastic sedimentary rocks. In *Advances in rock mechanics: Proceedings of the 3rd Congress of International Society of Rock Mechanics, Denver, Colorado, September*, volume IIA, pages 511–516.
- Huang, L., Dyaur, N., and Stewart, R. R. (2015). Elastic properties of 3D-printed physical models: Fluid substitution observations in cracked media. In *SEG Technical Program Expanded Abstracts 2015*. Society of Exploration Geophysicists. doi:[10.1190/segam2015-5915204.1](https://doi.org/10.1190/segam2015-5915204.1).
- Huyakorn, P. S., Taylor, C., Lee, R. L., and Gresho, P. M. (1978). A comparison of various mixed-interpolation finite elements in the velocity-pressure formulation of the Navier-Stokes equations. *Computers & Fluids*, 6(1):25–35. doi:[10.1016/0045-7930\(78\)90004-x](https://doi.org/10.1016/0045-7930(78)90004-x).
- Imperial College Consortium On Pore-Scale Modelling (2014a). Berea Sandstone. doi:[10.6084/m9.figshare.1153794](https://doi.org/10.6084/m9.figshare.1153794).
- Imperial College Consortium On Pore-Scale Modelling (2014b). C1 Carbonate. doi:[10.6084/m9.figshare.1189257](https://doi.org/10.6084/m9.figshare.1189257).
- Imperial College Consortium On Pore-Scale Modelling (2014c). LV60A Sandpack. doi:[10.6084/m9.figshare.1153795](https://doi.org/10.6084/m9.figshare.1153795).
- Ishutov, S., Hasiuk, F. J., Harding, C., and Gray, J. N. (2015). 3D printing sandstone porosity models. *Interpretation*, 3(3):SX49–SX61. doi:[10.1190/int-2014-0266.1](https://doi.org/10.1190/int-2014-0266.1).
- Jaeger, J. C. (2007). *Fundamentals of Rock Mechanics*. Wiley-Blackwell.
- Jardine, R. J., Symes, M. J., and Burland, J. B. (1984). The Measurement of soil stiffness in the triaxial apparatus. *Géotechnique*, 34(3):323–340. doi:[10.1680/geot.1984.34.3.323](https://doi.org/10.1680/geot.1984.34.3.323).
- Jasinski, L., Sangaré, D., Adler, P. M., Mourzenko, V. V., Thovert, J.-F., Gland, N., and Békri, S. (2015). Transport properties of a Bentheim sandstone under deformation. *Physical Review E*, 91(1). doi:[10.1103/physreve.91.013304](https://doi.org/10.1103/physreve.91.013304).

- Jiang, C., Zhao, G.-F., Zhu, J., Zhao, Y.-X., and Shen, L. (2016). Investigation of Dynamic Crack Coalescence Using a Gypsum-Like 3D Printing Material. *Rock Mech. Rock Eng.*, 49(10):3983–3998. doi:[10.1007/s00603-016-0967-3](https://doi.org/10.1007/s00603-016-0967-3).
- Jolley, S. J., Fisher, Q. J., and Ainsworth, R. B. (2010). Reservoir compartmentalization: an introduction. *Geological Society, London, Special Publications*, 347(1):1–8. doi:[10.1144/sp347.1](https://doi.org/10.1144/sp347.1).
- Keller, H. B. (1977). Numerical solution of bifurcation and nonlinear eigenvalue problems, applications of bifurcation theory. *Numerical Solution of Bifurcation and Nonlinear Eigenvalue Problems*, pages 359–384.
- Keranen, K. M., Weingarten, M., Abers, G. A., Bekins, B. A., and Ge, S. (2014). Sharp increase in central Oklahoma seismicity since 2008 induced by massive wastewater injection. *Science*, 345(6195):448–451. doi:[10.1126/science.1255802](https://doi.org/10.1126/science.1255802).
- Kouznetsova, V. G. (2004). *Computational homogenization for the multi-scale analysis of multi-phase materials*. phdthesis, Technische Universiteit Eindhoven.
- Kuhn, H. and Medlin, D., editors (2000). *Mechanical Testing and Evaluation*, volume 8 of *ASM Handbook*. ASM International.
- Lapusta, N. and Rice, J. R. (2003). Nucleation and early seismic propagation of small and large events in a crustal earthquake model. *Journal of Geophysical Research: Solid Earth*, 108(B4). doi:[10.1029/2001jb000793](https://doi.org/10.1029/2001jb000793).
- Lapusta, N., Rice, J. R., Ben-Zion, Y., and Zheng, G. (2000). Elastodynamic analysis for slow tectonic loading with spontaneous rupture episodes on faults with rate- and state-dependent friction. *Journal of Geophysical Research: Solid Earth*, 105(B10):23765–23789. doi:[10.1029/2000jb900250](https://doi.org/10.1029/2000jb900250).
- Larson, R. E. and Higdon, J. J. L. (1989). A periodic grain consolidation model of porous media. *Physics of Fluids A: Fluid Dynamics*, 1(1):38–46. doi:[10.1063/1.857545](https://doi.org/10.1063/1.857545).
- Leblond, J.-B. and Morin, L. (2014). Gurson’s Criterion and Its Derivation Revisited. *J. Appl. Mech.*, 81(5):051012. doi:[10.1115/1.4026112](https://doi.org/10.1115/1.4026112).
- Lesueur, M., Casadiego, M. C., Veveakis, M., and Poulet, T. (2017). Modelling fluid-microstructure interaction on elasto-visco-plastic digital rocks. *Geomechanics for Energy and the Environment*, 12:1–13. doi:[10.1016/j.gete.2017.08.001](https://doi.org/10.1016/j.gete.2017.08.001).
- Lesueur, M., Poulet, T., and Veveakis, M. (2020). Three-scale multiphysics finite element framework (FE3) modelling fault reactivation. *Comput. Methods Appl. Mech. Eng.*, 365:112988. doi:[10.1016/j.cma.2020.112988](https://doi.org/10.1016/j.cma.2020.112988).
- Lin, J., Sari, M., Veveakis, E., and Poulet, T. (2019). A heuristic model inversion for coupled thermo-hydro-mechanical modeling of triaxial experiments. *Comput. Geotech.* doi:[10.31223/osf.io/9gkwd](https://doi.org/10.31223/osf.io/9gkwd).
- L’vov, B. (2007). *Thermal Decomposition of Solids and Melts*, volume 7 of *Hot Topics in Thermal Analysis and Calorimetry*. Springer-Verlag GmbH. doi:[10.1007/978-1-4020-5672-7](https://doi.org/10.1007/978-1-4020-5672-7).
- Mackenzie, J. K. (1950). The Elastic Constants of a Solid containing Spherical Holes. *Proceedings of the Physical Society. Section B*, 63(1):2–11. doi:[10.1088/0370-1301/63/1/302](https://doi.org/10.1088/0370-1301/63/1/302).
- Manwart, C., Aaltosalmi, U., Koponen, A., Hilfer, R., and Timonen, J. (2002). Lattice-Boltzmann and finite-difference simulations for the permeability for three-dimensional porous media. *Physical Review E*, 66(1). doi:[10.1103/physreve.66.016702](https://doi.org/10.1103/physreve.66.016702).

- Marks, P. (2011). 3D printing takes off with the world's first printed plane. *New Sci.*, 211(2823):17–18. doi:[10.1016/s0262-4079\(11\)61817-4](https://doi.org/10.1016/s0262-4079(11)61817-4).
- Marone, C. (1998). Laboratory-derived friction laws and their application to seismic faulting. *Annu. Rev. Earth Planet. Sci.*, 26(1):643–696. doi:[10.1146/annurev.earth.26.1.643](https://doi.org/10.1146/annurev.earth.26.1.643).
- Meagher, D. (1982). Geometric modeling using octree encoding. *Computer Graphics and Image Processing*, 19(2):129–147. doi:[10.1016/0146-664x\(82\)90104-6](https://doi.org/10.1016/0146-664x(82)90104-6).
- Melis, P. E. C., Marrink, S., Thallmair, S., Blass, A., Spandan Arza, V., Nijkamp, J., Janssen, N., and Závodszy, G. (2018). On the use of 3D printing for scientific visualization. Technical report, 3DATAPRINT - SURF Open Innovation Lab.
- Mironov, V., Boland, T., Trusk, T., Forgacs, G., and Markwald, R. R. (2003). Organ printing: computer-aided jet-based 3D tissue engineering. *Trends Biotechnol.*, 21(4):157–161. doi:[10.1016/s0167-7799\(03\)00033-7](https://doi.org/10.1016/s0167-7799(03)00033-7).
- Mohr, O. (1900). Welche Umstände bedingen die Elastizitätsgrenze und den Bruch eines Materials. *Zeitschrift des Vereins Deutscher Ingenieure*, 46(1524-1530):1572–1577.
- Morin, R. H. (2006). Negative correlation between porosity and hydraulic conductivity in sand-and-gravel aquifers at Cape Cod, Massachusetts, USA. *J. Hydrol.*, 316(1-4):43–52. doi:[10.1016/j.jhydrol.2005.04.013](https://doi.org/10.1016/j.jhydrol.2005.04.013).
- Morris, A., Ferrill, D. A., and Henderson, D. B. (1996). Slip-tendency analysis and fault reactivation. *Geology*, 24(3):275. doi:[10.1130/0091-7613\(1996\)024<0275:staafr>2.3.co;2](https://doi.org/10.1130/0091-7613(1996)024<0275:staafr>2.3.co;2).
- Mostaghimi, P., Blunt, M. J., and Bijeljic, B. (2012). Computations of Absolute Permeability on Micro-CT Images. *Math. Geosci.*, 45(1):103–125. doi:[10.1007/s11004-012-9431-4](https://doi.org/10.1007/s11004-012-9431-4).
- Nacht, P. K., De Oliveira, M., Roehl, D. M., and Costa, A. M. (2010). Investigation of geological fault reactivation and opening. *Mecánica Computacional*, XXIX:8687–8697.
- Narváez, A., Yazdchi, K., Luding, S., and Harting, J. (2013). From creeping to inertial flow in porous media: a lattice Boltzmann–finite element study. *J. Stat. Mech.: Theory Exp.*, 2013(02):2–38. doi:[10.1088/1742-5468/2013/02/p02038](https://doi.org/10.1088/1742-5468/2013/02/p02038).
- Ngwenya, B. T., Kwon, O., Elphick, S. C., and Main, I. G. (2003). Permeability evolution during progressive development of deformation bands in porous sandstones. *Journal of Geophysical Research: Solid Earth*, 108(B7). doi:[10.1029/2002jb001854](https://doi.org/10.1029/2002jb001854).
- Nitka, M., Combe, G., Dascalu, C., and Desrues, J. (2011). Two-scale modeling of granular materials: a DEM-FEM approach. *Granular Matter*, 13(3):277–281. doi:[10.1007/s10035-011-0255-6](https://doi.org/10.1007/s10035-011-0255-6).
- Olsson, R. and Barton, N. (2001). An improved model for hydromechanical coupling during shearing of rock joints. *Int. J. Rock Mech. Min. Sci.*, 38(3):317–329. doi:[10.1016/s1365-1609\(00\)00079-4](https://doi.org/10.1016/s1365-1609(00)00079-4).
- Parker, S. P. (2003). *McGraw-Hill Dictionary of Scientific and Technical Terms*. New York : McGraw-Hill, sixth edition.
- Peterie, S. L., Miller, R. D., Intfen, J. W., and Gonzales, J. B. (2018). Earthquakes in Kansas Induced by Extremely Far-Field Pressure Diffusion. *Geophys. Res. Lett.*, 45(3):1395–1401. doi:[10.1002/2017gl076334](https://doi.org/10.1002/2017gl076334).

- Peterson, J. W., Lindsay, A. D., and Kong, F. (2018). Overview of the incompressible Navier–Stokes simulation capabilities in the MOOSE framework. *Adv. Eng. Software*, 119:68–92. doi:[10.1016/j.advengsoft.2018.02.004](https://doi.org/10.1016/j.advengsoft.2018.02.004).
- Petrusch, J., Meier, F., Friess, H., and Steinfeld, A. (2008). Tomography based determination of permeability, Dupuit–Forchheimer coefficient, and interfacial heat transfer coefficient in reticulate porous ceramics. *Int. J. Heat Fluid Flow*, 29(1):315–326. doi:[10.1016/j.ijheatfluidflow.2007.09.001](https://doi.org/10.1016/j.ijheatfluidflow.2007.09.001).
- Piane, C. D., Clennell, M. B., Keller, J. V., Giwelli, A., and Luzin, V. (2017). Carbonate hosted fault rocks: A review of structural and microstructural characteristic with implications for seismicity in the upper crust. *J. Struct. Geol.*, 103:17–36. doi:[10.1016/j.jsg.2017.09.003](https://doi.org/10.1016/j.jsg.2017.09.003).
- Pizzino, L., Quattrocchi, F., Cinti, D., and Galli, G. (2004). Fluid geochemistry along the Eliki and Aigion seismogenic segments (Gulf of Corinth, Greece). *Comptes Rendus Geoscience*, 336(4-5):367–374. doi:[10.1016/j.crte.2003.11.012](https://doi.org/10.1016/j.crte.2003.11.012).
- Popescu, D., Zapciu, A., Amza, C., Baciu, F., and Marinescu, R. (2018). FDM process parameters influence over the mechanical properties of polymer specimens: A review. *Polym. Test.*, 69:157–166. doi:[10.1016/j.polymertesting.2018.05.020](https://doi.org/10.1016/j.polymertesting.2018.05.020).
- Poulet, T., Lesueur, M., Hue, L., Veveakis, M., and Regenauer-Lieb, K. (2018a). Modelling the formation of Bonanza-grade ore deposits. In *TIGeR Conference*.
- Poulet, T., Lesueur, M., Veveakis, M., and Regenauer-Lieb, K. (2018b). Propagating mineralising fluids through chemical shear zones. In *AGU Fall Meeting*.
- Poulet, T., Paesold, M., and Veveakis, M. (2017). Multi-Physics Modelling of Fault Mechanics Using REDBACK: A Parallel Open-Source Simulator for Tightly Coupled Problems. *Rock Mech. Rock Eng.*, 50(3):733–749. doi:[10.1007/s00603-016-0927-y](https://doi.org/10.1007/s00603-016-0927-y).
- Poulet, T., Veveakis, E., Regenauer-Lieb, K., and Yuen, D. A. (2014a). Thermo-poro-mechanics of chemically active creeping faults: 3. The role of serpentinite in episodic tremor and slip sequences, and transition to chaos. *Journal of Geophysical Research: Solid Earth*, 119(6):4606–4625. doi:[10.1002/2014JB011004](https://doi.org/10.1002/2014JB011004).
- Poulet, T. and Veveakis, M. (2016). A viscoplastic approach for pore collapse in saturated soft rocks using REDBACK: An open-source parallel simulator for Rock mEchanics with Dissipative feedBACKs. *Comput. Geotech.*, 74:211–221. doi:[10.1016/j.compgeo.2015.12.015](https://doi.org/10.1016/j.compgeo.2015.12.015).
- Poulet, T., Veveakis, M., Herwegh, M., Buckingham, T., and Regenauer-Lieb, K. (2014b). Modeling episodic fluid-release events in the ductile carbonates of the Glarus thrust. *Geophys. Res. Lett.*, 41(20):7121–7128. doi:[10.1002/2014gl061715](https://doi.org/10.1002/2014gl061715).
- Rattez, H., Stefanou, I., and Sulem, J. (2018). The importance of Thermo-Hydro-Mechanical couplings and microstructure to strain localization in 3D continua with application to seismic faults. Part I: Theory and linear stability analysis. *J. Mech. Phys. Solids*, 115:54–76. doi:[10.1016/j.jmps.2018.03.004](https://doi.org/10.1016/j.jmps.2018.03.004).
- Reches, Z. and Lockner, D. A. (1994). Nucleation and growth of faults in brittle rocks. *Journal of Geophysical Research: Solid Earth*, 99(B9):18159–18173. doi:[10.1029/94jb00115](https://doi.org/10.1029/94jb00115).
- Regenauer-Lieb, K. and Yuen, D. A. (1998). Rapid conversion of elastic energy into plastic shear heating during incipient necking of the lithosphere. *Geophys. Res. Lett.*, 25(14):2737–2740. doi:[10.1029/98GL02056](https://doi.org/10.1029/98GL02056).
- Ribes, A., Bruneton, A., and Geay, A. (2017). SALOME: an Open-Source simulation platform integrating ParaView. doi:[10.13140/rg.2.2.12107.08485](https://doi.org/10.13140/rg.2.2.12107.08485).

- Rice, J. R. (2006). Heating and weakening of faults during earthquake slip. *Journal of Geophysical Research: Solid Earth*, 111(B5). doi:[10.1029/2005jb004006](https://doi.org/10.1029/2005jb004006).
- Roscoe, K. H. and Burland, J. B. (1968). On the generalised stress-strain behaviour of ‘wet’ clay. In *Engineering Plasticity*, pages 535–609. Cambridge University Press.
- Ross, C. T. F. (1999). *Mechanics of Solids*. Woodhead Publishing.
- Rutqvist, J., Birkholzer, J., Cappa, F., and Tsang, C.-F. (2007). Estimating maximum sustainable injection pressure during geological sequestration of CO₂ using coupled fluid flow and geomechanical fault-slip analysis. *Energy Convers. Manage.*, 48(6):1798–1807. doi:[10.1016/j.enconman.2007.01.021](https://doi.org/10.1016/j.enconman.2007.01.021).
- Sari, M. (2019). *A Multi-Physics Visco-Plasticity Theory for Porous Sedimentary Rocks*. PhD thesis, University of New South Wales.
- Scheidegger, A. E. (1974). *The physics of flow through porous media*. University of Toronto Press.
- Scholz, C. H. (2002). *The Mechanics of Earthquakes and Faulting*. Cambridge University Press. doi:[10.1017/cbo9780511818516](https://doi.org/10.1017/cbo9780511818516).
- Schroeder, W. J. and Martin, K. M. (2005). The Visualization Toolkit. In *Visualization Handbook*, pages 593–614. Elsevier. doi:[10.1016/b978-012387582-2/50032-0](https://doi.org/10.1016/b978-012387582-2/50032-0).
- Segall, P. (1989). Earthquakes triggered by fluid extraction. *Geology*, 17(10):942–946. doi:[10.1130/0091-7613\(1989\)017<0942:etbfe>2.3.co;2](https://doi.org/10.1130/0091-7613(1989)017<0942:etbfe>2.3.co;2).
- Segall, P., Grasso, J.-R., and Mossop, A. (1994). Poroelastic stressing and induced seismicity near the Lacq gas field, southwestern France. *J. Geophys. Res.*, 99(B8):15423–15438. doi:[10.1029/94jb00989](https://doi.org/10.1029/94jb00989).
- Segall, P. and Pollard, D. D. (1983). Nucleation and growth of strike slip faults in granite. *J. Geophys. Res.*, 88(B1):555. doi:[10.1029/jb088ib01p00555](https://doi.org/10.1029/jb088ib01p00555).
- Serra de Souza, A. L. and Lima Falcão, F. O. (2015). R&D in Reservoir Geomechanics in Brazil: Perspectives and Challenges. In *OTC Brasil*. Offshore Technology Conference. doi:[10.4043/26205-ms](https://doi.org/10.4043/26205-ms).
- Sibson, R. H., Robert, F., and Poulsen, K. H. (1988). High-angle reverse faults, fluid-pressure cycling, and mesothermal gold-quartz deposits. *Geology*, 16(6):551–555. doi:[10.1130/0091-7613\(1988\)016<0551:harffp>2.3.co;2](https://doi.org/10.1130/0091-7613(1988)016<0551:harffp>2.3.co;2).
- Smilauer, V., Catalano, E., Chareyre, B., Dorofeenko, S., Duriez, J., Dyck, N., Elias, J., Er, B., Eulitz, A., Gladky, A., Guo, N., Jakob, C., Kneib, F., Kozicki, J., Marzougui, D., Maurin, R., Modenese, C., Scholtes, L., Sibille, L., Stransky, J., Sweijen, T., Thoeni, K., and Yuan, C. (2015). *Yade Documentation 2Nd Ed*. Zenodo. doi:[10.5281/zenodo.34073](https://doi.org/10.5281/zenodo.34073).
- Springmann, M. and Kuna, M. (2005). Identification of material parameters of the Gurson–Tvergaard–Needleman model by combined experimental and numerical techniques. *Computational Materials Science*, 33(4):501–509. doi:[10.1016/j.commatsci.2005.02.002](https://doi.org/10.1016/j.commatsci.2005.02.002).
- Stokes, G. G. (1845). On the theories of the internal friction of fluids in motion, and of the equilibrium and motion of elastic solids. *Transactions of the Cambridge Philosophical Society*, 8:287–319.

- Sulem, J. and Famin, V. (2009). Thermal decomposition of carbonates in fault zones: Slip-weakening and temperature-limiting effects. *J. Geophys. Res.*, 114(B3). doi:[10.1029/2008jb006004](https://doi.org/10.1029/2008jb006004).
- Sulem, J., Vardoulakis, I., Ouffroukh, H., and Perdikatsis, V. (2005). Thermo-poro-mechanical properties of the Aigion fault clayey gouge-Application to the analysis of shear heating and fluid pressurization. *Soils and Foundations*, 45(2):97–108. doi:[10.3208/sandf.45.2_97](https://doi.org/10.3208/sandf.45.2_97).
- Talabi, O. and Blunt, M. J. (2010). Pore-scale network simulation of NMR response in two-phase flow. *Journal of Petroleum Science and Engineering*, 72(1-2):1–9. doi:[10.1016/j.petrol.2010.01.013](https://doi.org/10.1016/j.petrol.2010.01.013).
- Taylor, C. and Hood, P. (1973). A numerical solution of the Navier-Stokes equations using the finite element technique. *Computers & Fluids*, 1(1):73–100. doi:[10.1016/0045-7930\(73\)90027-3](https://doi.org/10.1016/0045-7930(73)90027-3).
- Taylor, D. W. (1948). *Fundamentals of Soil Mechanics*, volume 66. LWW. doi:[10.1097/00010694-194808000-00008](https://doi.org/10.1097/00010694-194808000-00008).
- Teklu, T. W., Zhou, Z., Li, X., and Abass, H. (2016). Experimental Investigation on Permeability and Porosity Hysteresis in Low-Permeability Formations. In *SPE Low Perm Symposium*. Society of Petroleum Engineers. doi:[10.2118/180226-ms](https://doi.org/10.2118/180226-ms).
- Terzaghi, K. v. (1923). Die berechnung der durchlassigkeitsziffer des tones aus dem verlauf der hydrodynamischen spannungserscheinungen. 132:125–138.
- Teufel, L. W., Rhett, D. W., and Farrell, H. E. (1991). Effect of Reservoir Depletion And Pore Pressure Drawdown On In Situ Stress And Deformation In the Ekofisk Field, North Sea. In *The 32nd U.S. Symposium on Rock Mechanics (USRMS)*. American Rock Mechanics Association.
- Tezduyar, T., Mittal, S., Ray, S., and Shih, R. (1992). Incompressible flow computations with stabilized bilinear and linear equal-order-interpolation velocity-pressure elements. *Comput. Methods Appl. Mech. Eng.*, 95(2):221–242. doi:[10.1016/0045-7825\(92\)90141-6](https://doi.org/10.1016/0045-7825(92)90141-6).
- Toro, G. D., Han, R., Hirose, T., Paola, N. D., Nielsen, S., Mizoguchi, K., Ferri, F., Cocco, M., and Shimamoto, T. (2011). Fault lubrication during earthquakes. *Nature*, 471(7339):494–498. doi:[10.1038/nature09838](https://doi.org/10.1038/nature09838).
- Tse, S. T. and Rice, J. R. (1986). Crustal earthquake instability in relation to the depth variation of frictional slip properties. *J. Geophys. Res.*, 91(B9):9452. doi:[10.1029/jb091ib09p09452](https://doi.org/10.1029/jb091ib09p09452).
- Tung, R., Poulet, T., Alevizos, S., Veveakis, E., and Regenauer-Lieb, K. (2017). Shear heating in creeping faults changes the onset of convection. *Geophys. J. Int.*, 211(1):270–283. doi:[10.1093/gji/ggx295](https://doi.org/10.1093/gji/ggx295).
- Tvergaard, V. (1981). Influence of voids on shear band instabilities under plane strain conditions. *Int. J. Fract.*, 17(4):389–407. doi:[10.1007/bf00036191](https://doi.org/10.1007/bf00036191).
- Veveakis, E., Alevizos, S., and Poulet, T. (2017). Episodic Tremor and Slip (ETS) as a chaotic multiphysics spring. *Phys. Earth Planet. Inter.*, 264:20–34. doi:[10.1016/j.pepi.2016.10.002](https://doi.org/10.1016/j.pepi.2016.10.002).
- Veveakis, E., Alevizos, S., and Vardoulakis, I. (2010). Chemical reaction capping of thermal instabilities during shear of frictional faults. *J. Mech. Phys. Solids*, 58(9):1175–1194. doi:[10.1016/j.jmps.2010.06.010](https://doi.org/10.1016/j.jmps.2010.06.010).

- Veveakis, E., Poulet, T., and Alevizos, S. (2014). Thermo-poro-mechanics of chemically active creeping faults: 2. Transient considerations. *Journal of Geophysical Research: Solid Earth*, 119(6):4583–4605. doi:[10.1002/2013jb010071](https://doi.org/10.1002/2013jb010071).
- Wang, K. and Sun, W. (2018). A multiscale multi-permeability poroplasticity model linked by recursive homogenizations and deep learning. *Comput. Methods Appl. Mech. Eng.*, 334:337–380. doi:[10.1016/j.cma.2018.01.036](https://doi.org/10.1016/j.cma.2018.01.036).
- Whitaker, S. (1986). Flow in porous media I: A theoretical derivation of Darcy's law. *Transp. Porous Media*, 1(1):3–25. doi:[10.1007/bf01036523](https://doi.org/10.1007/bf01036523).
- Wibberley, C. A. J., Yielding, G., and Di Toro, G. (2008). Recent advances in the understanding of fault zone internal structure: a review. *Geological Society, London, Special Publications*, 299(1):5–33. doi:[10.1144/sp299.2](https://doi.org/10.1144/sp299.2).
- Wilson, M. P., Foulger, G. R., Gluyas, J. G., Davies, R. J., and Julian, B. R. (2017). Hi-Quake: The Human-Induced Earthquake Database. *Seismol. Res. Lett.*, 88(6):1560–1565. doi:[10.1785/0220170112](https://doi.org/10.1785/0220170112).
- Wiprut, D. and Zoback, M. D. (2000). Fault reactivation and fluid flow along a previously dormant normal fault in the northern North Sea. *Geology*, 28(7):595–598. doi:[10.1130/0091-7613\(2000\)28<595:fraffa>2.0.co;2](https://doi.org/10.1130/0091-7613(2000)28<595:fraffa>2.0.co;2).
- Wong, R. and Li, Y. (2001). A Deformation-Dependent Model for Permeability Changes in Oil Sand due to Shear Dilation. *J. Can. Pet. Technol.*, 40(08). doi:[10.2118/01-08-03](https://doi.org/10.2118/01-08-03).
- Xie, S. Y. and Shao, J. F. (2006). Elastoplastic deformation of a porous rock and water interaction. *Int. J. Plast.*, 22(12):2195–2225. doi:[10.1016/j.ijplas.2006.03.002](https://doi.org/10.1016/j.ijplas.2006.03.002).
- Xiong, Q., Baychev, T. G., and Jivkov, A. P. (2016). Review of pore network modelling of porous media: Experimental characterisations, network constructions and applications to reactive transport. *J. Contam. Hydrol.*, 192:101–117. doi:[10.1016/j.jconhyd.2016.07.002](https://doi.org/10.1016/j.jconhyd.2016.07.002).
- Yoon, H., Kang, Q., and Valocchi, A. J. (2015). Lattice Boltzmann-Based Approaches for Pore-Scale Reactive Transport. *Rev. Mineral. Geochem.*, 80(1):393–431. doi:[10.2138/rmg.2015.80.12](https://doi.org/10.2138/rmg.2015.80.12).
- Zabaras, N. and Samanta, D. (2004). A stabilized volume-averaging finite element method for flow in porous media and binary alloy solidification processes. *Int. J. Numer. Methods Eng.*, 60(6):1103–1138. doi:[10.1002/nme.998](https://doi.org/10.1002/nme.998).
- Zhang, Y., Clennell, M. B., Delle Piane, C., Ahmed, S., and Sarout, J. (2016). Numerical modelling of fault reactivation in carbonate rocks under fluid depletion conditions – 2D generic models with a small isolated fault. *J. Struct. Geol.*, 93:17–28. doi:[10.1016/j.jsg.2016.10.002](https://doi.org/10.1016/j.jsg.2016.10.002).
- Zick, A. A. and Homsy, G. M. (1982). Stokes flow through periodic arrays of spheres. *J. Fluid Mech.*, 115:13–26. doi:[10.1017/s0022112082000627](https://doi.org/10.1017/s0022112082000627).
- Zoback, M. and Zinke, J. (2002). Production-induced Normal Faulting in the Valhall and Ekofisk Oil Fields. *Pure Appl. Geophys.*, 159(1):403–420. doi:[10.1007/978-3-0348-8179-1_17](https://doi.org/10.1007/978-3-0348-8179-1_17).
- Zoback, M. D. and Gorelick, S. M. (2012). Earthquake triggering and large-scale geologic storage of carbon dioxide. *Proceedings of the National Academy of Sciences*, 109(26):10164–10168. doi:[10.1073/pnas.1202473109](https://doi.org/10.1073/pnas.1202473109).

Appendix A

Bezier interpolation algorithm

We avoid a linear interpolation which would not account for the peak permeability values at the centre of the shear zone very well (see Fig. 4.4). Instead, we chose an interpolation using Bezier curves, which allows us to capture both the peak of the bell curve (since one of the interpolation points is exactly at the centre of the fault) and reduce the number of sampling points to a minimum.

The interpolation between the sampling points is essentially one dimensional across the fault and is therefore well adapted for Bezier curves within each segment, which are characterised by the location of their anchor points, which fix the value of the interpolation function at those points, as well as control points, which determine the tangent of the function at the anchor points. Every cubic Bezier segment is defined by the parametric equation:

$$\mathbf{B}(t) = (1-t)^3\mathbf{A}_0 + 3(1-t)^2t\mathbf{C}_1 + 3(1-t)t^2\mathbf{C}_2 + t^3\mathbf{A}_3, 0 \leq t \leq 1 \quad (\text{A.1})$$

where $\mathbf{A}_0(x_0, y_0)$ and $\mathbf{A}_3(x_3, y_3)$ are the two (end) anchor points and $\mathbf{C}_1(x_1, y_1)$ and $\mathbf{C}_2(x_2, y_2)$ their respective control points. Varying the variable $0 \leq t \leq 1$ draws the segment from \mathbf{A}_0 (for $t = 0$) to \mathbf{A}_3 (for $t = 1$). For the case we're interested in, permeability remains a function of the distance x across the fault. For a given value of x we can then identify easily the corresponding segment and the value of the t parameter, solution of the equation

$$(1-t)^3x_0 + 3(1-t)^2tx_1 + 3(1-t)t^2x_2 + t^3x_3 - x = 0 \quad (\text{A.2})$$

which can be solved with a Newton Raphson algorithm up to a numerical tolerance to get the corresponding value of interpolated permeability with Eq. A.1.

We select every pair of consecutive sampling points as anchor points and introduce two control points in between to ensure an overall smooth curve, but also a nicely defined peak at the centre of the fault and flat tangents at the extremities. As such, most of the control points are positioned on the tangent of the parabolic curve passing through the corresponding anchor point considered and its two neighbouring anchor points (see Fig. A.1a). For the segments at the extremities, which have no neighbour anchor points on one side, a horizontal tangent is selected

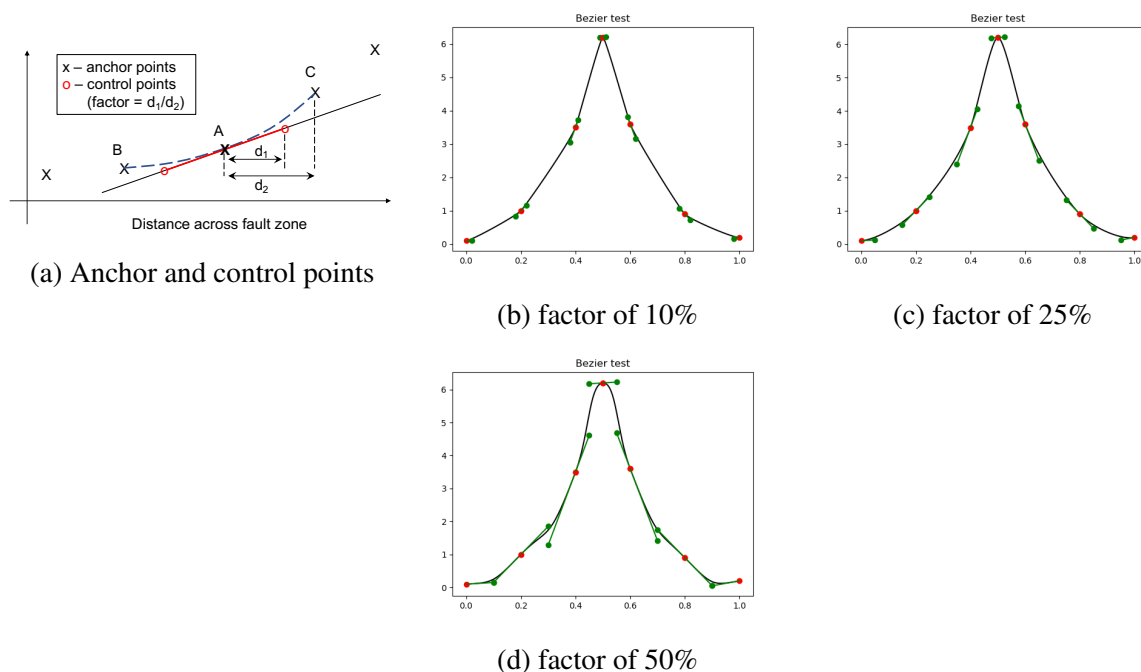
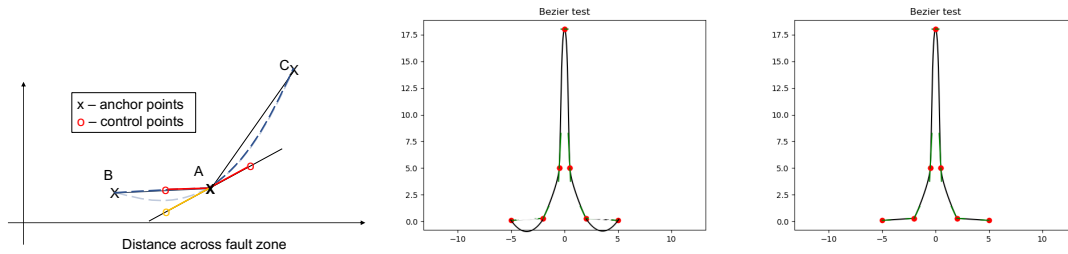


Fig. A.1 Comparison of different weights used to calculate the distance of the control points to the anchor point in the Bezier interpolation of the permeability profile.

to reflect a constant porosity away from the fault zone. Finally, the control points around the anchor point at the centre of the fault zone are selected to generate horizontal tangents in order to capture the peak at the centre. Some flexibility remains to control the distance between the control points and their respective anchor point. We fix that distance as a fraction of the length of the corresponding segment, as shown in Figs. A.1b-A.1c-A.1d where respective factors of 0.1, 0.25 and 0.5 are tested, and select the value of 0.25 for the remainder of the study.

There remains a potential problem with the position of the control points on the tangent of the parabolic curve passing through three consecutive anchor points, when the interpolated function marks a sharp peak at the centre, as is the case during a reactivation event. Indeed, in such cases where the interpolated function suddenly picks up, there is a risk of undershooting when following the parabolic guide line as shown in Fig. A.2a. In this case, we chose the control points on the linear segment connecting two anchor points (A-B on Fig. A.2a) when the following anchor point (C) is such that the angle \widehat{ABC} falls below six degrees. Fig. A.2b illustrates the problem we would encounter without this correction in the presence of a sharp permeability peak, with interpolated value falling below the limit values, which is unrealistic. Fig. A.2c shows the corrected profile, which compares well with the shape of the porosity profile.

When integrated in the meso/macro-scale framework, the Bezier algorithm provides overall a good interpolation for the profile of permeability outputted in our fault reactivation simulations, as shown in Fig. A.3 where Bezier matches well the non-interpolated law. It represents a great advantage over a simple linear interpolation, particularly providing a much better match in Fig. A.3b.



(a) Control point selection on (b) Permeability profile using (c) Permeability profile using linear segment rather than on parabolic tangents on the first linear tangents for the first and the tangent of the parabolic point that makes the permeabil- last segment. curve to avoid undershooting. ity in the first segment reach lower than the initial value.

Fig. A.2 Problem (left) and solution (right) with the tangents used for the Bezier interpolation of the permeability profile.

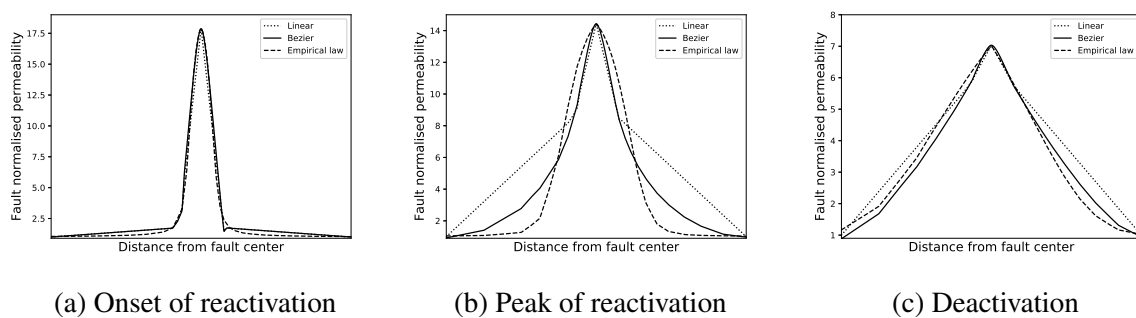


Fig. A.3 Comparison of the profile of permeability across of the fault at different times for a fault reactivation simulation interpolated linearly or with Bezier between the same five sampling points. The two interpolated laws are compared with an empirical law defined as $\frac{1-\phi_0}{1-\phi} \phi^{1.1}$